

INSTITUT DE PHYSIQUE DU GLOBE DE PARIS

SORBONNE PARIS CITE

Ecole Doctorale des Sciences de la Terre

Thèse présentée pour obtenir le titre de
Docteur de l'Institut de Physique du Globe de Paris
Spécialité: Géophysique

# ANALYSIS OF UNUSUAL EARTHQUAKE AND TREMOR SEISMICITY AT THE MENDOCINO TRIPLE JUNCTION AND PARKFIELD, CALIFORNIA

***Aurélie Guilhem***

Thèse en co-tutelle dirigée par Douglas S. Dreger (University of California, Berkeley)
et Jean-Paul Montagner (Institut de Physique du Globe de Paris)

Soutenance prévue le 28 mars 2012

Jury :

| | | |
|---|---|---|
| **Nikolai Shapiro** | Institut de Physique du Globe de Paris | **Président** |
| **Michel Campillo** | Université Joseph Fourier de Grenoble | **Rapporteur** |
| **Luis Rivera** | Ecole et Observatoire des Sciences de la Terre - Strasbourg | **Rapporteur** |
| **Raul Madariaga** | Ecole Normale Supérieure de Paris | **Examinateur** |
| **Douglas S. Dreger** | University of California, Berkeley | **Co-directeur de thèse** |
| **Jean-Paul Montagner** | Institut de Physique du Globe de Paris | **Co-directeur de thèse** |

# Résumé

La détection et l'analyse des évènements sismiques dits inhabituels tels que les séismes lents de la région du point triple de Mendocino ainsi que les trémors non volcaniques et les multiplets près de Parkfield – Cholame, peuvent permettre d'obtenir une image plus précise et une meilleure compréhension de la rhéologie des failles, de leur mécanismes, et plus généralement de la tectonique active de Californie. La modélisation de séismes lents pour lesquels les magnitudes ($M_w$ et $M_L$) à hautes et basses fréquences différent, indique que cette différence provient de la source sismique plutôt que de la propagation des ondes dans un milieu fortement atténué. Cependant, le nombre restreint de ces évènements limite leur étude ainsi qu'à une plus grande échelle, une interprétation précise des processus complexes ayant lieu dans cette région de Mendocino. Nous proposons une nouvelle procédure qui utilise un scanning continu des formes d'ondes filtrées à longues périodes et des inversions de tenseurs des moments pour la détection automatique et la caractérisation des séismes réguliers et inhabituels qui ont lieu dans la région, et ayant des magnitudes plus grandes que 3,5. Une approche similaire est proposée pour la détection rapide de forts tremblements de terre le long de la zone de subduction des Cascades et au Japon. Celle-ci prend en compte des fonctions de Green combinées pour une interprétation proche de ruptures finies dans une technique d'inversion de point source. De plus, cette méthode peut être potentiellement incluse dans de futurs systèmes d'alerte aux séismes et aux tsunamis.

Les trémors non volcaniques d'un autre coté, près de Parkfield, donnent des informations sur les variations du champ de contraintes dans les zones de failles à grande profondeur et par conséquence donnent des indications sur un possible chargement des contraintes le long de la faille de San Andréas à proximité de la zone de rupture du séisme de Fort Tejon qui a eu lieu en 1857. Les trémors sont en effet modulés par de faibles variations des contraintes (de l'ordre du kPa), transmises par des séismes locaux, régionaux, et/ou télésismiques. Comprendre et quantifier l'activité des trémors est essentiel pour une meilleure compréhension de la physique des tremblements de terre et des processus de faille tels que la nucléation de séismes et leur dépendance vis-à-vis de l'état des contraintes. Des épisodes de trémors d'un autre coté, permettent d'illustrer de profonds glissements lents ayant des magnitudes équivalentes à 5 sur l'échelle de Richter le long de la faille de San Andréas, alors qu'aucune autre donnée n'a pour le moment permis de les mettre en valeur. Ceci démontre que l'occurrence de grands évènements sismiques peut être, à l'avenir, mieux comprise à l'aide de la modélisation de micro-séismes atypiques, mais ayant des temps de récurrence plus courts.

Comprendre les caractéristiques de la sismicité dite inhabituelle de la Californie du Nord permet d'obtenir des aperçus sur les processus responsables des tremblements de terre, petits et grands, de cette région. Et cela peut aider dans le futur la communauté sismologique dans pour le développement de meilleurs modèles de tremblements de terre.

# Abstract

The detection and the analysis of unusual seismic events such as slow/low-stress-drop earthquakes in the Mendocino Triple Junction (MTJ), and nonvolcanic tremors and repeating earthquakes near Parkfied-Cholame can be used to provide a clearer picture and a better understanding of fault rheology, mechanics, and active tectonics in California. Modeling of cataloged slow earthquakes, which show large high-frequency/low-frequency magnitude differentials, indicates that the differences come from the source rather than from strongly attenuated propagation paths. Because the restricted number of these events limits their study and a precise comprehension of the complex processes occurring in the MTJ, a new procedure is proposed using continuous scanning of long-period seismic waveforms and moment tensor inversions to automatically detect and characterize regular and slow events, with magnitude larger than 3.5 occurring in the region. A similar approach using quasi-finite-source Green's functions in a point-source inversion method is proposed for the fast detection and characterization of large and potentially tsunamigenic earthquakes along the Cascadia Subduction Zone as well as in other subduction zone regions such as offshore Japan. Furthermore, this approach has the potential to be included in future earthquake and tsunami early warning systems.

Nonvolcanic tremors on the other hand, near Parkfield, inform on the variations in the state of stress in the deep fault zone and as a consequence in possible loading of the San Andreas Fault (SAF) at the proximity of the 1857 Fort Tejon earthquake rupture. Tremors are indeed strongly modulated by small stress changes (i.e. in the order of kPa) transmitted by local and regional earthquakes into their source region, below the seismogenic zone. The effects on tremors can last from a few seconds to several years after local, regional, and/or teleseismic earthquakes. Understanding and quantifying the tremor activity is essential for understanding the physics underlying the earthquake and fault zone processes such as earthquake nucleation, stress dependences, and state of fault stress. Episodes of tremors are found for example to exhibit deep M~5 slow slip events along the SAF, where no other datasets have yet revealed them. Hence, the occurrence of large events might be better understood through modeling of atypical, and numerous micro-earthquakes, whose recurrence times are shorter.

Understanding the characteristics of the unusual seismicity in northern California gives insights on the processes responsible for the occurrence of regular small and large earthquakes in the region that might help the seismological community to develop better earthquake forecasting models in the future.

*"Quand on veut, on peut." - "Where there is a will there is a way."*

A ma famille - To my family.

# Contents

# List of Figures

# List of Tables

# Acknowledgments

My journey at Berkeley started in an unexpected manner with a 6-month internship on nonvolcanic tremors in the Berkeley Seismological Laboratory (BSL) during my master at ENS-Paris in 2005. This work fascinated me and I wanted to learn more about it. My very first thank-you goes to Barbara Romanowicz who gave me six amazing months for my master internship and who later pushed me to apply for a PhD here. She also convinced me to accept the offer when I was getting cold feet because I was already afraid to fail the qualifying exam. Barbara, you have helped me so much and you have been so generous with me during all these years that I will always be very grateful to you.

I would like to express my most sincere thanks to Doug Dreger, the best advisor I could have in these projects! Doug, you have shown me outstanding patience, understanding, knowledge, and help during these 5+ years working with you. You have never made me feel bad when my results were not as good as expected and instead you have always encouraged me, especially when I thought that things were impossible. However, I cannot tell you how much I disliked one of your expressions: "You will figure it out". But you were right, I did eventually figure these things out and it made me move forward. As a longtime supporter of the 49ers, you showed me your passion for the football, but I am sorry to say that I will continue to call it "American football".

I am very thankful to my second advisor in this dissertation, Bob Nadeau. Bob, you have been the person with who I have worked the most at Berkeley. I am very grateful to have had the chance to continue to work with you on tremors at the time they became such an exciting research topic. You are one of a kind researcher who has fathered so many great discoveries especially with the repeating earthquakes and nonvolcanic tremors near Parkfield. I am sure that like you said, you will discover something new and exciting for our science. Working with you has been a pleasure. You helped me getting better in seismology, active tectonics, and with my AWK scripts that you are the guru of!

I also would like to thank Roland Bürgmann for being a very encouraging advisor and professor during my stay at Berkeley. It has been my pleasure to work with you and to join your journal club. I would like to add here my co-director in IPGP, Jean-Paul Montagner who helped me with my co-direction idea in order to keep a foot in France despite my oversea study. I truly appreciate the discussions we have had in your office in Paris and during the conferences we both went to.

My stay in Berkeley would not have been the same without the incredible graduate students of the BSL. First of all, my special thanks go to all the students of Doug: Ahyi Kim, Sean Ford, Andrea Chiang, Dennise Templeton, and Junkie Rhie, who made me feel part of their family and helped me during the years to become what I am today. Thank you

to the other students of the BSL: Mei, Ved, Aimin, Akiko, Rob, Sanne, Shan, Mong-Han, Kelly, Amanda, Holly, Gilead, Trey, Allen, Scott, Patrick... The postdoc members of the lab also helped me through the years and I would like to let them know how much I enjoyed the discussions we had about research as well as about life in general. So, Nicolas, Laurent, Paul, Isabelle, Seung-Hoon, thank you very much!

But the seismo lab is not a place where researchers and students are left alone. We are extremely lucky to be taken care of by great people in the administrative staff, in the computer operation group, and by the field engineers. Just to name a few people, I would like to present my sincere gratitude to Eleanor, Yolanda, Kristen, Tina, Marion, Margie, Charley, and Stephen.

Research is like a roller coaster where down moments are followed by great positive feelings. There is a perpetual calling into question that is fundamental for the development of our field. I am particularly grateful to Sierra Boyd, my friend and housemate, for all the moments she patiently listened to my hesitations and fears, and for all the support she gave me everytime that I needed it. She has been there for me so many times that I once told her that she was my psychologist! Sisi, I thank you very much for everything and I wish you the best of luck in this new journey that you are starting. I will always cherish all the wonderful moments we spent together: at the house, in vacation, and in the computer room.

Five years far away from my family would have been extremely long if I did it alone. I would like to thank my boyfriend, Golf/Sutee for being there for me and for encouraging me to always work harder in order to reach great goals. It has not always been fun to have you questioning my ability to pass the many challenging moments of these five years but I now realize that by doing so, you forced me to always give the best of myself. Like you say: "Practice makes perfect".

Finally, I am extremely grateful to my parents who have always believed in me and who accepted my decision to come to Berkeley even if it was difficult. I can't tell you how much I loved these few hours chatting with you every Sunday, and how I have been looking forward to every trip back to France. Thank you so much for all your help and support when I needed it! I have tried and I will always try to make you feel proud of me. My last words go to my sister, Blandine who has been a very important link for me between Berkeley and my family with our almost-daily online exchanges. Blandine, I thank you very much for all the support and encouragements you gave me and I wish you the best in your new position as a science teacher. If you need any advice from a seismologist, you now know who to ask!

# Chapter 1

# Introduction

Two of the most important challenges in seismology are linked to the identification of regions with potential earthquake hazards, and to the understanding of the nucleation process of large and damaging earthquakes. Analyses of catalogs of past seismic activity as well as the consideration of additional datasets such as geodetic measurements help provide a better understanding of the fault rheology and kinematics of the active tectonics of a region of interest. These are fundamental for providing constraints on the size and rupture modes of expected events.

It has been observed from numerous seismic events that earthquakes in nonvolcanic regions are relatively uniform in character and may be represented effectively by a double-couple point-source at long periods, unlike seismic events in volcanic regions that exhibit a wide range of behaviors and mechanisms [Dreger and Helmberger, 1993; Dziewonski and Woodhouse, 1983; Hellweg, 2000; Julian et al., 1998; Kawakatsu, 1995; Scott and Kanamori, 1985]. This model has permitted the rapid monitoring of earthquakes in many regions [Dreger et al., 1998; Fukuyama et al., 1998; Pasyanos et al., 1996]. Nonetheless, there are many examples of departures from impulsive events as well as from their pure double-couple source models in nonvolcanic and volcanic settings [Ide et al., 2003; Julian et al., 1998; Minson et al., 2007; Obara, 2002; Tkalcic et al., 2009]. Similar to what seismic activity reveals in volcanic environments, complications in the source must be considered such as the presence of unsteady flow and the properties of the elastic response of surrounding rocks [Hellweg, 2000; Kedar et al., 1996]. Analysis of these special seismic events can provide additional constraints on the presence of fluids in the deep fault zones, illuminate contrasting materials across faults, and differences in the tectonic regimes along fault lines. Consequently, their comprehensive characterization should help increase our overall knowledge of the mechanics of fault zones.

Several types of unusual seismic events in nonvolcanic settings have been reported in the past decades: nonvolcanic tremors [Obara, 2002], slow/low-stress-drop earthquakes [Ekström, 2006; Pérez-Campos et al., 2003], and repeating earthquakes [Nadeau and Johnston, 1998]. Because their behaviors diverge from those of the majority of the seismic events in

terms of waves' generation, amplitude, source duration, dimension, and seismic moment release, they are not easily monitored, if detected, using current implemented methods. All three types of unusual events have been identified in California. Their exotic behavior is important to study as they can reveal information towards a better understanding of the rheology, mechanics, and kinematics of the active faults in California as well as in other regions in the world.

In this dissertation, I undertake to describe and quantify the unusual seismicity in northern and central California: in the region of the Mendocino Triple Junction as well as in the vicinity of Parkfield along the San Andreas Fault. By modeling and contrasting the activity of the three different types of exotic seismic events mentioned earlier, I demonstrate that they can give unique clues on the tectonic regimes where they occur and on their interactions with other events. In addition, because these unusual seismic events require new methods to accurately detect them, they lead to the development of modern streaming data algorithms that can be more generally adapted to regular earthquakes. This gives the advantage of using a single procedure for the detection of all types of events, from small magnitude to potentially tsunamigenic earthquakes.

This dissertation comprises three main sections: 1) an earthquake source study mostly considering moment tensor inversions for the detection and characterization of slow, regular, and potentially tsunamigenic earthquakes (Chapters 2 to 4), 2) a spatio-temporal analysis of nonvolcanic tremors in the Parkfield region that informs us on their sensitivity to low stress changes at depth along the fault zone and also helps us detect dip slow slips in the fault zone (Chapters 5 to 7), and 3) the testing of a discussable hypothesis, the accelerating moment release, first formulated as a possible way toward future earthquake forecasting.

Chapter 2 presents a source analysis of slow/low-stress-drop earthquakes mostly located offshore in the vicinity of the Mendocino Triple Junction. This chapter provides a detailed introduction of the region where the slow earthquakes occur as well as the method employed to detect them. By comparing seismic events exhibiting a unusual slowness in their rupture with others that correspond to regular earthquakes, I isolate their specificities in terms of waveform and frequency contents and I discuss hypotheses for their occurrence. However, the current procedure for their detection can potentially fail and Chapter 2 shows evidence that moment tensors performed on long-period data could potentially enhance their detection toward obtaining a more complete catalog of their activity.

Chapters 3 and 4 develop on the use of moment tensors for a more general detection of earthquakes in two regions of interest: the Mendocino Triple Junction, California, and offshore Japan. By continuously inverting for moment tensors they show that it is possible with a single procedure to automatically detect, locate and determine source parameters of any earthquake, from magnitude 3.5 to larger than 8 located in both the near- and far-field.

The detection and characterization of large earthquakes is improved when quasi-finite-source Green's functions are used in a point-source moment tensor approach as they represent to some extent the rupture's finiteness and directivity. Solutions can be obtained within several minutes after the origin time of the earthquake using a limited number of stations, and could therefore be used as part of a near-source tsunami early warning system, capable of providing tens of minutes of possible warning depending on the distance of the earthquake rupture from the coast. Chapter 3 makes use of synthetic waveforms of model large earthquakes to test the method whereas Chapter 4 illustrates the use of quasi-finite-source Green's functions and very long-period (100-200 sec) records from K-NET in the GridMT (Kawakatsu, 1998) framework to demonstrate the approach for the 2011 M9 Tohoku-oki earthquake. It validates the use of this method for the development of a tsunami early warning capability using local to regional distance seismic stations. The results show that it would be possible to independently detect, locate, and estimate an unsaturated moment magnitude within 8 minutes of the occurrence of mega-thrust earthquakes, possibly giving upwards of 10 to 20 minutes of early warning before the arrival of large amplitude and damaging tsunami waves.

Chapters 5, 6, and 7 focus on an extended spatio-temporal analysis of nonvolcanic tremor activity in central California. Nonvolcanic tremors occur adjacent to locked faults and may be closely related to the generation of earthquakes. Chapter 5 shows that monitoring of the San Andreas Fault in the Parkfield, California region, revealed that after two strong local/regional earthquakes tremor activity increased in a nearly dormant tremor zone, became periodic in a previously active zone, and has remained elevated and followed a periodic behavior for over four years. Static shear- and Coulomb- stress increases from the earthquakes of 6-14 KPa are coincident with step increases in tremor rates. Chapter 6 further focuses on the interaction tremors – earthquakes and shows evidence of triggered tremors associated with the surface waves of large regional earthquakes in central California where teleseismically triggered tremors have been observed. In addition, this chapter reveals that regionally and teleseismically triggered tremors as well as ambient tremors are not limited in frequency content unlike what has been published previously but that they have significant high frequency (i.e., above 20 Hz) as well. Long-period and large-amplitude surface waves from both regional and teleseismic events are found to have a greater potential of triggering tremor in the same region, and that the inferred minimum triggering dynamic stress is $\sim$1 kPa. Finally, Chapter 7 presents a detailed analysis of tremor episodes that reveals occurrence of slow slip events beneath the seismogenic zone of the San Andreas Fault. Comparison of multiple seismicity catalogs (tremors, low-frequency earthquakes, and repeating earthquakes) helps to constrain the region where these episodes of seismic activity come from along the fault zone, and to characterize the source parameters of these deep slips.

Chapter 8 searches for evidence of interactions between earthquakes in space and time. It presents a series of quantitative tests of the Accelerating Moment Release (AMR) hypothesis presented by Bowman et al. [1998] in which there is increased regional seismic activity with

AMR prior to a mainshock. As opposed to previous studies that searched retrospectively for AMR prior to large earthquakes with optimal parameters, I carry out a systematic grid search for AMR and I compare its results with calculated models of stress accumulation in southern California. If seismicity rates rise in areas where peak stress increases, and prior to large events this approach would be the appropriate method to test and implement the AMR concept in earthquake forecasting efforts. Indeed, even if the stress changes can be questionable, the areas that sustained stress increases approaching plausible stress drop values should be closer to failure and should differ from $c$-values (parameter used Bowman et al. [1998] to quantify the acceleration of the seismicity) obtained from a random earthquake catalog analysis. Chapter 8 shows that no distinction between regions of apparent high stress and regions of apparent low stress can be made using this approach. Consequently I find the concept of AMR as it is currently formulated to be inadequate for improved earthquake forecasts.

Chapter 9 summarizes the results presented in each chapter, and presents conclusions and recommendations.

# Chapter 2

# Identification and analysis of slow/low-stress-drop earthquakes in the vicinity of the Mendocino Triple Junction

Advisor: Douglas S. Dreger

## 2.1 Introduction

Slow/low-stress-drop earthquakes have been reported in northern California, primarily in the vicinity of the Mendocino Triple Junction (MTJ). Unlike regular earthquakes they show extended source duration as exhibited by their large energy content in long periods and their relative lack of high-frequency waves [Ekström, 2006; Pérez-Campos et al., 2003]. Because of these characteristics their detection at short-periods is limited, where only a small number of slow earthquakes have been reported [Ekström, 2006]. Most of them have been located offshore, along transform-ridge faults at teleseismic distances [Abercrombie and Ekström, 2003; Ekström, 2006; Pérez-Campos et al., 2003], however there are issues regarding the determination of their radiation patterns due to the attenuation of high-frequency energy at teleseismic distances. One the other hand, the MTJ slow earthquakes are located at regional distances from the seismic stations in northern California, which allows the study of their waveforms and spectrum. They also allow the comparison of our results with other more typical seismic events that do not demonstrate anomalies in their rupture characteristics.

In this chapter, we first introduce the tectonic setting of the MTJ, we present the background of slow earthquakes as they have been studied in other regions, and we introduce how they have been detected in northern California using magnitude differentials that give insight to the source spectrum of these slow earthquakes. In order to obtain a more complete catalog of their activity we employ methods used for the detection of repeating earthquakes in central California as well as in the MTJ region [Nadeau and McEvilly, 2004]. Finally, we analyze a slow earthquake identified by Ekström [2006] in our study region that was origi-

nally missing from seismicity catalogs. We show by using triangulation, particle motion, and more importantly with long-period moment tensor inversions that this event was detectable by the regional network. Because of the success of the moment tensor method focusing on the large long-period waves of this slow earthquake we propose that similar analyses could be performed routinely to facilitate the detection of these unusual earthquakes and to develop a more complete catalog of their occurrence. This would thus help to provide a greater understanding of the complex processes occurring in the MTJ, the degree of coupling between the Gorda and North America plates, and the time-varying aspects of the slip deficit accumulation in the region. All of which are critical for the accurate assessment of the seismic hazard in this arguably most seismically active area of California.

## 2.2 Tectonic setting and slow earthquakes

### 2.2.1 The Mendocino Triple Junction

The Mendocino Triple Junction (MTJ) off the coast of Cape Mendocino in northern California occupies a structurally complex region of tectonic and lithologic diversity where three tectonic plates interact: the North American, the Pacific, and the Gorda/Juan de Fuca plates (Figure 2.1). It constitutes an unstable fault-fault-trench triple junction that migrates northwestward at approximately 40 mm/yr [Henstock and Levander, 2003]. To the west of the triple junction, the Mendocino Transform Fault (MTF) separates the Pacific plate from the Gorda plate with a right-lateral strike-slip motion of about 56 cm/yr [Dicke, 1998]. This area also represents the northernmost section of the San Andreas Fault (SAF), a right lateral strike-slip fault separating the Pacific and the North American plates with an average slip rate of 45 mm/yr. And finally, the MTJ corresponds to the southern termination of the Cascadia Subduction Zone (CSZ) where the Gorda plate subducts beneath the North American plate at a rate of 34 mm/yr in an east-northeasterly direction near the triple junction [Schwartz and Hubert, 1997].

Because of the presence of the three plates, the MTJ is very seismically active. Indeed, it is where more than 25% of the total seismic energy in California has been released in the past 50 years [Merritts, 1996]. With about 80 magnitude (M) 3 intra- and inter-plate earthquakes every year [Oppenheimer, 2007], this region corresponds to the most seismically active region of northern California. All types of earthquake mechanisms are observed with: 1) pure right-lateral strike-slip events along the MTF and the SAF, 2) left-lateral strike-slip earthquakes within the Gorda plate highly deformed between the North American continent and the Pacific plate [McCrory, 2000; Velasco et al., 1994], 3) reverse mechanisms linked to the slab, and 4) deep normal faulting events also associated with tensile stresses in the subducting slab. The moment tensor solutions of the re-

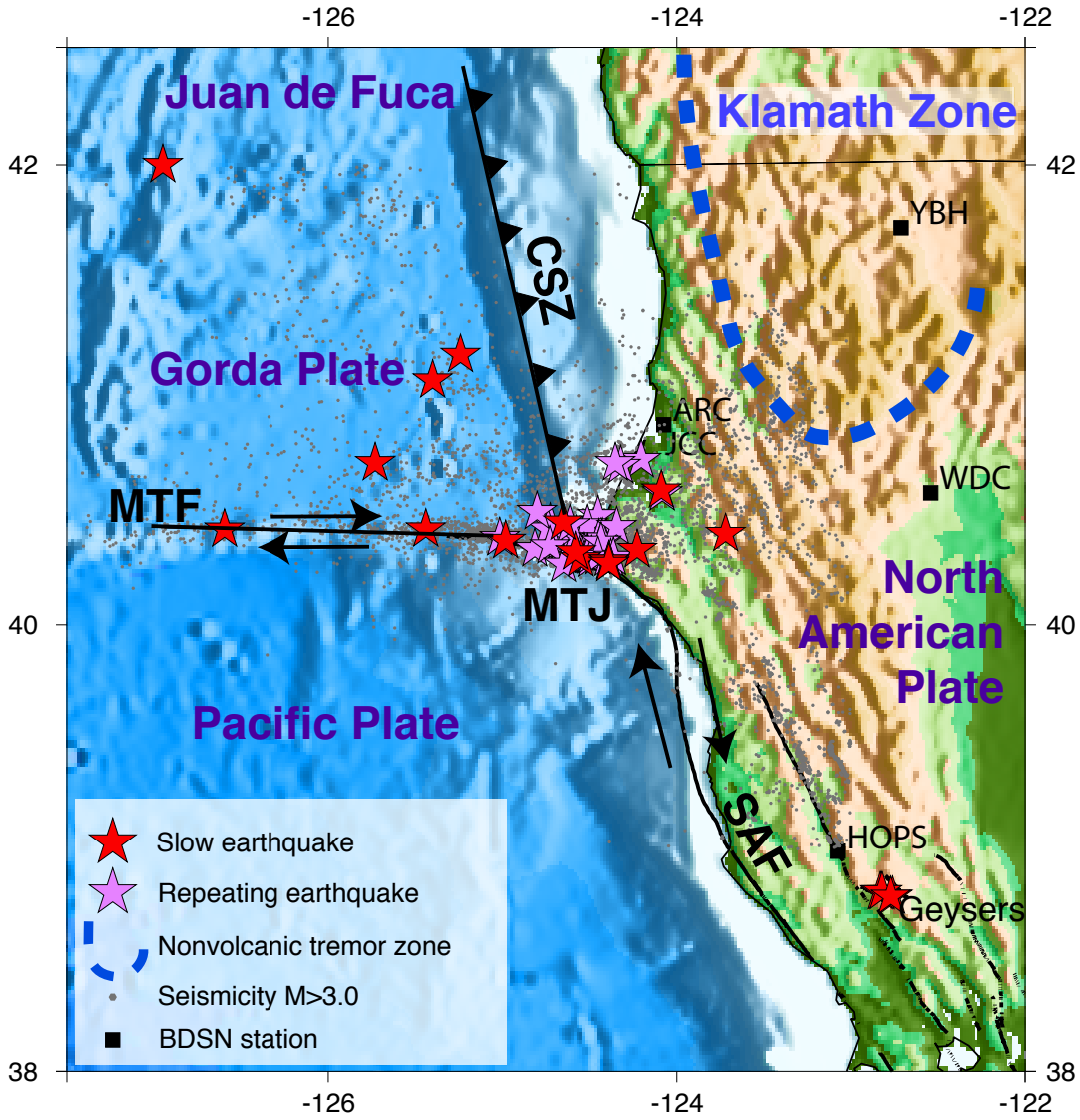


Figure 2.1: Map of the Mendocino Triple Junction (MTJ) region showing the tectonic setting and the unusual seismic activity. SAF: San Andreas fault, CSZ: Cascadia Subduction Zone, MTF: Mendocino Transform fault.

gional seismicity are compiled in the Berkeley Moment Tensor Catalog since 1992 [BMTC – `http://seismo.berkeley.edu/~dreger/mtindex.html`]. The seismicity varies at depth from the first few kilometers of the crust to over 40 km. The deep seismicity occurs in the thickened Gorda plate and within the subducting slab east of the triple junction. Despite the large number of small and moderate offshore earthquakes, great earthquakes also affect the region. Indeed the great 1906 M7.9 San Francisco earthquake ruptured the SAF from the San Francisco Bay Area to Mendocino County, south of the MTJ. Evidence for large subduction zone earthquakes with magnitude above 8 originating at or near the triple junction has also been found from paleoseismic studies [Clarke and Carver, 1992; Goldfinger et al., 2008; Merritts, 1996; Prentice et al., 1992]. The latest known megathrust event occurred in January 1700 with an estimated M9 rupture extending from the MTJ to Vancouver Island [Satake et al., 1996].

This region is also remarkable for its variety of seismic events. Three unusual event-types have been identified in the vicinity of the MTJ: 1) nonvolcanic tremors, 2) repeating earthquakes, and 3) slow/low-stress-drop earthquakes. The existence of nonvolcanic episodic tremor and slip events have been reported by Szeliga et al. [2004] and later by Brudzinski and Allen [2007] along the CSZ and in particular in the Klamath zone near the MTJ (Figure 2.1). A preliminary search for repeating earthquake activity in the MTJ region using methods for the identification of repeating earthquakes in central California has also revealed distributed sites of repeating micro-earthquake sequences [Taira and Nadeau, 2011] (Figure 2.1). Finally, slow earthquakes have been reported in the BMTC, in the vicinity of the MTJ and, for some of these, they occur in close proximity to the repeating earthquakes (Figure 2.1).

### 2.2.2 Identification of slow/low-stress-drop earthquakes

For most earthquakes in the Mendocino region different earthquake magnitude estimates ($M_L$, $M_w$, $M_d$, $M_s$) are similar except where typical magnitude saturation effects are important. What we call slow earthquakes or low-stress-drop earthquakes behave otherwise. They have a large discrepancy between their local and moment magnitudes, $M_L$ and $M_w$, respectively. These two magnitudes are obtained using seismic data filtered at different frequency passbands, and are therefore sensitive to different parts of the earthquake source spectrum. $M_L$ is calculated from body-waves on records filtered with a short-period Wood-Anderson instrument response and is sensitive to periods shorter than 1 second. $M_w$ is calculated from complete waveform seismic moment tensor analysis utilizing data filtered to periods longer than 10 seconds [Dreger et al., 1998; Gee et al., 2003, 1996; Pasyanos et al., 1996]. If an earthquake shows a larger $M_w$ than $M_L$ it tends to indicate that the seismic records are depleted in high frequency waves, and inversely, enriched in lower frequency waves. Differences between $M_w$ and $M_L$ due to saturation effects typically occur for magnitudes greater than 6.5. For smaller events, the corner frequencies of the slow earthquakes are observed to be lower than the corner frequencies of typical earthquakes of similar size. For example in

the MTJ region, a slow event with $M_L$4 and $M_w$5.2 may have a corner frequency of 0.1 Hz, whereas a typical event with the same $M_L$ should have a corner frequency of at least a 1 to 3 Hz. The slow earthquakes of the MTJ share properties similar to other slow events found in other regions of the world [Ekström, 2006; Pérez-Campos et al., 2003]. They are mainly located on oceanic transform faults, and they are characterized as slow on the basis of their weak seismic radiation at high frequencies.

Several hypotheses have been proposed to explain this type of seismic event. Because of their relatively low Brune stress drops, Ide et al. [2003] argued that they could correspond to ruptures that are larger than rupture dimensions typically considered for regular seismic events. Pérez-Campos et al. [2003] proposed that another option would be that the slip during the earthquake is slow and/or that the rupture velocity is low, eventually due to rheological and frictional properties of the transform faults [Amoruso et al., 2004]. To the contrary, Abercrombie and Ekström [2003] argued that for some slow earthquakes, and perhaps for all of them, the slow behavior was suspect. Indeed they propose that these events, studied at teleseismic distances, are affected by crustal structure in the source region on surface wave amplitudes, and that uncertainties in modeling procedures could affect their analysis. Ekström [2006] later explained that the reduced P-wave amplitudes could be explained by the radiation pattern of the earthquakes and by the distribution of the recording seismic stations. Furthermore, Schramm and Stein [2009] argued that the apparent slowness of oceanic transform earthquakes was a result of a method bias in the source mechanism after comparing the body-wave magnitude ($M_b$) to the surface wave magnitude ($M_S$), and $M_b$ versus the seismic moment (Mo) between oceanic transform, ridge, and intraplate events, and investigating the effects the focal mechanisms on the magnitude differences.

In northern California, earthquake monitoring is a joint effort between the United States Geological Survey (USGS) at Menlo Park and the Berkeley Seismological Laboratory (BSL) [Gee et al., 2003]. The USGS detects, locates, and determines the duration magnitude ($M_d$) of earthquakes occurring in the region. The BSL then determines $M_L$ if $M_d$ exceeds 3.0. If the computed $M_L$ is greater than 3.5 a moment tensor inversion is automatically performed, providing $M_w$. Moment tensor solutions are reviewed and for some regions, if the signal-to-noise levels are adequate, moment tensors may be obtained for events with $M_L$ less than 3.5. The BMTC reports the reviewed seismic activity in central and northern California with magnitude larger than 3.5 since 1992. It provides information regarding the origin time, location, magnitudes $M_L$ and $M_w$, and focal mechanism of the regional seismicity. We searched for $M_w$-$M_L$ discrepancies larger than 0.5 between 1992 and 2008 as an indication of an anomalous source spectrum. We identified and cataloged 21 unusual, possibly slow, earthquakes with a wide range of magnitudes (between 3.5 to 6.8). Out of the 21 slow events, 18 are located in the vicinity of the MTF and also within the Gorda plate (Table 2.1 and Figure 2.1). Their mechanisms, mainly pure strike-slip, are consistent with the fault motion in the region. The additional three anomalous earthquakes that complete the catalog are

Table 2.1: List of slow earthquakes in the Mendocino region

| Day | Hour | Latitude | Longitude | Depth (km) | ML | Mw | Mw-ML |
|---|---|---|---|---|---|---|---|
| 04/25/92 | 18:06 | 40.33 | -124.23 | 8 | 6.3 | 6.8 | 0.5 |
| 06/05/92 | 21:46 | 40.29 | -124.55 | 21 | 4.8 | 5.5 | 0.7 |
| 03/04/95 | 21:51 | 40.71 | -125.73 | 18 | 3.5 | 4.6 | 1.1 |
| 11/11/95 | 20:19 | 40.40 | -123.72 | 30 | 3.5 | 4 | 0.5 |
| 12/24/95 | 07:41 | 42.00 | -126.95 | 5 | 4.4 | 5.3 | 0.9 |
| 01/22/97 | 07:17 | 40.27 | -124.39 | 24 | 4.8 | 5.6 | 0.8 |
| 01/26/97 | 06:23 | 40.28 | -124.39 | 21 | 4 | 5.2 | 1.2 |
| 10/06/97 | 12:00 | 41.07 | -125.40 | 24 | 4.1 | 4.6 | 0.5 |
| 02/15/99 | 06:00 | 40.28 | -124.39 | 27 | 3.8 | 4.7 | 0.9 |
| 12/26/99 | 19:41 | 40.27 | -124.39 | 24 | 4.2 | 4.8 | 0.6 |
| 01/08/03 | 05:41 | 40.42 | -125.44 | 8 | 4.2 | 4.7 | 0.5 |
| 02/18/03 | 14:44 | 41.18 | -125.24 | 11 | 3.7 | 4.2 | 0.5 |
| 04/22/03 | 10:46 | 40.59 | -124.09 | 27 | 3.9 | 4.4 | 0.5 |
| 06/26/03 | 03:39 | 40.40 | -126.57 | 14 | 4.1 | 4.6 | 0.5 |
| 07/04/03 | 20:52 | 40.32 | -124.58 | 21 | 3.7 | 4.3 | 0.6 |
| 08/26/03 | 02:29 | 40.45 | -124.65 | 24 | 3.9 | 4.4 | 0.5 |
| 03/18/05 | 07:23 | 40.37 | -124.98 | 18 | 4.4 | 5 | 0.6 |
| 01/24/07 | 13:42 | 40.31 | -124.58 | 20 | 3.7 | 4.4 | 0.7 |

located in the Geysers geothermal region of northern California, where unusual non-double-couple earthquakes have been identified [Boyd et al., 2011; Frohlich, 1994; Julian et al., 1998] (figure 2.1).

## 2.3 Modeling slow earthquakes

In order to understand the characteristics of the unusual slow earthquakes occurring in the vicinity of the triple junction, we performed a series of analyses that successively consider the wave propagation between the source and the broadband seismic stations, and the source itself of these events. We compare the slowest earthquake with an earthquake of similar size that: 1) is located nearby, 2) does not exhibit discrepancies in its magnitudes, and 3) has similar focal mechanisms.

Here, we focus on the most unusual slow earthquake identified in the vicinity of the MTJ that shows a magnitude discrepancy of 1.2, with $M_L$=4.0 and $M_w$=5.2. It occurred

Table 2.2: Characteristics of two collocated earthquakes

| | Day | Hour | Latitude | Longitude | Depth (km) | Ml | Mw | Mw-Ml |
|---|---|---|---|---|---|---|---|---|
| Slow earthquake | 26 Jan 1997 | 06:23 | 40.28 | -124.39 | 21 | 4.0 | 5.2 | 1.2 |
| Regular earthquake | 13 Jan 1997 | 14:54 | 40.28 | -124.41 | 24 | 4.0 | 4.2 | 0.2 |

on 26 January 1997, offshore along the MTF (Table 2.2). Earlier in the same month, on 13 January 1997, another earthquake struck the region in the same location (Table 2.2). This earthquake however does not exhibit a large discrepancy in the two magnitudes that are reported in the BMTC ($M_L$=4.0 and $M_w$=4.2).

Because the two events are located in a very close proximity ($\sim$ 1.7 km), the travel paths of the seismic waves from the two sources to the regional stations located between 70 and 325 km can be approximated to be identical. We performed a detailed moment tensor analysis of the two earthquakes in order to precisely determine their source parameters and verify the $M_w$ reported in the BMTC (Figure 2.2). We downloaded 5-min window velocity seismograms at five BDSN stations (ARC, BKS, HOPS, ORV, and YBH), corrected the data from the instrumental responses, and we integrated them to displacement. Data were then filtered between 20 and 50 sec period, which is the frequency band typically used by the BSL for earthquakes of this size in northern California in both the automated and reviewed moment tensor analyses. Using the Gil7 model typically used for the routine source inversions in the region, we find that the focal mechanisms of the two events are very similar in terms of the strike, rake and dip directions and validate further the waveform comparison between the two events (Figure 2.2).

Figure 2.3 shows that the waveforms of the two earthquakes are similar at frequencies between 0.02 and 0.1 Hz. However, when filtered at higher frequencies (i.e between 0.02 and 0.5 Hz, and between 0.02 and 1.0 Hz), they are markedly different in terms of waveform and frequency content. It is interesting to note that for the slow event, the observed waveform in all three passbands is very similar. The amplitude displacement spectrum (Figure 2.4) shows that the corner frequency for the slow event is approximately 0.08 Hz instead of 1 to several Hz expected for an event with a $M_w$ of 4.2. A corner frequency of $\sim$1 Hz is indeed what we find for the $M_L$ 4 regular earthquake (Figure 2.4).

We performed waveform modeling of the regular seismic event using the Gil7 model as a starting model. The synthetics that best fit the data are shown in Figure 2.3 (red trace). The

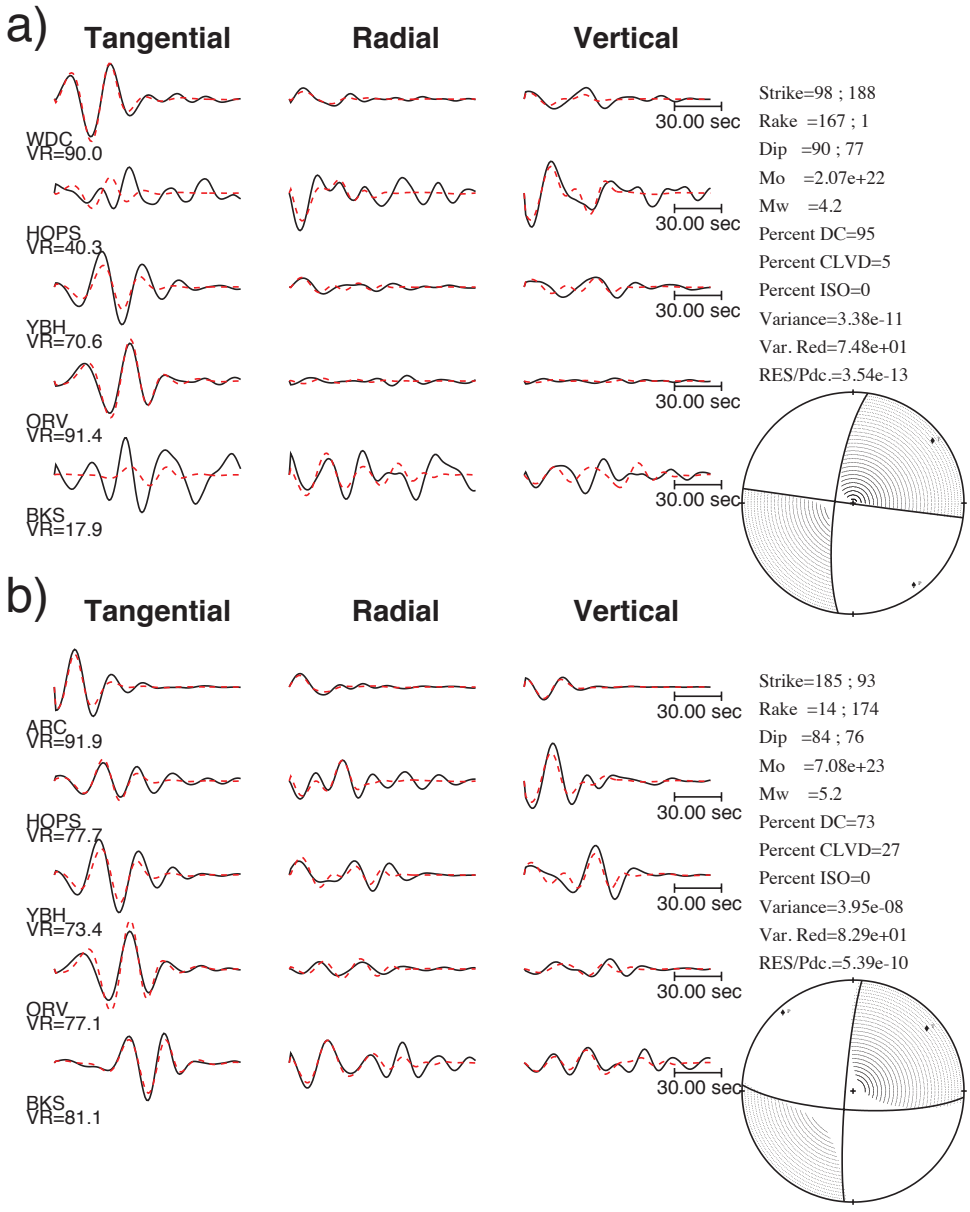


Figure 2.2: Moment tensor solutions of the regular earthquake at 27 km depth (a) and slow earthquake at 24 km depth (b) using Gil7 model.

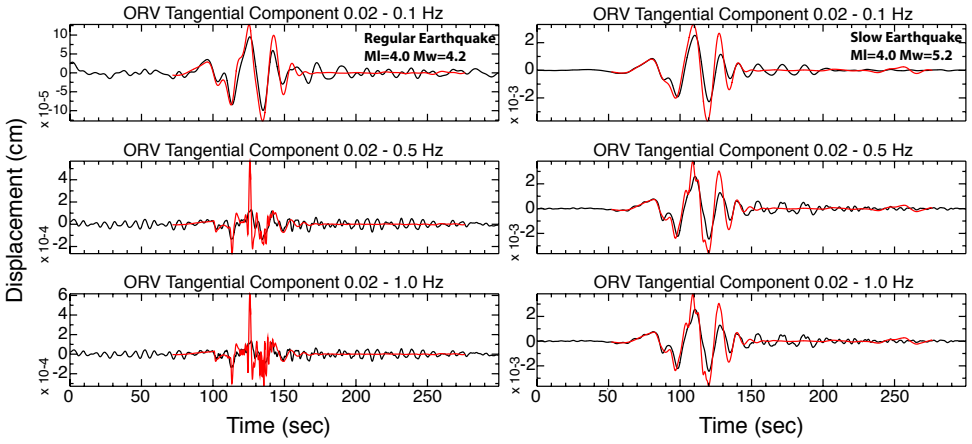


Figure 2.3: Waveform comparison of a regular earthquake (left) and of a slow earthquake (right) at different frequency bands. Data for ORV station shown in black and synthetic waveforms in red. for the regular earthquake, red traces show the Green's functions only. For the slow earthquake, red traces show the Green's functions convolved with a 10-sec source time function.

amplitudes and phase arrivals of the regular earthquake are well reproduced by the synthetics at 0.02-0.1 Hz using the updated velocity model. At higher frequencies, the amplitudes are found to be too large but the phase arrivals are reproduced. However the synthetics could not match the waveforms of the slow earthquake using the updated velocity model. To enhance the fit in the three frequency bands shown in Figure 2.3 it was necessary to convolve the Green's functions with a 10 second duration source time function. However, for the regular earthquake no source duration was added. The inclusion of a 10 second source duration is unusual for either a $M_L$4.0 or a $M_w$5.2 earthquake. In fact, Wells and Coppersmith [1994] proposed an empirical relationship between the magnitude $M_w$ and the rupture length $L$ of an earthquake such that:

$$L = 10^{-2.44+0.59M_w} \tag{2.1}$$

Following this observation, a typical $M_w$4.2 earthquake has an expected length of about 1.1 km and a rupture duration of about 0.4 seconds assuming a rupture speed of 3 km/s. On the other hand, an average $M_w$5.2 event would correspond to a 4.2 km long rupture happening in about 1.4 seconds. Both estimations are substantially shorter than what we modeled for the slowest earthquake of the catalog. From the Wells and Coppersmith [1994] relationship the 10 second rise time found from waveform modeling corresponds to a $M_w$6.5-6.6 event. These calculations assume that the event ruptured with a typical rupture velocity and that the long source duration is due to an unusually large fault with slip consistent with a much lower $M_w$.

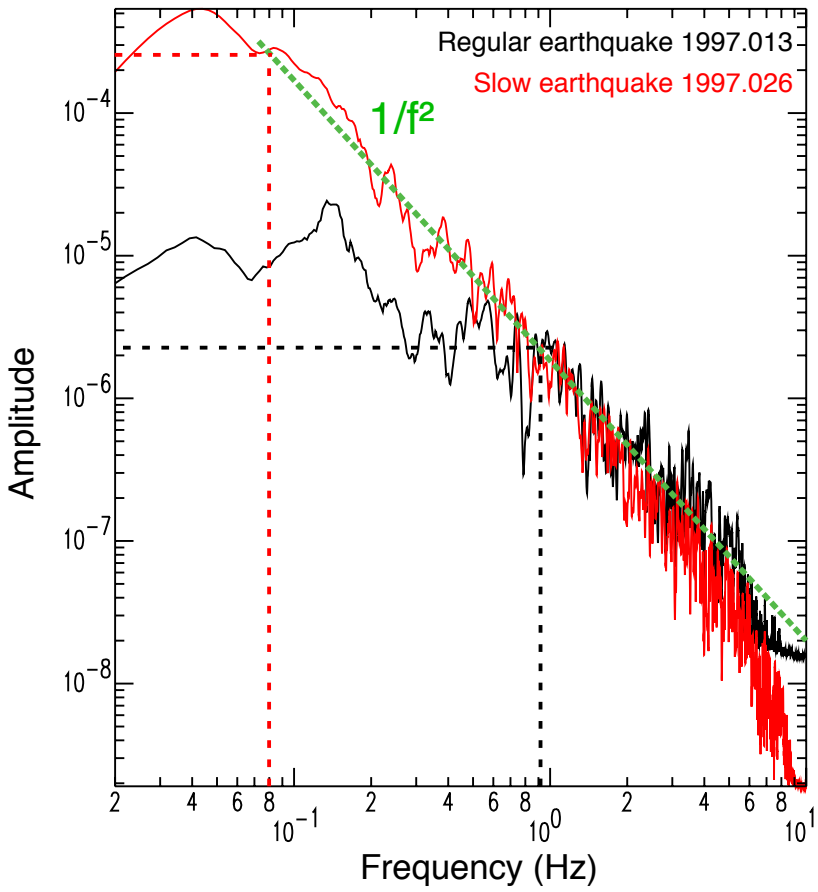


Figure 2.4: Displacement spectra of the transverse component of the collocated regular (blue) and slow earthquakes (red) recorded at WDC. The corner frequency of the slow earthquake (0.08 Hz) is lower than expected compared to the one of the regular event (0.9 Hz).

Three possible interpretations can be drawn out of this result. A slow earthquake could result from: 1) a unusually large rupture, 2) unusually slow slip or slow rupture velocity, or 3) a combination of 1) and 2). The anomalous large source duration required in the waveform modeling does not help distinguish which solution better explains the slow earthquake. If one can assume a rupture of 4.2 km length for a typical $M_w$ 5.2 from Wells and Coppersmith [1994] and solve for the average slip speed, the rupture velocity would need to be 420 m/s or slower given the modeled duration. This is unusually slow compared to the typical rupture velocity of $\sim$ 3 km/s considered for most crustal earthquakes. Based on the rise time alone it is not possible to distinguish between the two possibilities for explaining the anomalous source duration and spectrum. It may be possible to resolve this with more detailed study of the spatio-temporal analysis of finite-source rupture, if the station coverage could be shown to be adequate for this offshore region.

However, the analysis successfully shows that the observation of a slow earthquake does not result from limitation in the observation bandwidth due to attenuation as proposed for the occurrence of slow earthquakes on offshore transform faults at teleseismic distances [Ekström, 2006]. Here, we indeed compared two collocated earthquakes that are located offshore but less than 10 km away from the coast, and exhibiting a same focal mechanism and wave travel path. Our observation confirms that the source terms between the two events are indeed different.

## 2.4 Searching for repeating slow/low-stress-drop earthquakes

Because the current procedure for identifying slow/low-stress-drop earthquakes is based on the BMTC in which we find seismic events exhibiting a discrepancy between $M_L$ and $M_w$ larger than 0.5 magnitude unit, it is possible that additional slow earthquakes are not reported. The BSL only computes moment tensors for events with $M_L$ larger than 3.5 when the signal to noise ratio is high enough to allow the determination of the source parameters. In the offshore environment the detection of low magnitude events is difficult given the limited station distribution and azimuthal coverage of the radiation pattern of the events. This potentially leads to incorrect magnitude estimates and could affect the identification of slow earthquakes.

Table 2.1 shows that four slow earthquakes with $M_w$ between 4.7 and 5.6 (i.e. 1997/01/22, 1997/01/26, 1999/02/15, and 1999/12/26) occurred in very close proximity to each other. Figure 2.5 presents the waveforms of the four events located about 72 km west of station ARC. The data are filtered at three different frequency bands. The seismic traces of the four

events are very similar to the others, in particular for the lower magnitude earthquakes and at frequencies up to 0.5 Hz. The largest earthquake (1997/01/22) shows a longer source duration in the first wave arrivals that have larger periods. Because of the remarkable similarities in the source locations and waveforms we can hypothesize that these events correspond to localized repeated ruptures of a fault segment whose properties ease the generation of slow slip. If so, potential additional slow earthquakes might originate from this fault patch and have gone undetected.

To search for missing slow earthquakes we investigated continuous broadband seismic datasets of four BDSN stations in the vicinity of the MTJ over a 14-year period starting in 1993. We employed a cross-correlation technique using two of these four well-identified slow earthquakes of the catalog as template events: the 26 January 1997 $M_w$5.2 and the 26 December 1999 $M_w$4.6 earthquakes (Figure 2.5). This method is similar to the one used for the identification of repeating earthquakes in northern California [Nadeau and McEvilly, 2004]. We used velocity seismograms recorded at four BDSN stations (ARC/JCC, ORV, WDC, and YBH) sampled at 1 sample per second and bandpass filtered between 0.01 and 0.2 Hz using a Butterworth acausal filter. Station ARC was relocated in 2001 and was renamed JCC. The seismograms were cut into 24-hour data files before entering the cross-correlation analysis. The templates were also processed following the same characteristics and centered in a 500-sec window. The cross-correlation was performed using a window of 512 sec length moving every 128 sec and we searched for hits with a cross-correlation coefficient larger than 0.6 that were found at a minimum of three stations.

Table 2.3 shows the results of the cross-correlation analysis using the two slow earthquakes as references. We found that the two templates cross-correlate with their own signal at 99 %, which verifies that the protocol is performing correctly. We do not find strong correlations outside of the occurrence times of known seismic events, which could have indicated the presence of unidentified slow earthquakes within the region. The slow earthquakes that are located in the vicinity of the template events (i.e. 01/22/97 and 02/15/99) show large cross-correlation coefficients as high as 0.96 for the 15 February 1999 earthquake using the 26 December 1999 template. This verifies that their initial locations are indeed correct and supports the visual similarity of the waveforms (Figure 2.5). However, even though the 22 January 1997 slow earthquake results in a cross-correlation greater than 0.7, it has the lowest coefficient. One noticeable difference for this event is its larger $M_L$ magnitude: $M_L$=4.8 as opposed to 4.0±0.2 for the three other earthquakes, and its correspondingly larger $M_w$ of 5.6. The higher frequency records in Figure 2.5 indicate that this event has additional arrivals that may indicate that in addition to being a slow earthquake it may be a compound event with several patches that generate the high frequency radiation.

Three other slow earthquakes also result in coefficients larger than 0.6. However, their catalog locations indicate that they originated further west, offshore. Nonetheless, this could

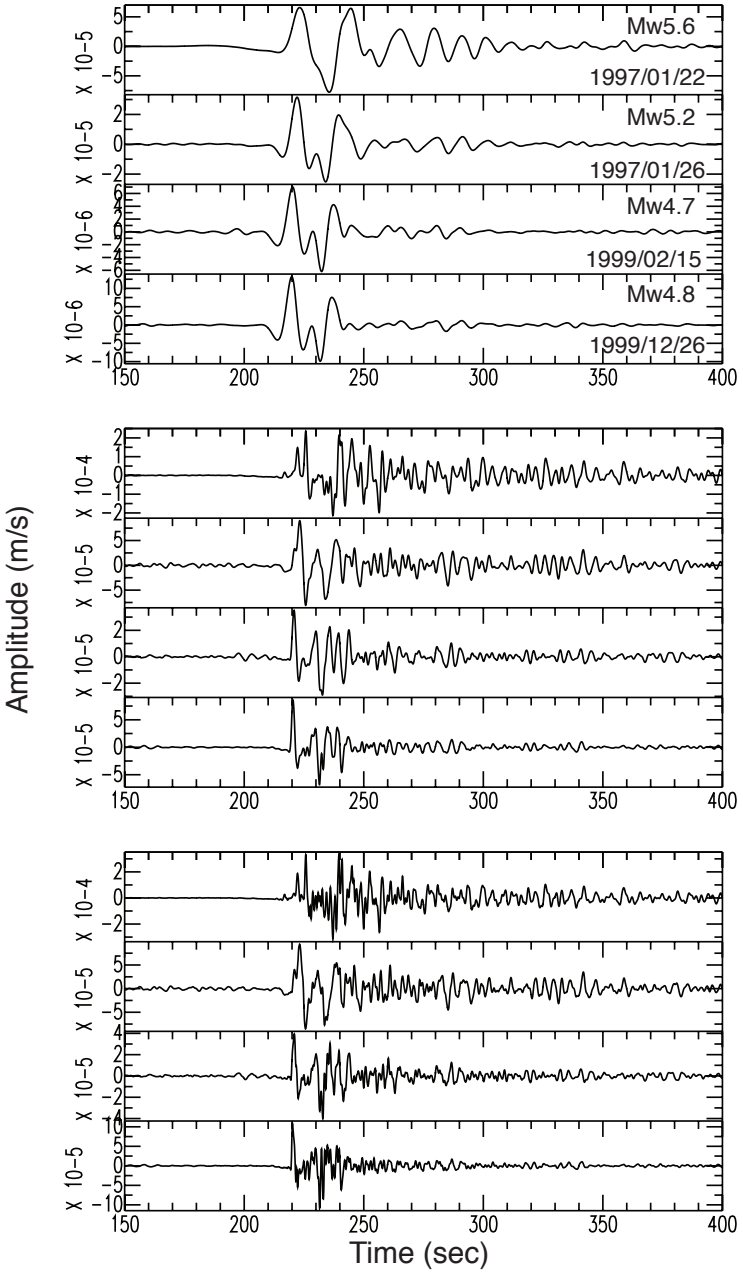


Figure 2.5: Velocity seismograms of collocated four slow earthquakes recorded at station ARC (East component) and filtered between 0.02 and 0.1 Hz (top), 0.02 and 0.5 Hz (middle), and between 0.02 and 1.0 Hz (bottom). Start time for each trace corresponds to 200 sec before the earthquake origin time. The waveforms are very similar taking into account the difference in magnitude of the events.

illuminate potential mislocations of these events. Finally, the method did detect a series of teleseismic earthquakes with magnitudes between 6 and 7 because of the arrivals of impulsive P-and S-waves.

In sum, the cross-correlation approach was unsuccessful in identifying additional slow earthquakes, while confirming with strong correlations the events already detected and identified with magnitude discrepancies. Building an expanded waveform stencil database for this cross-correlation method could eventually help, however implementing a continuous scanning algorithm for the seismic moment tensor [Kawakatsu, 1998] could serve as a better method moving forward for the identification of offshore slow earthquakes as well as for other seismic events.

## 2.5 Detection and characterization of a unknown slow earthquake

Goran Ekström, from Columbia University, identified an onshore slow earthquake with a magnitude of 4.8 that occurred in December of 2000 [Ekström, 2006]. This earthquake was initially located in northern California near the BDSN YBH station (Figure 2.6). Nonetheless, this earthquake was apparently not analyzed by the BSL because no moment tensor solution was found in the BMTC. Here, we show that using several methods such as body wave triangulation, Rayleigh wave particle motion analysis and triangulation, and a moment tensor grid search using low frequency (0.02 to 0.05 Hz) waves that this event actually originated offshore along the Blanco Transform fault.

### 2.5.1 An unidentified event

Goran Ekström presented an event-detection algorithm for surface waves that was motivated by the possibility that seismic events at the global scale that might reflect unusual source spectra, could go undetected by the traditional methods, which focus on short-period body waves [Ekström, 2006]. By searching the seismic signals at longer periods, it opened opportunities to detect slow earthquakes. Using this technique, 1301 new earthquakes were identified that were not reported in global catalogs between 1993 and 2003 with magnitudes larger than 4.6. While most of these events are located in ridge and transform environments, others are located in areas with unexpected seismicity (i.e. Greenland) or in areas where regional seismic networks usually provide reliable monitoring of small earthquakes (i.e. California, Japan) [Ekström, 2006]. Two earthquakes out of the 1301 events are located in the vicinity of the MTJ. One of them was already included in our catalog of slow earthquakes

Table 2.3: Cross-correlation results using the 01/26/1997 and 12/26/1999 slow earthquakes as templates.

| Day | Hour | Latitude | Longitude | Depth (km) | ML | Mw | Mw-ML | Correlation 01/26/97 | Correlation 12/26/99 |
|---|---|---|---|---|---|---|---|---|---|
| 04/25/92 | 18:06 | 40.33 | -124.23 | 8 | 6.3 | 6.8 | 0.5 | | |
| 06/05/92 | 21:46 | 40.29 | -124.55 | 21 | 4.8 | 5.5 | 0.7 | | |
| 03/04/95 | 21:51 | 40.71 | -125.73 | 18 | 3.5 | 4.6 | 1.1 | | |
| 11/11/95 | 20:19 | 40.40 | -123.72 | 30 | 3.5 | 4.0 | 0.5 | | |
| 12/24/95 | 07:41 | 42.00 | -126.95 | 5 | 4.4 | 5.3 | 0.9 | 0.77 | 0.72 |
| 01/22/97 | 07:17 | 40.27 | -124.39 | 24 | 4.8 | 5.6 | 0.8 | 0.86 | 0.72 |
| 01/26/97 | 06:23 | 40.28 | -124.39 | 21 | 4.0 | 5.2 | 1.2 | 0.99 | 0.92 |
| 10/06/97 | 12:00 | 41.07 | -125.40 | 24 | 4.1 | 4.6 | 0.5 | | |
| 02/15/99 | 06:00 | 40.28 | -124.39 | 27 | 3.8 | 4.7 | 0.9 | 0.89 | 0.96 |
| 12/26/99 | 19:41 | 40.27 | -124.39 | 24 | 4.2 | 4.8 | 0.6 | 0.90 | 0.99 |
| 01/08/03 | 05:41 | 40.42 | -125.44 | 8 | 4.2 | 4.7 | 0.5 | | |
| 02/18/03 | 14:44 | 41.18 | -125.24 | 11 | 3.7 | 4.2 | 0.5 | | |
| 04/22/03 | 10:46 | 40.59 | -124.09 | 27 | 3.9 | 4.4 | 0.5 | | |
| 06/26/03 | 03:39 | 40.40 | -126.57 | 14 | 4.1 | 4.6 | 0.5 | | |
| 07/04/03 | 20:52 | 40.32 | -124.58 | 21 | 3.7 | 4.3 | 0.6 | 0.92 | 0.87 |
| 08/26/03 | 02:29 | 40.45 | -124.65 | 24 | 3.9 | 4.4 | 0.5 | 0.78 | 0.72 |
| 03/18/05 | 07:23 | 40.37 | -124.98 | 18 | 4.4 | 5.0 | 0.6 | | |
| 01/24/07 | 13:42 | 40.31 | -124.58 | 20 | 3.7 | 4.4 | 0.7 | | |

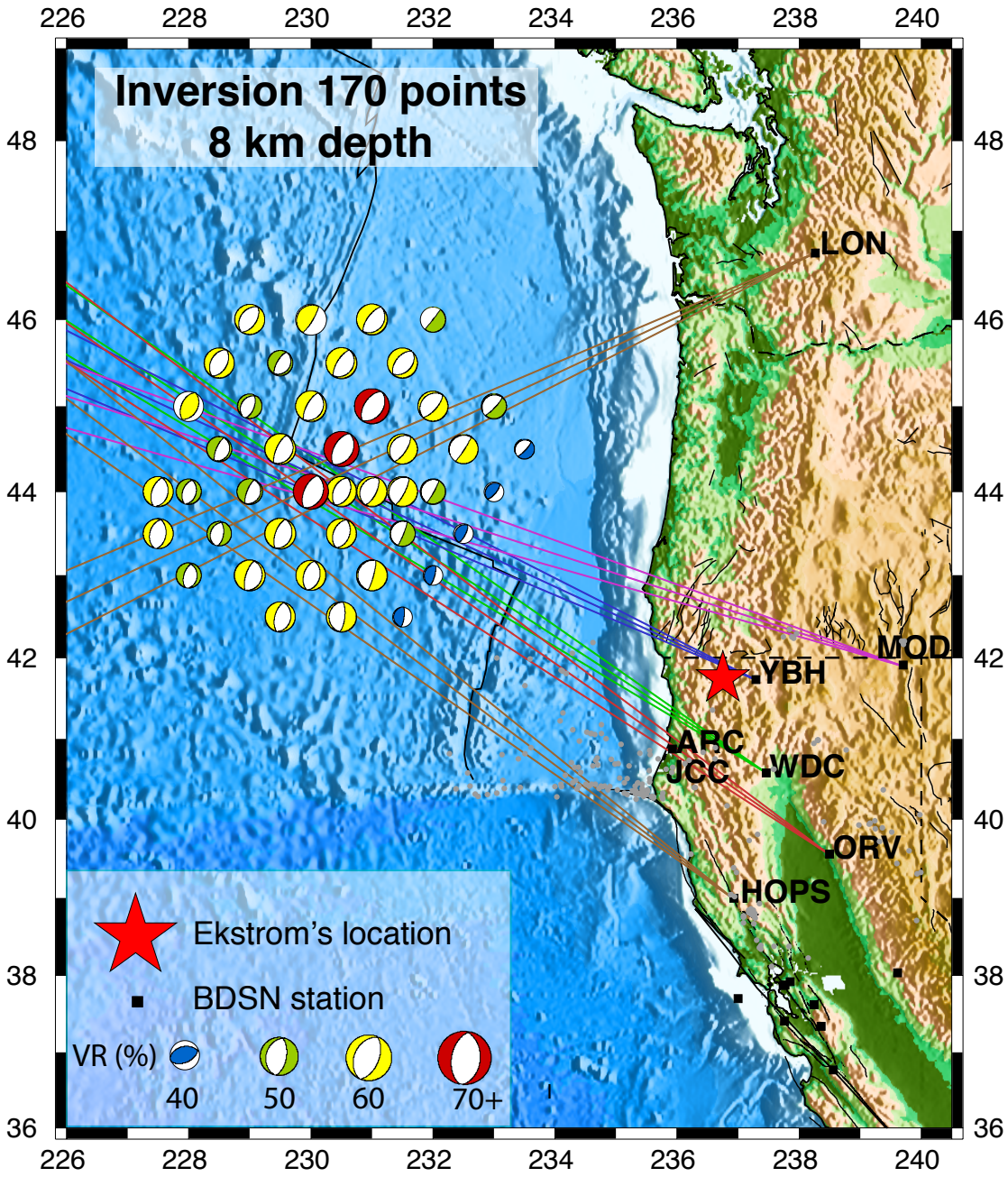


Figure 2.6: Map showing the results from the propagation and source analysis performed on the unknown slow earthquake identified by Goran Ekström. The lines indicates the directions of the back-azimuths obtained from the particle motion analysis. The beachball diagrams are color-coded by variance reductions. The star shows the initial location of the event in the vicinity of the MTJ.

(the 01/26/1997 $M_w$5.2).

The other slow earthquake occurred on 6 December 2000 at 08:06:16 UTC with a magnitude of 4.8 (Figure 2.6). Its location within the BDSN network in the vicinity of the triple junction and its moderate magnitude should have permitted its detection and characterization by the USGS at Menlo Park and by the BSL. However, no entries were found in the PDE and ISC catalogs as well as in the NCSN, and the ANSS catalogs by Goran Ekström and by us in early 2007. Thus this event was apparently undetected. To evaluate this event we downloaded the seismic data at six stations of the BDSN network and we searched for the waveforms of this missed earthquake. The raw broadband seismic data do not exhibit a clear earthquake signature expected for a M4.8 in the region (Figure 2.7). The data are indeed very noisy but one can notice high frequency content at some stations like ARC and ORV, suggesting a seismic event. An earthquake waveform signature is however very clear after filtering the seismograms at long periods between 20 and 50 sec (Figure 2.7). Ekström's location places this earthquake between YBH and ARC, closer to YBH than ARC. However, Figure 2.7 shows a net move-out of the waveforms, from ARC, then to YBH, and later to ORV at long periods indicating that the earthquake originated in the offshore Mendocino region compared to its original location. Moreover, the moment tensor solution obtained using the Gil7 velocity model and assuming Ekström's location is poor (Figure 2.8), with a VR fit of only 6.4%. The poor fit in the moment tensor solution and the Rayleigh – Pnl time inferred from the long-period waveforms indicates that this event was mislocated.

### 2.5.2 Triangulation and particle motion analysis

In order to establish the correct location and source characteristics of the earthquake we identified the arrival times of the Pnl and S waves at the six BDSN stations shown in Figures 2.6 and 2.7. Large uncertainties in the phase picking from the noisy records at long periods resulted in large uncertainties in the location of the earthquake. Nonetheless, this initial analysis confirmed an offshore location at more than 300 km from the coast.

We verified this observation by performing a particle motion study of the Pnl waves at the six BDSN stations as well as at a station located in Washington State, LON. This last station allowed us to increase the azimuthal coverage and to better cover the radiation pattern of the earthquake waves. Consequently, it helped us obtain a more precise location. The analysis of the Pnl particle motion gave us the back-azimuth directions between the stations and the epicenter, shown in Figure 2.6 by the $\pm 3$ degrees lines. The station-epicenter azimuths were used to rotate the horizontal components into the radial and transverse components. Further verification was done by observing that rotated records at the six stations displayed Rayleigh waves with retrograde elliptical motion on the radial and vertical components (Figure 2.9). The back-azimuth directions from the seismic stations intersect offshore and converge on the

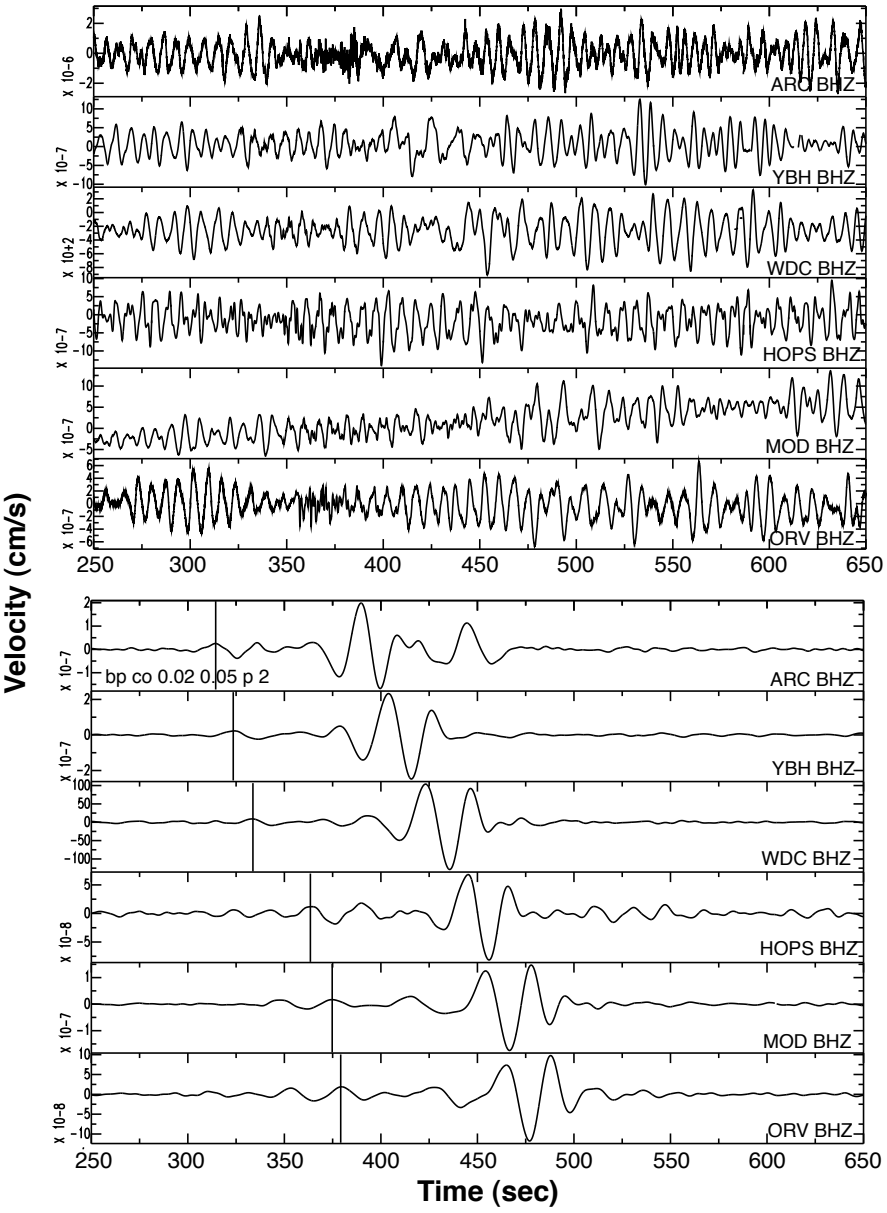


Figure 2.7: Unfiltered (top) and filtered (bottom) velocity waveforms at BDSN stations at the time of the undetected slow earthquake. The earthquake signature is clear at long periods, between 20 and 50 sec. The lines show the Pnl phase on each filtered vertical seismogram.

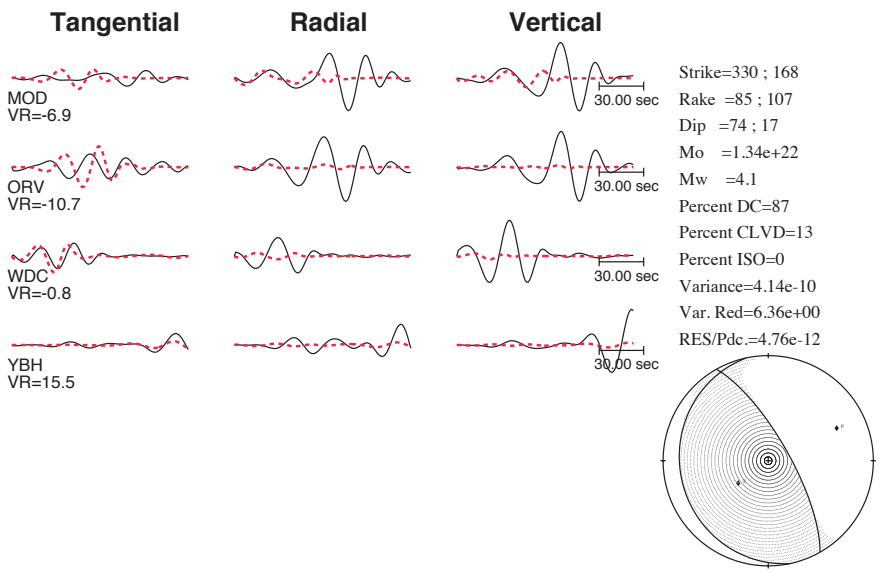


Figure 2.8: Moment tensor analysis performed at the initial location of the undetected earthquake identified by Goran Ekström. Black: data - red: synthetics filtered between 20 and 50 sec.

Blanco Transform Fault that separates the Juan de Fuca plate and the Pacific plate. This strengthens the hypothesis that the event was mislocated and originated from the oceanic region.

### 2.5.3 Moment tensor analysis

Despite the fact that the wave triangulation and particle motion studies confirmed that the initial location of the earthquake was incorrect, and favored a location more than 400 km offshore from the MTJ, they did not provide enough constraints on the location of the earthquake epicenter. By performing a series of moment tensor inversions for sources distributed over the region it was possible to refine the earthquake epicenter. We used four BDSN stations distributed in the vicinity of the triple junction (Figure 2.6) and we filtered their displacement data between 20 and 50 sec. The variance reduction fit between the data and the Green's functions varies depending on the tested locations (Figure 2.6). The best moment tensor solution is obtained on the Blanco Transform Fault where the back-azimuth alines with what we obtained from the particle motion analysis (Figure 2.6). The solution gives a Mw4.5 with a normal mechanism fitting at a 71.4 % level (Figure 2.10).

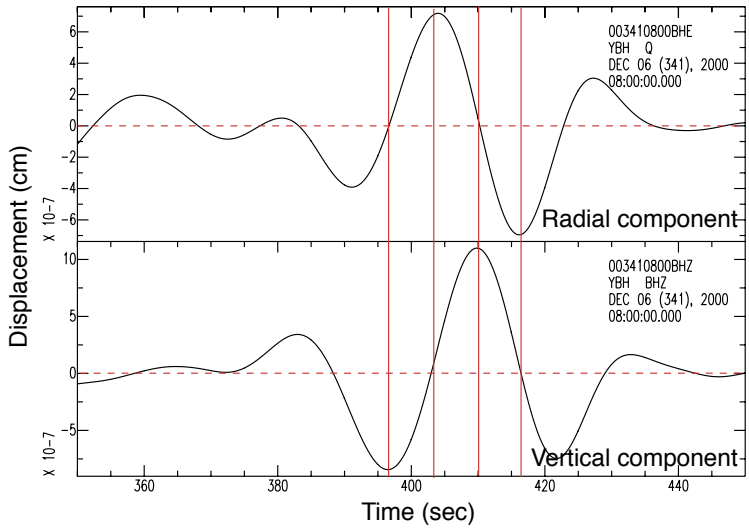


Figure 2.9: Comparison of the retrograde motion of the Rayleigh waves on radial (top) and vertical (bottom) components at YBH

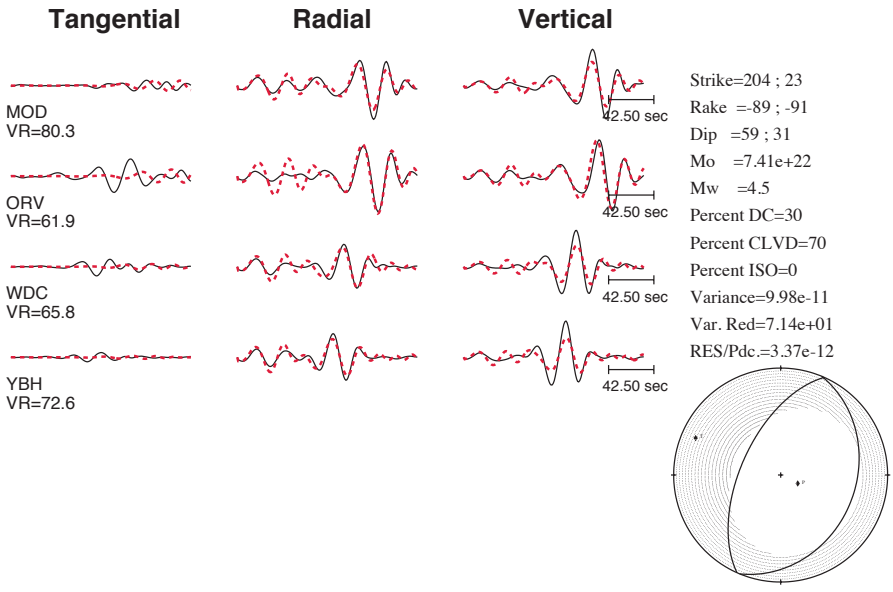


Figure 2.10: Best moment tensor solution for Ekström's slow earthquake

The source mechanism obtained here is not consistent with the main slip motion of the Blanco Transform Fault that is a right-lateral strike-slip fault. However it is consistent with the other solutions calculated on the grid. This could reflect issues with the velocity structure used to generate the Green's functions, which is a velocity model utilized for northern California with a Moho at 25 km depth and that does not correspond to the real structure of the region of the oceanic transform fault. Nonetheless, the Blanco Transform Fault presents a scarp in its central part exhibiting a small extensive zone where earthquakes with normal mechanisms have been found [Braunmiller and Nabelek, 2008]. This normal environment is located about 100 km away from our best solution. The limited azimuthal coverage associated with an incorrect velocity structure might be responsible for the error in location. But the variance reduction of 71.4 % indicates a significant improvement in the location compared to the initial moment tensor analysis performed with the initial location of the earthquake onshore northern California, and proves that our reviewed location is more appropriate (Figure 2.10 versus Figure 2.8).

Figure 2.10 also shows that this event has an unusually large CLVD component. Several hypotheses can be proposed for explaining the large CLVD component. First is that it results as an artifact due to the use of an inadequate velocity model. Second, this earthquake could correspond to a compound seismic event compatible with a shear event occurring in a volcanic environment, which is compatible with the ridge segment located near-by. Or it could indicate the presence of fluids in the fault zone where the earthquake occurred. Or third, that the origin time of the earthquake is not well identified and might provide some inappropriate phase timing in the moment tensor inversion. To answer the first concern, we performed some preliminary tests with two other earthquakes of similar magnitudes located in two regions of the Blanco transform: along the strike-slip section and within the ridge segment, using the same velocity model. Contrary to the slow earthquake studied here, these two events recovered nearly pure double-couple solutions with focal mechanisms that are in agreement with their tectonic setting. This indicates that the Green's functions do not produce a bias towards non-double-couple solutions.

It is not possible to prove or disprove the second possibility of the event being a compound source, or possibly a volcanic event with a volume compensation mechanism that gives a CLVD solution. This region experienced an intense seismic swarm activity with more than 600 earthquakes in 10 days in April 2008 and two mainshocks with magnitude of 4.5 and 4.6. The events were located using the SOund SUrveillance System (SOSUS) hydrophone arrays. In response to this swarm, a cruise was scheduled for departure and for sampling water content on site. However no clear water-column temperature and water content anomalies associated with magmatic activity were found during real-time sampling at the swarm location [`http://www.pmel.noaa.gov/vents/events/oregon-quakes-synopsis.html`]. The absence of evidence for the association of seismic and volcanic activity in the region does not rule out the possibility of there being a volcanic signature in the long-period waveforms,

Table 2.4: Results of the analysis of the undetected slow earthquake

| | Latitude | Longitude | Depth (km) | Magnitude |
|---|---|---|---|---|
| This study | 44.0 | -130.0 | 8 | Mw 4.5 |
| ANSS catalog | 43.9 | -128.4 | 10 | Mb 4.7 Ms 3.9 |

however it cannot be proved.

On the other hand, by taking the uncertainties in the origin time of the event into account it is possible to obtain solutions with a larger double-couple component. While, this event was not present in the seismicity catalogs at the beginning of our study, however it was subsequently studied due to Ekström's detection, and the event was located and placed in the Advanced National Seismic System (ANSS) catalog. This location agrees with our assessment in terms of the magnitude and location ± 100 km (Table 2.4). The $M_w$ of 4.5 established in our study compares well with the two magnitudes entered in the catalog (i.e. $M_b$=4.7 and $M_S$=3.9). The catalog also provides more information regarding the origin time of the event (i.e. 08:04:13.44 UTC or about 14 sec after the origin time considered previously), which is about 14 seconds later than what we considered. Using the ANSS catalog location and origin time the earthquake focal mechanism is confirmed to be normal. However, the non-double-couple component of the event significantly decreased from 70% to 5% with the inversion of 170 seconds of data.

Finally, it is unclear whether this earthquake truly belongs to the family of the slow earthquakes studied here. Nonetheless it demonstrates that by only studying long-period waves, which are strong for slow earthquakes, it is possible to perform reliable source studies and identify unusual events. This procedure could be used in a streaming manner (e.g. Kawakatsu [1998]) to search for slow earthquakes and eventually help identify additional and missing slow events if their information is absent from the seismicity catalog and/or if they do not meet the criteria of $M_L$>3.5 for a complete routine moment tensor analysis at the BSL.

## 2.6 Discussion and conclusion

We identified 18 slow earthquakes between 1992 and 2007 that are located in the vicinity of the MTJ using discrepancies between magnitudes calculated at long-periods ($M_w$) and at short-periods ($M_L$) in the BMTC. The moment magnitudes for these events vary between 4.0 and 6.8 and the focal mechanisms are primarily strike-slip, which is consistent with the

motion of the MTF and the faulting within the Gorda plate. Modeling of their waveforms at stations located at regional distances shows that they require a much longer source time duration than what similar magnitude earthquakes located in the same fault require. Unlike slow earthquakes reported in far offshore transform fault environments where doubts relative to their lack of high frequency waves have been raised [Abercrombie and Ekström, 2003; Ekström, 2006; Schramm and Stein, 2009], these events occur on fault segments located between 50 and 300 km from regional seismic network. It is clear however that these events have characteristics different from most of the seismicity of the region. Nonetheless, their offshore locations and the limited azimuthal coverage (i.e. only to the east of the epicenters) result in large uncertainties in their detection and source characterization.

Using a cross-correlation technique similar to the one used for the monitoring of repeating earthquakes in central California we showed that a few of the identified slow events present high correlation coefficients, however, it did not result in any new detections of slow earthquakes within the focused region at the triple junction in the 14-year scanning period. Revisions of the choice of template events based on their location, and of the frequency bands to be used might improve the search and allow the detection of other unusual earthquakes.

Nonetheless we showed that a grid of moment tensor inversions can be used for the identification of all types of earthquakes (i.e. slow and regular) when performed after filtering the seismic data at long periods, which are strong for slow earthquakes, using only a few stations of a seismic network with even poor azimuthal coverage. We obtained waveform fits with more than 70 % variance reduction for an earthquake that was located well outside the BSL coverage region, west of the Oregon coast. Used routinely, this approach could lead to the discovery of more slow earthquakes and allow us to produce a more accurate catalog of this unusual seismicity located in the MTJ region. In Chapters 3 and 4 we further develop and implement this method first proposed by Kawakatsu [1998].

# Chapter 3

# Rapid detection and characterization of large earthquakes using quasi-finite-source Green's functions in continuous moment tensor inversion

modified from **Rapid detection and characterization of large earthquakes using quasi-finite-source Green's functions in continuous moment tensor inversion** by
Aurélie Guilhem and Douglas S. Dreger,
published in *Geophysical Research Letters* (2011)

## 3.1 Introduction

As recently demonstrated by the 2004 magnitude ($M_w$) 9.0 Sumatra, the 2010 $M_w$8.8 Chile and the 2011 $M_w$9.0 Japan seismic events, great subduction zone earthquakes are capable of triggering devastating, high-fatality tsunamis in their near field, in addition to producing intense local ground shaking [Bryant, 2001; Hirshorn and Weinstein, 2009]. With increasing continuously recording seismic networks, current efforts provide earthquake and tsunami early warnings within 5 to 10 min after the origin time [Lomax and Michelini, 2009]. Current procedures focus on earthquake location, depth, magnitude, and slowness [Hirshorn and Weinstein, 2009]. But initial tsunami early warning statements are commonly issued without knowing the focal mechanism of the earthquake, which has first order importance, together with the magnitude and focal depth, on the excitation of tsunami waves.

Kanamori and Rivera [2008] proposed the use of the fast-propagating long-period W-phase in an automated manner for moment tensor inversions. Complete earthquake source parameters can be known within 20 minutes following the earthquake origin time [Kanamori and Rivera, 2008] and is now computed at the Pacific Tsunami Warning as well as in Japan [Tsuruoka et al., 2009b]. However, it remains limited in its ability to provide useful near-field tsunami early warnings because of its intrinsic time delay [Lay et al., 2005]. Considering

datasets closer to the earthquake rupture may improve the processing time for the source characterization by putting a lower distance bound on the useable data. But the rupture dimensions of M8+ events violate the point-source assumptions applied in moment tensor inverse methods. Even if finite-source inversions solve this problem, their realtime implementations are computationally demanding [Dreger et al., 2005; Dreger and Kaverina, 2000]. Also, while it is possible to rapidly obtain solutions within a 20 min time frame for M6+ offshore events [Dreger, 2010] the scaling of finite-source model for great earthquakes precludes their implementation in realtime. On the other hand, Kawakatsu [1998] proposed a realtime approach to automatically detect, locate and determine the source parameters of earthquakes occurring within a predefined region by computing moment tensors at each point of a grid from continuously streaming long-period (>10 sec) waveform data. With a limited number of stations and assuming a point-source representation, this method gives correct results in terms of detection and source characterization of up to M7 earthquakes offshore Japan [Tsuruoka et al., 2009a].

Here, we present an adapted version of Kawakatsu [1998]'s method, focusing on the most seismically active region of northern California: the Mendocino Triple Junction (MTJ), where small to potentially tsunamigenic earthquakes occur. For major earthquakes (M8+), we propose a point-source moment tensor inversion that takes into account the finiteness of the rupture zone by constructing quasi-finite-source Green's functions (GFs). It becomes possible to monitor all M>3.5 earthquakes with a direct procedure that autonomously detects, locates, and computes source parameters. This is performed using a single step procedure in contrast to the standard cascade-type analysis currently employed in northern California [Gee et al., 2003].

## 3.2 Data and Method

### 3.2.1 The Mendocino Triple Junction

With approximately 80 earthquakes with magnitude larger than 3 every year, the MTJ is known as the most seismically active region in northern California [Oppenheimer, 2007]. Its seismicity is mostly located offshore: along the Mendocino Transform Fault (MTF), within the highly deformed Gorda plate, and along the Cascadia Subduction Zone (CSZ) (Figure 3.1 and see Section 2.2.1). Paleoseismic evidence of great earthquakes along the CSZ [Atwater, 1987], including radiocarbon dating and several offshore turbidite episodes of deformation in the last 2000 years [Clarke and Carver, 1992], indicate that the CSZ is capable of multiple M8+ earthquakes, as large as M9 [Goldfinger et al., 2008; Heaton and Hartzell, 1987; Satake et al., 1996].

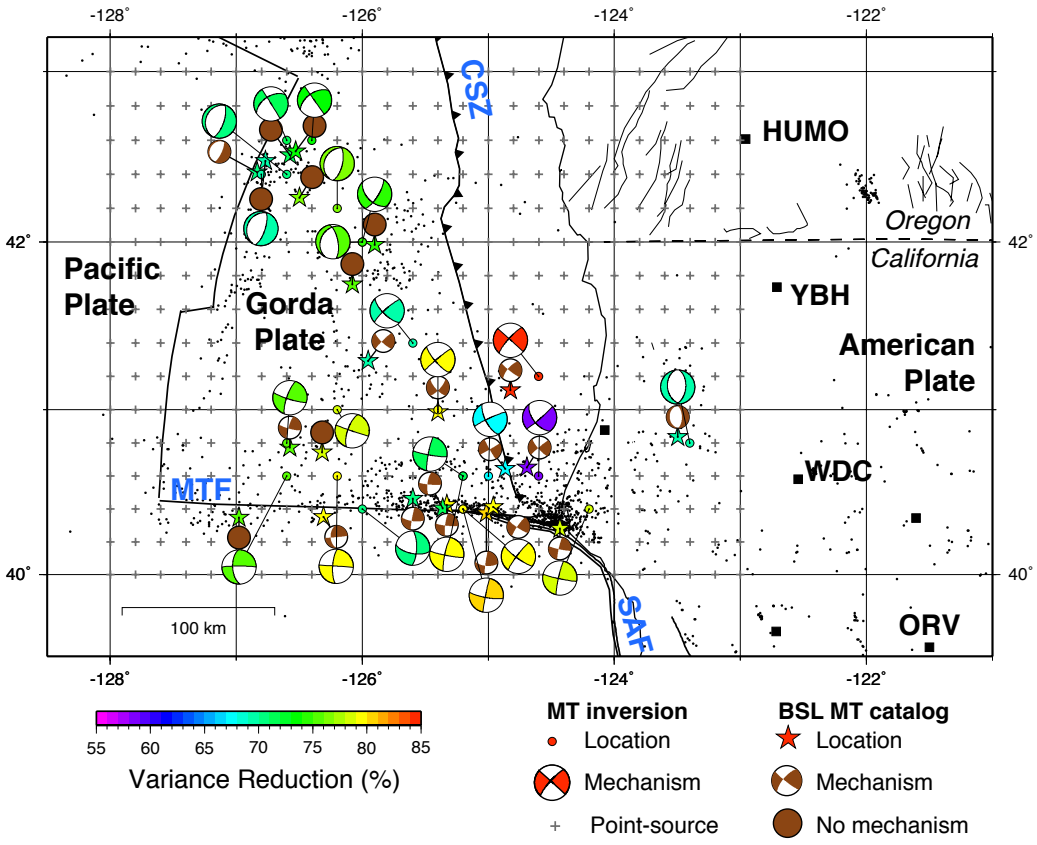


Figure 3.1: Map of the Mendocino Triple Junction region showing the grid of point sources (crosses). The four seismic stations used are HUMO, ORV, WDC and YBH. Black dots show the regional seismicity (M3+) since 1990. The studied events are shown in brown for the catalog solutions and are color-coded by the variance reduction for the inversion solutions. CSZ, MTF, and SAF mark the Cascadia Subduction Zone, the Mendocino Transform Fault, and the San Andreas Fault, respectively.

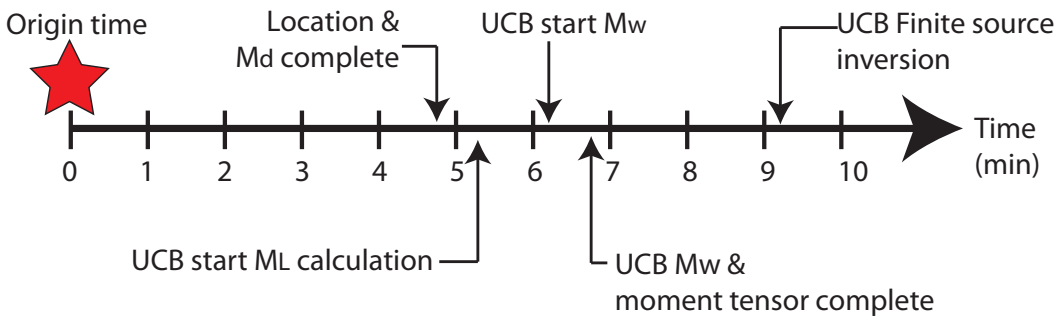


Figure 3.2: Timeline for the M5.6 2007 Alum Rock earthquake in the San Francisco Bay Area

In northern California, current realtime earthquake monitoring is performed sequentially by the U.S. Geological Survey at Menlo Park and the Berkeley Seismological Laboratory [Gee et al., 2003]. Figure 3.2 shows the successive steps toward the automated characterization of the 2007 M5.6 Alum Rock earthquake that correspond to the largest seismic event to occur in the San Francisco Bay Area since the 1989 M6.9 Loma Prieta earthquake. Each parameter depends on previously known ones. The preliminary location and magnitude transmitted by the USGS at Menlo Park has direct consequences on the successful completion of the calculation of the local magnitude ($M_L$) and later, on the correct moment tensor analysis, which is launched only when $M_L$ is found to be 3.5 or larger. However for the Mendocino region, because seismic stations are located onshore, poor azimuthal coverage of the seismic wave radiation patterns often leads to difficulties in detecting and locating events, and thus in determining their full source parameters. There is a need to implement a system that will automatically characterize earthquake sources and will not depend on the successful completion of multi-stage processing.

### 3.2.2 Data

Routine moment tensor inversions at the Berkeley Seismological Laboratory are performed using displacement seismograms. However, in order to avoid the integration from velocity to displacement in the realtime algorithm, we download and invert the velocity seismograms (LH channels) at the four selected broadband seismic stations of the Berkeley Digital Seismic Network (BDSN) for testing purpose. Similarly, the inversions for the M8+ events shown below are also performed using velocity synthetic seismograms. Nonetheless for the realtime approach, we plan to use high-sampled (100 Hz) velocity channels (HH channels) at the four stations to invert for the source parameters of M3.5-to-7 earthquakes because of the short latency required. Regarding larger earthquakes along the CSZ, we propose to in-

vert the strong-motion data (HL channels) to account for the strong shaking in the near- field.

We used the frequency wave number integration method written by Chandan Saikia, FKRPROG [personal communication, 1994] to create a catalog of velocity GFs for all the spatial points of a grid and for a predefined set of seismic stations (described later). They were computed using a 1D velocity model (GIL7) that is utilized for routine earthquake analyses in northern California [Baise et al., 2003]. In this model, the MOHO depth is at 25 km.

### 3.2.3 Moment tensor inversions for earthquake detection

Kawakatsu [1998] proposed to continuously invert the long period seismic wavefield (>10 sec) for moment tensors at grid points representing virtual sources distributed over a region. At each station, the data $d$ are represented directly as the convolution of the GF tensor, $G$, describing the wave propagation between the source and the receiver, and the moment tensor components $m$ of the source:

$$d = G \cdot m \tag{3.1}$$

The least-square solution for the moment tensor ($M$) can be obtained by:

$$M = \left(G^T G\right)^{-1} G^T d \tag{3.2}$$

where the $(G^T G)^{-1} G^T$ matrix for each point-source can be computed in advance knowing a priori the grid distribution and the set of pre-selected seismic stations. The multiplication of this matrix with streaming data can be performed continuously as soon as the data arrives at a central site. Earthquake detection is given when the variance reduction (VR) exceeds a detection threshold:

$$VR = \left[1 - \frac{\sum_i \sqrt{(data_i - synth_i)}}{\sum_i \sqrt{(data_i)^2}}\right] \times 100 \tag{3.3}$$

where *data*, and *synth* are the discrete data and GF time series, respectively, and the summation is performed for all stations and components.

We propose to implement a moment tensor grid search covering the MTJ using four broadband seismic stations of the Berkeley Digital Seismic Network (BDSN) and nearly 5,000 virtual sources located every 0.2° in latitude and longitude and every 3 km in depth, between 5 and 38 km (Figure 3.1). We suggest running in parallel a system for small to moderate earthquakes and a second one for large (M8+) earthquakes along the CSZ. Regarding M3.5-7 earthquakes, the inversion of 380 sec of data is performed every 2 seconds after filtering the seismic wavefield between 20 and 50 sec. This allows sufficient time for the propagation of the full seismic waveforms to reach the seismic stations. For the second

system, we invert a longer record (i.e. 480 sec) and filter the data between 100 and 200 sec. In addition, for large earthquakes, the source time function becomes a significant parameter that needs to be considered. We choose to include an 84-sec source time function to the GFs, which corresponds to the rupture duration of the synthetic M8.2 earthquake we present below. However it is possible to consider several different source time function durations to better target specific types of events (i.e. $M_w$ 8.0, 8.5, 9.0, etc.).

### 3.2.4 Use of quasi-finite-source Green's functions for large earthquakes

For M8+ earthquakes along the CSZ, we propose to invert for moment tensors only at the grid points that are distributed in the slab. This significantly lowers the number of calculations and permits us to focus on the most hazardous region of the grid. It is then possible to consider earthquake scenarios in advance and to invert for them in realtime. However, this grows into a near-field problem in which the stations are sensitive to different parts of the overall rupture. We propose here to employ quasi-finite-source adjusted GFs where GFs of $n$ grid points are averaged to generate composite GFs, *Gtot*, that take into account the source-receiver back-azimuth and thereby the effective radiation patterns of each component (Figure 3.3):

$$G_{tot}(t) = \frac{\sum_{i=1}^{n} G_i(t)}{n} \tag{3.4}$$

The prefixed number of points $n$ has an effect on the complexities of the pre-defined earthquake scenarios considered in the realtime inversions. Directivity can also be pre-included in the composite GFs, giving constraints on the nature of the finite-rupture, whether unilateral or bilateral (Figure 3.3):

$$G_{tot} = \frac{\left[G_1(t) + \sum_{i=2}^{n} G_i(t) \cdot \left(\frac{\Delta_{1-n}}{v_r}\right)\right]}{n} \tag{3.5}$$

where $\Delta_{1-n}$ is the distance between Source 1 (reference source) and Source $n$ and $v_r$ is the rupture velocity. The moment tensor inversion itself is performed assuming a point-source analysis method, which maintains the computational speed. One of the point-sources of the composite GF is considered as a reference because information about the corresponding azimuths between the selected grid-point and the seismic stations is needed to rotate the GFs into the East, North and vertical components for the realtime inversion.

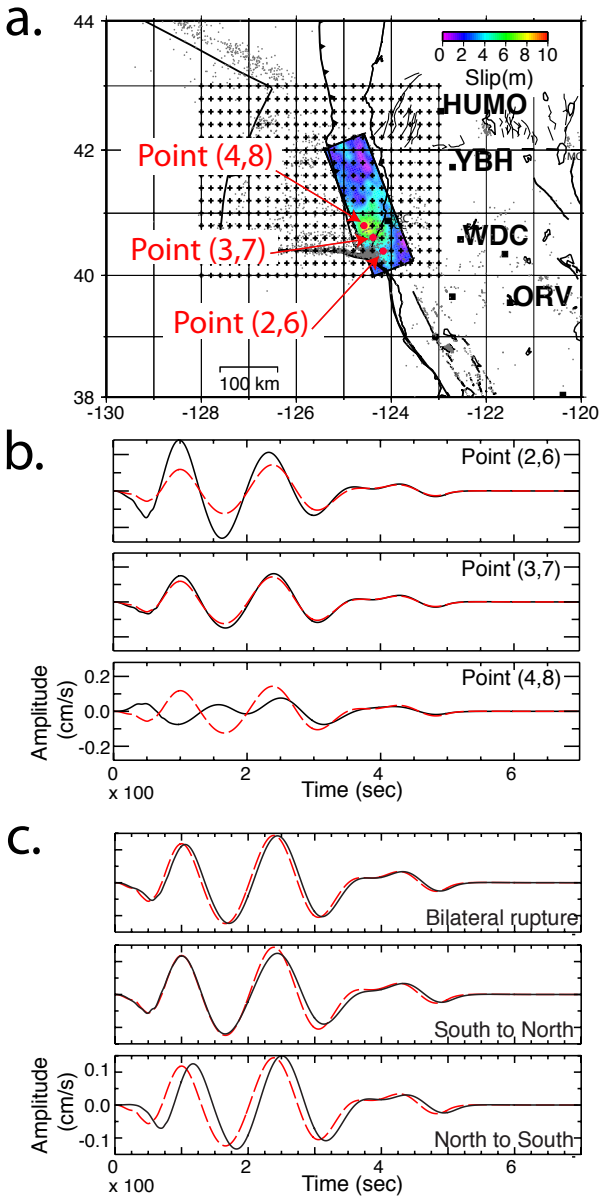


Figure 3.3: Effect of the finite-fault on the waveforms. a) Map of the slip model of a synthetic M8.2 earthquake (rectangle). Arrows point to the three grid-points (in red) considered in the generation of quasi-finite-source GFs. b) Synthetic EW components at WDC computed for the three different grid-points (black, solid traces) compared to the quasi-finite-source GF computed using the three selected grid points (red, dashed traces). c) Directivity in the quasi-finite-source GF (black, solid traces) compared to the GFs without directivity of b) (red, dashed traces).

## 3.3 Results

### 3.3.1 Detection and characterization of small to moderate earthquakes

We test the concept on M4 to M7.1 earthquakes (Figure 3.1 and Table 3.1). The solutions obtained using a 1 D velocity model agree well with the Berkeley Moment Tensor Catalog solutions confirming that the system proposed by Kawakatsu [1998] is suitable for implementation in the MTJ region.

Using this approach and a VR threshold fixed at 65% similar to the one predefined in Japan [Tsuruoka et al., 2009a], we are able to detect all the events, including the M3.5 earthquakes, to the exception of the M6.5 mainshock that occured in January 2010. The average VR for the tested events is 74.4%, with the lowest VR being 58.5% for the M6.5 earthquake and the largest one being 84.7%. In term of location, the GridMT approach allows us to obtain the locations in latitude and longitude within a grip space considering the current grid definition, with an average horizontal difference between the USGS location and the code's solution of 18.7 km. However, because of the use of a single 1 D velocity model over the entire region, we are not constraining very well the depths of the earthquakes, especially for those that are far offshore. For these far oceanic earthquakes the best solutions are obtained at greater depths than those reported in the earthquake catalog because of a unique MOHO depth in the velocity model at 25 km. Nonetheless, for earthquakes that are located in the vicinity of the triple junction, the code better constrains the depths because the velocity model is in a better agreement with the region. The average depth difference between the two catalogs for the 19 studied events is 18 km. In term of origin time we obtain the origin time of the events within + or - 3 sec of the catalog origin times. And finally, the GridMT technique helps recover the moment magnitudes with an averaged discrepancy of 0.1 unit.

### 3.3.2 Detection of potentially tsunamigenic earthquakes

Unlike what we found previously, the 20-50 sec inversions of 380 sec long records for a synthetic M8.2 reverse event with uniform slip fail to recover the earthquake parameters, yielding only $M_w$ 6.7 and a poor fit, VR = 47% (Figure 3.4). Because of the narrow band processing, the point-source inversion only fits a small part of the record and is not sensitive to the total seismic moment. The source corner frequency of the event ($\sim$ 0.011 Hz) is indeed lower than the frequency band considered. In contrast, the 100-200 sec passband works better (VR= 54.6% in Figure 3.4) and gives a point-source location near the fault centroid, the correct $M_w$ and focal mechanism.

Table 3.1: Table of the source parameters obtained for the tested M4 to 7 earthquakes

| | ANSS catalog | | | | | Continuous moment tensor analysis | | | | | | | | | Differences | | | |
|---|---|---|---|---|---|---|---|---|---|---|---|---|---|---|---|---|---|---|
| Date | Origin time | Lat | Lon | Depth | M | Origin time | Lat | Lon | Depth | $M_w$ | Strike | Rake | Dip | VR | Horizontal distance (km) | Vertical distance (km) | Origin time | $M_w$ |
| 08/15/2003 | 09:22:15 | 40.985 | -125.430 | 8.6 | 5.3 | 09:22:16 | 41.0 | -125.4 | 23 | 5.1 | 230 | 14 | 85 | 79.56 | 3.0 | 14.4 | 00:00:01 | 0.20 |
| 12/22/2004 | 20:47:27 | 42.479 | -126.768 | 10.0 | 5.1 | 20:47:26 | 42.4 | -126.8 | 38 | 5.1 | 18 | -94 | 70 | 69.81 | 9.2 | 28.0 | 00:00:01 | 0.00 |
| 03/07/2005 | 02:34:34 | 42.512 | -126.575 | 10.0 | 5.3 | 02:34:34 | 42.6 | -126.6 | 38 | 5.2 | 328 | -143 | 89 | 71.30 | 10.0 | 28.0 | 00:00:00 | 0.10 |
| 03/07/2005 | 02:48:20 | 42.534 | -126.529 | 10.0 | 5.2 | 02:48:24 | 42.6 | -126.4 | 38 | 5.1 | 145 | 145 | 89 | 73.82 | 12.9 | 28.0 | 00:00:04 | 0.10 |
| 06/15/2005 | 02:50:54 | 41.292 | -125.953 | 16.0 | 7.2 | 02:51:12 | 41.4 | -125.6 | 38 | 7.0 | 228 | 20 | 80 | 69.70 | 31.9 | 22.0 | 00:00:18 | 0.20 |
| 06/17/2005 | 06:21:43 | 40.773 | -126.574 | 12.0 | 6.6 | 06:21:44 | 40.8 | -126.6 | 38 | 6.6 | 107 | 165 | 81 | 75.93 | 3.7 | 26.0 | 00:00:01 | 0.00 |
| 03/22/2006 | 05:42:03 | 40.744 | -126.319 | 10.0 | 5.0 | 05:42:08 | 41.0 | -126.2 | 38 | 5.0 | 109 | 159 | 88 | 78.92 | 19.4 | 28.0 | 00:00:05 | 0.00 |
| 03/25/2006 | 03:16:05 | 41.749 | -126.080 | 10.0 | 5.1 | 03:16:08 | 42.0 | -126.0 | 26 | 4.9 | 349 | -108 | 66 | 75.39 | 13.4 | 16.0 | 00:00:03 | 0.20 |
| 03/25/2006 | 20:14:07 | 41.983 | -125.902 | 10.0 | 5.0 | 20:14:06 | 42.0 | -126.0 | 32 | 4.9 | 32 | -39 | 73 | 74.47 | 8.3 | 22.0 | 00:00:01 | 0.10 |
| 07/19/2006 | 11:41:43 | 40.281 | -124.433 | 20.7 | 5.0 | 11:41:50 | 40.4 | -124.2 | 29 | 4.9 | 102 | 174 | 86 | 78.16 | 23.8 | 8.3 | 00:00:07 | 0.10 |
| 02/26/2007 | 12:19:54 | 40.643 | -124.866 | 0.0 | 5.4 | 12:19:56 | 40.6 | -125.0 | 23 | 5.4 | 245 | 22 | 84 | 67.80 | 12.3 | 23.0 | 00:00:02 | 0.00 |
| 05/09/2007 | 07:50:04 | 40.375 | -125.016 | 0.2 | 5.2 | 07:50:04 | 40.4 | -125.2 | 23 | 5.3 | 191 | 11 | 87 | 80.35 | 15.9 | 22.8 | 00:00:00 | 0.10 |
| 06/25/2007 | 02:32:25 | 41.117 | -124.825 | 3.4 | 5.0 | 02:32:32 | 41.2 | -124.6 | 26 | 4.9 | 312 | -170 | 89 | 84.68 | 21.0 | 22.6 | 00:00:07 | 0.10 |
| 03/15/2008 | 14:44:36 | 42.412 | -126.835 | 10.0 | 5.7 | 14:44:40 | 42.4 | -126.6 | 39 | 5.7 | 19 | -92 | 68 | 70.32 | 19.4 | 29.0 | 00:00:04 | 0.00 |
| 04/30/2008 | 03:03:07 | 40.836 | -123.497 | 29.1 | 5.4 | 03:03:10 | 40.8 | -123.4 | 35 | 5.3 | 5 | -81 | 51 | 69.19 | 9.1 | 5.9 | 00:00:03 | 0.10 |
| 07/30/2008 | 13:39:34 | 40.425 | -125.330 | 18.0 | 4.2 | 13:39:38 | 40.6 | -125.2 | 26 | 4.2 | 101 | 171 | 84 | 79.62 | 22.3 | 8.0 | 00:00:04 | 0.00 |
| 11/28/2008 | 13:42:19 | 40.348 | -126.978 | 10.0 | 5.9 | 13:42:28 | 40.6 | -126.6 | 38 | 5.9 | 270 | -149 | 86 | 75.63 | 42.7 | 28.0 | 00:00:09 | 0.00 |
| 11/04/2009 | 02:16:56 | 40.462 | -125.600 | 15.5 | 4.2 | 02:16:50 | 40.4 | -126.0 | 29 | 4.1 | 2 | -27 | 71 | 70.67 | 34.6 | 13.5 | 00:00:06 | 0.07 |
| 01/10/2010 | 00:27:39 | 40.652 | -124.692 | 29.3 | 6.5 | 00:27:48 | 40.6 | -124.6 | 26 | 6.4 | 49 | -31 | 85 | 58.53 | 9.7 | 3.3 | 00:00:09 | 0.10 |
| 02/04/2010 | 20:20:22 | 40.412 | -124.961 | 23.6 | 5.9 | 20:20:20 | 40.4 | -125.2 | 23 | 5.8 | 217 | 10 | 83 | 79.43 | 20.3 | 0.6 | 00:00:02 | 0.08 |
| 04/15/2010 | 08:36:00 | 40.352 | -126.307 | 26.8 | 3.9 | 08:36:02 | 40.6 | -126.2 | 38 | 4.5 | 274 | -163 | 89 | 79.92 | 29.1 | 11.2 | 00:00:02 | 0.56 |
| 05/13/2010 | 05:35:12 | 42.263 | -126.499 | 10.0 | 5.3 | 05:35:18 | 42.2 | -126.2 | 35 | 5.2 | 13 | -96 | 65 | 76.10 | 25.7 | 25.0 | 00:00:06 | 0.10 |
| 03/06/2011 | 13:46:38 | 40.404 | -125.363 | 24.7 | 4.5 | 13:46:42 | 40.6 | -125.2 | 26 | 4.5 | 100 | 172 | 84 | 71.46 | 32.3 | 1.3 | 00:00:04 | 0.00 |

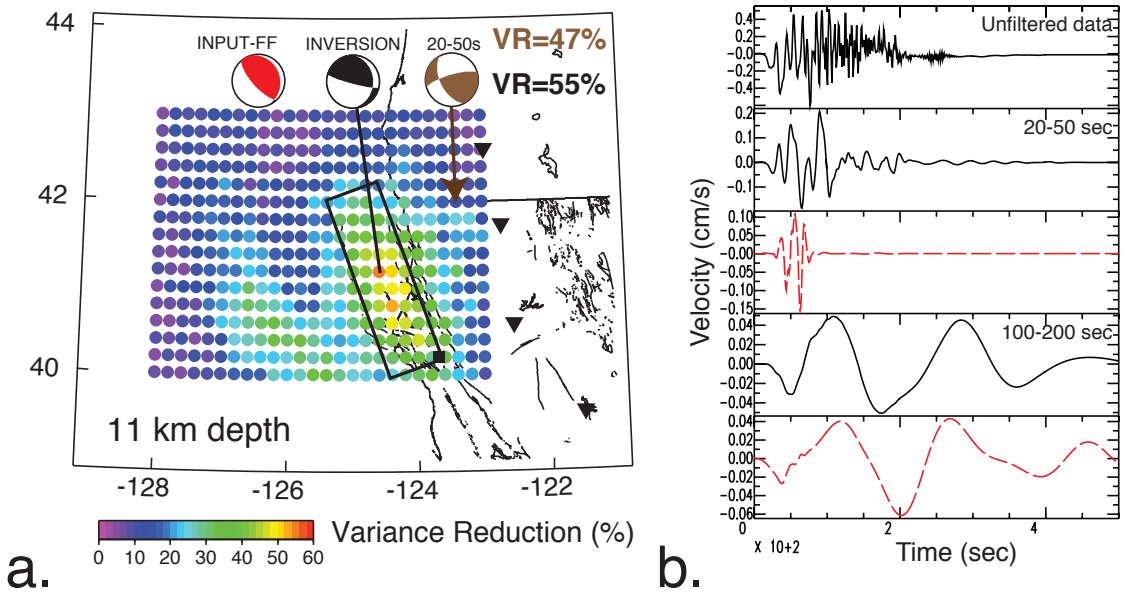


Figure 3.4: Short periods versus long periods in moment tensor inversions. a) Map of grid points (dots) at 11 km depth color-coded by their best variance reduction for a modeled M8.2 earthquake with uniform slip (rectangle). The best solution shown by the black beach-ball diagram (center, VR=54.6%) at 100-200 sec period is compared to the input mechanism (red, left) and to the best solution (VR=47% for $M_w$6.7) obtained with the 20-50 sec passband (brown, right). b) Unfiltered, 20-50 sec period, and 100-200 second period vertical component velocity waveforms at WDC for the fault rupture shown in a) are compared (back, solid traces). The point-source GFs in the respective passbands (red, dashed traces) are scaled by the scalar moment obtained from the respective moment tensor inversions shown a). Note that in the 20-50 second passband only a fraction of the time series is fit, whereas in the 100-200 second passband the same point-source Green′s functions can fit most of the data.

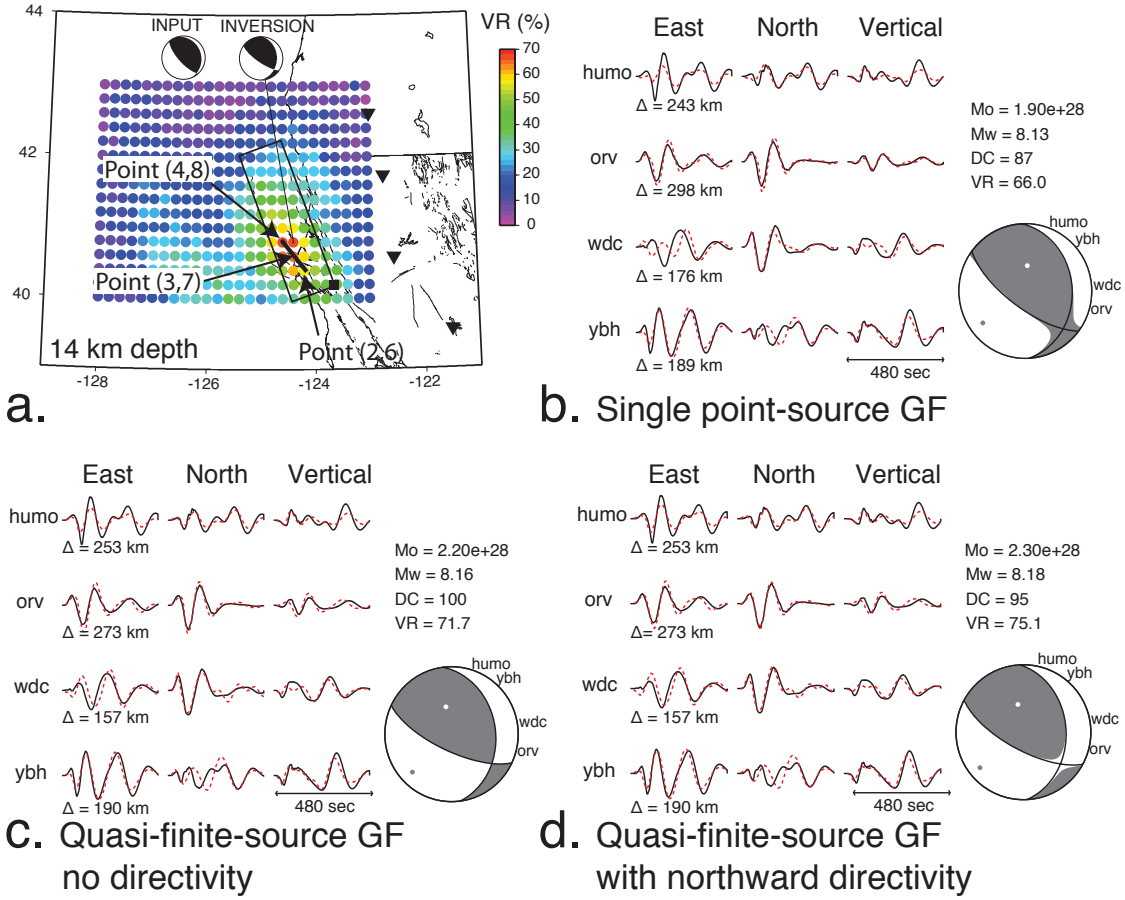


Figure 3.5: Comparison of the moment tensor solutions for a M8.2 earthquake. a) Map of the best VRs at 14 km depth obtained for a point-source moment tensor inversion for a synthetic M8.2 earthquake (rectangle). The best mechanism (top, right) is compared to the input mechanism (top, left). Arrows point to the points that are considered in the multi-point source inversion. b) Best moment tensor solution obtained at Point (3,7). c) Moment tensor solution for the multi-point source inversion (no directivity). d) Moment tensor solution for the multi-point source inversion with a northward directivity.

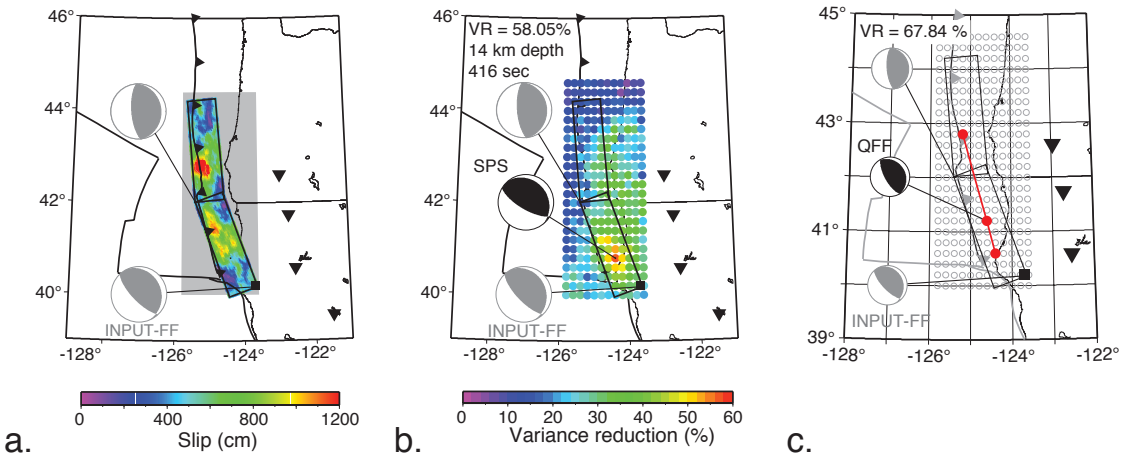


Figure 3.6: Test for a synthetic $M_w$8.4 earthquake. a) Slip model of the synthetic earthquake. INPUT-FF indicates the focal mechanisms (gray) of the input model that is composed of two M8 rupture (black square: rupture initiation). The gray region shows the area of the point-sources used in b). Triangles locate the four seismic stations. b) Best VRs at 14 km depth using single-point-source (SPS) GFs. The focal mechanism (black) of the best VR (58.05%) is shown and obtained 16 sec after the origin time of the synthetic test. c) Red dots show the three points that are combined to generate composite GFs and to which a northward rupture is included. The VR increases to 67.84% (Table 3.3) and the mechanism (QFF) in black is very similar to the input mechanism.

Similar results are obtained for a variety of additional slip models ($M_w$8.2 and 8.4) using a single point-source moment tensor inversion with point-source GFs (Figures 3.5a,b and 3.6). As Figure 3.5a shows, the best solution obtained for a synthetic M8.2 earthquake with variable slip is found within the rupture segment near the centroid. We find that more realistic variable slip distributions are better represented by a point-source assumption at longer periods as proposed by Fukuyama and Dreger [2000]. Regarding the M8.4 earthquake that results from the combination of two M8.2 earthquakes, Figure 3.6b shows that the best solutions at 14 km depth for the synthetic M8.4 earthquake are located slightly to the south of the main slip region of the southern rupture segment when using single-point GFs in a point-source moment tensor inversion. Also, in Figure 3.6 the main slip area of the northern segment is not well represented. This observation is found to be caused by the interference of the waves originating from the two rupture zones. Indeed, we find that when we cancel out one of the segments we are able to correctly observe the other one (Figure 3.7), with VRs up to 82%. In this case, the northern segment alone is better represented because of its larger distances from the seismic stations, which better satisfy the point-source assumption used in the moment tensor inversion.

Table 3.3: Results for variable slip models of a M8.2 reverse earthquake (Figure 3.5) and a M8.4 reverse earthquake (Figure 3.6). The time is given relative to the origin time of the synthetic events.

| | | 1 point | 3 points / no delay | South to North | North to South | Bilateral |
|---|---|---|---|---|---|---|
| M8.2 | VR (%) | 66.53 | 71.69 | 75.12 | 66.78 | 72.69 |
| | Time (sec) | 12 | 6 | -4 | -4 | 0 |
| | $M_w$ | 8.2 | 8.2 | 8.2 | 8.2 | 8.2 |
| M8.4 | VR (%) | 58.05 | 46.12 | 68.22 | 11.05 | 47.96 |
| | Time (sec) | 16 | 20 | 0 | 0 | -4 |
| | $M_w$ | 8.1 | 8.2 | 8.3 | 8 | 8.3 |

Even if the previously described tests return the detection of synthetic earthquakes, we show that it is possible to improve the fit between the synthetics and the data (Figures 3.5c and 3.6c) after simultaneously summing the GFs of several grid points centered on the event centroid. Figure 3.5d shows that, by considering a northward rupture in the composite GFs and a rupture velocity of 3 km/sec, the corresponding earthquake solution has a larger VR and better estimates the focal parameters (Table 3.3). Similar results are obtained for a M8.4 synthetic seismic event, which presents an extended rupture (i.e. 480 km) and two major slip areas (Figure 3.6c). This method permits raising the detection level of large earthquakes and allows us to obtain more precise source parameters (Table 3.3), by considering

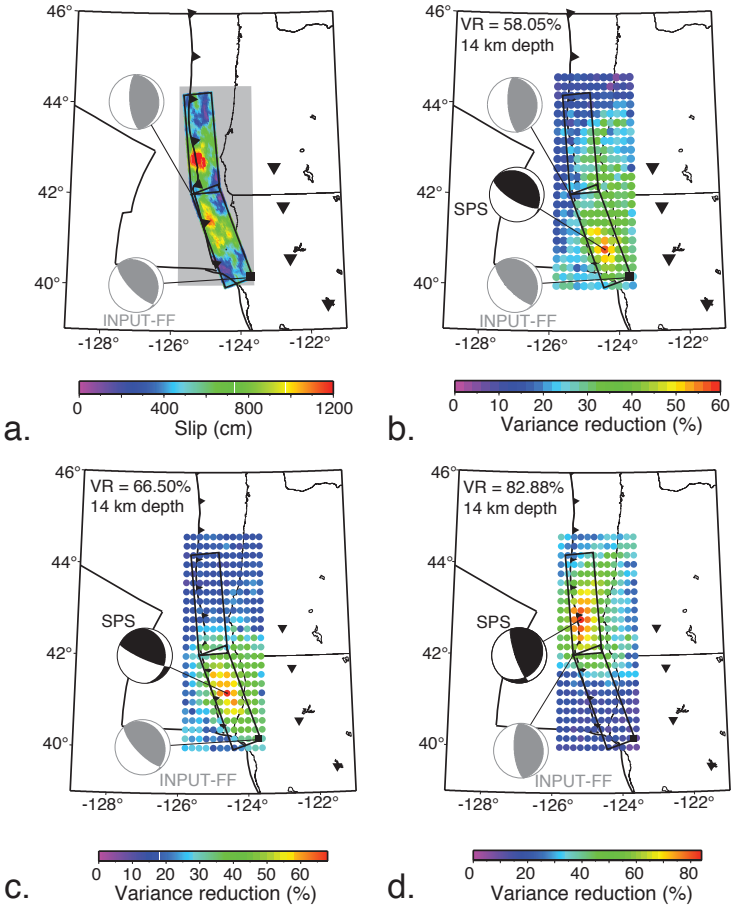


Figure 3.7: Influence of a compound fault rupture in the moment tensor inversion for a M8.4 earthquake (Figure 3.6). a) Slip model of the synthetic earthquake. INPUT-FF indicates the focal mechanisms in gray of the input model (black square: rupture initiation). The gray region shows the area of the point-sources used in b). Triangles locate the four seismic stations. b) Best VRs at 14 km depth using single-point-source (SPS) GFs for the test using the entire rupture. The focal mechanism (black) of the best VR (58.05%) is shown and obtained 16 sec after the origin time of the synthetic test. c) Best VRs at 14 km depth using single-point-source (SPS) GFs for the southern rupture only. The slip of the northern segment is fixed at 0. The focal mechanism (black) of the best VR (58.05%) is shown and obtained 16 sec after the origin time of the synthetic test. d) Best VRs at 14 km depth using single-point-source (SPS) GFs for the northern rupture only. The slip of the southern segment is fixed at 0. The focal mechanism (black) of the best VR (82.88%) is shown and obtained 16 sec after the origin time of the synthetic test

a range of quasi-finite-source GFs for different directivity scenarios and source time duration.

## 3.4 Additional tests

### 3.4.1 Problems with realtime data

The advantage of this proposed technique is its possibility to compute earthquake source parameters on long-period streaming data in a realtime process. However, one has to be aware of potential issues directly linked to the use of such realtime data. One of the problems that this approach can meet is the absence of data, either because one or several seismic stations (or components) are not properly working or because of extended time delay in the data transmission between the station and the seismic center. In this proposed scheme we indeed need long continuous records (i.e. about 6 minutes for small and moderate earthquakes, and 8 minutes for large subduction zone earthquakes).

We test the effects of missing data in the characterization and detection of a moderate earthquake: the M5.0 Mendocino earthquake that occurred in the vicinity of the triple junction in July 2006. We choose to compute the earthquake source by representing the missing seismic channels with a zero trace. By doing so, we do not need to modify the general approach of the procedure that considers a default number of stations and components. We choose to model several cases in which we change: 1) the number of missing channels, from 1 to 3 out of the 12 predefined channels from the four broadband stations, and 2) the number of missing stations, from 1 to 3 stations. We need to have at least one station working in order to perform the algorithm. We find that the event is well characterized, within + or - 15 degrees in the plane azimuths when stations are missing (Figure 3.8). The use of one station does not affect with the correct definition of the source mechanism taking into account the fact that we use full waveforms that contain the radiation patterns for the P, S and surface waves together. Nonetheless, we find that when individual components are zeroed out, there are more uncertainties in the plane orientations (Figure 3.9) than when all the three components of the stations are missing. This is due to the fact that some components record more or less energy from the earthquake, depending on the source radiation pattern and the station coverage. If one component that does not show large amplitude waves is zeroed out, the resulting mechanism will not differ by a lot from the reference mechanism. However, if we simultaneously cancel out one of several components that recorded major phase information, then the output mechanism will most likely be different from the reference one. We also notice that the magnitude range is larger when 3 components are missing than when 3 stations are missing, indicating larger uncertainties in the moment tensor analysis.

The VRs are also by consequence affected by the missing data and this has direct impli-

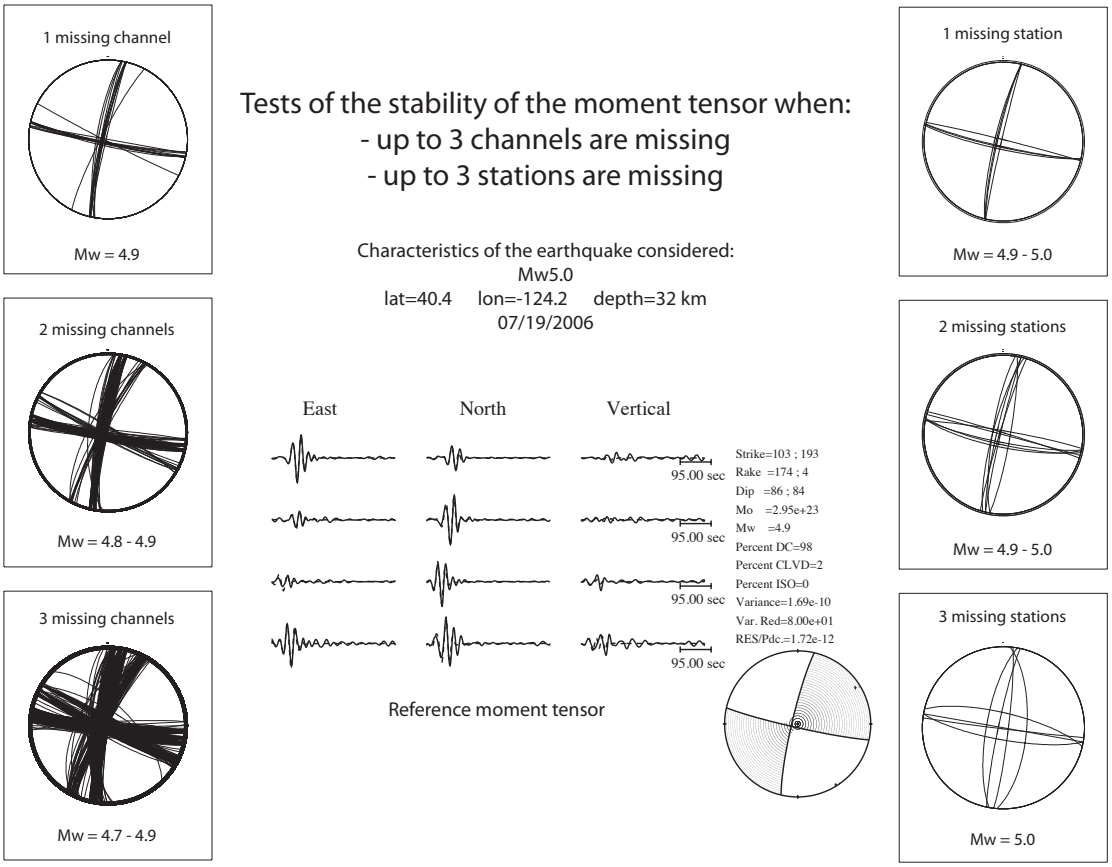


Figure 3.8: Stability test of the detection of a $M_w5.0$ earthquake. Missing components are modeled with amplitudes set at 0. Missing stations are not considered in the moment tensor inversion.

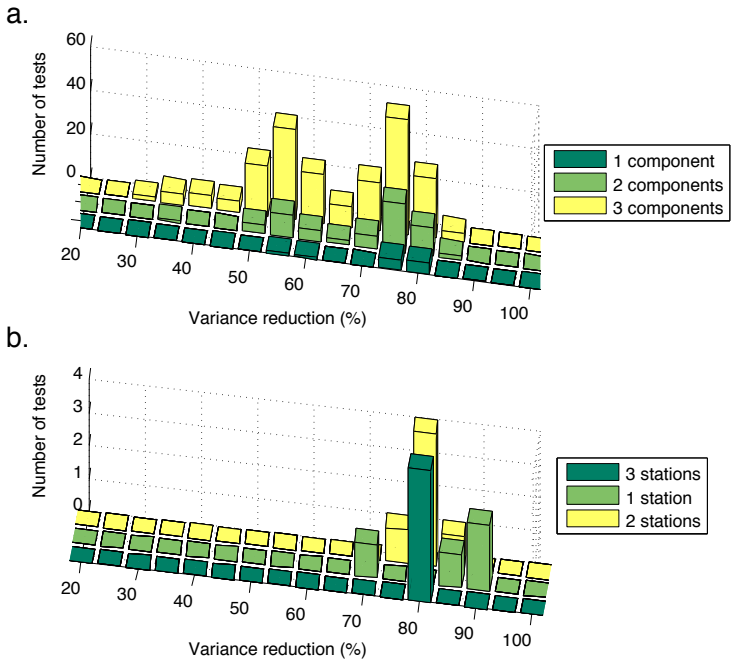


Figure 3.9: Effect of missing channels and stations for the detection of a $M_w$5.0 earthquake on its detection (Figure 3.8). a) Effect of missing components, from 1 to 3. Here, the missing component(s) is represented with a zero-amplitude trace and is considered in the calculation of the variance reduction. b) Effect of the number of stations considered in the moment tensor inversion. The missing station(s) is not considered in the calculation of the variance reduction.

cation on the detection level of earthquakes in such condition of limited seismic ressources. Figure 3.9 shows the range of VRs obtained for each tests with missing channels and missing stations. In the case of this particular earthquake we find that missing stations, even up to 3, does not affect its detection if we were fixing a VR threshold at 65%. However, this statement becomes wrong when channels are missing because, in these situations, we observe a tendency of lowering the VRs to about 30%. This test shows that even one missing component affects the detection in this moderate earthquake with some VRs around 50% (Figure 3.9).

### 3.4.2 Noise and teleseisms

We tested the approach on 630 seconds of seismic noise (Figure 3.10) in which no local, regional, and teleseismic earthquakes are reported in the ANSS catalog. We recorded a maximum VR of 4.9% and 22% for data filtered between 20 and 50 sec and between 100 and 200

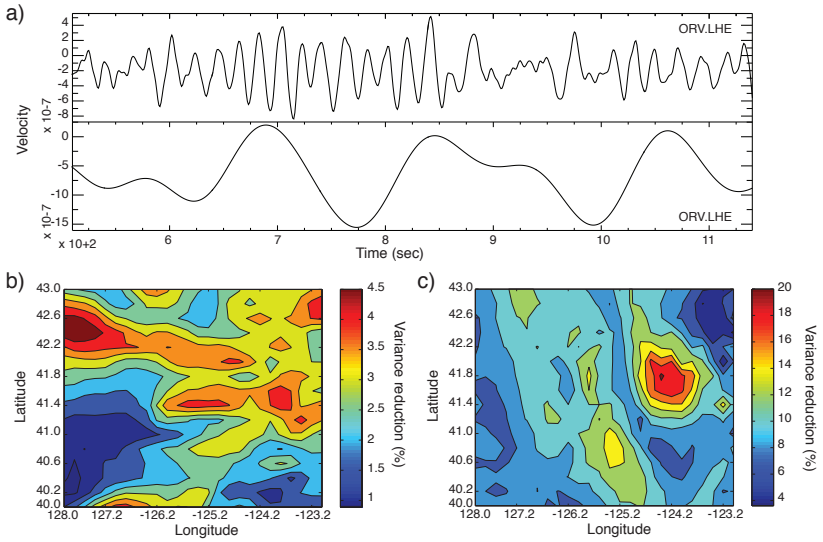


Figure 3.10: Results of the moment tensor inversion results on seismic noise. a) Horizontal component waveforms of seismic noise recorded at ORV and filtered at 20-50 sec and 100-200 sec period scanned in the moment tensor algorithm. b) Map view of the best VRs on the grid at 32 km depth for data filtered between 20 and 50 sec period. c) Same as b) with data filtered between 100 and 200 sec.

sec, respectively. These VRs are well below a possible VR threshold that would be used for earthquake detection (for example 65% used in Japan [Tsuruoka et al., 2009a]) indicating that no detection would have been made at 20-50 sec and 100-200 sec periods. These best VRs yield $M_w3$ and $M_w5$ at the shorter and longer periods, respectively.

Another test (Figure 3.11) was performed over a 45-minute period following the 2009/03/19 M7.9 Tonga earthquake in which the major seismic energy of the earthquake travelled through the network with noticeable phase arrivals (P, S, and surface waves). For data filtered between 20 and 50 sec we found a maximum VR of 19.3%. However, the VR increased up to 56% for the 100-200 sec passband. This last solution shows that depending on the VR threshold used for earthquake detection, this teleseismic event could be falsely identified as a local/regional earthquake, however its magnitude would be given to be only 6.0 and therefore could be excluded for additional consideration as an actual offshore great earthquake. Detections using the 100-200 sec passband should only be considered for M8+ earthquakes. Indeed, we found previously that the 20-50 sec passband gives satisfactory results for earthquakes with magnitude up to 7 located within the region (Figure 3.1 and Table 3.1).

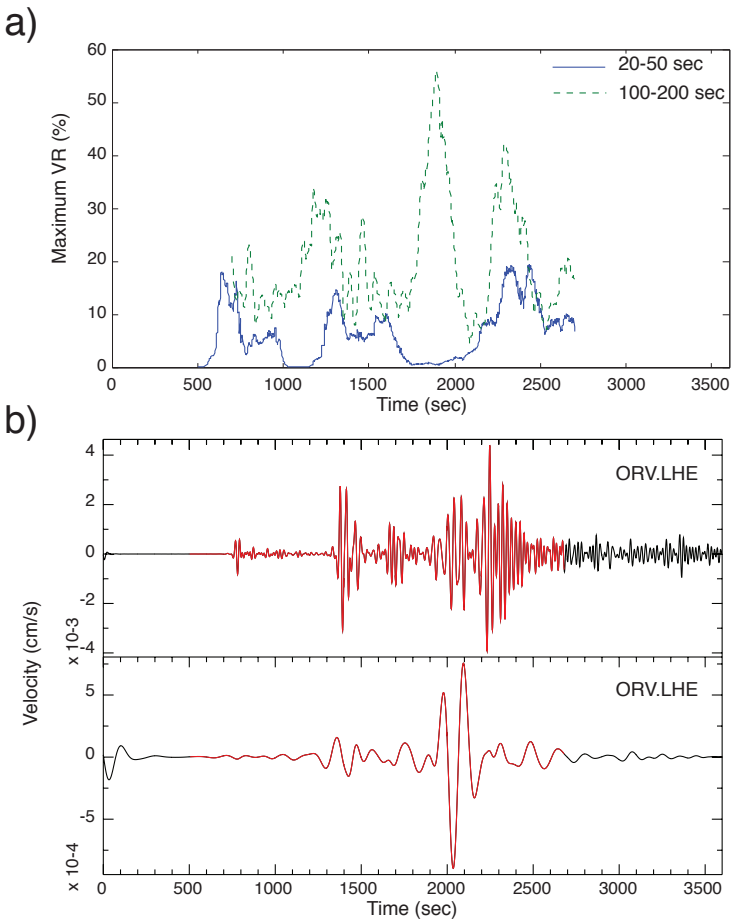


Figure 3.11: Results of the moment tensor inversions on a teleseism, the 2009/03/19 M7.5 Tonga earthquake. a) Time evolution of the best VRs over the grid every 2 seconds at 32 km depth for data filtered between 20 and 50 sec, and for 100-200 sec periods. b) Waveforms recorded at station ORV (vertical component) considered in the moment tensor inversions. In red, data considered in the inversions.

### 3.4.3 Detection of a M9 earthquake

On March 11th, 2011 a great earthquake occurred off the coasts of Japan and was followed by a large scale tsunami that affected the local and regional coasts as well as the coastlines across the Pacific Ocean, including California. The magnitude of the mainshock was underestimated at first, with an initial magnitude of 7.9, followed a couple of hours later by a revised magnitude of 8.9 and a couple days later to another revised magnitude in the lower 9 range. Thanks to a very dense seismic network composed of broadband and strong-motion stations, this earthquake gives us the opportunity to test the approach presented here for an equivalent M9 earthquake occurring off the coast of Mendocino.

We used the finite-fault model (model 3) of Shao et al. [2011] of the recent 2011 M9.1 Japan earthquake and adapted it for the MTJ region (Figure 3.12). The resulting rupture segment is wider than other tested models (Figures 3.3, 3.4, and 3.6). Its rupture extends downdip below most of the pre-selected seismic stations. Figure 3.13 demonstrates that in the very-long periods, the velocity seismograms obtained from the strong-motion data recorded at station MYG004 (K-NET) in Japan, which recorded a maximum acceleration of about 3 g in the 2011 M9 earthquake, are comparable with records expected at station YBH for a M9.1 and M8.5 earthquake along the CSZ, even when the source-caused complexities observed in the unfiltered data of station MYG004 are taken into account. Because of this downdip extension, the amplitudes of the strong-motion data are larger than expected compared to a $M_w$8.5 earthquake in the same region (Figure 3.13). Using the very long period (100-200 sec) velocity records of this adapted $M_w$9.1 event and point-source GFs, we are able to correctly detect the occurrence of the large earthquake within 8 minutes, and to determine its centroid location, correct magnitude and focal mechanism (i.e. dip slip). Our best solution has a VR of 85%, indicating that such event would be very well detected by the proposed approach. The compactness of the slip is well represented by the point-source assumption (Figure 3.12). We expect that quasi-finite-source GFs could further improve the fit to the data (see Chapter 4 for direct application to the M9 Tohoku-oki earthquake).

## 3.5 Discussion and conclusion

We show that it is possible to detect and characterize the seismic activity of the MTJ region using an algorithm that performs moment tensor inversions using streaming waveform data. The powerful addition of quasi-finite-source GFs enables better definition of the centroid location, the correct source mechanism and magnitude of large earthquakes. Used in a point-source formalism, they allow more rapid detection of major events and more precise determination of their source parameters than is likely to be available using standard processing systems. This approach may enable applications for tsunami early warning in

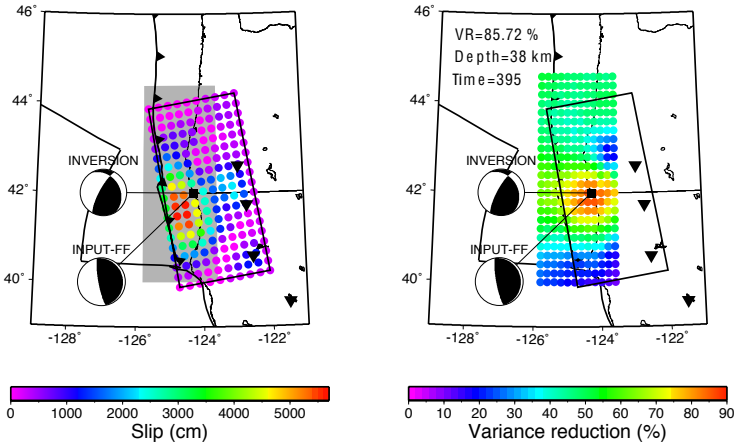


Figure 3.12: Simulation of the equivalent of the 2011 M9 Japan earthquake using Shao et al.'s [2011] slip model for the MTJ region (left) and map of the best VRs obtained between 75 sec before and 125 sec after the origin time of the earthquake (right). The input mechanism (INPUT-FF) of the simulation is compared with the best solution from the very-long period single point source GFs (INVERSION). Our best solution is found with VR=85% and $M_w$9.1.

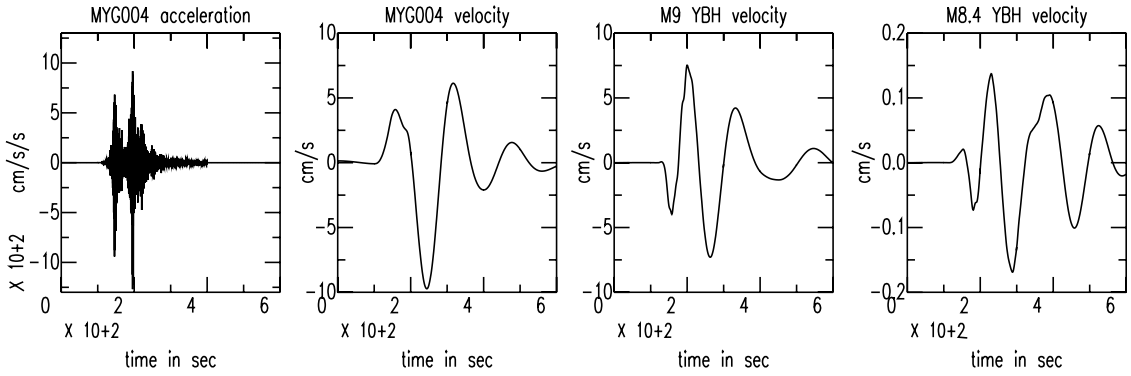


Figure 3.13: Comparison of East-West components for large earthquakes. Unfiltered strong-motion record (acceleration) and filtered (100-200 sec), integrated strong-motion data at MYG004 (K-NET) of the M9 Japan earthquake compared with 100-200 sec velocity record at YBH for a synthetic M9 event offshore Mendocino (Figure 3.12), and for a synthetic M8.5 earthquake (Figure 3.12), from left to right respectively. MYG004 is located about 175 km from the JMA location (294°/113° azimuth) and YBH is located about 143 km from synthetic hypocenter (101°/282° azimuth).

the near-field of large coastal earthquakes. Detections from the automated moment tensor inversion can be as fast as the length of the inverted seismic records. Complete earthquake information is retrieved about 6 minutes after a M4-7 earthquake and 8 minutes after a M8+ earthquake. To this time, data telemetry latency ($\sim$ 2 sec) and a negligible ($\ll$ 1 sec) delay for filtering and resampling need to be added as well as a few tens of seconds to assess fit and determine a maximum in the VRs [Tsuruoka et al., 2009a].

In the open ocean, the velocity of tsunami propagation is proportional to the water depth. Depending on the distance of the area of uplift from the coast, the open-ocean transit times for tsunami waves may be about 6 to 20 minutes. However, the actual transit time is likely to be closer to 20 minutes due to decreasing water depth, and as reported after a $M_w$7.1 earthquake in 1992 that occurred at Cape Mendocino [Oppenheimer, 1993]. Its largest amplitudes, from an edge wave, arrived 3 hours after the event [Gonzales et al., 1995]. The devastating tsunami waves following the 2011 $M_w$9.0 Japan earthquake arrived about 20-30 minutes after the rupture [Okada, 2011]. The method we propose may allow for tens of minutes of warning in the near-field.

Strong motion data of the 2011 M9.0 Japan earthquake reveals that 100-200 sec accelerations can be recorded with high signal-to-noise levels with modern instrumentation (Figure 3.13). After adapting Shao et al. [2011]'s slip model of the M9.0 Japan event for the MTJ region, we find good detection and characterization of the earthquake with VRs up to 85% (Figures 3.12 and 3.13). Finally, seismic instrumentation could clip from the strong shaking of a large local/regional earthquake. One or several near-field stations could also be rendered non-operational at the time of the earthquake affecting the algorithm performance. Overcoming this issue is possible by using secondary seismic stations or only a subset of the stations. However this could affect the VRs and lead to a non-detection (Figures 3.8 and 3.9). High-rate continuous GPS data could also provide on-scale observations for even the largest earthquakes [Avallone et al., 2011; Larson et al., 2003]. Using adequately calibrated velocity models and a proper grid distribution, this grid search approach can be implemented to include both seismic and geodetic datasets in any region that experiences intense and potentially tsunamigenic seismic activity.

# Chapter 4

# Moment tensors used for rapid characterization of megathrust earthquakes: the example of the 2011 M9 Tohoku-oki, Japan earthquake

Advisor: Douglas S. Dreger

## 4.1 Introduction

The great M9.0 Tohoku-oki earthquake that struck offshore of Japan on 11 March 2011 caused very strong ground shaking, with a recorded maximum ground acceleration reaching nearly 3 g. It ruptured a region extending several hundred kilometers, and produced peak velocity of 1 m/s [Okada, 2011]. The mainshock also generated a large tsunami on the local and regional coastlines with run-up heights reaching 37.9 m [Lay et al., 2011; Mori et al., 2011]. The significant tsunami was experienced throughout the Pacific basin. This event followed a sequence of other great subduction zone earthquakes such as the 2004 M9.2 Banda Aceh and the 2010 M8.8 Maule earthquakes, that became notorious for their large scale tsunamis [Lay et al., 2005; Yamazaki and Cheung, 2011]. These three earthquakes demonstrate the need to rapidly detect and correctly characterize seismic events from both near- and far-field observations. The analysis of near-field/regional-distance observations is an important contribution toward developing a local tsunami warning capability.

Data from continuously recording and telemetered seismic networks help to rapidly provide earthquake and tsunami warnings as soon as an earthquake's location and magnitude are known. However, great earthquakes pose a series of significant problems for tsunami warning purposes. First, the amplitudes of the seismic waves that they produce can exceed the dynamic range of the broadband and weak motion seismic instruments typically used for earthquake detection and location in the local and regional distance range. The use of strong motion instrumentation, or even continuous GPS estimates of dynamic ground motions can alleviate this problem [Blewitt et al., 2009; Clinton and Heaton, 2002; Yue and

Lay, 2011]. Secondly, these events rupture extended areas along the subduction plane over long periods of time, several minutes for the largest ones. Traditional earthquake characterization techniques are not formulated to consider their long period waves (>50 sec for example). Consequently they rely on information above the corner frequency of these large events and therefore suffer saturation problems. This leads to the underestimation of the seismic moment and magnitude of the events. In the case of the M9 Tohoku-oki earthquake, the Japanese Meteorological Agency [Okada, 2011] first announced the magnitude of the event as 7.9. Magnitude updates were progressively published by the JMA finally reaching magnitude 9.0 on 13 March 2011. Similarly, the United States Geological Survey (USGS) initially announced a M7.9 for the event [Hayes et al., 2011], and the first bulletin of the Pacific Tsunami Warning Center (PWTC) reported the same magnitude [PWTC, 2011].

The use of far-field seismic stations is common for tsunami early warning purposes as they can provide accurate information regarding the earthquake [Kanamori and Rivera, 2008]. However, while the utilization of the far-field stations enables warnings for teleseismic distances, warnings for local and regional coastlines remains an issue due to the time it takes for the seismic waves to travel to the far-field stations. In addition, because the extent of rupture in these great earthquakes is finite, common local and regional distance point-source techniques suffer from over-simplification of the Green's function and the computational demands of a full finite-source inversion technique. Finally, initial tsunami early warnings based on teleseismic observations are commonly issued without knowing the type of earthquake rupture [Hirshorn and Weinstein, 2009; Lomax and Michelini, 2009], which can have significant effects on the generation and amplitudes of the tsunami waves.

In 2008 Kanamori and Rivera proposed an automated moment tensor inversion scheme using the very-long period W-phase that travels between the P and S waves at teleseismic distances. Like mentioned in Chapter 3, the main advantage of this method is that it can provide complete earthquake source parameters, and an unsaturated estimate of scalar moment within 20 minutes of an earthquake using far-field stations. At the time of the 2011 M9.0 Tohoku-oki earthquake the W-phase source inversion algorithm was running in real-time [Duputel et al., 2011]. In contrast to other techniques the reports from the use of the W-phase announced that the earthquake magnitude was 8.8 to 9.0 within the 40 minutes of the origin time [Duputel et al., 2011]. These results show that it is possible to rapidly detect and characterize the source parameters of large earthquakes, however the solution was too late to provide useful tsunami early warnings for the local coastlines. The initial low-amplitude tsunami waves were followed 20 to 30 minutes after the event's origin time by the damaging tsunami waves. Their arrival was still within the 40 minute processing time of the W-phase method [Duputel et al., 2011; Hayashi et al., 2011; Okada, 2011].

Kawakatsu [1998] proposed the GridMT method to automatically detect, locate and determine the source parameters of any earthquake by inverting long-period (>10 sec) seismic

waveforms and computing moment tensors in realtime at each point of a grid that would cover a region of interest. Although this approach was successfully implemented in Japan and has given good results in terms of detection, location and characterization of the offshore seismicity for up to $M_w$ 7 [Tsuruoka et al., 2009a], it failed to detect the M9 earthquake as the broadband records of the F-NET network were clipped in the strong shaking of the M9 mainshock. Running the GridMT algorithm on strong motion data streams avoids this problem. We implemented the GridMT method for the Mendocino Triple Junction region, and suggested modifying the approach by considering two GridMT algorithms running in parallel (see Chapter 3, Guilhem and Dreger [2011]). One is similar to that currently used in Japan [Tsuruoka et al., 2009a]. The other is for characterizing large earthquakes (i.e. M>7). In the latter case, longer period waveforms (i.e. 100 to 200 sec) are considered, and a longer time window (i.e. about 8 minutes) is employed, so that the full wavefield including Rayleigh and Love waves can reach a limited number of seismic stations located at distances of several hundred kilometers. Using synthetic M8 to 9 earthquakes, we showed that this approach can be used to correctly detect great earthquakes, locate them, and obtain their magnitude and mechanism. In addition, to properly account for the finiteness of the rupture of great earthquakes, we proposed the use of quasi-finite-source Green's functions to account for the finite extent of great earthquake ruptures in the point source moment tensor inversion method [Guilhem and Dreger, 2011].

Here, we use strong-motion data from the M9 Tohoku-oki mainshock recorded by the K-NET network to test the approach proposed by Guilhem and Dreger [2011]. We present the results of the single point-source moment tensor inversions using data from sets of four seismic stations, filtered between 100 and 200 sec period. We show that this method can correctly characterize the event without magnitude saturation about 8 minutes after its origin time. We also present tests using quasi-finite-source Green's functions representing several case scenarios of ruptures and slip directions. In addition, to retrieve the correct source parameters of the megathrust earthquake, this approach uses a limited amount of calculations compared to the more general application, by focusing the grid on the megathrust contact patch, and as a result it demonstrates its potential for realtime implementation in Japan as well as in other regions where great earthquakes occur. However, we find that some strong-motion stations show nonlinearity in their signal, which emphasizes the need to better understand the behavior of strong motion instruments and recording sites under strong ground shaking (i.e. tilt or other potential issues). We also discuss the importance of station configuration to enhance the detection and characterization of such events. Used in realtime, this method could allow at least ten or more minutes of warning for tsunami waves, and would improve estimates of tsunami size based on the moment magnitude and mechanism of the earthquake.

## 4.2 Data and method

### 4.2.1 Method

We modified the GridMT method proposed by Kawakatsu [1998] and used by Tsuruoka et al. [2009a], based on Guilhem and Dreger [2011]'s recommendations (Chapter 3). The GridMT approach considers the continuous inversion for the moment tensors of streaming realtime data at each point of a grid that represent virtual sources distributed over a region. We showed in Chapter 3 that, in order to correctly characterize large earthquakes (i.e. $M_w>$ 7) the algorithm needs to focus on very long period data (for example between 100 and 200 sec compared to 20 and 50 sec periods) over a longer time window in order to sample the flat part of the spectrum proportional to moment. At each station, the data $d$ can be represented directly as the convolution of Green's functions (GFs) $G$ between the source, $s$, and the receiver, $r$, and the moment tensor components m of the source:

$$d^k(t) = \sum_i G_i^{sr}(t) m_i^s \tag{4.1}$$

where the sum is carried out over the fundamental components of the moment tensor such as mxx, mxy, mxz, etc (e.g. Jost and Hermann [1989]). The least-squares solution to this representation can be obtained by computing the generalized inverse $(G^TG)^{-1}G^T$ and solving for the moment tensor ($M$):

$$M = \left(G^TG\right)^{-1} G^Td \tag{4.2}$$

The generalized inverse $(G^TG)^{-1}G^T$ can be pre-computed a-priori using a distribution of grid points, a given velocity model and a set of selected stations. The multiplication of this matrix with streaming data can be performed automatically in realtime. Earthquake detection is given when the variance reduction (VR), or fit between the data and the synthetics seismograms exceeds a predefined threshold.

This original method offers several advantages. It gives the possibility to: 1) use multiple datasets (displacement, velocity, or acceleration seismograms), 2) consider various earthquake scenarios in advance and to invert for them in realtime, and 3) incorporate the effects of 3D structure through the use of pre-computed GFs that are virtual-source-station specific. In Chapter 3 we demonstrated that in addition to computing simple point-source inversions, it was possible to employ quasi-finite-source adjusted GFs (QFS GFs) where GFs of $n$ grid points are pre-averaged to generate composite GFs, *Gtot*, that take into account the source-receiver back-azimuth and thereby the effective radiation patterns of each virtual source:

$$G_{tot}(t) = \frac{\sum_{i=1}^{n} G_i(t)}{n} \tag{4.3}$$

The prefixed number of points $n$ has an effect on the allowed complexity of the pre-defined

earthquake scenarios considered in the realtime inversions. This allows us to take into consideration the near-field problem in which the stations are sensitive to different parts of the overall rupture, with or without directivity. The moment tensor inversion itself is performed assuming a point-source analysis method, which maintains the computational speed. It is noted that if a specific target was sought it would be possible to simply convolve the streaming data against GFs that take the specific strike, rake and dip of the target event into account. We have elected to retain the inversion capability for these parameters since in addition to the megathrust events large intraplate earthquakes that rupture the slab are also possible.

### 4.2.2 Data

The dense seismic networks (F-NET, K-NET, Hi-NET) of the Japanese National Research Institute for Earth Science and Disaster Prevention (NIED) provide a remarkable dataset of geophysical observations of the M9.0 Tohoku-oki earthquake. The GridMT algorithm implemented in Japan by Tsuruoka et al. [2009a] uses a subnet of three stations of the broadband network F-NET for each of their processing grids. Analysis of these data shows that they went off-scale and suffered other linearity issues following the earthquake. Consequently they are not usable. On the other hand, strong-motion stations are known to be less vulnerable to clipping [Clinton and Heaton, 2002]. The strong-motion K-NET network in Japan has nearly 700 three-component stations distributed almost every 25 km and recording at 100 samples per second (sps). It offers the opportunity to study the Tohoku-oki event in details. We downloaded the acceleration data and selected stations that are located near the F-NET broadband stations used by Tsuruoka et al. [2009a] (Figure 4.1). We only considered stations with available records lasting at least 300 seconds. This was done to assure that most of the seismic signal from the mainshock was taken into account and to provide sufficient recording for the long-period moment tensor analysis (i.e. 100-200 sec period). This resulted in the selection of 12 strong-motion stations (Figure 4.1).

Because the proposed approach considers a minimum of 8 minutes of streaming data, we extended the available acceleration seismograms by adding zeros before and after the data segment. In this way, we generated 20-minute time series that were later processed before entering the streaming data moment tensor algorithm. Adding zeros was possible because of the large signal to noise ratios of the data.

Similarly to what is currently implemented in Japan [Tsuruoka et al., 2009a,b] and to what was proposed in Chapter 3 where we used velocity data, we integrated the acceleration records to obtain their equivalent in velocity. We then filtered them using a one-pass, 2-pole Butterworth bandpass filter as suggested by Guilhem and Dreger [2011] for large earthquakes, and we decimated the data to 1 sps. Integration of the strong-motion data to velocity in realtime may lead to instabilities, which can produce incorrect source inversion re-

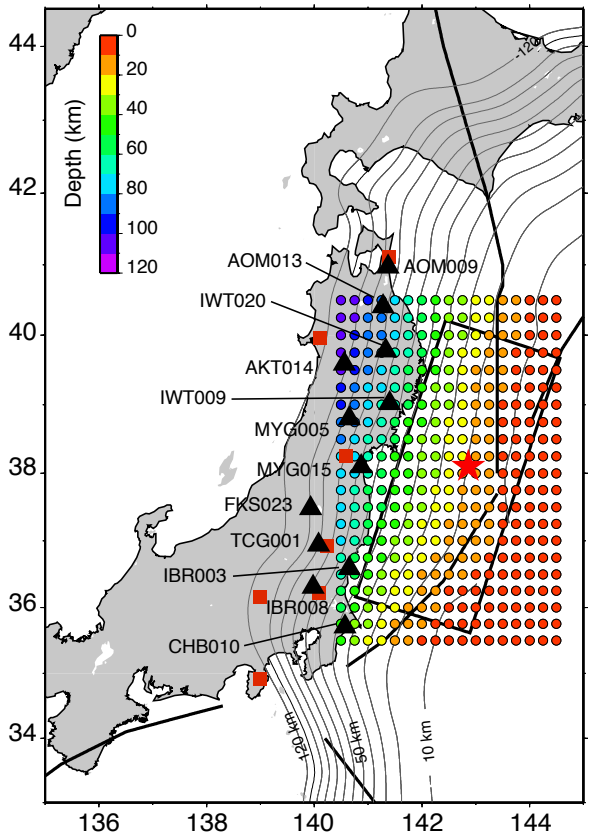


Figure 4.1: Grid point (dots) color-coded by the depth of the slab [Gayes and Wald, 2009] and K-NET strong-motion stations (triangles) compared with the locations of the broadband stations (red squares) used by Tsuruoka et al. [2009a]. The red star shows the JMA epicenter of the M9 Tohoku-oki earthquake and the rectangle shows the extension of its slip according the model of Shao et al. [2011]

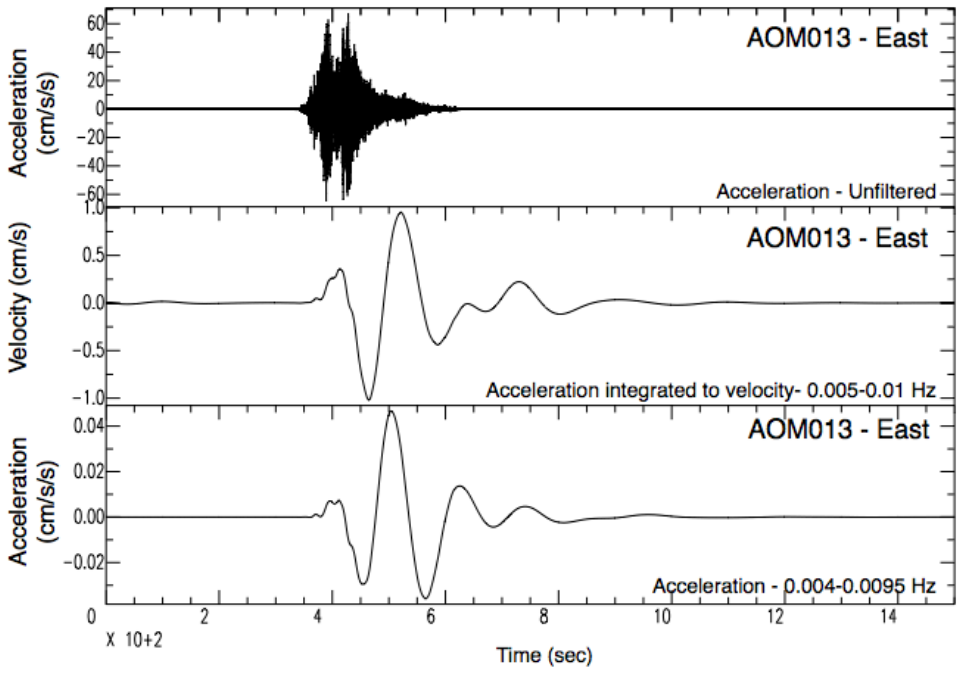


Figure 4.2: Top: raw, unfiltered strong-motion data. Middle: top seismogram integrated to velocity and bandpass filtered between 0.005 and 0.01 Hz. Bottom: top seismogram bandpass filtered between 0.004 and 0.0095 Hz.

sults. Therefore we also considered the acceleration records in the moment tensor inversion, and we compared the results from the two inversions. The 20-min acceleration segments were filtered with a one-pass, 3-pole Butterworth bandpass filter at 0.004 (250 sec) and 0.0095 (105 sec). This filter passband was chosen after comparing the acceleration data with that integrated to velocity (Figure 4.2). The goal was to obtain records with comparable spectral content, as the previous successful analysis cases which used velocity data in Chapter 3.

### 4.2.3 Grid and Green's functions

We implemented a grid of virtual sources (Figure 4.1) overlapping the rupture of the M9 earthquake extending between latitudes 35.5°N and 40.5°N and between longitudes 140.5°E and 144.5°E at intervals of 0.25°. Because great earthquakes, including the 2011 M9 Tohoku-oki earthquake, primarily rupture the subduction interface we implemented a grid of virtual sources distributed on a slab. The slab geometry followed that of Kamchatka, the Kurils, and Japan from the three-dimensional compilation of subduction zone geometries Slab1.0 [Gayes and Wald, 2009]. We discretized the slab depth with an 5 km spacing. The depths

considered range between 5 and 115 km (Figure 4.1).

We pre-computed a catalog of GFs and their associated generalized inverse matrices $(G^TG)^{-1}G^T$ using the one-dimensional velocity model used by Tsuruoka et al. [2009a] in their implementation of GridMT. We used a frequency-wavenumber integration code written by Chandan Saikia to compute the velocity GFs at the depth of the interpolated slab as well as 5 km shallower and 5 km deeper. It is important to use a complete wavefield method to compute the GFs to properly account for near- and intermediate-field terms considering the long-period passband and near-regional distance range. To account for the inversion of acceleration data we differentiated the velocity GFs to acceleration before to applying identical filters to those used for the strong-motion records. Finally, because of the long rupture duration of the great earthquakes we convolved the GFs with a source time function of 100 sec. The rise time is a free parameter and a suite of values needs to be tested to find optimal moment tensor solutions.

## 4.3 Detecting using single-point-source Green's functions

We find that the method utilizing the long-period waveforms and single-point-source inversions is able to correctly detect, locate, and determine the source characteristics (seismic moment and mechanism) of the great M9 Tohoku-oki earthquake unlike the short period case (Figure 4.3). It works for both acceleration records and velocity seismograms obtained from the strong-motion records. A maximum VR greater than 70% was obtained using either velocity or acceleration records.

The best solutions in both of the two long-period tests are located near the centroid of the earthquake, close to the JMA and USGS CMT locations. Like the CMT solution, the mechanism obtained is reverse with the strike direction approximating the slab orientation in this location. In contrast to other traditional source determination techniques, the approach does not saturate at large magnitudes and recovers a moment magnitude of 9.1, which is only 0.1 magnitude unit larger that the reported magnitude for this earthquake. The slight over prediction does not negatively impact the use of this method in tsunami early warning.

The method keeps pace with realtime streaming data but runs 8 minutes behind to ensure that the complete waveforms have been recorded by the most distant stations, and to capture the very long-period waves. The origin time of the earthquake was determined to be 05:46:42 UTC for the acceleration case (160 sec after the start time of the inversion in Figure 4.4), and 7 seconds later for the velocity inversion case (05:46:49 UTC or 167 sec in Figure 4.4). These origin times are within the range of origin times published for the event

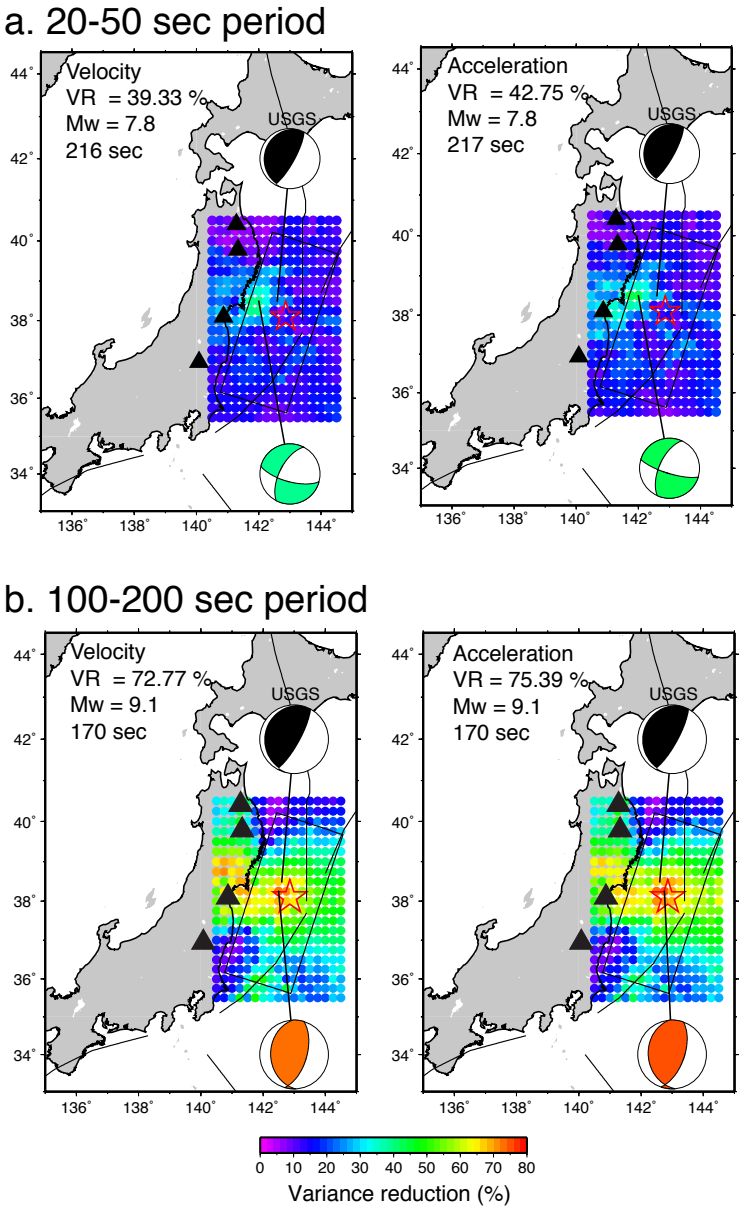


Figure 4.3: Maps of the best variance reductions per grid points (dots) obtained +/- 5 km from the slab depth using the data of four strong motion stations (triangles) integrated to velocity (left) and let as acceleration (right). a) Inversions using data filtered between 20 and 50 sec period. b) Inversions using data filtered between about 100 and 200 sec. The best solution is shown by the colored beach-ball diagram and is compared with the USGS CMT mechanism (black). The red star shows the JMA epicenter. Origin time is given with respect to the starting time of the inversion: 05:44:02 UTC.

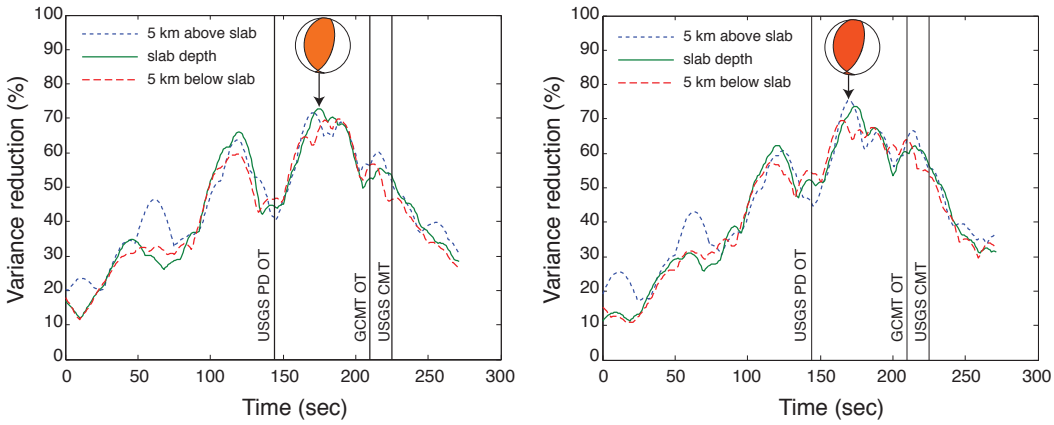


Figure 4.4: Temporal evolution of the maximum variance reductions for the velocity (a) and acceleration (b) inversions over the grid. The beach-balls show the best solutions (Figure 4.3). Inversions start at time 05:44:02 UTC (0 sec) and run for about 4.5 minutes, every second.

(05:46:23 UTC for the USGS catalog to 05:47:47 UTC for the USGS CMT solution). Figure 4.4 shows the temporal evolution of the best VRs calculated every second on the grid at the slab depth, 5 km above, and 5 km below. In general the VRs are found to be at or below 20% before the earthquake time, even when the later part of those 8-minute windows required in the inversion show evidence of the early arrivals of the earthquake. With time, the VRs increase until reaching a maximum value and then decrease rapidly once the wavefield passes through the time window of analysis. This is similar to what was observed by Tsuruoka et al. [2009a] and Guilhem and Dreger [2011] for small to large earthquakes in Japan and in northern California. Nonetheless, we notice the presence of peaks of higher VRs with a periodicity of approximately 100 sec that we interpret as cycle-shifting of the mechanism in which alternate peaks and troughs are fit as the data streams through the algorithm. This effect needs to be taken into account when scanning for the best VR and thus for defining the best solution, especially if the VRs are at or above the VR threshold.

## 4.4 Detection using quasi-finite-source Green's functions

For great earthquakes, Guilhem and Dreger [2011] proposed the use of QFS GFs to account for the rupture finiteness at short distances (see Chapter 3). We tested a series of QFS GFs that represent to some extent the extended dimensions of the rupture in which

we can also choose to add or not directivity (Figure 4.5). Here, we summed three, four, and five grid points to create a series of rupture scenarios with elongated or square QFS GFs. More complex geometries for the construction of the QFS GFs are possible however they require prior knowledge of the characteristics of rupture, which is usually not the case. Here, we only considered GFs at the slab depth and we search for the best VR every 2 seconds. This reduces the number of calculations for each time step from 1071 to 63. This number is also greatly reduced from the typical implementation in which the grid defines a regular 3D volume (e.g. Tsuruoka et al. [2009a] and Guilhem and Dreger [2011]) rather than a region surrounding the subduction zone contact path. Typical implementations use 5000-7000 grid nodes, thus the QFS case with nodes only along the contact patch reduce the number of calculations per time step by a factor of 100.

We find that the use of this limited number of QFS GFs applied to strong-motion records allow the rapid detection of the M9 Tohoku-oki earthquake with VRs exceeding 70% and reaching a maximum of nearly 77% (Figure 4.5). The mechanism, location, and origin times are generally well recovered, and are similar to those obtained with the single-point-source GFs. This is due to the very compact nature of this great earthquake compared to other recent events [Lay et al., 2005; Vigny et al., 2011; Yamazaki and Cheung, 2011]. In addition, when using a bilateral rupture or a North to South rupture (Table 4.1) we better recover the source parameters of the earthquake (i.e. larger VR) as we better image the actual rupture characteristics of the mainshock in which finite-fault models of the event indicate that the earthquake first ruptured the shallow portion of the slab near its epicenter and later propagated along slab strike direction and also downdip [Ammon et al., 2011; Lay et al., 2011; Shao et al., 2011; Yue and Lay, 2011].

Table 4.1: Effects of directivity in the moment tensor inversion for the 3-point case (Figure 4.5). Time is indicated in sec from the start of the inversion at 05:44:02 UTC

| Rupture | VR (%) | Lat | Lon | $M_w$ | Strike 1 | Rake 1 | Dip 1 | Strike 2 | Rake 2 | Dip 2 | Time (sec) |
|---|---|---|---|---|---|---|---|---|---|---|---|
| No directivity | 71.2 | 38.5 | 142.75 | 9.1 | 357 | 84 | 63 | 190 | 102 | 28 | 170 |
| South to North | 59.4 | 37.5 | 142.75 | 9.2 | 161 | 45 | 56 | 42 | 137 | 54 | 140 |
| North to South | 74.1 | 38 | 142.75 | 9.2 | 38 | 109 | 67 | 177 | 53 | 29 | 148 |
| Bilateral | 74.7 | 38.5 | 142.75 | 9.1 | 357 | 84 | 63 | 190 | 102 | 28 | 170 |

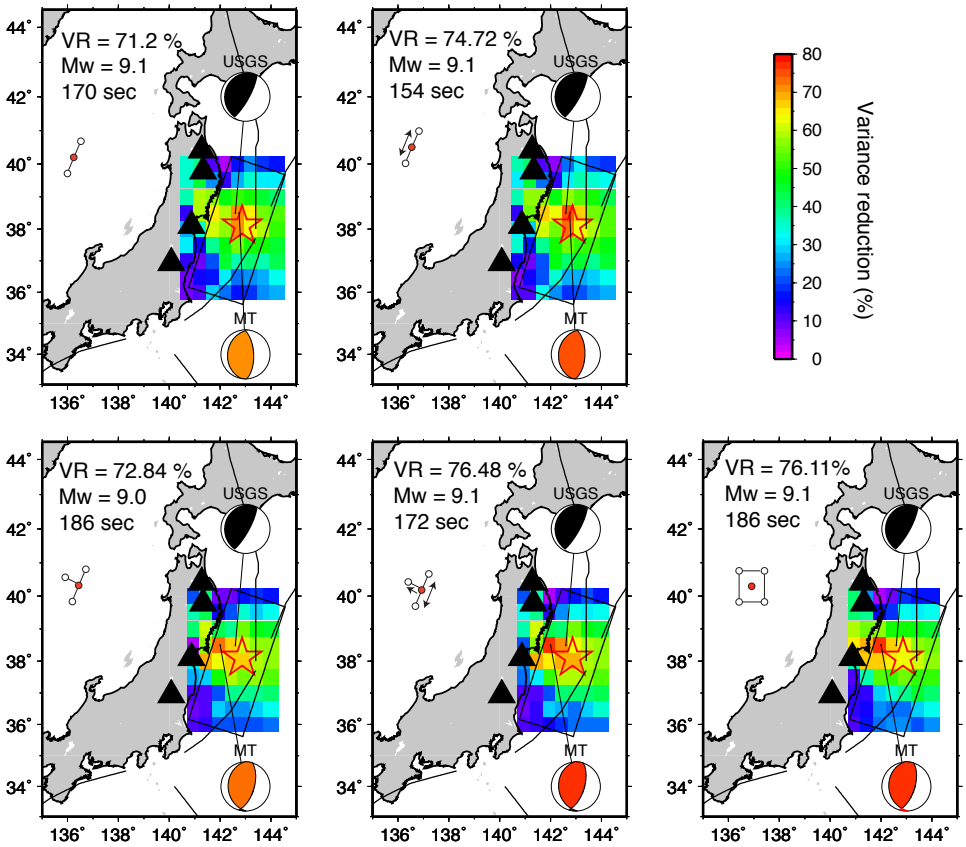


Figure 4.5: GridMT results for acceleration records at 4 stations at slab depth using different quasi-finite-source GFs. The different quasi-finite-source GFs shown by the white and red dots representing the combination of point sources (drawn to scale) with or without directivity (arrows). The red dots are considered as references for the rotations from transverse / radial components to east / north components and for the moment tensor inversions. See Figure 4.3 for additional description.

Because this approach is less computatively intensive with the restricted number of inversions required, it is possible to invert simultaneously for several rupture models (i.e. multiple QFS structures with and without directivity, and use different source time durations) in order to better reflect the range of anticipated ruptures in a region of interest. Furthermore, if additional constraints are available specific rupture scenarios may be tested in the same way. In fact, it would be possible to extend this approach to consider true finite source cases simply by testing the cross-correlation of those cases. It is noted however that it is presently not possible to invert for full finite-source models given the 8-minute, realtime processing time frame, and considering the additional degrees of freedom, increased uncertainty, and uniqueness issues of such analyses. In any case, Figure 4.5 demonstrates that very simple rupture scenarios with only three points can be used for the rapid characterization of this earthquake, which is similar to results from Guilhem and Dreger [2011]'s tests for large earthquakes on faults with longer ruptures along the Cascadia Subduction Zone (Chapter 3).

These results show that at long periods it is possible to detect and characterize a megathrust earthquake with a limited number of source inversions and with limited knowledge of the regional structure, earthquake rupture and duration using near-regional observations. Nonetheless, it is likely that additional tests will be necessary to better calibrate of the filters and GFs for each region of monitoring interest. The results show that the proposed method can help to provide information that could be utilized for tsunami early warning within minutes after a large earthquake. Finally, the temporal evolution of the VRs when considering QFS GFs is similar to that observed with the single-point-source analysis (Figure 4.6). The VRs increase until reaching a maximum value and then decrease afterwards. We notice however that the VRs measured prior to the earthquake origin time are slightly lower for the QFS GFS than they are for the single-point-source test. This could be due to the single depth section considered in the later test compared to the results for three depths for the first one.

Even if no major difference is found in the change of the VRs over time (Figure 4.6), these results show that using QFS GFs helps to enhance the systems ability to detect a large earthquake by reducing computational demands. Nonetheless, the design of the QFS GFs using more or less distant source points has direct effects on the capability of the system to detect the M9 earthquake (Figure 4.7). Although the location is found to remain stable, using only three points with increasing separation for the generation of QFS GFs progressively decreases the VRs from 70% to about 58% (Figure 4.7) as the assumed rupture exceeds the actual main slip zone of the earthquake. The mechanism is also affected and we obtain here a normal solution at a later time corresponding approximately to the GCMT origin time (Figure 4.6). We interpret the time delay and the opposite focal mechanism as the results of phase shifting in the streaming algorithm.

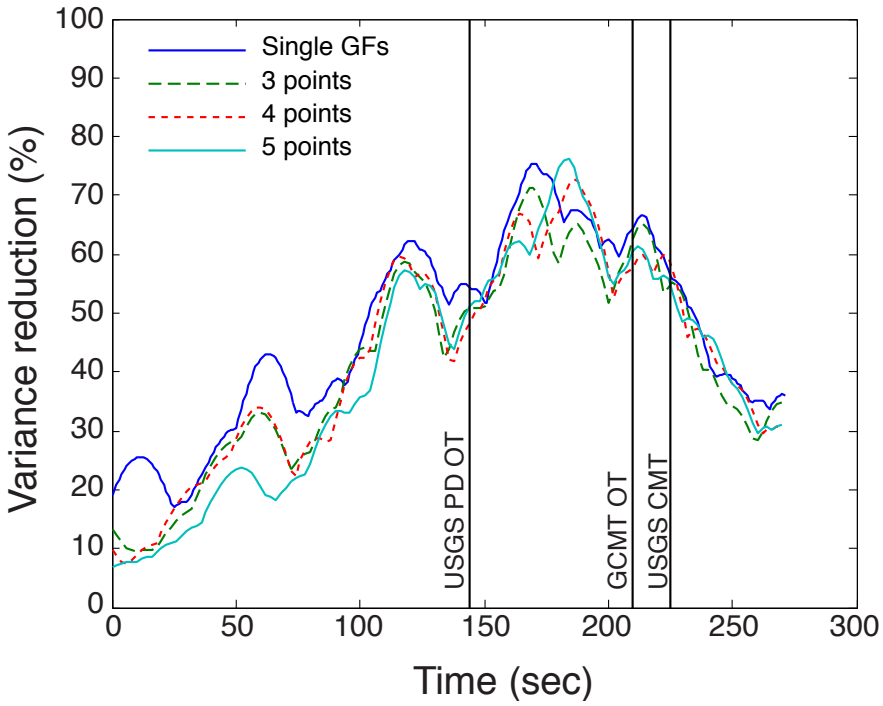


Figure 4.6: Comparison of the temporal evolution of the variance reductions for the GridMT using acceleration with single-point-source GFs (blue) and with QFS GFs (no directivity) from Figure 4.5

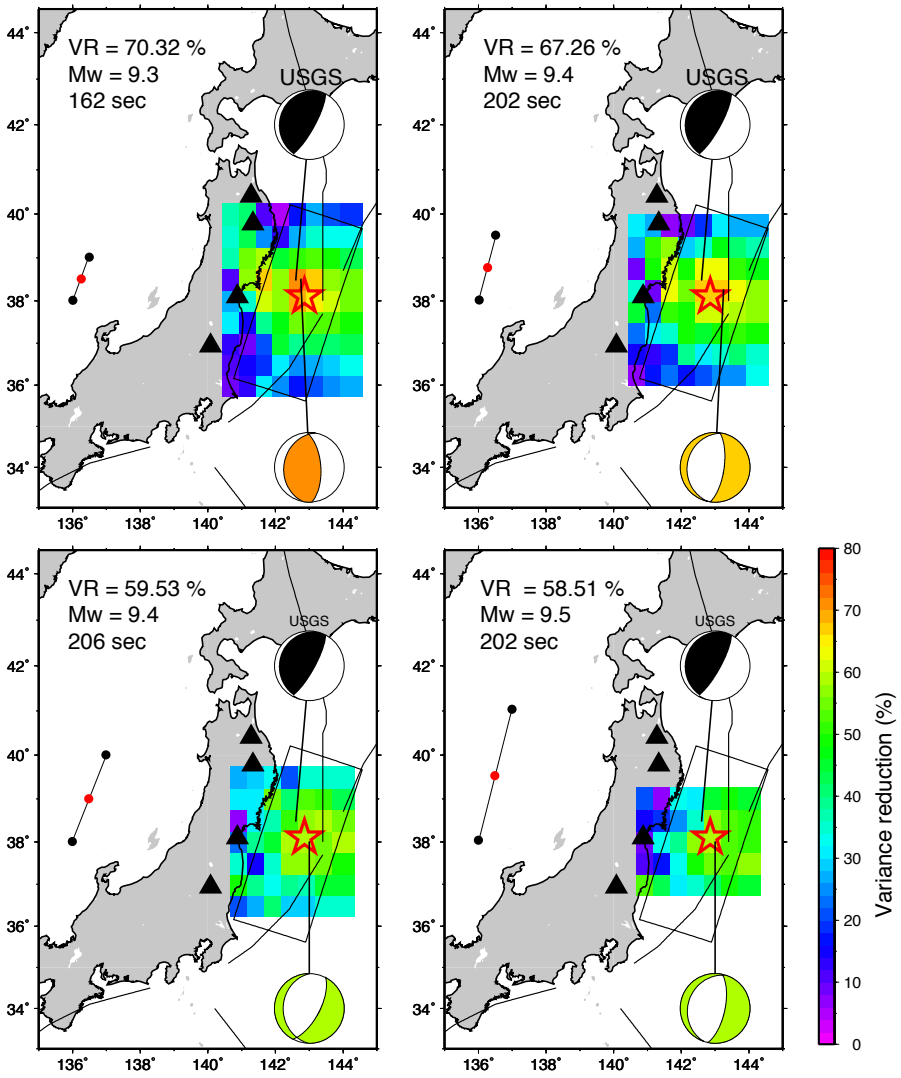


Figure 4.7: Effect of the increasing length of the QFS GFs on the GridMT capability to detect the M9 Tohoku earthquake. The QFS GFs are built using three point-sources (black and red dots) and the moment tensor analysis is performed using the position of the center point (red dots), every 0.5° in latitude and longitude.

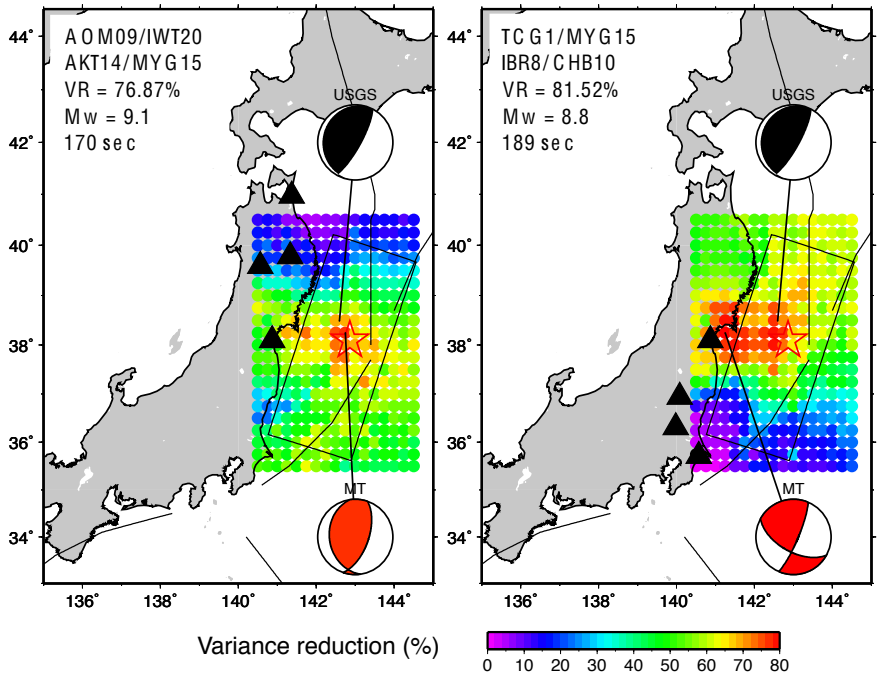


Figure 4.8: GridMT results obtained with different station configurations: stations located in the northern part of the rupture (left) and in the southern part of the rupture (right)

## 4.5 Discussion and Conclusion

An appropriate grid arrangement and station configuration is important in order to correctly retrieve robust results. Figure 4.8 shows that the location of the seismic stations considered in the inversions has an effect on the results, but in each of the cases it shows that location, mechanism and magnitude are reasonably well constrained. In the case where the station subnet is to the south, the nodes with highest variance reduction shift to the north (the opposite is seen for the northern subnet). This case does not recover the correct mechanism, however it should be noted that the moment magnitude is 8.8 and based on that value alone there could still be some benefit for local/regional tsunami early warning. These sensitivity tests demonstrate that it is important to have a subnet of stations that span the expected rupture dimensions of the target earthquake.

Table 4.2 shows that the source time function convolved with the GFs prior to any moment tensor calculations influences the output moment magnitude as well as the fit between the synthetics and the data. The moment magnitude is found to increase with increasing source duration. On the other hand, the origin time of the earthquake is found to decrease

with increasing source duration. A source time function of 100 sec was chosen in the analysis because it best recovers the data in the moment tensor inversion (Table 4.2). We find that the variation in the rise time has very limited effects on the best location, and on the mechanism of the earthquake. This is encouraging for further studies and applications to other earthquakes in the area as well as in other regions where great earthquakes occurs. For comparison, in Chapter 3 we used a source time function of 84 sec for their analysis of synthetic $M_w$8.2 to $M_w$8.4 earthquakes off the coast of Mendocino in northern California.

Table 4.2: Effect of the source time duration on the moment tensor algorithm using acceleration data for the mainshock.

| Source duration (sec) | Lat | Lon | Origin time (sec) | $M_w$ | Strike 1 | Rake 1 | Dip 1 | Strike 2 | Rake 2 | Dip 2 | VR (%) |
|---|---|---|---|---|---|---|---|---|---|---|---|
| 25 | 38.25 | 142.75 | 193 | 8.8 | 20 | 102 | 61 | 176 | 69 | 31 | 65.53 |
| 50 | 38.25 | 142.75 | 183 | 8.9 | 21 | 103 | 61 | 175 | 67 | 31 | 71.96 |
| 100 | 38.25 | 142.75 | 170 | 9.1 | 19 | 102 | 61 | 175 | 69 | 31 | 75.39 |
| 150 | 38.25 | 142.25 | 163 | 9.2 | 17 | 101 | 62 | 175 | 71 | 30 | 74.61 |
| 200 | 38.25 | 142.75 | 158 | 9.3 | 16 | 100 | 61 | 176 | 72 | 30 | 72.39 |

The main advantage of using data from strong-motion stations is the capability of that instrumentation to record motions on scale (± 4g) with a response in acceleration flat to DC. Modern strong motion instruments have very large dynamic range (>140db) enabling robust recording of even very low frequency acceleration. We note however that there can be problems with these data. For example, when processing the data of the selected strong-motion stations of the K-NET network we found that several (IBR003, IWT009, and FKS023) lead to incorrect moment tensor inversions. Inspection of the raw acceleration records did not reveal any obvious problems. However, after integration to velocity, the records displayed kinks on all three components (Figure 4.9) suggesting that they suffered from loss of linearity due to a loss of phase-lock in the feedback mechanisms. Another possibility is that the accelerometers are sensitive to ground tilt. Ellsworth (personal communication, 2011) compared nearby continuous GPS records and found that at several sites the accelerometers appeared to suffer some bias due to ground tilt, especially on the horizontal components that are more sensitive to tilt. More analyses of the behavior of strong-motion instruments driven by high levels of ground shaking and possible large amplitude tilts are necessary for a better understanding of their response to such motions, and for a better preparation of the site installations for long-period acceleration response.

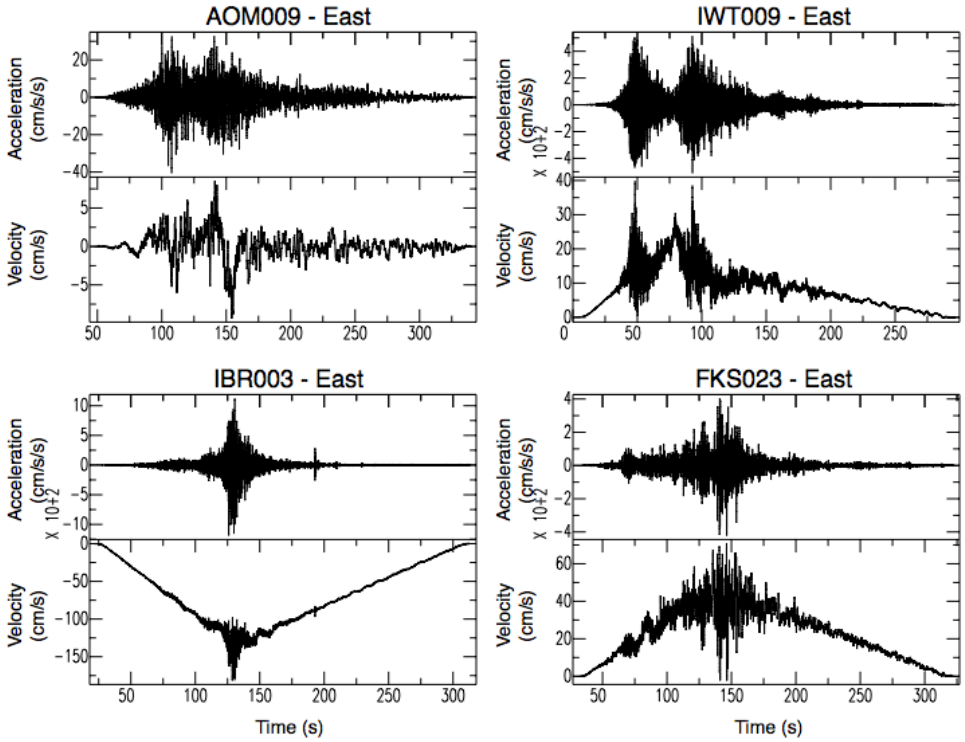


Figure 4.9: Nonlinearity in the acceleration seismograms observed at some K-NET stations after integration. For each station, the top row shows the unprocessed strong-motion records and the bottom row shows the velocity seismogram obtained after integration of the acceleration seismogram. IWT009, IBR003, and FKS023 show evidence of sensor nonlinearity whereas AOM009 integrates correctly.

Both clipping in raw weak motion data and data from continuous high rate GPS instruments could be used to verify whether an event is large and the strong motion data should be preferred in its analysis. Figure 4.10 compares the theoretical velocity output of a radially oriented STS1 instrument in digital counts at station MYG015 for modeled reverse point-source earthquakes with magnitudes ranging between 6 and 9 located at the Tohoku-oki epicenter. The displacement for the M9 earthquake is over-estimated by the point-source because the slip is forced to be concentrated at a single point. Nonetheless for the other magnitudes, the distance to the station does not preclude the point-source assumption. Figure 4.10 shows that the digital signal clips between a M6 and a M7 earthquake at 175 km distance. However, these two model events do not produce significant static offsets unlike the M8 and M9 seismic events (Figure 4.10). Tracking the digital counts of the raw weak motion data and the static offset from continuous GPS data could help to better monitor the seismicity especially when the best solutions obtained by the short and long period scanning algorithms provide similar VRs. As a consequence they could be used to confirm whether a significant earthquake occurred. This emphasizes the need to continuously record strong-motion data. This is currently not done at the K-NET network, where data acquisition is event-triggered.

We show that the inversion of low-frequency, long-period (100-200 seconds) acceleration records at local to regional distance stations of the NIED K-NET could detect and locate the 2011 M9 Tohoku-oki earthquake, as well as recover unsaturated estimates of the seismic moment tensor. The analysis shows that robust results could be obtained within 8 minutes following the origin time of the mainshock and therefore could be utilized for tsunami early warning if the method were included in the realtime processing scheme. Using very long-period waveforms (100-200 sec) and an extended inversion window (8 minutes) we show that the system does not saturate for very large earthquakes, unlike classical techniques. Indeed we recover the moment magnitude and can specify the moment tensor of the event with confidence greater than 70%. This demonstrates that the proposed method in Chapter 3 is efficient on recorded strong-motion data. By limiting the inversions to be performed to the slab itself and using QFS GFs for multiple source points to better image the extended rupture earthquake, we show that only 1/5 of the virtual source locations are needed and that detection, location and source parameter estimation are not adversely affected. This reduces computer processing time significantly. This in turn may allow the use of more stations that could provide better constraints, or the consideration of complexities such as multiple-point-source cases and different rupture velocity and source rise time. This method has been shown to correctly characterize earthquakes in the near-field in northern California [Guilhem and Dreger, 2011] and in Japan [Tsuruoka et al., 2009a], as well as for great earthquakes. To implement it in other regions, the sensitivity of results to assumed velocity structures, optimal frequency passbands, and station availability and distribution need to be considered.

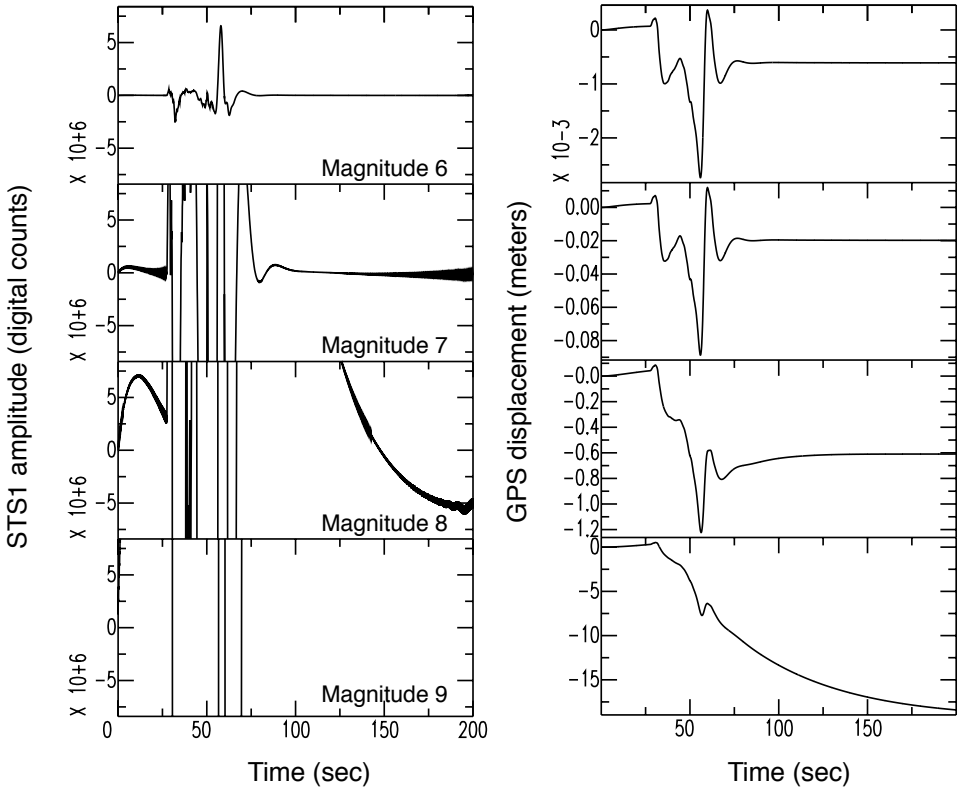


Figure 4.10: Comparison of the theoretical STS1 radial velocity component (amplitude in digital counts) for model reverse M6 to M9 earthquakes located at the M9 Tohoku-oki epicenter and recorded at 175 km (at station MYG015) and the corresponding model displacement measured at the station in meters.

# Chapter 5

# Nonvolcanic tremor evolution and the San Simeon and Parkfield, California earthquakes

modified from **Nonvolcanic tremor evolution and the San Simeon and Parkfield, California earthquakes** by Robert M. Nadeau and Aurélie Guilhem, published in *Science* (2009)

## 5.1 Introduction

Volcanic tremors are seismic events lasting from several minutes to several days, preceding and/or accompanying volcanic eruptions, reflecting the internal dynamics and in particular the migration of fluids in volcanic structures [Konstantinou and Schlindwein, 2002]. In 2002, tremor-like signals were discovered in nonvolcanic regions along the southwest Japan subduction zone and were dubbed nonvolcanic tremors [Obara, 2002]. These events are deep, located in proximity of the Mohorovic discontinuity at about 30 to 40 km depth. Since then, similar events have been observed along other subduction zones: in Cascadia [Brudzinski and Allen, 2007; Rogers and Dragert, 2003], in Japan [Obara, 2002; Obara et al., 2004], in Mexico [Payero et al., 2008] and Central America [Schwartz and Rokosky, 2007]. These events typically last continuously from a few minutes to a few days with a predominant frequency range of 1 and 15 Hz [Brudzinski and Allen, 2007; Obara, 2002; Payero et al., 2008] and they have no clear P- and S- phase arrivals. They have generally been observed in transition zones between freely slipping and locked faults [Brudzinski and Allen, 2007; Liu and Rice, 2007; Nadeau and Dolenc, 2005; Obara, 2002; Payero et al., 2008; Rogers and Dragert, 2003; Schwartz and Rokosky, 2007; Shelly et al., 2006]. In many of these locations, tremor activity increased with detectable transient fault zone deformation (slow-slip events) [Hiramatsu et al., 2008; Hirose and Obara, 2006; Payero et al., 2008; Rogers and Dragert, 2003] or with dynamic stress changes from tides and surface waves of teleseismic (distant) earthquakes [Gomberg et al., 2008; Miyazawa and Mori, 2006; Peng and Chao, 2008; Rubinstein et al., 2009, 2008; Thomas et al., 2009]. These spatial and temporal associations suggest that tremor activity is closely related to the processes responsible for generating earthquakes.

In 2005, Nadeau and Dolenc [2005] reported the discovery of nonvolcanic tremors in a different tectonic setting, within a transform fault boundary zone, along the San Andreas Fault (SAF) in the region of Parkfield-Cholame, California. These tremors show many of the same characteristics as previously observed along subduction zones: depth (between 15 and 40 km), frequency range (1-15 Hz) and waveform character. However their duration is shorter, typically less than 20 minutes compared to hours to days for the subduction zone tremor.

The origin of the nonvolcanic tremors has yet to be determined, though several hypotheses have been proposed. Recent studies have first suggested that tremors are related to fluid migration associated with subduction on the slab interface. Fluid-related tremors may result either from shear coupling between rocks and flowing fluids or by hydraulic fracturing [Julian, 2002; Melbourne and Webb, 2003; Obara, 2002; Shelly et al., 2006; Szeliga et al., 2004]. However, this fluid hypothesis does not explain the tremor activity recorded at Parkfield because of the absence of subduction along the central SAF, unless, as suggested by Nadeau and Dolenc [2005], an unknown fluid source exists below the seismogenic zone of this SAF segment. Also recent studies reveal the amplification and triggering of nonvolcanic tremors by small dynamic stress changes from tides and the passage of surface waves from teleseismic events [Gomberg et al., 2008; Richardson and Marone, 2008; Rubinstein et al., 2008; Thomas et al., 2009].

To investigate the possible relation between tremor occurrence and earthquakes we analyzed the tremor activity in the Parkfield region between 27 July 2001 and 21 February 2009. During this period, the region experienced two strong earthquakes: the moment magnitude ($M_w$) 6.5 San Simeon earthquake in December 2003 [Hardebeck et al., 2004] and the $M_w$6.0 Parkfield earthquake in September 2004 [Langbein et al., 2005]. These two events offer the opportunity to investigate the role of the static and dynamic stress changes associated with their occurrence on the activation of tremors.

This chapter first presents the processing methods employed to detect, locate and catalog the activity of tremors. We then characterize the spatial and temporal NVT behavior and compare it with regional deformation, seismicity and aftershock activity. We calculate static shear, normal and Coulomb stress changes from the two strong events on the tremor locations and compare these stress levels with the dynamic stress changes computed for the passage of the surface waves of 2002 Denali earthquake [Rubinstein et al., 2008] and earth tides in the region [Thomas et al., 2009]. We also discuss persistent changes in the tremor behavior that we observe following the Parkfield earthquake.

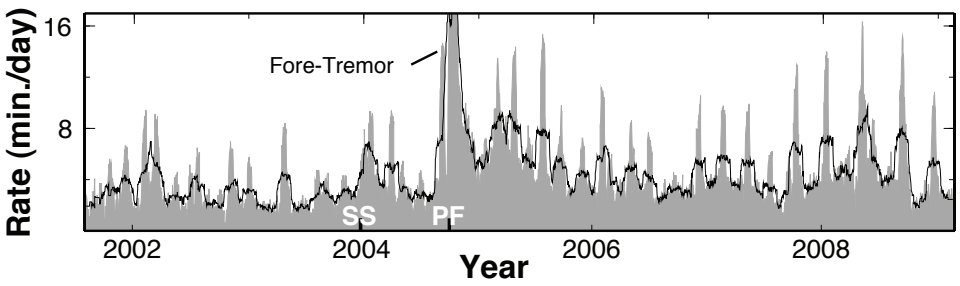


Figure 5.1: Temporal evolution of tremor activity. (a) Fifteen-day (gray) and 45-day (black) smoothed rate histories for all tremors in the study area. Times of the San Simeon and Parkfield earthquakes are indicated by SS and PF, respectively. Intense fore-tremor activity occurred $\sim$ 3 weeks before PF.

## 5.2 Detection of nonvolcanic tremors

### 5.2.1 Data and method

Owing to their significantly greater sensitivity compared to surface stations and their central location within the study region, data recorded continuously at 20 Hz sampling frequency by 8 borehole stations of the High Resolution Seismic Network (HRSN) at Parkfield, California were used for detection. Seismic data acquisition and tremor detections were made by Robert M. Nadeau at the Berkeley Seismological Laboratory using a series of steps described below. 2198 tremors were detected between July 2001 and February 2009, which corresponded to 12547 minutes of cumulative tremor activity (Figure 5.1). The tremor events lasted from 3 to nearly 21 minutes. Significant activity also occurred below our detection threshold. Between 3-8 Hz, the average seismic energy released during the tremors was typically equivalent to a $M_w \sim 0.5$ earthquake, and energies ranged over 1.5M units among tremors not coincident with earthquakes. Frequency content of the tremors (based on 250-Hz sampled data) was also typically above background between 1-15 Hz.

In order to detect tremors, one horizontal data channel from each station was used (Figure 5.2). Gain corrections were applied to the seismic data to account for differences among the data channels and then a 3 to 8 Hz bandpass filter was applied. Twenty-four hour root mean squared (RMS) envelope seismograms of these data were then generated using a moving 201 sample boxcar window stepped every 0.5 sec for each UTC day, yielding daily RMS seismograms with 2-Hz sampling frequency. Typical 24-hour background noise levels for each channel were also characterized by computing the channels median RMS seismogram over 28 days and by smoothing the median seismogram with a 5- minute window to produce the channel's RMS noise signature. In general noise signatures were recomputed

annually. The daily RMS seismograms for each of the data channels were then divided by the channel's 24-hour noise signature to produce signal-to-noise envelope seismograms. This helps account for differences in local site attenuation and typical site-specific diurnal noise fluctuations from instrument electronics and cultural activity. In the final processing step, 24-hour summary envelopes of the signal-to-noise seismograms were constructed for each day after computing the median amplitude of the signal-to-noise seismograms from among the stations at each 0.5 sec sample (Figure 5.2). Stations with exceptionally high variability in cultural noise levels were not included in the computation of the summary envelopes. Hence typically only 5 of the 8 stations were used.

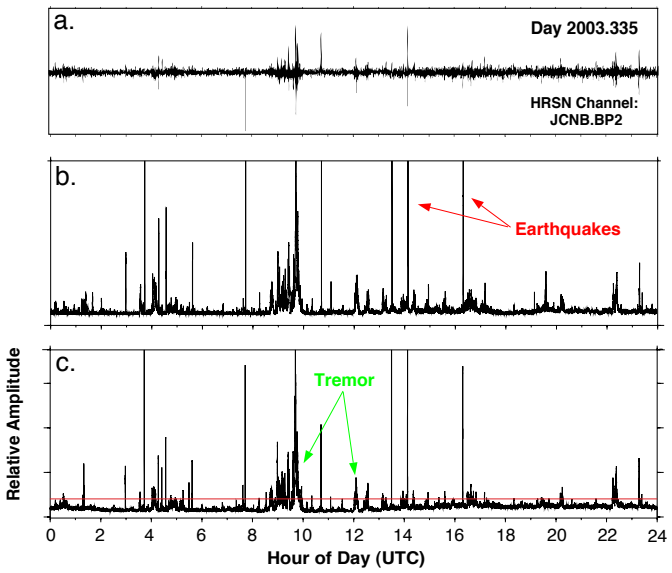


Figure 5.2: Data processing for tremor detection. a) 24-hour horizontal component at HRSN borehole station JCNB filtered between 3 and 8 Hz for Day 2003.335. b) 24-hour RMS envelope from a). c) 24-hour summary RMS envelope obtained from the HRSN stations combined. Spikes indicate earthquake activity and tremors are shown by extended higher amplitude signals. The red line shows the minimum amplitude threshold for tremor detection.

Nonvolcanic tremor (NVT) detection was carried out in 2 stages. First, initial detections were made automatically by identifying periods when the amplitude of the summary envelopes remained at or above a specified threshold for 3 minutes or longer. And later, visual inspection of the seismograms was done to assure the tremor occurrences. An amplitude threshold of 3.0 was used for data subsequent to UTC day 310 of 2003. Changes in HRSN operational parameters phased in during UTC days 232-237 and 308-310 of 2003 improved the signal to noise of the data by approximately a factor of 1.82 [Brenguier et al.,

2008]. To compensate for this, the amplitude threshold used prior to the HRSN parameter changes was 1.65, and during the change period thresholds of 3.0 and 1.65 were applied on a station-by-station basis. Comparisons of NVT rates before, during and after the changes, but prior to the San Simeon earthquake on UTC day 356 of 2003, show that no significant rate variations occurred in association with the different threshold levels, indicating that uniform NVT sensitivity was preserved (Figure 5.3).

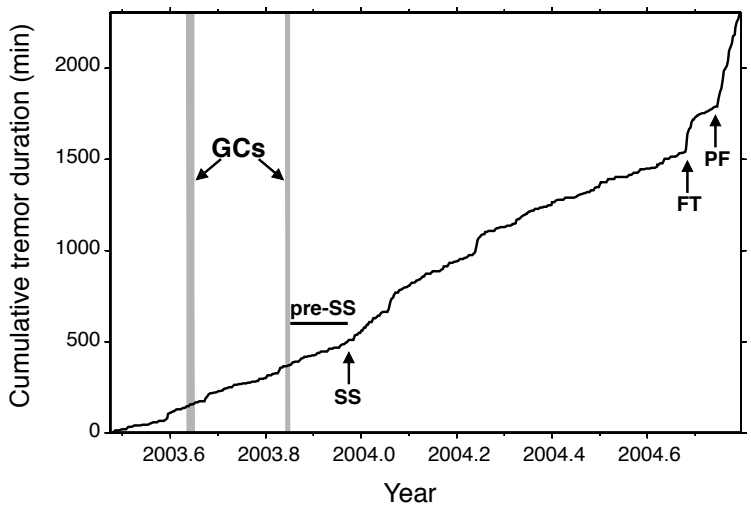


Figure 5.3: Cumulative tremor activity from 6 months prior to the 2003 San Simeon earthquake to 20 days after the 2004 Parkfield earthquake. Vertical grey bars (GCs) indicate the six and three day periods when changes in HRSN operational parameters where phased in. No significant variations in the rate of tremor detection are associated with these changes, indicating that the detection threshold adjustments used to correct for the changes are appropriate. SS and PF are times of the 2003 San Simeon and 2004 Parkfield earthquakes, respectively. Horizontal black bar (pre-SS) is the 45-day pre-San Simeon period referred to in the main text. FT indicates the 5-day fore-tremor episode that preceded the Parkfield earthquake by $\sim$3 weeks.

### 5.2.2 Exclusions and visual inspection

Excluded from the analysis were data for the hours of the UTC day that followed the 22 December 2003, M6.5 San Simeon and 28 September 2004, M6.0 Parkfield California mainshocks and for the two days following these events. Data for these periods was dominated by amplitude transients from 1000s of frequently overlapping aftershock signals, making accurate and complete NVT detections impractical. Also excluded were 31 (of a total 2767) days

of data when gaps in the HRSN continuous data streams were unacceptably high. Specifically, UTC days 264-278 of 2001, 359-360 of 2003, 364-366 of 2004, 002-004 and 007-012 of 2005, and 001 and 361 of 2006 were excluded. The automated selection criteria were generally successful in excluding detections from most earthquakes and spurious cultural and electronic noise sources. However on occasion, transients not associated with NVT activity were also detected by the automated processing. Such transients include earthquake multiplets and swarms, unusual cultural noise signals (e.g., from deep scientific drilling activity of the San Andreas Fault Observatory at Depth (SAFOD) experiment [Hickman et al., 2004]), and similarly timed multi-station artifacts that sometimes occur during network operations (e.g., severe solar regulator spiking). To remove these non-NVT transients from the automated detection list, a second stage of processing was carried out. This stage involved the visual inspection of the gain corrected and filtered seismograms from all 8 data channels and identification and exclusion of the non-NVT activity. High-amplitude transients that showed artifacts or that did not show temporal coherence of primary and secondary amplitude fluctuations (sometimes called pearls or bursts) lasting at least 3 minutes on at least 3 of the 8 stations were rejected. Periods of superposed NVT and earthquake activity were not rejected, however NVTs with superposed local or regional earthquakes were generally flagged as unsuitable for location. No effort was made to exclude tremors triggered by the passage of surface waves from teleseismic events.

In total 7.6 % of the automatically determined detections were excluded during the visual inspection process, leaving a total of 2,198 NVT events in the detection catalog for the period from July 27, 2001 through February 21, 2009. During the study period, only 6 (i.e., $< 0.3\%$) of the 2,198 detected tremors were triggered by teleseismic surface waves.

### 5.2.3 Tremor durations

The duration of each NVT is defined as the length of the NVTs detection period. Specifically, it is the length of time between the automated detections start time (i.e., when the amplitude of the summary envelope first exceeds the detection threshold) and the detections end time (i.e., the time following the start time when the envelopes amplitude falls below the detection threshold). Because a minimum duration of 3 minutes is required for detection, minimum NVT durations in our catalog are 3 minutes. The first, second (median), third quartiles and maximum catalog durations were 3.61, 4.65, 6.78 and 20.78 minutes, respectively. In total, 12546.8 minutes of NVT activity were detected during the study period. However significantly more activity typically occurs outside the detection periods at lower amplitudes, and frequently in concert with the detected tremor signals.

## 5.3 Locations of nonvolcanic tremors

### 5.3.1 Method and station selection

Continuously recorded seismic velocity data in the study region from 87 stations of 5 networks (i.e., High Resolution Seismic Network (HRSN, BP), Northern California Seismic Network (NCSN, NC), Berkeley Digital Seismic Network (BDSN, BK), Southern California Seismic Network (SCSN, CI), and EarthScopes USArray network (TA)) were first downloaded over the internet from the Northern and Southern California Earthquake Data Centers (NCEDC and SCEDC, respectively). Short period surface sensors from the NC network were used primarily, with additional coverage provided by NC, BK, CI and TA surface broad-band and BP borehole high-frequency broad-band installations. Sampling frequencies of these data ranged from 20 to 250 Hz. The majority of stations recorded only vertical component data, so for consistency only vertical component channels were used for locating the tremors. Subsequent processing revealed that only 76 of the initial 87 channels provided data of sufficient quality for locating tremor (i.e., 56 NC, 13 BP, 4 CI, 2 BK, and 1 TA) (Figure 5.4).

For each of the location candidates, 60 minute long snippets of vertical-component seismic data centered on the middle of the tremor detection period were extracted from the continuous data. Gain corrections, demeaning, decimation to 20Hz sampling and 3 to 8 Hz band-pass filtering were then applied. Root mean squared (RMS) envelope seismograms of these data are then generated using a moving 101 sample boxcar window stepped every 0.1 sec to yield RMS envelope seismograms with 10-Hz sampling frequency. A 2-pass, low-pass 0.070Hz filter was then applied to the RMS envelopes. Stations whose envelopes showed anomalous amplitude fluctuations (e.g., due to glitches or spiking in the original seismic records) during the tremor detection period were excluded from the analysis. Due to the generally low seismic amplitudes of tremor signals relative to background amplitudes and to the spatial and temporal variations in background, cultural, and instrumental noise levels among the stations, only envelopes from stations with good signal-to-noise levels were used.

We found that the automated envelope based location of superposed earthquake and tremor signals typically leads to locations consistent with the earthquake's location rather than the tremors. For this reason, tremors from the detection catalog that were flagged as unsuitable for location during the detection stage of processing were excluded from the location analysis. By far, the largest fraction of tremor excluded on this basis occurred in the days following the Parkfield earthquake (e.g., $\sim$42% in the 30 days following the event). For the entire study period, 91.8% (i.e., 2017) of the detected tremors were found suitable for location.

The fundamental timing information used for locating the tremors was based on differ-

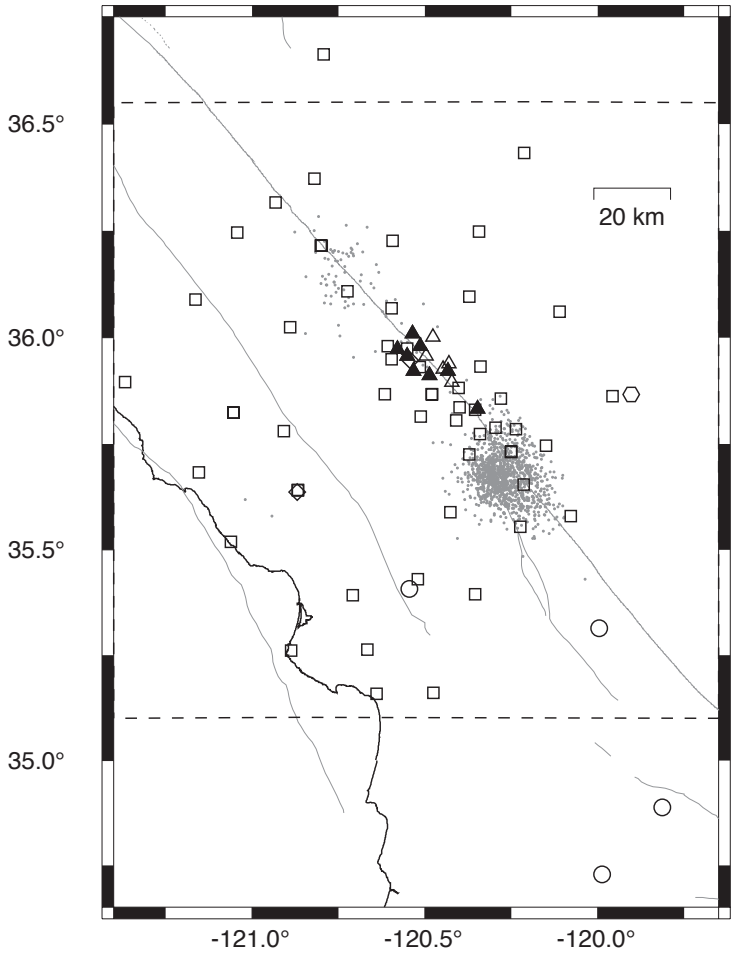


Figure 5.4: Seismic stations used for detecting (filled) and locating (open and filled) the tremors. Squares, triangles, circles, diamonds, and hexagon indicate stations of the NCSN (NC), HRSN (BP), SCSN (CI), BDSN (BK) and USArray (TA), respectively. Grey dots are well located tremors. Dashed lines encompass region shown in Figure 5.5.

ential arrival time measurements of tremor signals between pairs of stations. We obtained these station-pair differential times by cross-correlating the selected stations RMS envelopes for all possible pair combinations having station separation distances of 100 km or less. Six-minute windows of envelope data, centered on the 3-minute portion with the highest signal-to-noise, were used for the cross-correlations. Consequently station-pair differentials for only one portion of each tremor were determined. The same 6-minute period of envelope data was used for all the stations. Only differential times with maximum cross-correlation coefficients of 0.70 or greater were used for locating the tremor. Subsequent to the data filtering and to the removal of outliers from spurious noise and culturally generated artifacts, timing information from a median average of 25 stations per tremor remained available for locating the 2017 candidate tremors, with the minimum, first quartile, third quartile, and maximum number of stations being 2, 18, 31 and 50, respectively. For each tremor, we converted the station-pair differential time measurements into a best fit set of relative arrival times for the resulting stations by choosing the station with the most cross-correlation measurements with other stations as the reference station and then performing a least squares inversion to generate arrival times relative to the reference stations arrival. Before inversion, any station pairs that were not linked (directly or indirectly) to the reference station through cross-correlation measurements were excluded.

### 5.3.2 Locations

Locations of the tremors were made using the migrating grid search code BW-RELP designed to locate events with sparse station coverage [Uhrhammer et al., 2001]. In the location inversion, an L2-norm solution was used and we assumed that tremor energy propagates at S-velocities. The velocity model used was a gradient layer over a half- space with velocities and gradients based on the regional velocity model used by the USGS for their NCSN earthquake catalog [Oppenheimer, 1993], thus allowing for more accurate comparisons of tremor and earthquake locations. Specifically, we used a surface S-velocity of 2.644 km/s with a gradient down to 40 km depth of 0.05968 (km/s)/km and an S-velocity of 5.0316 km/s below 40 km. No station corrections were applied in the location process. The tremors were first located using all the available relative arrival times. If there were stations with travel-time residuals larger than 5 sec then the station with the largest residual was identified, all station-pair differential data involving the station was removed, the best-fit relative arrival times were recomputed and the tremor was again relocated. This procedure was repeated up to 5 times if more than 5 sec residuals persisted and in the 5th iteration, all stations with residuals larger than 5 sec were removed before a final location was attempted. Slightly less than 2.7% of the relative arrival time phases were removed during this large residuals exclusion process. Ten of the attempted 2017 tremor events failed to locate, leaving 2007 final locations.

Because the BW-RELP program is designed to locate events with sparse station coverage, it locates events with very few stations and with marginal station coverage. While in some applications having locations with poor coverage and low accuracy are preferred over having no locations at all, for the purposes of resolving the general distribution of tremors in the study area we applied some additional basic criteria on location quality to generate a catalog subset of well located tremors. First, tremor locations that occurred at or above Earth's surface (air-tremors) or that used less than 14 phases were excluded. This reduced the catalog size by $\sim$ 15 %. Secondly, locations with azimuthal gaps in station coverage of over 180 degrees as well as locations where depths were less than the distance to the nearest station (i.e., 45 degree depth to distance angle) were also excluded. These two basic sets of criteria reduced the final location catalog by 37.7%, leaving 1250 tremor locations in our catalog of well located tremors.

The median 95% uncertainty bounds for the well located tremors in the horizontal direction are +/- 4.7 km with 1st and 3rd quartile values of +/- 4.1 and +/- 5.5 km, respectively. In the depth direction the 95% uncertainties are +/- 4.5 km (1st and 3rd quartile, +/- 3.7 and +/- 5.2 km, respectively). Due to the relatively uneven station coverage and our application of a simplified velocity model in a region of strong lateral heterogeneity, the absolute position of the tremor zones, particularly with respect to the SAF boundary, are somewhat ambiguous. Tests using several plausible velocity models (i.e., with velocity contrasts across the SAF ranging between 7.5% and 15% and half space depths ranging from 20 to 50 km) suggest that the constellations of tremors in the Monarch Peak and Cholame regions could be shifted in absolute position by 3 to 5 km, though the apparent broad dimensions of the zones remain essentially the same (Figure 5.5).

## 5.4 Observations

### 5.4.1 Change in tremor rates

A sudden increase and subsequent decay of tremor activity (aftertremors) began immediately after the 2003 San Simeon and 2004 Parkfield earthquakes (Figures 5.1 and 5.3). Cumulatively, there were 145 minutes of tremor activity in the 45 days preceding the San Simeon event and 312 minutes of activity in the 45 days following that earthquake (Figure 5.6). An even larger increase in activity followed the Parkfield event – 850 minutes in the 45 days after Parkfield compared to 137 minutes for a same duration prior to the event (Figure 5.6). In addition, approximately 3 weeks before the Parkfield earthquake, an unusually strong episode of activity (foretremor) lasting $\sim$ 5 days also occurred (Figures 5.1 and 5.3). During the 5-day episode we detected 164 minutes of tremor, representing an over 10-fold rate increase compared to the 45-day pre-San Simeon period. The peak daily activity during

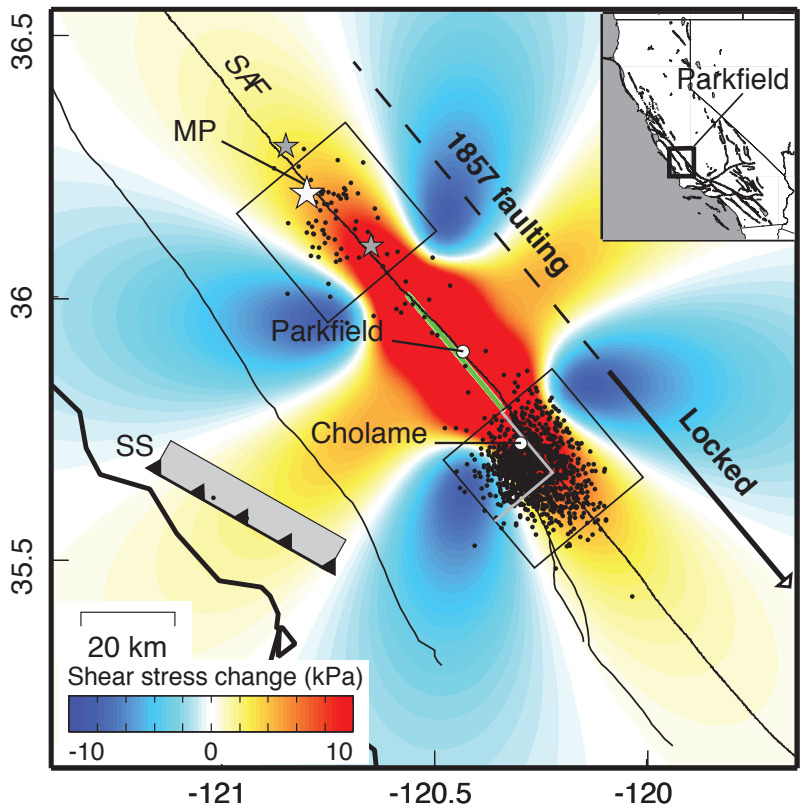


Figure 5.5: Study region with 1250 well located tremors (black dots). Thirty kilometer square boxes (black) define the Monarch Peak (MP) and Cholame tremor zones. Color contours give regional shear-stress change at 20 km depth from the Parkfield earthquake (green segment) along the San Andreas Fault (SAF). The thrust type San Simeon earthquake rupture is represented by the grey rectangle and hatched line labeled SS. The currently locked Cholame segment is $\sim$ 63 km long (solid portion of arrow) and is believed capable of rupturing on its own in an $\sim$ M7 earthquake. The dashed line shows the northern extent of the 1857 M7.9 Fort Tejon earthquake that occurred on the SAF.

the episode was 82 minutes. The largest daily peak prior to the foreshock episode was 43 minutes and it occurred about 98 days after the San Simeon earthquake.

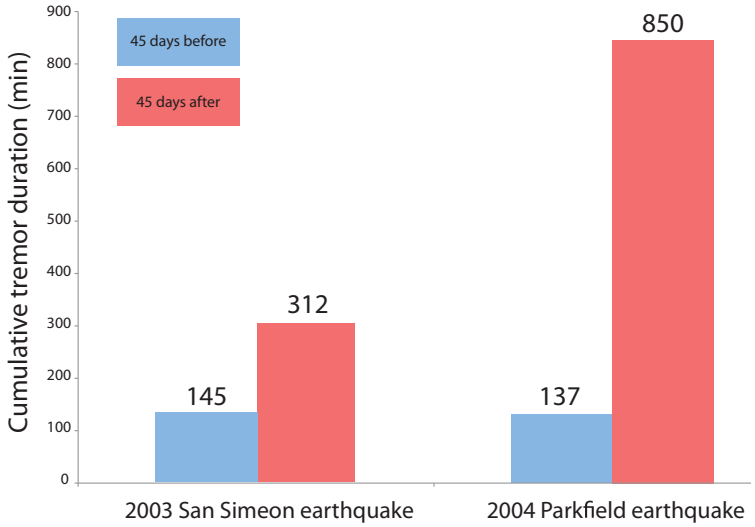


Figure 5.6: Histogram of the cumulative duration of tremors before and after the earthquakes

The decay of tremor activity after the Parkfield event continued until mid-2006 when annual activity rates had decreased to 150% of the rate for the year preceding the San Simeon earthquake. Since mid-2006 annual rates have generally increased, reaching ∼181% of the pre-San Simeon level during 2008 (Figure 5.7a).

The data also show that zones relatively devoded of detectable tremor can transition into a state of long-term elevated activity as a result of perturbations from a nearby moderate earthquake. For example, before the Parkfield earthquake, tremor activity in the Monarch Peak tremor zone (Figure 5.5) was low (i.e., 14 tremors in $\sim$ 3.2 years) (Figure 5.7b). However, beginning $\sim$ 10 days after the Parkfield event, activity in this zone increased significantly and it has continued at an elevated rate (i.e., 98 tremors in $\sim$ 4.4 years) (Figure 5.7b). The 10-day delay may be reflecting an anelastic redistribution of stress in the ductile lower crust.

### 5.4.2 Emergence of tremor episodes

After the Parkfield earthquake, persistent episodes of quasi-periodic tremor emerged along the SAF that are reminiscent of episodic tremor observed in some subduction zones

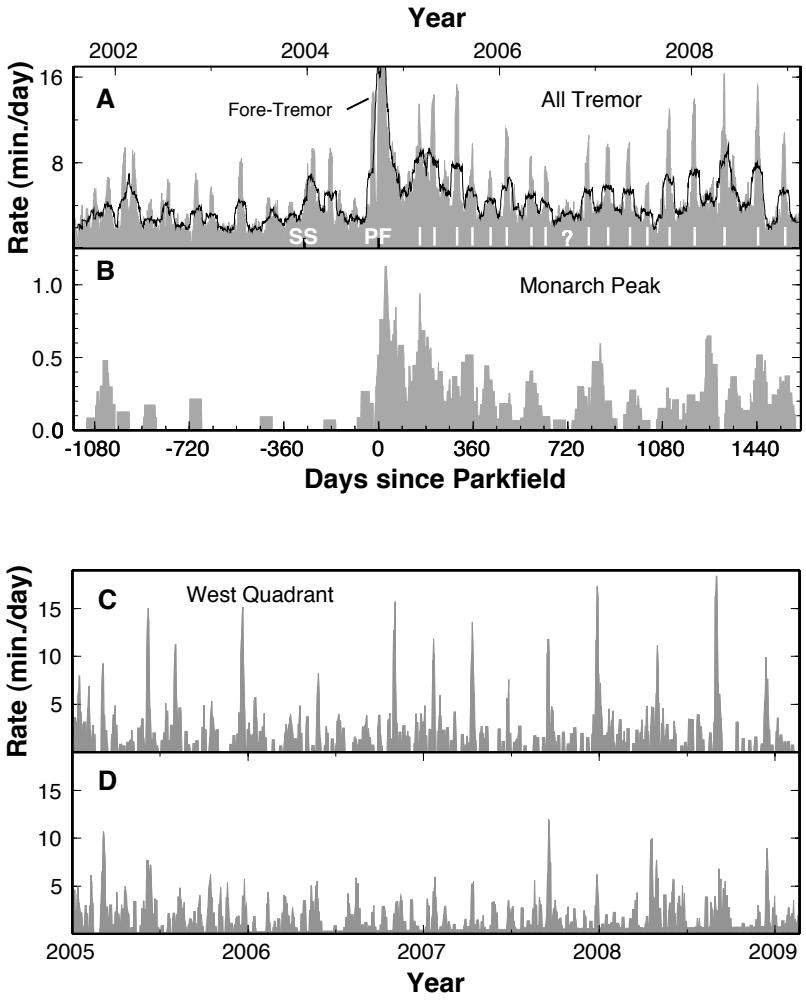


Figure 5.7: Time histories of tremor activity. (A) Fifteen-day (grey) and 45-day (black) smoothed rate histories for all tremors in the study area. Times of the San Simeon and Parkfield earthquakes are SS and PF, respectively. Intense foretremor (Fore-Tremor) activity occurred $\sim$ 3 weeks before PF. Fifteen- and 45-day peak values just after PF are 31.1 and 18.9 minutes/day, respectively. White bars are interpreted times of quasi- periodic episodes. Label –?– indicates the time of a weak or missing episode. (B) History of tremor in the Monarch Peak zone (45-day smoothed). (C) History since 2005 of activity (5-day smoothed) in the western quadrant of the Cholame zone (Figures 5.5) (423 tremors; 2835 cumulative minutes of activity) showing strong episodic behavior. (D) Same as (C) for Cholame tremors outside the west quadrant (416 tremors; 2423 cumulative minutes) showing significantly less episodic behavior.

(Figure 5.7a) [Hirose and Obara, 2006; Rogers and Dragert, 2003]. However, unlike many subduction zone tremors where recurrence of dominant episodes is typically 6 months or longer and is accompanied by relatively low amplitude inter-episode activity, the SAF episodes show progressively increasing recurrence intervals ranging from $\sim$ 50 days (in 2005) to $\sim$ 100 days (in 2008) and are accompanied by more energetic inter-episode activity (Figures 5.1 and 5.7a). The SAF tremors have also typically occurred in bursts of $\sim$ 3 - 10 days rather than 1 - 7 weeks as is more common in subduction zones. These differences may, in part, be related to the tectonic environment, and/or the much smaller dimensions of the SAF tremor zones.

The episodic tremors are not ubiquitous throughout the central part of the SAF. Rather, they seem to have been most persistent and regular in the western quadrant of the Cholame tremor zone that is bounded by the SAF to the northeast and by the seismic / aseismic transition into the locked Cholame segment to the southeast (Figures 5.5, 5.7c, 5.8 and 5.9). This localization of tremor behavior suggests that there are differences in the process generating tremor in different subregions of the SAF. It also supports the argument that tremor in the Cholame zone is distributed both normal to and along strike of the SAF at depth (Figures 5.8 and 5.9). Tremors in the Cholame zone are also spatially clustered, and $>$ 55% of the tremors are separated by $\sim$ 2 km from at least four other tremors and, in some cases, from as many as 35 other events. Precise relative locations of Cholame tremor activity with waveforms similar to a low frequency earthquake showed that during a 24 hour period the similar tremor formed a deep, near- linear SAF parallel structure within the Cholame zone at $\sim$ 26 km depth [Shelly et al., 2009]. Taken together the fault-normal distribution, clustering and near-linear fault-parallel alignment of at least some tremor suggest that the SAF may broaden into several distinct sub- parallel zones as it extends into the ductile lower crust.

Chapter 7 presents a detailed analysis of the episodic behavior of tremors.

## 5.5 Stress change dependency

In order to quantify the stress change associated with the $M_w$6.5 San Simeon and the $M_w$6.0 Parkfield earthquakes in the tremor source region we use the Coulomb failure criterion,

$$\Delta\sigma_c = \Delta\tau + \mu'\Delta\sigma_n \tag{5.1}$$

, in which failure is hypothesized to be promoted when the Coulomb stress change ($\Delta\sigma_c$) is positive. Here, $\Delta\sigma_c$ is the change in Coulomb stress on the receiver fault caused by slip on the source fault(s), $\Delta\tau$ is the change in shear stress (reckoned positive when sheared in the direction of fault slip), $\Delta\sigma_n$ is change in normal stress (positive in unclamping of the fault), and $\mu'$ is effective coefficient of friction on the fault. Coulomb, shear and normal

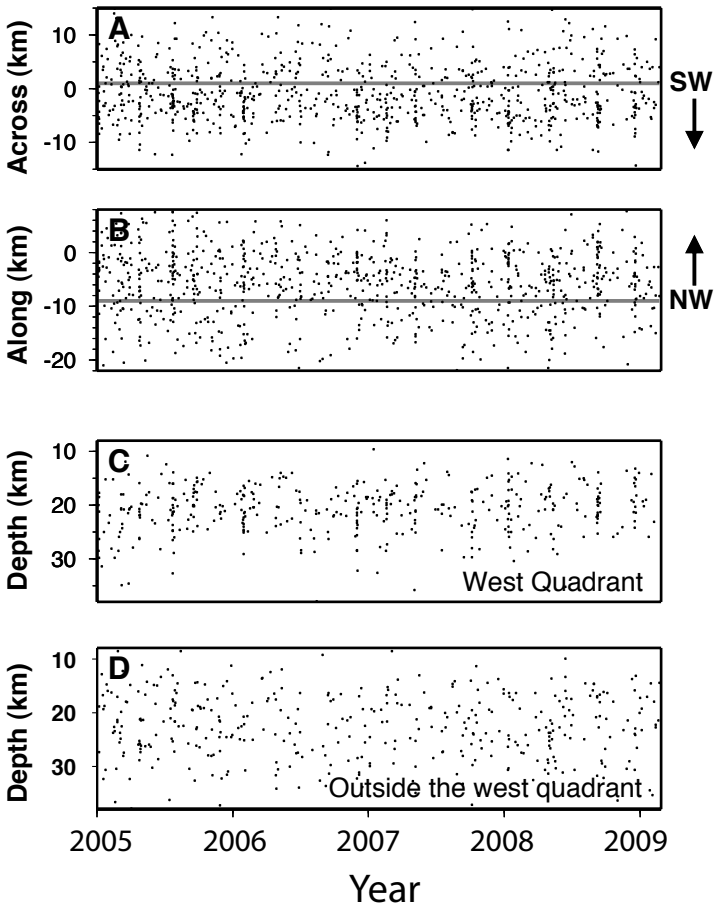


Figure 5.8: Occurrence of Cholame zone tremors through time since the beginning of 2005 in the across-fault (A), along-fault (B) and depth (C and D) directions. Here all tremor locations, regardless of location quality, are considered. Local coordinate system has origin at Cholame (populated place), latitude 35.7239°N, longitude 120.2956°W and orientation N40°W. Grey lines in (A) and (B) are boundaries defining the west quadrant shown in map view in Figure 5.5 and show the primary localization of episodic behavior to this quadrant. Panel (C) shows occurrence through time in depth for only those tremors located in the west quadrant. Panel (D) shows the same as (C) but for tremors located outside the west quadrant where episodes of tremor are more temporally diffuse or non-existant.

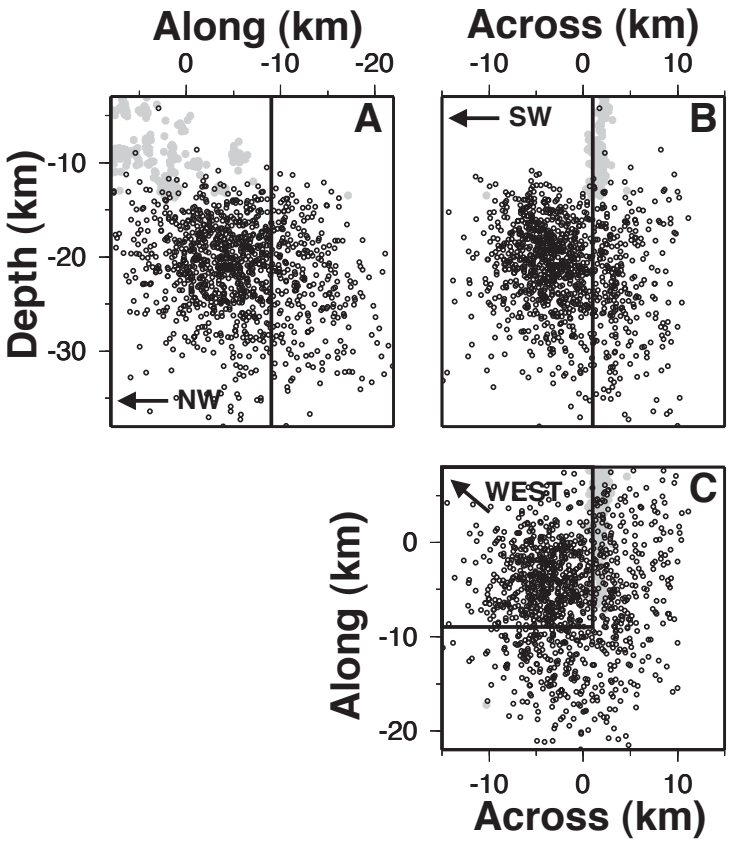


Figure 5.9: Depth section and map views of well located tremors (black) and greater than M1 earthquakes from the USGSs NCSN catalog (grey) in the Cholame zone. Local coordinate system is the same as that used in Figure 5.8. Velocity model for the tremor locations is based on the same model used for locating the earthquakes [Oppenheimer et al., 1993]. Interestingly, the boundaries defining the west quadrant (black lines) appear to correspond to two boundaries in the shallower seismogenic zone defined by the seismicity, the approximate seismic-aseismic transition into the Cholame locked segment (A) and the SAF (B). In addition to being more episodic in nature, tremors in the west quadrant (C) are spatially less diffuse.

stress changes associated with the 2003 San Simeon and 2004 Parkfield earthquakes (Figures 5.5 and 5.10, and Table 5.1) were calculated using uniform rupture models based on finite-source models of the San Simeon and Parkfield earthquakes [Kim and Dreger, 2008; Rolandone et al., 2006]. Stress changes were computed for vertical planes parallel to the SAF (strike N40°W, rake 180° or right-lateral motion, and dip 90°) at a typical tremor depth of 20 km using the Coulomb 3.1 Graphic-rich deformation and stress change software [King et al., 1994; Toda et al., 2005]. An effective coefficient of friction ($\mu'$) of 0.40 was used for the coulomb stress change calculations. At $\mu' = 0.0$, Coulomb-stress change reduces to shear-stress change. Positive normal- and shear-stresses are in the extensional and right-lateral senses, respectively.

Static Coulomb- and shear-stress changes from the 2003 San Simeon and 2004 Parkfield earthquakes on planes aligned along the SAF at a depth of 20 km (Figures 5.5 and 5.10) are small in the Cholame and Monarch Peak tremor zones (Table 5.1), but both stress types increase with increases in tremor rates in the two zones. In the Cholame zone, modeled shear- and Coulomb-stress changes associated with the San Simeon earthquake are $\sim$ 6 to 8 kPa whereas those associated with the Parkfield event are $\sim$ 9 to 14 kPa (Table 5.1). In the Monarch Peak zone, shear- and Coulomb-stress changes from the San Simeon event, which failed to stimulate tremor, were negative (i.e., $\sim$ -4 to -9 kPa); however, stress changes for the Parkfield earthquake were positive ($\sim$ 6 to 9 kPa) and correspond to the post-seismic activation in tremor activity in this zone (Figure 5.7b). Static normal-stress changes from the earthquakes do not clearly correspond to the tremor rate changes in either zone (Figure 5.10 and Table 5.1). This lack of correlation suggests that either normal-stress change did not play an important role in stimulating tremor or that other circumstances (i.e., the generally low change in normal-stress compared to shear-stress or offsetting signs of shear and normal stress; Table 5.1) masked the effects of normal stress on tremor stimulation.

The static earthquake stress changes that stimulated the SAF tremors are roughly an order of magnitude smaller than those typically reported for the triggering of earthquakes [King et al., 1994]. This suggests that tremors are a more sensitive indicator of stress change than earthquakes. The small stress changes that stimulated the SAF tremor ($\sim$ 0.01 MPa or one-tenth of atmospheric pressure) are consistent with stress changes from tides or the passage of surface waves from large teleseismic events that have stimulated tremor in subduction zones [Peng and Chao, 2008; Rubinstein et al., 2009, 2008].

The periodic tremor and persistent elevated activity after the 2004 Parkfield earthquake (Figures 5.7) are not consistent with expectations of exponentially decaying post-seismic stress after an earthquake [Brenguier et al., 2008; Savage and Langbein, 2008]. It appears, therefore, that in the deep tremor zones the SAF may have transitioned into a new state of

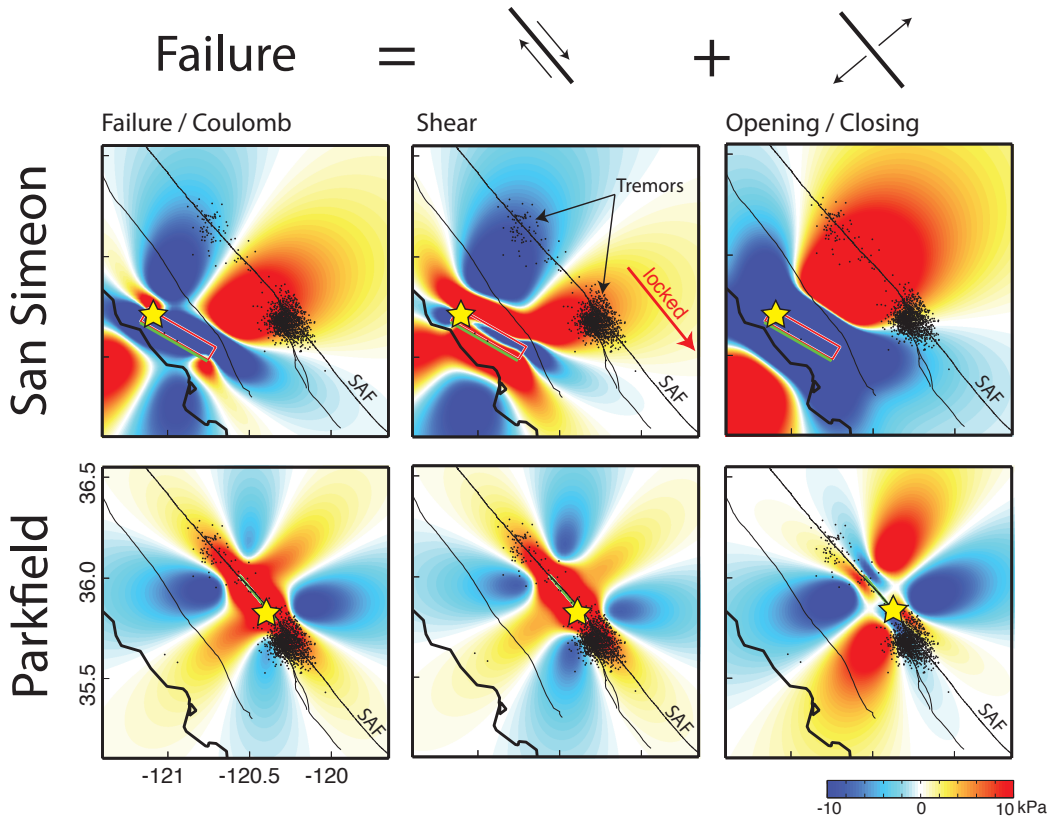


Figure 5.10: Calculated Coulomb-, shear- and normal- stress changes associated with the 2003 San Simeon (top) and 2004 Parkfield (bottom) earthquakes, respectively. The green line represents the surface trace of the two ruptures, and for San Simeon the red rectangle indicates the surface projection of its inclined (thrusting to the southwest) rupture plane. The Parkfield rupture plane was near vertical. Black dots represent the tremor locations.

Table 5.1: Calculated stress change statistics (Coulomb-, shear-, and normal-) from the San Simeon and Parkfield earthquakes in the 10-by-10 km square regions at 20 km depth.

| Stress values in 10-10km (kPa) | | | Min | 25 (%) | Median | 75 (%) | Max |
|---|---|---|---|---|---|---|---|
| Cholame | San Simeon | Coulomb | 5.15 | 6.19 | 7.12 | 8.19 | 9.69 |
| | | Shear | 5.09 | 5.86 | 6.37 | 7.06 | 8.30 |
| | | Normal | -1.33 | 0.75 | 1.81 | 3.10 | 4.66 |
| | Parkfield | Coulomb | 6.25 | 9.33 | 11.15 | 13.58 | 19.64 |
| | | Shear | 6.49 | 9.18 | 10.83 | 13.43 | 19.12 |
| | | Normal | -4.99 | -1.80 | 0.41 | 2.48 | 5.29 |
| Monach Peak | San Simeon | Coulomb | -6.10 | -5.22 | -4.59 | -4.09 | -3.01 |
| | | Shear | -9.89 | -8.95 | -8.34 | -7.78 | -7.01 |
| | | Normal | 7.03 | 8.16 | 9.35 | 10.58 | 12.26 |
| | Parkfield | Coulomb | 4.55 | 6.24 | 7.26 | 8.50 | 11.22 |
| | | Shear | 4.78 | 6.19 | 7.04 | 8.38 | 10.99 |
| | | Normal | -2.61 | -0.92 | 0.25 | 1.41 | 2.89 |

stress and/or deformation. Models of faulting imply that step-like stress perturbations from nearby earthquakes or pore pressure changes during episodic fluid release could cause deformation styles to transition between steady-state, transient, and quasi-periodic [Liu and Rice, 2007]. For such mechanisms to apply to the SAF, deep slow-slip events must be occurring and fluid pressures must be high in the tremor zones. Though deep slow-slip associated with the SAF tremors has not been detected, slow-slip events with moment release equivalents as large as M3 could occur in the tremor zones without being detected [Johnston et al., 2006].

## 5.6 Conclusion

The lack of correlation between normal-stress and tremor rate changes from the San Simeon and Parkfield earthquakes may imply that effective normal stress is low and pore-fluid pressure is high in the SAF zones. Recent studies of stimulation of tremor in the SAF by teleseismic events [Peng and Chao, 2008] and solid earth tides [Thomas et al., 2009] support this by showing that tremor rates correlate predominantly with variations in shear-stress even though normal- stress variations in some cases exceed shear-stress variations by roughly an order of magnitude [Thomas et al., 2009]. In subduction zones, dehydration of subducting oceanic crust elevates fluid-pressure [Shelly et al., 2006]. Although subduction no longer occurs along the SAF, two strong magnetic anomalies at Monarch Peak and Cholame [Wallace, 1990] suggest that serpentinite bodies are present at depth, and these could be fluid sources [Raleigh and Paterson, 1965] in the tremor zones. Alternatively, deep mantle derived fluids might also play a role [Kennedy and van Soest, 2007].

Because changes in SAF tremor activity have persisted for years beyond the last major quake in 2004, they could be signaling a shift in the process of deformation and stress accumulation beneath this portion of the SAF. The northwest tremor zone near Monarch Peak is an area of the SAF with anomalous structural complexity and low surface fault-creep rates [Rymer et al., 1984]. Two foreshocks ($\sim$ M6.1 and $\sim$ M5.6) occurred in this area within 2 hours of the 1857 M7.8 Fort Tejon earthquake. Faulting from the 1857 event appears to have propagated from the Monarch Peak area southeastward along the SAF for $\sim$ 350 km, through Parkfield and the Cholame tremor zone [Meltzner and Wald, 1999; Sieh, 1978; Toppozada and Branum, 2002] (Figure 5.5). The rupture zone of the great 1857 event is composed of multiple fault segments [USGS, 2008], including the Cholame segment immediately southeast of the Cholame tremor zone. This segment is now fully locked. Its estimated mean recurrence time is between 85 and 142 years [USGS, 2008], and it last ruptured as part of the great 1857 event.

# Chapter 6

# High-frequency identification of non-volcanic tremor triggered by regional earthquakes

modified from **High-frequency identification of non-volcanic tremor triggered by regional earthquakes** by Aurélie Guilhem, Zhigang Peng (Georgia Tech), and Robert M. Nadeau, published in *Geophysical Research Letters*

## 6.1 Introduction

Since their first discovery in Japan in 2002 [Obara, 2002], deep non-volcanic tremors have been mainly observed along subduction zones such as in the Nankai trough [Shelly et al., 2006], Cascadia [Brudzinski and Allen, 2007; Rogers and Dragert, 2003] and in Central America [Brudzinski et al., 2010; Payero et al., 2008]. Similar continuous bursts of tremor activity have also been found along the San Andreas Fault (SAF) transform plate boundary in central California near Parkfield-Cholame [Nadeau and Dolenc, 2005; Nadeau and Guilhem, 2009; Shelly and Hardebeck, 2010]. Recent studies of tremors in these environments have shown that they can be dynamically triggered by the passage of the seismic waves from large earthquakes at teleseismic distances (e.g., $>$ 1000 km), appearing as a series of a few-seconds-long high-frequency bursts with a periodicity similar to that of the surface waves [Gomberg et al., 2008; Miyazawa and Brodsky, 2008; Miyazawa et al., 2008; Miyazawa and Mori, 2005; Peng and Chao, 2008; Peng et al., 2009; Rubinstein et al., 2009, 2007]. Because both ambient and dynamically triggered tremors occur below the seismogenic zone, they provide important clues for understanding the fundamental processes at the deep roots of major plate-boundary faults [Rubinstein et al., 2006].

Nadeau and Guilhem [2009] showed that ambient tremor activity in the Parkfield-Cholame region was strongly modulated for over four years by two earthquakes occurring within 100 km: the 2003 Mw6.5 San Simeon and the 2004 Mw6.0 Parkfield events (see previous chapter). However to date, no dynamically triggered tremors have been observed from regional earthquakes at distances between 100 and 1000 km in either subduction or transform envi-

ronments. Rubinstein et al. [2009] explained the absence of regionally triggered tremor in Cascadia by the fact that P and S coda waves from regional earthquakes and local tremor share similar frequency passband (1 - 15 Hz) and waveform characteristics (i.e. long durations with no clear phase arrivals). Hence if the amplitude of regional earthquake coda is above that of the local tremor, the tremor signal will be masked, preventing it from being identified during passage of regional event surface waves. In comparison, large earthquakes have been shown to trigger microearthquakes at regional distances [Hill et al., 1993; Hill and Prejean, 2007]. In this case the masking effect is not significant because of the impulsive arrivals and relatively high-frequency content of the triggered earthquakes. In particular, Brodsky and Prejean [2005] conducted a systematic survey of triggered earthquakes by regional and teleseismic events around the Long Valley Caldera, and found that large-amplitude long-period surface waves have higher triggering potential than the short-period surface waves of similar amplitudes. Whether this is the case for triggered tremor remains an open question.

An effective way to separate the locally triggered tremors from the coda waves of regional earthquakes is to examine higher frequency bands [Peng et al., 2007], in particular frequencies higher than those previously used to identify teleseismically triggered tremors (i.e., 1-15 Hz). Because high-frequency signals recorded by surface stations in the Parkfield-Cholame area are often limited by analog telemetry issues or contaminated by near-surface noise sources, we take advantage of the high sampling rate and low noise data of the borehole High Resolution Seismic Network (HRSN) at Parkfield, California and apply high-frequency band-pass filters (in the range of 20-50 Hz) to identify tremor triggered by regional earthquakes.

Here, we show that tremors can be triggered by the passage of surface waves from regional earthquakes in the tremor region. This discovery exhibits a new aspect of triggered nonvolcanic tremors, which is their larger frequency content. Indeed we show that they have energy up to 50 Hz as seen on the borehole HRSN stations. Furthermore, we present evidence that the high-frequency content is not unique to regionally dynamically triggered tremors because similar observations are made for teleseismically triggered tremors and ambient tremors in the region of Parkfield. Finally, we find that long-period and large-amplitude surface waves from both regional and teleseismic events have a greater potential of triggering tremor in the region, and we discuss the stress perturbation associated with the passage of the waves in the tremor region.

## 6.2 Data and method

We search for tremors dynamically triggered by the passage of seismic waves from regional earthquakes of magnitude 5 or greater (based on the ANSS catalog), occurring between July 2001 and April 2010 (coincident with the updated ambient tremor catalog of Nadeau and

Guilhem [2009]), and distributed between 100 and 1200 km from the broadband seismic station PKD of the Berkeley Digital Seismic Network (BDSN) located at Parkfield (Figure 6.1). A minimum distance of 100 km is chosen because dynamic stresses are expected to dominate over static stresses at such distances [Freed, 2005]. In addition, it is difficult to separate the seismic signals from the main and triggered events at short distances. We use a maximum distance of 1200 km to allow partial overlap of our events with those of previously studied teleseismically triggered tremor (minimum distance of 1000 km) occurring in the same region [Peng et al., 2009].

A total of 99 regional earthquakes fulfilled these criteria and we systematically downloaded the 250 samples/s HRSN data for these events. We searched for triggered tremor within several overlapping frequency bands: 3-15 Hz, 15-30 Hz, and 25-40 Hz. We identify triggered tremors by visually searching for consecutive bursts of energy in the higher frequency bands that are phase-correlated with the passing surface waves. Out of the 99 events analyzed, we found four cases of tremor triggered by the following regional earthquakes: the 15 June 2005 M7.2 Mendocino (Figure 6.2), 04 January 2006 M6.6 Baja California (BC) (Figure 6.3), 03 August 2009 M6.9 BC (Figure 6.4), and 04 April 2010 M7.2 BC (Figure 6.5). Figure 6.2 shows an example of tremor triggered by the 2005 Mendocino earthquake. In the higher frequency bands the signal is composed of bursts of energy that are periodic and coincident in time with the surface wave train observed on the unfiltered PKD seismograms, similar to teleseismically triggered tremor in the same region [Peng and Chao, 2008; Peng et al., 2009] and elsewhere [Miyazawa and Brodsky, 2008; Peng and Chao, 2008; Rubinstein et al., 2009, 2007].

Filtering is an important step to identify non-volcanic tremors. In this study we first deconvolved the borehole HRSN seismograms as well as the surface PKD and PST stations to examine the full range of low-frequency signals associated with the HRSN data. We applied filtering routines in the Seismic Analysis Code (SAC), Seistool and Matlab and found that the obtained bandpass-filtered seismograms are similar to each other (Figure 6.6), suggesting that the observed triggered tremor signals are not generated by the analysis procedure. The bandpass-filtered seismograms showed in this study are generated by the SAC Butterworth two-pass, 4-pole bandpass filter (command bp) [Goldstein et al., 2003]. The HRSN instruments record signals with a sampling rate of 250 samples/s and have instrument corner frequencies of 2 or 4.5 Hz. Filtering their non-deconvolved records above 15 Hz gives also the same signal with a difference in the gain.

The same filtering procedures were applied to the surface stations. However, because their sampling rates are lower than those of the HRSN stations and because they are installed at shallower depths where attenuation can be a significant issue, they show a lower signal to noise ratio in the higher recorded frequency range. In addition, the majority of the surface stations in the area use analog telemetry in which a discriminator is incorporated

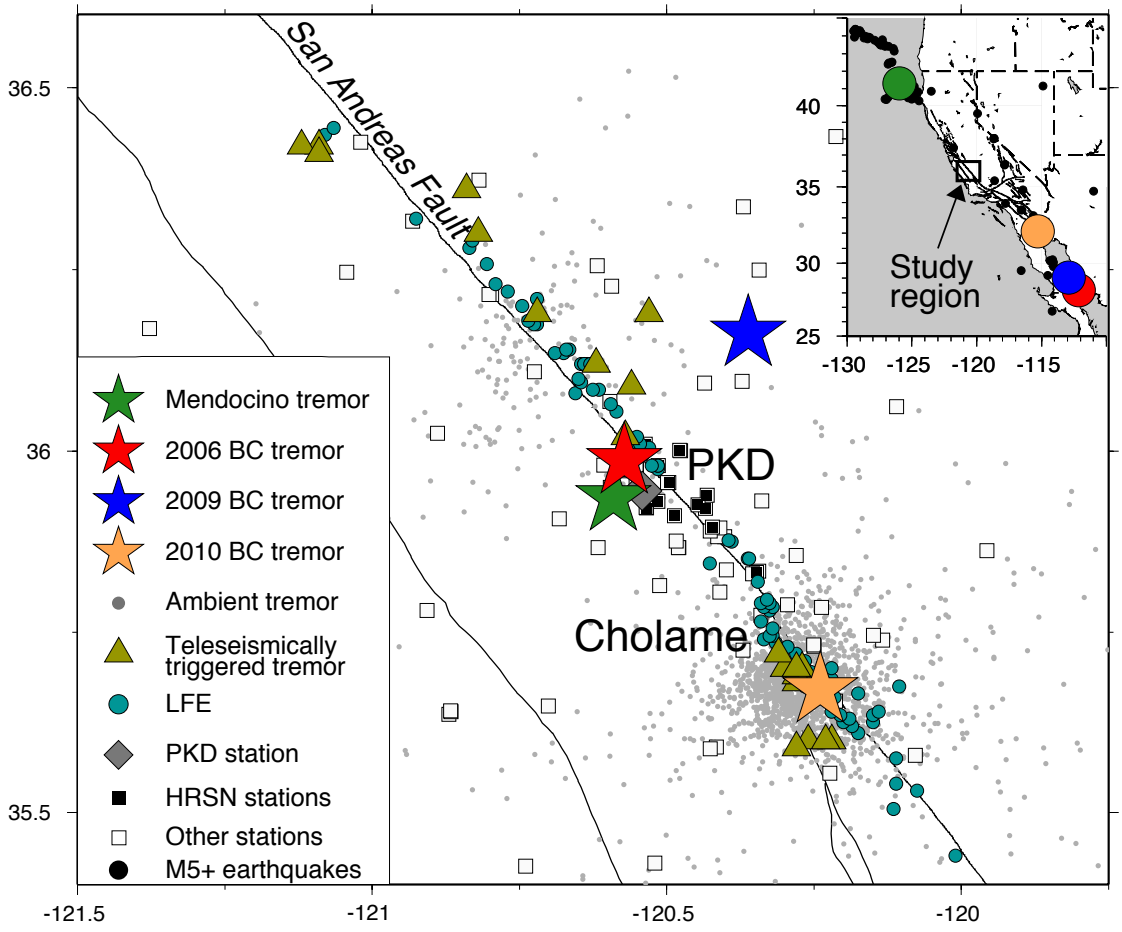


Figure 6.1: Location of dynamically triggered and ambient tremors along the Parkfield-Cholame section of the San Andreas Fault and the M5+ regional earthquakes distributed between 100 and 1200 km from the Berkeley broadband seismic station PKD (circles, inset). Stars show locations of the four triggered tremors and triangles show dynamically triggered tremors from teleseismic events [Peng et al., 2009]. Ambient tremors [Nadeau and Guilhem, 2009] are gray dots and borehole HRSN stations are black squares. Surface stations are the open squares. Low-frequency earthquakes (LFEs) are green circles [Shelly and Hardebeck, 2010].

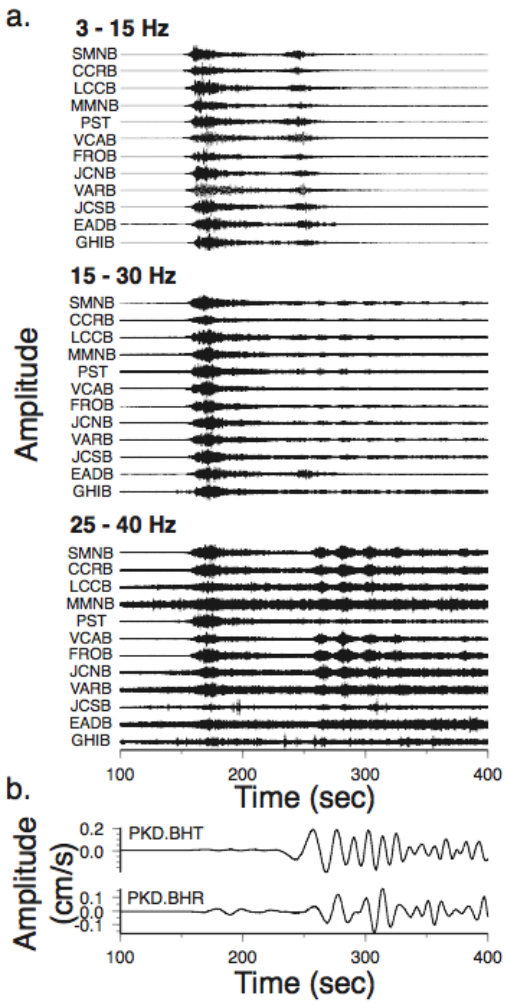


Figure 6.2: Dynamically triggered tremor by the M7.2 2005 Mendocino earthquake. a) Velocity seismograms recorded by the vertical (DP1) component of the borehole HRSN and surface NCSN station PST filtered at several frequency bands (3-15, 15-30 and 25-40 Hz from top to bottom respectively) for the tremor triggered by the 2005 Mendocino earthquake. Seismograms are ordered according to the along-strike (SAF) distance, from northwest (top) to southeast (bottom), and they are each scaled to their respective maximum and minimum values. The time scale is given in seconds after 02:50:00 UTC, and the triggered tremor is clearest between 250 and 350 s. b) Unfiltered, instrument-correlated transverse (BHT) and radial (BHR) components of the broadband surface station PKD showing the surface wave train (time scale same as in a).

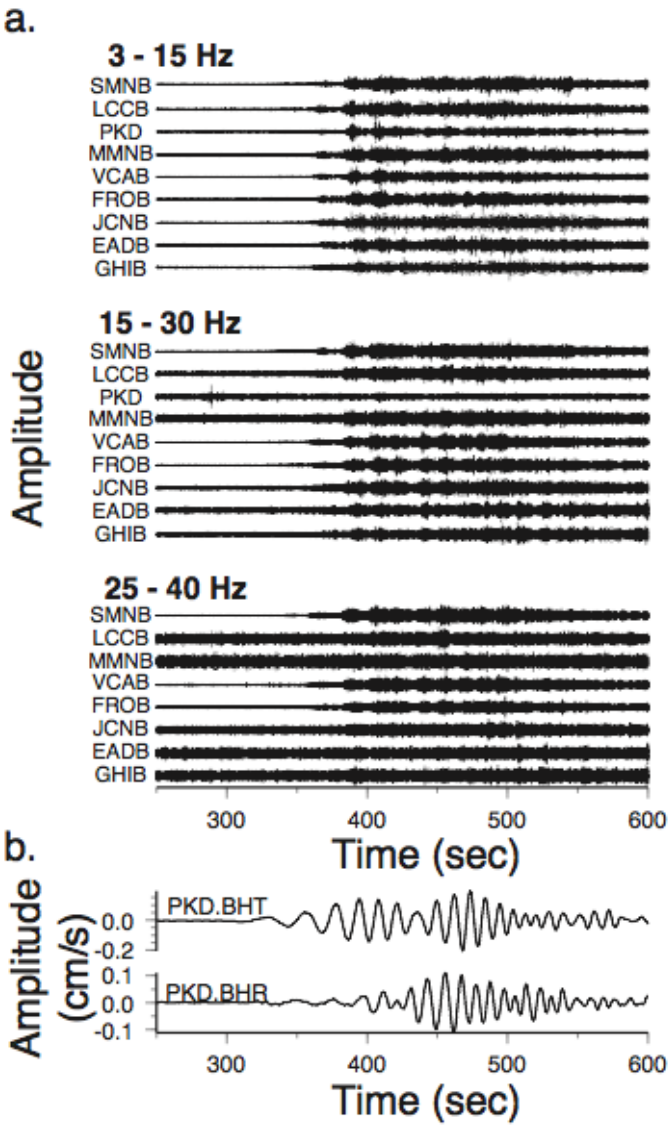


Figure 6.3: Dynamically triggered tremor by the M6.6 2006 Baja California earthquake. The triggered tremor is best observed between 350 and 550 sec after 08:32:00 UTC. See Figure 6.2 for detailed explanation.

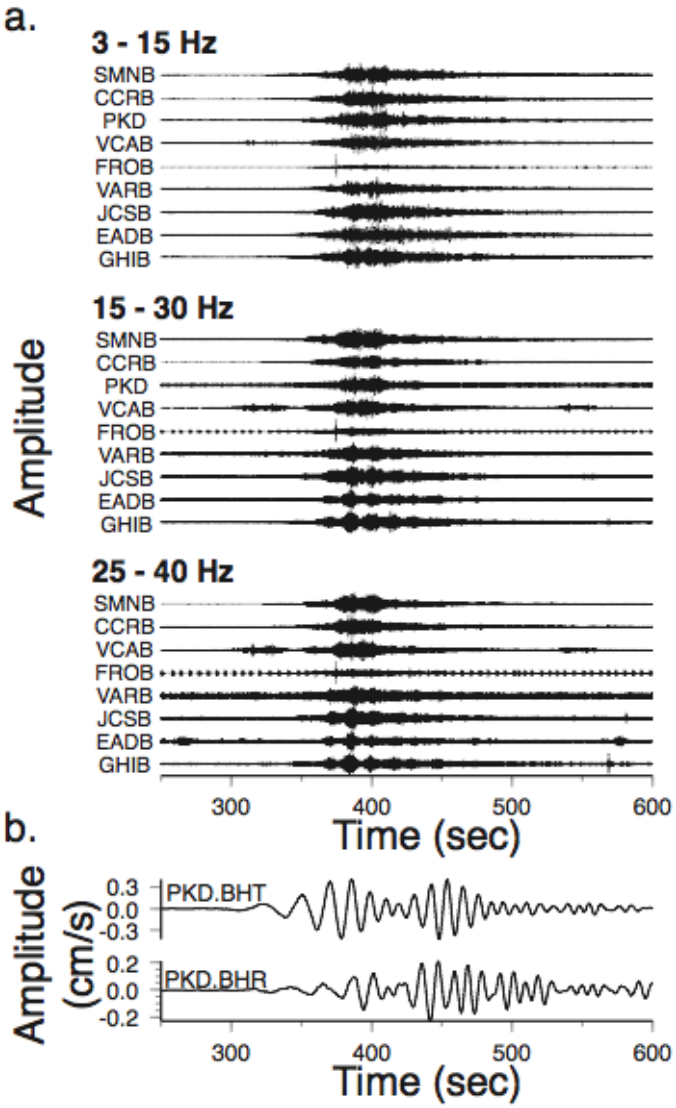


Figure 6.4: Dynamically triggered tremor by the M6.9 2009 Baja California earthquake. The triggered tremor is best observed between 350 and 550 sec after 17:59:00 UTC. See Figure 6.2 for detailed explanation.

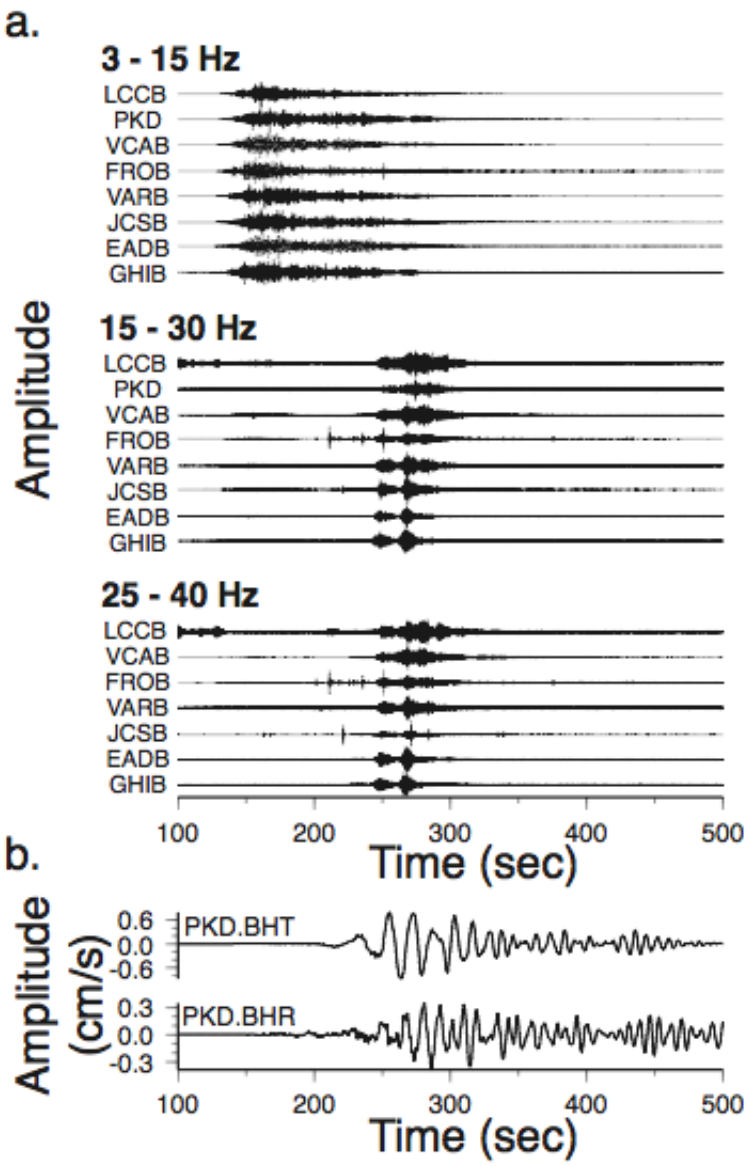


Figure 6.5: Dynamically triggered tremor by the M7.2 2010 Baja California earthquake. The triggered tremor is best observed between 200 and 350 sec after 22:40:00. See Figure 6.2 for detailed explanation.

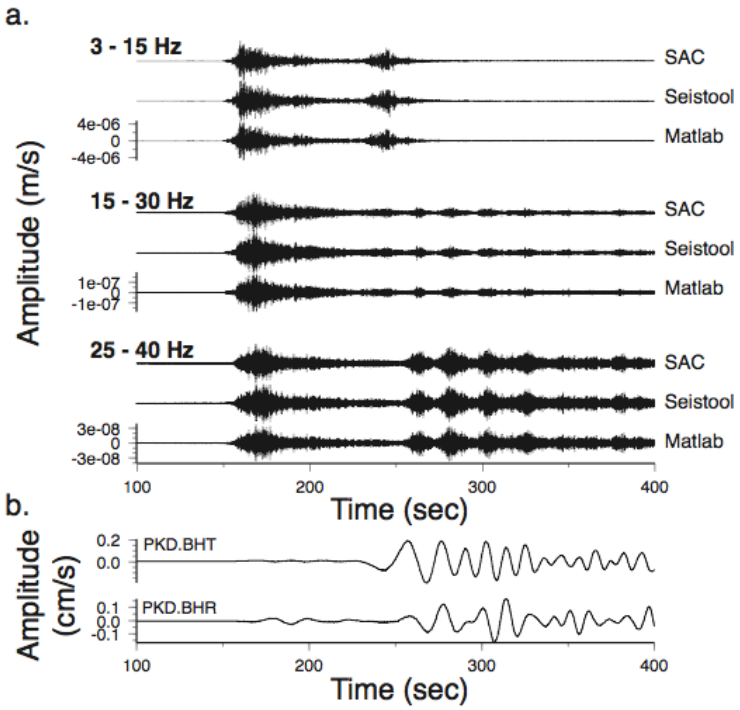


Figure 6.6: Stability of the filters. a) Comparison of three filtering routines in SAC, Seistool and Matlab for the 2005 Mendocino earthquake and tremor at the borehole SMNB station. For each frequency band the amplitudes (in m/s) of the three traces are the same. The time scale is given in seconds after 02:50:00 UTC, and the triggered tremor is clearest between 250 and 350 s. b) Unfiltered, instrument-correlated transverse (BHT) and radial (BHR) components of the broadband surface station PKD showing the surface wave train (time scale same as in a).

to prevent aliasing during transmission. This effectively reduces the usable frequency range of the data to less than 25 Hz. However triggered tremors are still observed at some of the surface stations such as PKD and PST that are not subject to the telemetry discriminator (Figures 6.2, 6.3, 6.4, and 6.5).

We located the four regionally triggered tremor sources by adapting the envelope based location algorithm for ambient tremors previously applied in the same region [Nadeau and Guilhem, 2009]. Because the signal to noise ratios are low above 20 Hz for most surface stations, the obtained tremor locations are primarily based on the borehole HRSN data but additional data from selected NCSN, SCSN, and BDSN surface stations are also used. Hence, the station coverage is limited. Locations were obtained after filtering the data between 10 and 30 Hz for the 2006 and 2010 Baja California earthquakes and between 20 and 40 Hz for the 2005 Mendocino and 2009 Baja California. Eight HRSN stations and the NCSN surface station PST were used for locating the 2005 Mendocino tremor. In comparison 16 stations including 6 surface stations located the 2006 Baja California tremor and 9 HRSN stations with 13 surface stations were used for the 2009 Baja California tremor. Finally 11 stations including 2 surface stations permitted the location of the 2010 Baja California tremor.

Figure 6.1 shows that the triggered tremor sources are located in the general vicinity of the Parkfield section of the SAF, close to the region where ambient and dynamically triggered tremors [Nadeau and Guilhem, 2009; Peng et al., 2009] as well as low-frequency earthquakes (LFEs) [Shelly and Hardebeck, 2010] have previously been found. The tremors triggered by the 2005 Mendocino, 2006 and 2010 BC earthquakes appear to be on or close to the SAF, while the tremor triggered by the 2009 BC earthquake occurs at a place about 25 km NE of the SAF.

## 6.3 Results

As shown in Figure 6.2, the HRSN data filtered between 3 and 15 Hz mainly show two emergent arrivals that are close to the predicted P and S arrivals from the 2005 Mendocino mainshock, similar to those reported for regional events in Cascadia [Rubinstein et al., 2009]. For the 04 January 2006 and 04 April 2010 earthquakes, the triggered tremors are best observed in the 15 to 30 Hz band and for the 15 June 2005 and 03 August 2009 events in the 25 to 40 Hz band (Figures 6.2, 6.3, 6.4, and 6.5). Most tremor signals occur in phase with the large-amplitude, low-frequency surface waves, suggesting a casual relationship between them (Figure 6.7).

To understand how surface waves trigger tremors, previous studies have examined the wave type (Rayleigh or Love), their amplitude, period, direction of propagation, etc [Hill, 2008, 2010; Miyazawa and Brodsky, 2008; Peng et al., 2009; Rubinstein et al., 2009]. The

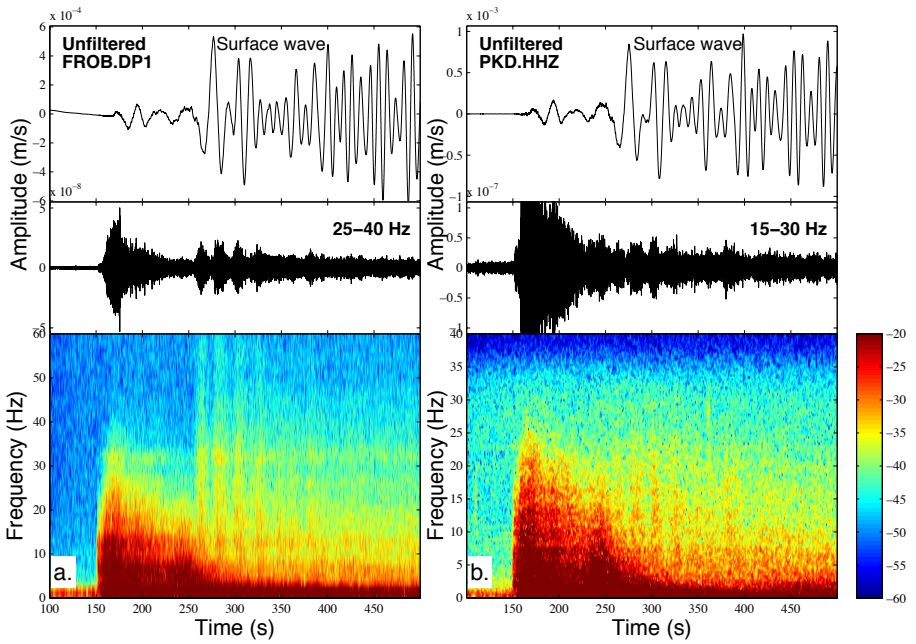


Figure 6.7: Spectrograms of the 2005 Mendocino tremor for a borehole station and a surface station. a) Unfiltered (top) and 25-40 Hz bandpass-filtered seismograms (middle) showing the broadband signals of the $M_w$7.2 Mendocino earthquake and triggered tremor observed at the borehole HRSN station FROB after 2006/06/15 02:50:00 UTC. The bottom panel shows the corresponding spectrogram in the frequency range of 0 and 60 Hz. The spectrogram is computed from a 0.5 Hz high-pass-filtered seismogram in order to suppress potential artifact from the short time windows in computing the spectra for long-period signals [Peng et al., 2010]. b) Unfiltered (top) and 15-30 Hz bandpass-filtered seismograms (middle) of the Mendocino earthquake and triggered tremor observed at the surface broadband station PKD after 02:50:00 UTC. The bottom panel shows the corresponding spectrogram in the frequency range of 0 and 40 Hz.

propagation directions of the four regional events that triggered tremors are close to the fault strike of the SAF, which is the optimal angle to produce fault-parallel shear stresses from the Love waves [Hill, 2008, 2010; Peng and Chao, 2008; Peng et al., 2009]. However, due to short propagation distances, it is relatively difficult to separate the Love and Rayleigh waves. Hence, in this study we only focus on how the amplitudes and periods of the surface waves affect their triggering potential.

We measured the peak ground velocities (PGVs) of the 99 regional earthquakes at the PKD station using the unfiltered transverse (Figure 6.8) and vertical components of the surface PKD station (BH channels) between the arrival time of the earthquake waves traveling at a velocity of 5.5 km/s and 1.5 km/s (Figure 6.9) after correcting for the instrumental response. Measurements were made on unfiltered and filtered (30-200 sec periods) PKD records. We also included an updated result of Peng et al. [2009] for teleseismic earthquakes to evaluate the triggering potential of surface waves in central California. Figure 6.8a shows that both regional and teleseismic events that triggered tremors have among the largest PGVs recorded at station PKD, supporting the view that large-amplitude surface waves favor tremor generation [Peng et al., 2009].

To further examine the frequency dependence of surface wave triggering potential, we applied a bandpass filter between 0.005 and 0.03 Hz (or 30 and 200 s) to the transverse-component seismograms before measuring the PGVs (Figure 6.8b). The major changes after applying the long-period bandpass filter are significant reductions of the PGVs for several moderate-size events (i.e. magnitudes between 5.0 and 6.0) relatively close to the study region. After filtering, the range of PGVs for the four regional earthquakes that trigger tremors is more comparable to those of the teleseismic earthquakes. If we use 0.01 cm/s as a threshold PGV to separate the triggering and non-triggering cases at regional distance, the corresponding dynamic stress is 1 kPa (with the nominal surface wave velocity of 3.5 km/s and the elastic modulus of 35 GPa at depth). The only events that did not satisfy the threshold criteria are teleseismic events. Regarding the vertical component (Figure 6.9), one regional earthquake that triggered tremors (i.e. the 2009 M6.9 Baja California) appears below the threshold while one that did not trigger (i.e. the January 2010 M6.5 Mendocino) is above the threshold. These few regional and teleseismic events that do not satisfy such criteria suggest that besides frequency and amplitude, other factors, such as the incident angles and the background tremor rate, could also influence the triggering potential [Hill, 2010; Rubinstein et al., 2009].

## 6.4 Discussion and conclusion

In this study we identified four cases of regionally triggered tremor along the Parkfield-Cholame section of the SAF by examining signals at frequencies above those typically used

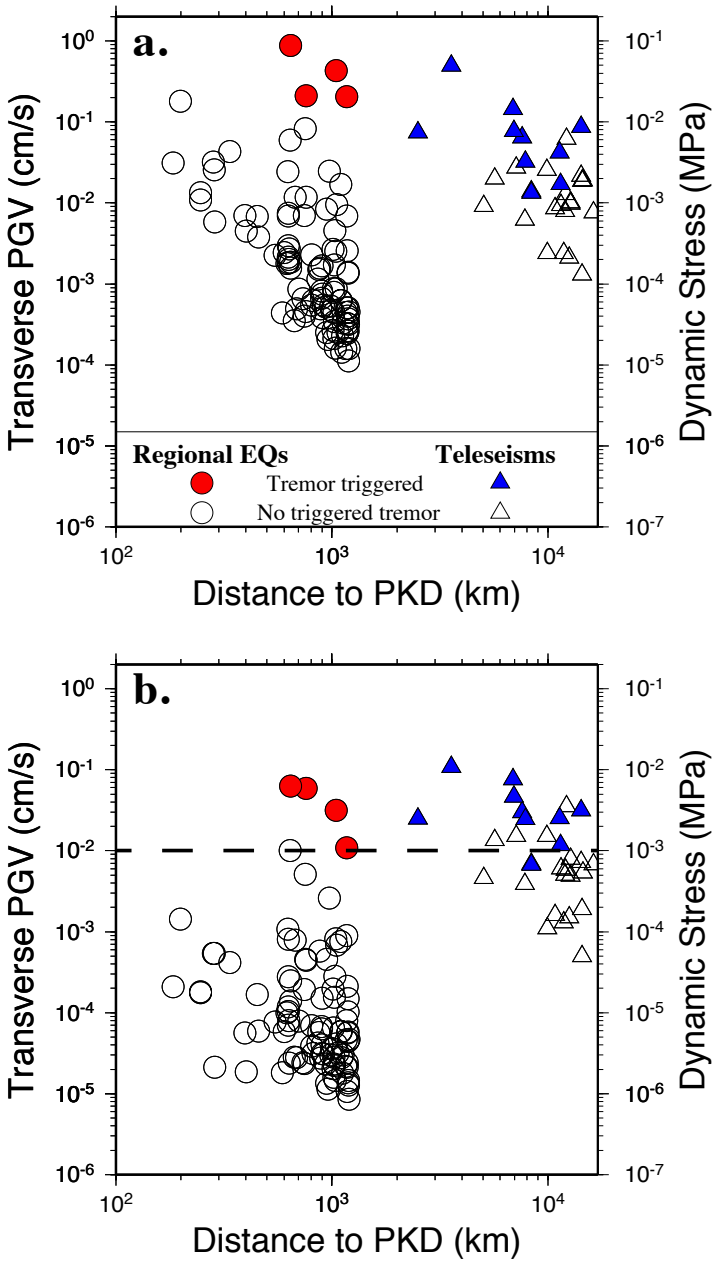


Figure 6.8: Transverse peak ground velocities (PGV). a) Recorded at broadband station PKD on the unfiltered transverse seismograms for regional and teleseismic (Teleseisms) earthquakes (EQs). Symbols for tremors triggered by regional and teleseismic events are filled. b) Same as a) but with transverse components filtered between the period of 30 and 200 s. Dashed line at 0.01 cm/sec marks the PGV threshold for tremor triggering in this pass-band.

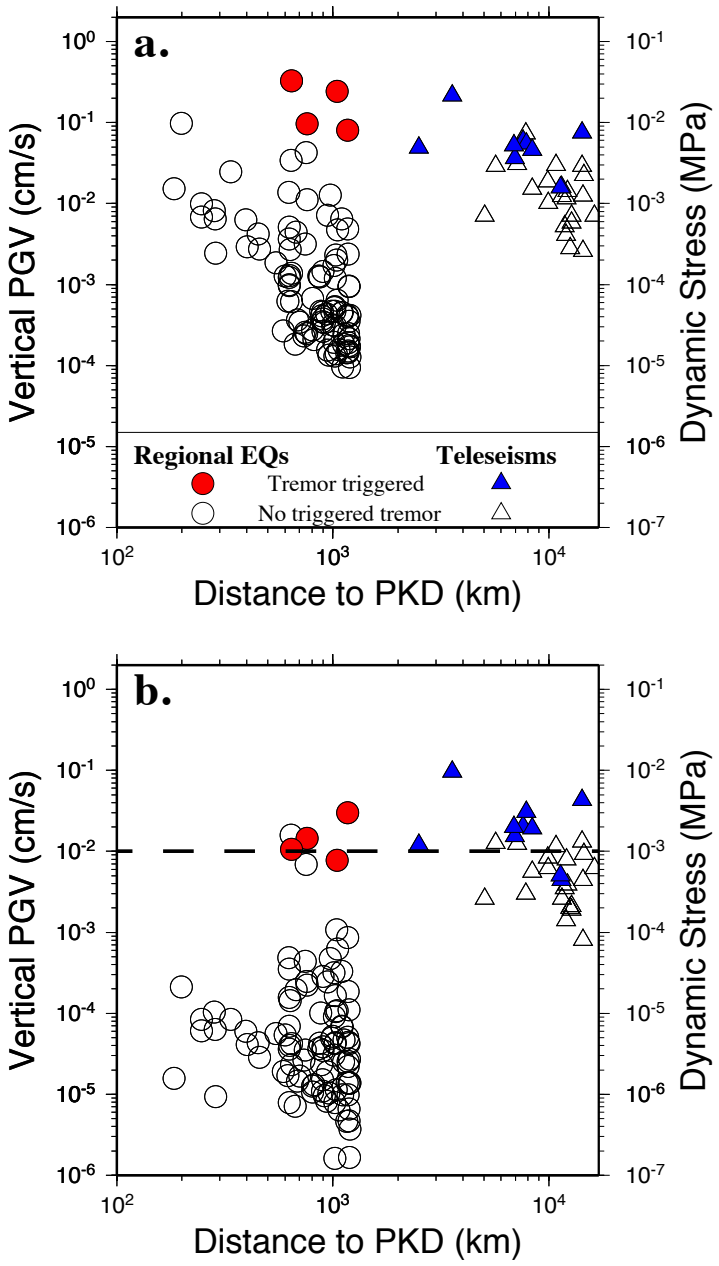


Figure 6.9: Vertical peak ground velocities (PGV). See Figure 6.8. The regional earthquake in b) with a PGV above that dashed line that did not trigger tremor is the January 2010 M6.5 Mendocino earthquake.

for identifying ambient [Nadeau and Dolenc, 2005; Nadeau and Guilhem, 2009] and triggered tremor [Peng et al., 2009] in the same region (i.e., above 1-15 Hz). The 1-15 Hz range appears sufficient for discriminating locally triggered tremor signals from teleseismic coda and surface waves, mainly due to the attenuation of 1-15 Hz coda energy at long propagation distances from the source region [Peng et al., 2009; Rubinstein et al., 2009]. However, separating locally triggered tremor signals from coda generated by regional earthquakes requires examination at higher frequencies, where the amplitude of triggered tremor signals exceed the amplitude of coda signals from regional events.

To show that the high-frequency content is not unique to the regionally triggered tremor alone, we examined a few teleseismically triggered tremors [Gomberg et al., 2008; Peng and Chao, 2008; Peng et al., 2009] and ambient tremors [Nadeau and Guilhem, 2009] in the Parkfield-Cholame region. We found that the high-frequency signals (25-40 Hz) are clearly visible for the teleseismically triggered tremor associated with the 2002 $M_w$7.9 Denali Fault and the 2008 $M_w$7.9 Wenchuan earthquakes (Figures 6.10 and 6.11). Similar high-frequency contents are also shown in at least some of the borehole stations during several long-duration ambient tremor events (Figure 6.12), suggesting that the processes responsible for generating the high-frequency signals in the ambient and triggered tremors could be similar (Figures 6.13 and 6.14). The high-frequency triggered and ambient tremor signals are observed on all three components from different types of seismic sensors and data loggers, indicating that they are not instrumentally generated. Furthermore, the fact that the local triggered tremor signals contain greater high frequency content than the P-wave energy from regional events (Figure 6.7) suggests that at the tremor source considerable high-frequency energy is generated and is not fully attenuated at local propagation distances. It remains unclear, however, whether or not the high-frequency content of these SAF tremors is generated by the same shear slip process responsible for the generation of LFEs (e.g., [Shelly et al., 2006], or by a related process such as damage zone microcracking associated with shear slow-slip events [Brantut et al., 2010]).

We also showed that large-amplitude ($> 0.01$ cm/s) and long-period surface waves ($> 30$ s) have a greater potential for triggering tremor at regional and teleseismic distances (Figures 6.8 and 6.9). These results are consistent with those found for triggered earthquakes in the Long Valley caldera [Brodsky and Prejean, 2005], although the amplitude threshold in that study is slightly larger ($> 0.05$ cm/s). Because triggered and ambient tremor occur at subseismogenic depths ($\sim$ 20-30 km), such frequency dependent effects may be explained by increased attenuation of short-period surface waves with depth [Brodsky and Prejean, 2005] and by differences in the mechanism of earthquakes that occur in the shallow, brittle crust and tremors occurring in the deeper, ductile crust. Our calculated dynamic stress change (1 kPa) is in the same range as the 1-3 kPa inferred from teleleseismically triggered tremor [Peng et al., 2009], tidal modulation of tremor [Thomas et al., 2009], and static triggering of tremor by nearby moderate earthquakes [Nadeau and Guilhem, 2009] in the same region.

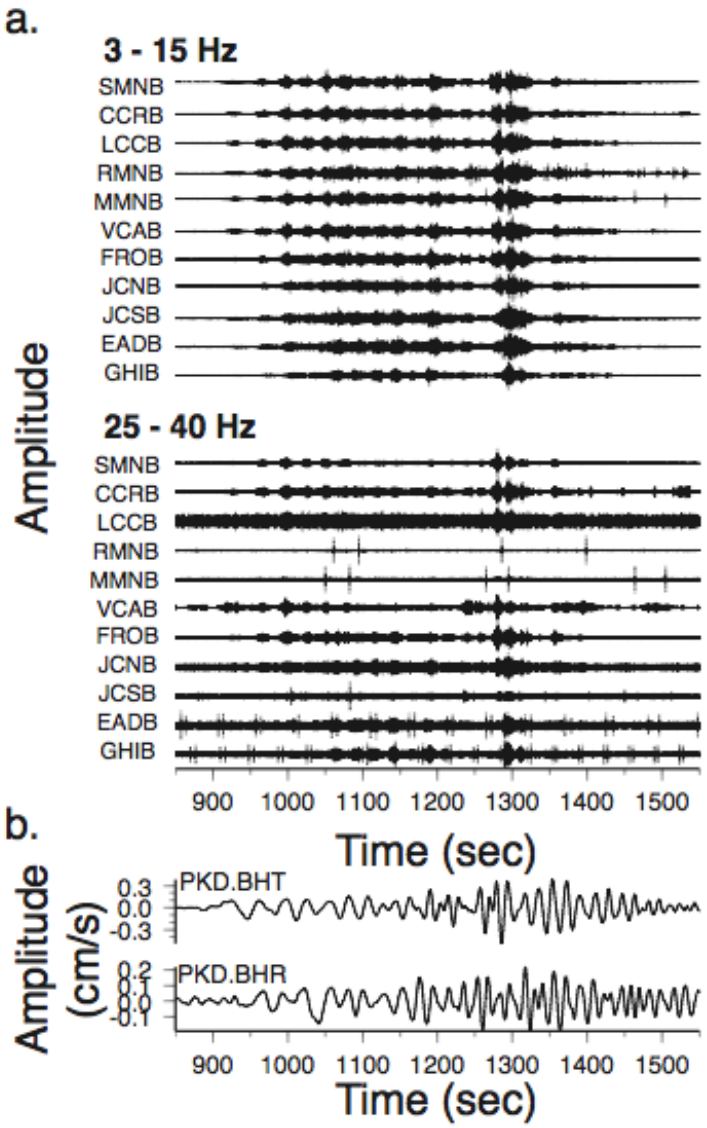


Figure 6.10: Nonvolcanic tremors triggered by the $M_w$7.9 2002 Denali Fault earthquake. a) Velocity borehole seismograms filtered between 3-15 and 25-40 Hz. The HRSN traces are ordered from northwest to southeast along the strike of the SAF, and they are each scaled to their respective maximum and minimum values. The triggered tremor is well observed between 900 and 1400 sec after 22:12:00 UTC at the two frequency ranges. b) Unfiltered horizontal components of the surface broadband PKD station showing the surface wave train between 900 and 1400 sec after 22:12:00 UTC.

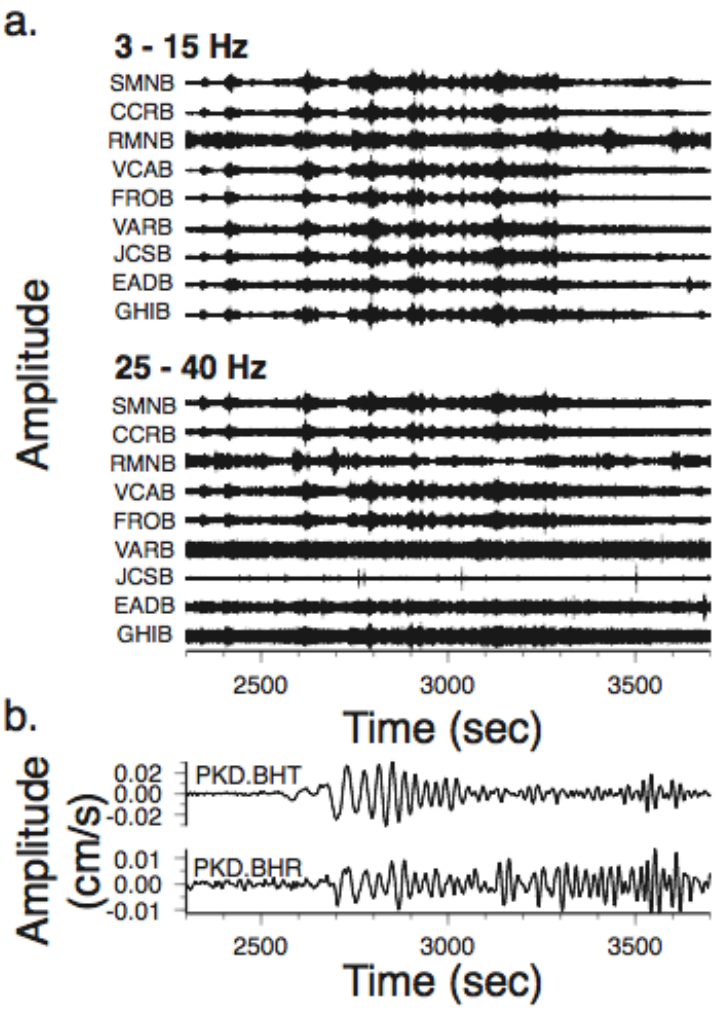


Figure 6.11: Nonvolcanic tremors triggered by the $M_w$7.9 2008 Wenchuan earthquake. a) Velocity borehole seismograms filtered between 3-15 and 25-40 Hz. The HRSN traces are ordered from northwest to southeast along the strike of the SAF, and they are each scaled to their respective maximum and minimum values. The triggered tremor is well observed between 2500 and 3300 sec after 06:28:00 UTC at the two frequency ranges. b) Unfiltered horizontal components of the surface broadband PKD station showing the surface wave train between 2500 and 3500 sec after 06: 28:00 UTC.

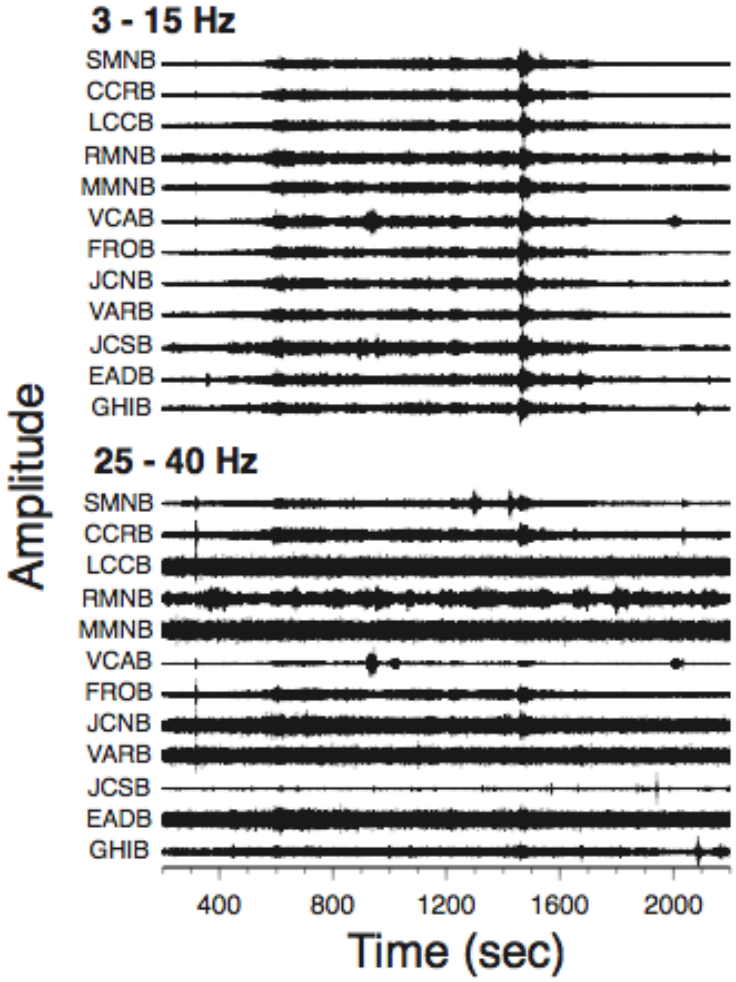


Figure 6.12: Ambient nonvolcanic tremor. Velocity borehole seismic records of the 12 April 2005 20-minutes-long ambient tremor filtered between 3-15 and 25-40 Hz. The HRSN traces are ordered from northwest to southeast along the strike of the SAF, and they are each scaled to their respective maximum and minimum values. The tremor is best observed between 550 and 1700 sec from 03:00:00 UTC.

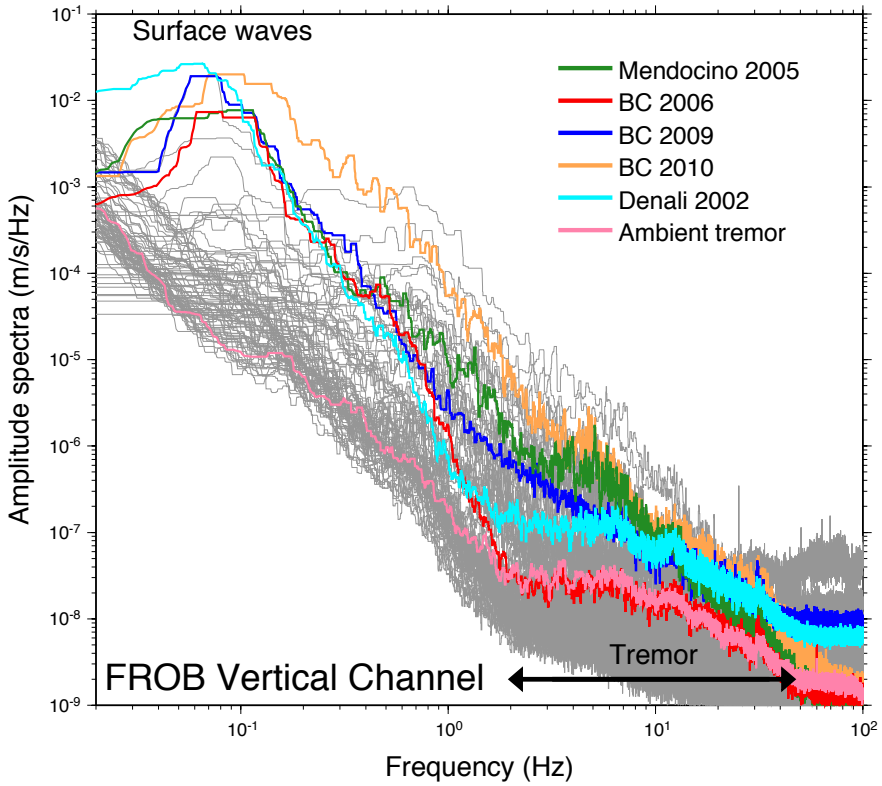


Figure 6.13: Velocity spectra of the vertical components at the HRSN station FROB for the 99 regional earthquakes of the study (gray: earthquakes that did not trigger tremors, green: 2005 Mendocino, red: 2006 BC, blue: 2009 BC, and orange: BC 2010), and the 2002 Denali Fault earthquake that triggered tremors (light blue), and of a 20-min-long ambient tremor (pink). Spectra are computed from the instrumented corrected borehole velocity seismograms with apparent velocities between 5 km/s and 1.5 km/s. The earthquakes that triggered tremors have peak energies observed around 20 s (or 0.5 Hz), which correspond to the surface waves. One earthquake that did not trigger tremor has a similar energy at 20 s as compared with other triggering events. It corresponds to a foreshock that occurred about 4 minutes before the 2010 BC earthquake. The spectra of the foreshock overlaps with the upcoming surface waves of the mainshock, which triggered tremors.

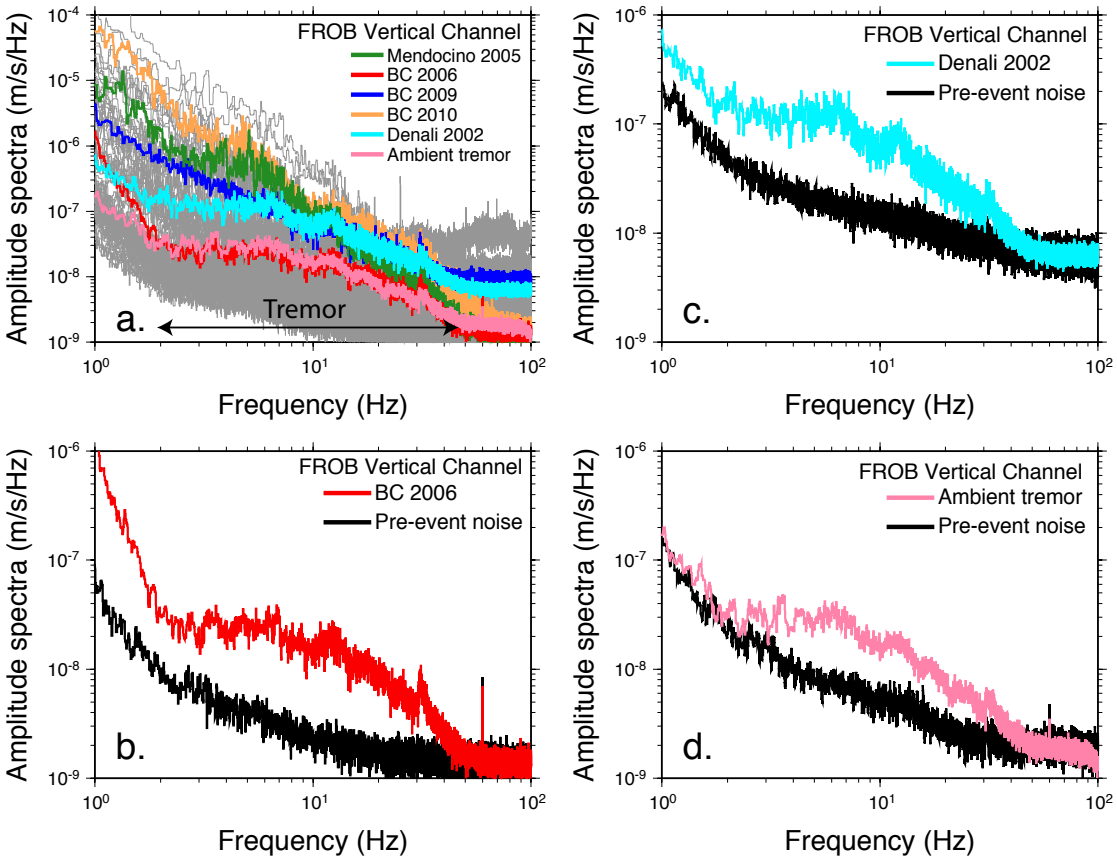


Figure 6.14: High-frequency content of tremors. a) Comparison of the velocity spectra between 1 and 100 Hz of the vertical components at the HRSN station FROB for the 99 regional earthquakes of the study (see Figure 6.13). b) Velocity spectra for the 2006 Baja California (red) and its pre-event noise (black). c) Velocity spectra for the 2002 Denali (blue) and its pre-event noise (black). d) Velocity spectra for a 2005 ambient tremor (pink) and its pre-event noise (black).

These results, together with other recent studies, suggest that tremor is very sensitive to small stress changes at depth, most likely due to near-lithostatic fluid pressures [Thomas et al., 2009]. Given such stress sensitivities, it is important to continue monitoring the tremor activity in this region and elsewhere for a better understanding of fault mechanics in the deep crust and its relationship to large earthquake cycles.

# Chapter 7

# Episodic tremors reveal deep slow-slip events in central California

Advisor: Robert M. Nadeau

## 7.1 Introduction

Nonvolcanic tremors (NVT) have been shown to be dynamically triggered by the surface waves from large earthquakes when dynamic stresses from passing waves reach values on the order of 1 kPa [Gomberg et al., 2008; Guilhem et al., 2010; Miyazawa and Brodsky, 2008; Miyazawa et al., 2008; Miyazawa and Mori, 2005; Peng and Chao, 2008; Peng et al., 2009; Rubinstein et al., 2009, 2007]. Static stress changes of a few kPa induced by local and regional earthquakes also modulate tremor activity in deep fault zones, as observed following the 2003 $M_w$6.5 San Simeon and 2004 $M_w$6.0 Parkfield earthquakes [Nadeau and Guilhem, 2009]. In addition, stress modulations from earth tides of a few 100 Pa that are too small to trigger regular and repeating earthquakes, have also been found to modulate NVT activity [Rubinstein et al., 2008; Thomas et al., 2009].

Following the 2004 Parkfield earthquake, a persistent change in tremor behavior occurred when a strong quasi-periodic pattern of tremor episodes emerged in conjunction with an overall increased rate of ambient tremor activity [Guilhem and Nadeau, 2008; Nadeau and Guilhem, 2009]. The absence of this strong quasi-periodicity before the Parkfield earthquake and its return to a less periodic behavior after a 4-year period makes this transition unique among tremor zones.

Because NVTs are generally believed to be associated with deep fault deformation beneath large locked fault zones such as slow slip events (SSEs) [Rogers and Dragert, 2003], and because the NVTs in this region occur at a critical location beneath the southeast and northwest ends, respectively, of the quasi-regular M6 Parkfield and 1857 M7.9 Fort Tejon locked zones, understanding the spatial and temporal behavior of the San Andreas Fault (SAF) NVTs and the physical mechanisms responsible for their occurrence is important for

understanding the deep fault zone processes beneath locked faults that are capable of generating large earthquakes. But despite a significant increase in overall NVT activity after both the San Simeon and Parkfield earthquakes [Brenguier et al., 2008; Nadeau and Guilhem, 2009], the detection of SSEs in the deep SAF tremor source zone has yet to be reported and its absence is largely attributed to the relatively small moment release expected for slow-slip events (SSEs) on the SAF [Johnston et al., 2006; Smith and Gomberg, 2009]. This implies that along this portion of the SAF tremor activity may be the only available means for inferring the deep stress and strain changes that play a role in the estimation of earthquake hazard potential in the area.

In this chapter we employ catalogs of NVT, repeating and regular earthquakes, as well as catalogs of low-frequency earthquakes, and we categorize the different patterns of SAF tremor behavior observed in the area (i.e., ambient, triggered, episodic, fore-tremor, and after-tremor) to obtain insights on the stressing conditions in the deep SAF. By characterizing the NVT episode patterns in terms of recurrence times and durations, and analyzing their spatial distribution we find that the episodic behavior is more pronounced on the western side of the Cholame tremor zone along an $\sim$ 25 km long segment of the SAF. This gives insights on the implication of the dimensions and fault lateral distribution of the episodic tremor zone in terms of possible SSEs and processes related to tremor-genesis. We investigate the degree of coupling between the seismogenic zone (upper $\sim$12 km of the crust) and the deep Cholame tremor zone by comparing episodes to characteristically repeating microearthquakes (REQs) and results from Cascadia that link NVT activity to deep slow-slip. We interpret the emergence and retreat of strong quasi-periodic tremor episodes as a prolonged postseismic deformational response associated with the 2004 Parkfield earthquake, similar to that seen for REQs. Finally, we explore implications of the episodes for source characteristics of inferred slow-slip, and we compare them with estimates of physical conditions (e.g. stress change, and fault strength, and fluid participation) from observation and theory.

## 7.2 Data

### 7.2.1 Nonvolcanic tremor (NVT)

We use the updated catalog of Nadeau and Guilhem [2009] spanning from 27 July 2001 through 21 March 2011. 2791 tremors having durations of 3 to 21 minutes are included in the catalog (Figure 7.1). Detections of the NVTs (see Chapter 5) are based on root-mean-squared envelopes using high-frequency broadband records from borehole stations of the High Resolution Seismic Network (HRSN). The detection involves two stages: 1) an initial automated processing procedure and 2) a subsequent visual inspection of the automated detections to remove outliers and artifacts. During the automated stage, initial detections were declared when the amplitude of the summary envelopes remained at or above 300 %

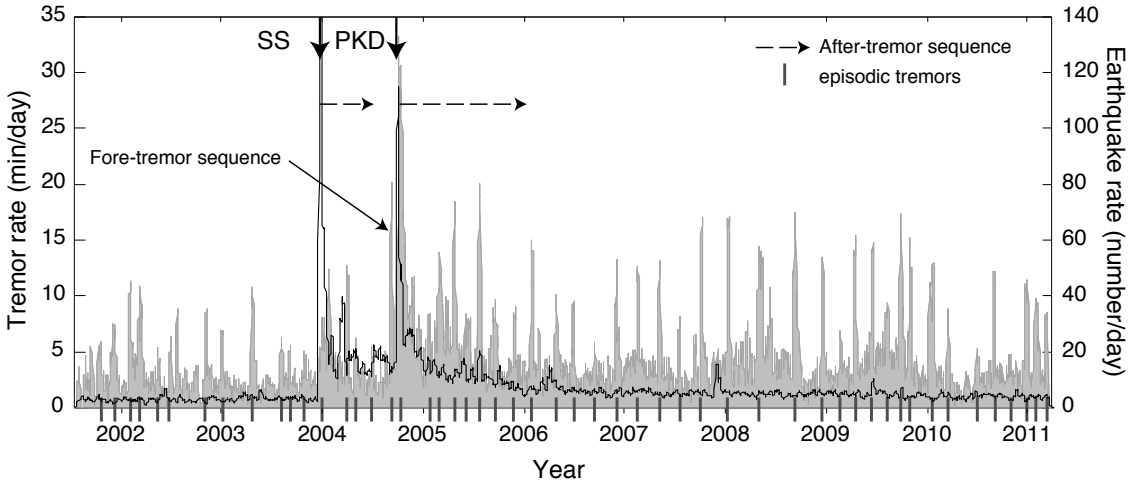


Figure 7.1: Tremor activity between July 2001 and March 2011 smoothed 10 days. The top vertical arrows indicate the occurrence times of the 2003 San Simeon (SS) and the 2004 Parkfield (PKD) earthquakes. The episodic tremors are shown by vertical marks on the x-axis. The 10-days-smoothed activity of M0+ earthquakes (black line) located within 100 km of Parkfield (35.9°N, -120.433°E) overlays the tremor activity (grey) also smoothed over 10 day periods.

of the long-term background level for at least 3 minutes. These criteria help reduce false detections and also preclude detections of NVT wavetrains with shorter ($< 3$ min) durations and lower amplitude. Hence our NVT catalog represents more energetic (i.e. longer duration and higher amplitude) periods of NVT activity.

### 7.2.2 Earthquakes

We also use the Advance National Seismic System (ANSS) catalog of earthquakes with magnitudes larger than 0 that occurred over the same time period and located up to 100 km away from Parkfield, to compare the daily rates of seismic events to the rates of NVTs (Figure 7.1). The earthquake catalog contains the background seismicity of the region as well as two moderate earthquakes, the 2003 M6.5 San Simeon and the 2004 M6.0 Parkfield earthquakes (Figure 7.1), and their aftershock sequences.

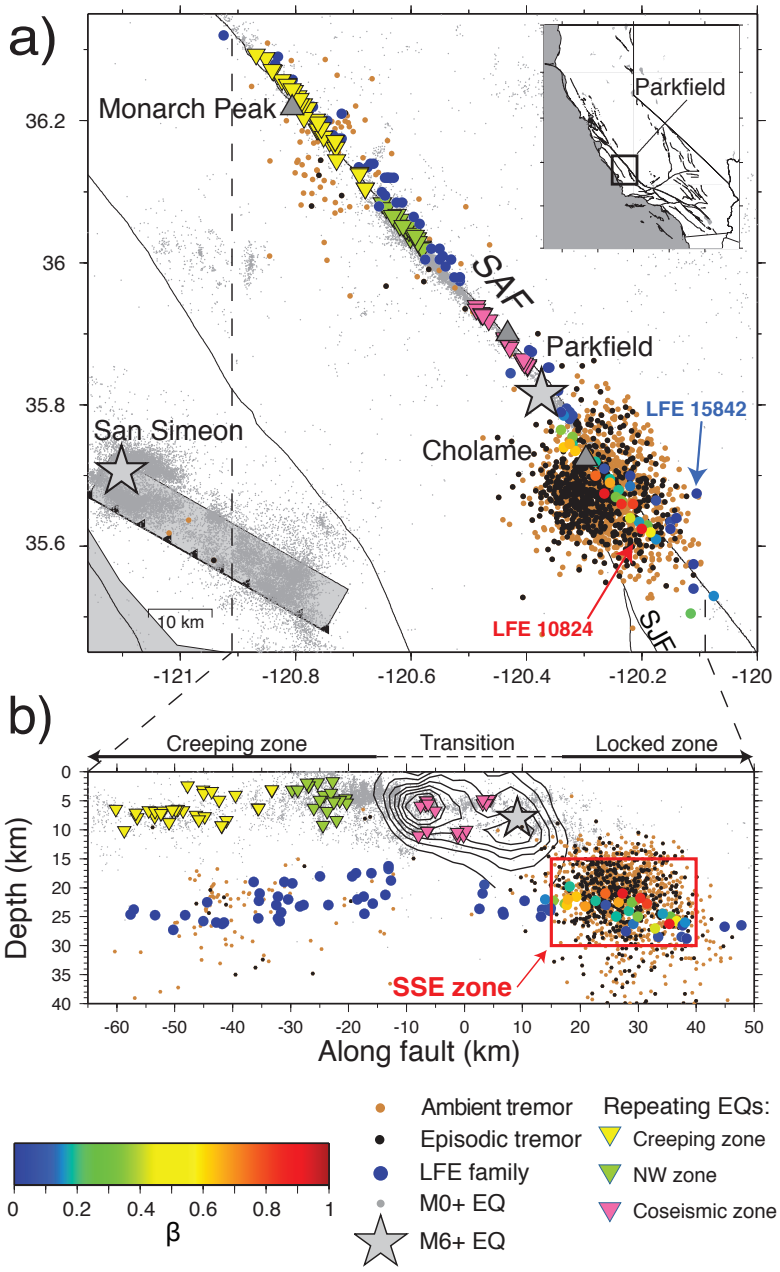


Figure 7.2: Location of NVT activity in central California. a) Map view of the NVT activity (black dots), LFE (colored dots), and REQs (inverted triangles) in the vicinity of Parkfield. The LFE families (circles) are color-coded by the degree to which their episodic behavior is similar to the episodic behavior of the NVTs (warm color: similar, cold color: different – saturated at 0). The stars indicate the locations of the epicenters of the 2003 San Simeon and 2004 Parkfield earthquakes. Seismicity between 2001 and 2010 from the ANSS catalog is shown (gray). b) Cross-section view of the seismic activity. The coseismic slip model of the 2004 Parkfield earthquake is shown by the black lines [Johanson et al., 2006].

### 7.2.3 Repeating earthquakes (REQs) and Deep Low-Frequency Events (LFEs)

We use the catalog of repeating earthquakes (REQs) compiled by Robert M. Nadeau for the time period corresponding to the NVT catalog [Nadeau and McEvilly, 2004]. We distinguish three groups of REQs located at three distinct sections of the SAF. These three groups are composed of: 1) 30 micro-earthquake sequences to image the slip behavior of the creeping section of the SAF (yellow inverted triangles in Figure 7.2), 2) 18 REQ sequences to represent the northwest part of the 2004 Parkfield earthquake zone (in green in Figure 7.2), and finally 3) 18 others located directly in the coseismic rupture segment of the 2004 mainshock (in pink in Figure 7.2). The magnitudes of the events range between 1 and 3.5, and they are located at depth between 1 and 12 km.

We also compare our NVT activity to the catalog of low-frequency earthquakes (LFEs) composed of 88 families of events [Shelly and Hardebeck, 2010].

## 7.3 Tremor behaviors at Parkfield

### 7.3.1 NVTs versus LFEs

Our use of the term nonvolcanic tremor (NVT) refers to seismic events that occur in the deep SAF zone and differ from earthquakes in their lack of clear P and S phase arrivals, their lower frequency content, and their longer duration of ground shaking. Similar definitions of NVTs have also been referred to as tectonic tremors or more generally tremors.

LFEs with locations, depths, and predominate frequency content similar to NVTs were first recognized in nonvolcanic regions of subduction zones in Japan [Katsumata and Kamaya, 2003; Nishide et al., 2000; Obara and Hirose, 2006; Ohmi and Obara, 2002]. Unlike NVTs, these events have distinct body wave phase arrivals, and durations of shaking consistent with those from individual earthquakes. LFEs have been found to occur in temporal isolation but also to frequently occur during periods of extended NVT and slow-slip activity [Ohmi and Obara, 2002; Katsumata and Kamaya, 2003; Obara and Hirose, 2006], leading Shelly et al. [2006] to make the hypothesis that NVTs may simply represent swarms of LFEs.

This hypothesis, however, has been difficult to confirm universally, given the rare and infrequent presence of identifiable LFE signals in some NVT wavetrains [Katsumata and Kamaya, 2003; Obara and Hirose, 2006], the inability to fully match NVT activity with LFE templates in many cases, and the greater abundance of higher frequency energy in many NVTs than is generally reported for LFEs [Guilhem et al., 2010], suggesting damage processes occurring during NVTs that may not be explainable by LFE activity alone [Brantut et al., 2010]. The pattern matching approach of LFE detection is similar to that

used for detecting REQs, suggesting that LFEs may reflect a process similar to repeating events [Shelly and Hardebeck, 2010]. However, REQs are known to represent only a minor fraction of the overall seismicity in a region and to occur primarily within the central core zone of creeping faults. In a number of locations, repeating seismicity is also effectively nonexistent, despite large numbers of non-repeating events [Templeton et al., 2008]. By analogy, then, it seems plausible to interpret LFEs, like REQs, as representing the repeating portion of tremor activity occurring primarily within the central core of the active fault zone.

LFEs are clearly present within NVTs along the SAF [Shelly et al., 2009]. Comparison of the LFE catalog with our NVT catalog between July 27, 2001 and December 31, 2009 reveals that while most of the NVT events contain at least one LFE, 43 NVTs including several with duration larger than 10 minutes have unmatched LFEs. Also, only 28% of the duration of NVT activity can be matched with LFE activity (based on 4-sec LFE templates). Over 85% of the LFEs occur outside of the intense 3 to 21 minute periods of NVTs. Matches with LFE templates do not necessarily signify that all the NVT energy is generated by LFEs because of additional superposed signals of comparable or higher frequency. Conversely, failure to match NVT with LFEs does not necessarily imply the absence of LFE energy, because superposed signals can significantly reduce the efficacy of LFE detection, and complete LFE matching would require a catalog of templates for all possible LFE waveforms. Even if NVTs are composed entirely of intense LFE swarms, the fact that most identifiable LFE activity occurs outside the periods of intense NVT activity suggests that the longer duration, more energetic NVT wavetrains we focus on here represent a unique process worthy of investigation.

In this study we compare and contrast the spatio-temporal behavior of NVT and LFE catalogs whether or not LFE matches have been found, to help constrain the source region of the episodic component of tremor activity and the mechanics of possible slow-slip events associated with the episodes.

### 7.3.2 Diverse NVT types

We differentiate the NVT activity of the Parkfield region into five basic types based on their temporal occurrence patterns, their correlation with the passage of regional and teleseismic earthquake waves, and their occurrence with respect to the relatively local 2003 San Simeon M6.5 and 2004 Parkfield M6.0 earthquakes. Except for the triggered tremors, the seismic signature of NVT consists of 3 to 21 minute bursts of continuous seismic activity with varying amplitudes and dominant frequency content in the 1-15 Hz band (Figure 7.3). Our classification into event-types primarily reflects periods of time when different rates of tremor activity occur, with additional distinction given to periods of activity related to the occurrence of significant earthquakes.

Ambient tremor reflects a background rate of tremor bursts in the region and excludes the episodic tremor discussed below.

Triggered tremors (Figure 7.3) are relatively rare and can be directly associated with the passage of waves from regional and teleseismic earthquakes [Gomberg et al., 2008; Guilhem et al., 2010; Miyazawa and Brodsky, 2008; Miyazawa et al., 2008; Miyazawa and Mori, 2005; Peng and Chao, 2008; Peng et al., 2009; Rubinstein et al., 2009, 2007]. Modulations in the triggered NVT amplitudes occur in phase with the long-period surface waves, with cycles of amplitude modulations lasting several seconds. Because these modulations are of short duration ($<<$ 3 minutes), this type of tremor is rarely captured by the tremor detection scheme used for generating our NVT catalog. Hence they do not play a significant role in our analysis. However, the possible effect of longer-term stimulation from large teleseismic waves on non-triggered NVT is considered.

Episodic tremors correspond to temporally clustered groups of NVT bursts that are otherwise indistinguishable from NVT bursts comprising ambient, fore- and after- tremor activity. In general, the rate of bursts during episodes is at least 3 times higher than during periods of ambient NVT activity (Figure 7.1).

Nadeau and Guilhem [2009] identified fore- and after-tremors related to the 2003 $M_w$6.5 San Simeon and 2004 $M_w$6.0 Parkfield earthquakes (Figure 7.1) that are analogous to the fore- and after-shocks that accompany mainshocks. The identified foretremor was a short and strong NVT episode that occurred about 21 days before the nearby 2004 Parkfield earthquake and represented a 5-fold increase in NVT rate relative to the ambient background rate [Nadeau and Guilhem, 2009]. The aftertremors (Figure 7.1) represent longer-lasting elevated rates of NVT activity occurring after both the 2003 San Simeon and 2004 Parkfield earthquakes.

## 7.4 Episode characteristics: timing, periodicity, and durations

### 7.4.1 Episode detection

Nadeau and Guilhem [2009] observed significant variations in the average rate of NVT activity over time-scales of several days to years in the Parkfield-Cholame area, and the emergence of quasi-periodic NVT following the 2004 Parkfield earthquake (see Chapter 5). To quantify the episodic pattern, we define the times of the tremor episodes by scanning a 50-day episode-template through the record of cumulative NVT activity during the study period using cross-correlation.

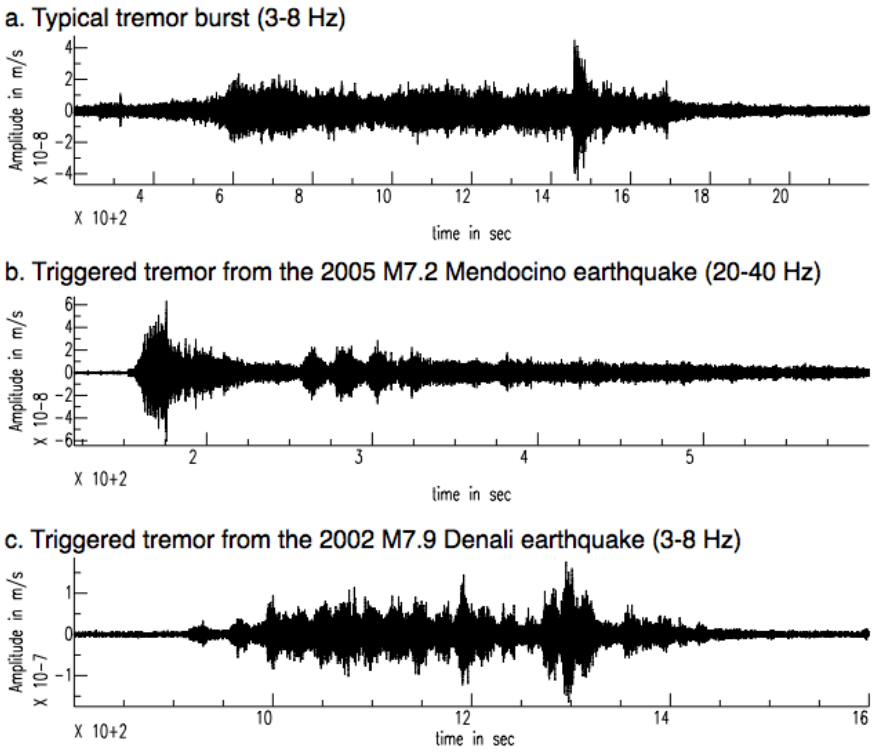


Figure 7.3: Waveforms of nonvolcanic tremors recorded at the FROB station (HRSN network). a) Typical tremor burst found in ambient, episodic, fore-, and after-tremor NVT types. Waveform of a 20-min long ambient tremor that occurred on 12 April 2005, filtered between 3 and 8 Hz. b) Waveform of triggered tremors (between 250 and 400 sec) by the regional M7.2 Mendocino earthquake, filtered between 20 and 40 Hz. c) Waveform of triggered tremors by the distant M7.9 Denali earthquake, filtered between 3 and 8 Hz.

The episode-template is constructed empirically by first stacking the normalized cumulative activity spanning 30 days before through 20 days after the 17 episodes reported by Nadeau and Guilhem [2009] (Figure 7.4a). A template of at least 50-days was necessary to stabilize the cross-correlation scans. Because of the dramatic increase in tremor activity associated with the Parkfield mainshock, an asymmetric template window is needed to ensure the selection of the fore-tremor episode occurring 21 days before the earthquake. The stacked and normalized cumulative data are detrended and yield the final episode-template (Figure 7.4b). In light of the substantial non-episodic (ambient) component of the NVT activity, we found that cross-correlation scans with detrended data provided a more robust discriminant of episode occurrence.

Cross-correlation sweeps of the cumulative NVT activity with the episode-template are then carried out by: 1) extracting and detrending 50-days of cumulative activity, 2) cross-correlating with the template, and 3) moving forward one day in the cumulative activity and repeating steps 1) and 2) (Figure 7.4c). Time steps with cross-correlations larger than 0.55 are bundled into groups whose sequential times are separated by 20 days or less. The times of the episodes are defined as those days within groups containing at least two $> 0.55$ correlated days that had the highest cross-correlation value. Because the intensity of the episodes varies substantially from cycle to cycle, because episodes occur over as few as 3 days or as many as 10 days, and because the rate of non-episodic tremor can vary significantly through time, matches to the episode-template vary substantially (Figure 7.4c). Secondary episodes also serve to retard consistent high cross-correlation matches for the predominate episodes. We imposed a temporal proximity criterion to limit the shortest episode recurrence times to 20 days or greater, and when this criterion applies, it imposes the assumption that dominant and secondary episodes occurring within 20 days of each other are effectively parts of the same episode. This may or may not always be the case. Nonetheless the criteria described above provide a necessary and objective standard for defining episode times that was consistent with visibly identifiable episodes.

### 7.4.2 Episode Timing and Periodicity

Fifty-two episodes, including the two mainshocks and the fore-tremor burst, are detected between July 2001 and March 2011 (Figure 7.1 and Table 7.1). Their repeat times obtained using the times of their maximum cross-correlation (Table 7.1) vary between about 30 days and 130 days. Before the 2004 Parkfield earthquake the episodes are very irregular in time (Figure 7.5). We also note that the occurrence of the San Simeon earthquake that modulated the overall tremor activity near Cholame [Nadeau and Guilhem, 2009] does not affect this

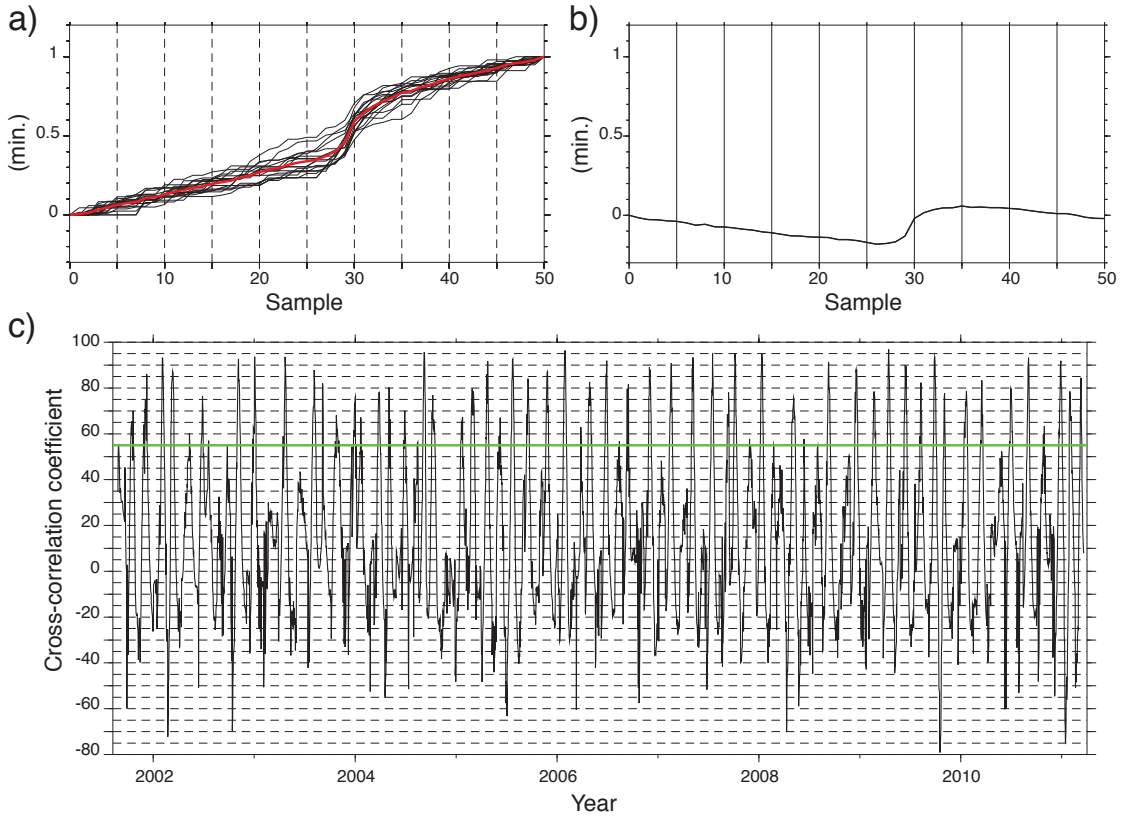


Figure 7.4: Detection of the tremor episodes. a) Stack (red) of the normalized cumulative activity (black) spanning 30 days before through 20 days after the 17 episodes reported by Nadeau and Guilhem [2009]. b) Detrended stacked and normalized cumulative data. c) Cross-correlation of the tremor catalog with the template (b). The green line marks the 0.55 threshold.

Table 7.1: List of the 52 episodes detected with the automated algorithm. The cumulative duration of tremors per episode is calculated for periods of 10 days centered on the episode times. The seismic moment (Mo) and the moment magnitude ($M_w$) for each tremor episode are obtained from the cumulative duration of tremors during episodes using Equations 7.2 and 7.3.

| Episode number | Time of maximum cross-correlation | Maximum cross-correlation | Recurrence time (day) | Cumulative duration (min) | Seismic moment (Mo) in Nm | Mw | Remarks |
|---|---|---|---|---|---|---|---|
| 1 | 2001.293 | 70.1 | - | 46.1 | 3.99e+16 | 5.03 | |
| 2 | 2001.342 | 86.0 | 49.2 | 61.7 | 5.35e+16 | 5.12 | |
| 3 | 2002.034 | 93.1 | 56.9 | 104.0 | 9.01e+16 | 5.27 | |
| 4 | 2002.070 | 87.2 | 36.8 | 93.2 | 8.07e+16 | 5.24 | |
| 5 | 2002.131 | 60.2 | 61.0 | 50.2 | 4.35e+16 | 5.06 | |
| 6 | 2002.179 | 76.5 | 47.0 | 50.0 | 4.33e+16 | 5.06 | |
| 7 | 2002.309 | 92.7 | 130.4 | 85.0 | 7.36e+16 | 5.21 | |
| 8 | 2003.003 | 93.7 | 58.8 | 65.7 | 5.69e+16 | 5.14 | |
| 9 | 2003.113 | 93.6 | 110.1 | 108.2 | 9.38e+16 | 5.28 | |
| 10 | 2003.217 | 87.8 | 104.8 | 53.4 | 4.62e+16 | 5.08 | |
| 11 | 2003.248 | 82.1 | 30.4 | 48.8 | 4.23e+16 | 5.05 | |
| 12 | 2003.298 | 68.0 | 50.0 | 43.5 | 3.77e+16 | 5.02 | San Simeon |
| 13 | 2004.001 | 76.4 | 69.0 | 57.8 | 5.01e+16 | 5.1 | |
| 14 | 2004.088 | 78.2 | 86.1 | 109.4 | 9.48e+16 | 5.28 | |
| 15 | 2004.123 | 80.2 | 35.4 | 54.7 | 4.74e+16 | 5.08 | |
| 16 | 2004.181 | 70.1 | 57.7 | 54.7 | 4.74e+16 | 5.08 | |
| 17 | 2004.251 | 95.6 | 69.4 | 184.9 | 1.60e+17 | 5.44 | Fore-tremor |
| 18 | 2004.282 | 77.0 | 31.2 | 294.9 | 2.55e+17 | 5.57 | Parkfield |
| 19 | 2005.024 | 67.4 | 108.1 | 78.6 | 6.81e+16 | 5.19 | |
| 20 | 2005.059 | 79.5 | 34.8 | 120.3 | 1.04e+17 | 5.31 | |
| 21 | 2005.115 | 91.7 | 55.7 | 180.9 | 1.57e+17 | 5.43 | |
| 22 | 2005.160 | 67.1 | 45.2 | 73.2 | 6.34e+16 | 5.17 | |
| 23 | 2005.206 | 92.6 | 46.0 | 189.2 | 1.64e+17 | 5.44 | |
| 24 | 2005.261 | 84.1 | 55.2 | 96.7 | 8.38e+16 | 5.25 | |
| 25 | 2005.331 | 87.2 | 70.3 | 85.4 | 7.40e+16 | 5.21 | |
| 26 | 2006.030 | 96.4 | 63.5 | 137.9 | 1.19e+17 | 5.35 | |
| 27 | 2006.118 | 82.6 | 88.6 | 92.7 | 8.04e+16 | 5.24 | |
| 28 | 2006.180 | 91.9 | 62.1 | 94.8 | 8.22e+16 | 5.24 | |
| 29 | 2006.258 | 81.6 | 78.1 | 58.6 | 5.08e+16 | 5.10 | |
| 30 | 2006.335 | 89.0 | 76.5 | 112.5 | 9.75e+16 | 5.19 | |
| 31 | 2007.049 | 90.8 | 79.2 | 122.0 | 1.06e+17 | 5.32 | |
| 32 | 2007.127 | 93.3 | 77.9 | 127.7 | 1.11e+17 | 5.33 | |
| 33 | 2007.198 | 95.1 | 71.2 | 70.7 | 6.12e+16 | 5.16 | |
| 34 | 2007.279 | 95.2 | 81.2 | 162.7 | 1.41e+17 | 5.40 | |
| 35 | 2008.011 | 94.9 | 96.8 | 159.4 | 1.38e+17 | 5.39 | |
| 36 | 2008.126 | 75.8 | 115.7 | 124.6 | 1.08e+17 | 5.32 | |
| 37 | 2008.254 | 91.3 | 126.8 | 175.1 | 1.52e+17 | 5.42 | |
| 38 | 2008.353 | 88.1 | 98.9 | 134.8 | 1.17e+17 | 5.34 | |
| 39 | 2009.052 | 78.5 | 65.1 | 59.8 | 5.18e+16 | 5.11 | |
| 40 | 2009.105 | 96.8 | 52.9 | 147.1 | 1.27e+17 | 5.37 | |
| 41 | 2009.165 | 90.0 | 60.2 | 128.6 | 1.11e+17 | 5.33 | |
| 42 | 2009.222 | 82.3 | 56.8 | 84.5 | 7.33e+16 | 5.21 | |
| 43 | 2009.271 | 93.6 | 49.3 | 173.1 | 1.50e+17 | 5.42 | M7.9 Wenchuan |
| 44 | 2009.307 | 77.9 | 35.9 | 125.0 | 1.08e+17 | 5.32 | |
| 45 | 2010.020 | 78.6 | 78.9 | 109.1 | 9.45e+16 | 5.28 | |
| 46 | 2010.076 | 83.4 | 55.9 | 88.5 | 7.67e+16 | 5.22 | |
| 47 | 2010.181 | 79.9 | 105.2 | 49.1 | 4.25e+16 | 5.05 | |
| 48 | 2010.246 | 93.2 | 64.1 | 114.3 | 9.90e+16 | 5.30 | |
| 49 | 2010.302 | 63.4 | 57.0 | 47.8 | 4.14e+16 | 5.04 | |
| 50 | 2010.362 | 91.9 | 59.6 | 103.8 | 9.00e+16 | 5.27 | |
| 51 | 2011.030 | 78.6 | 32.6 | 97.2 | 8.42e+16 | 5.25 | |
| 52 | 2011.070 | 84.5 | 40.1 | 77.1 | 6.68e+16 | 5.18 | M9 Japan |

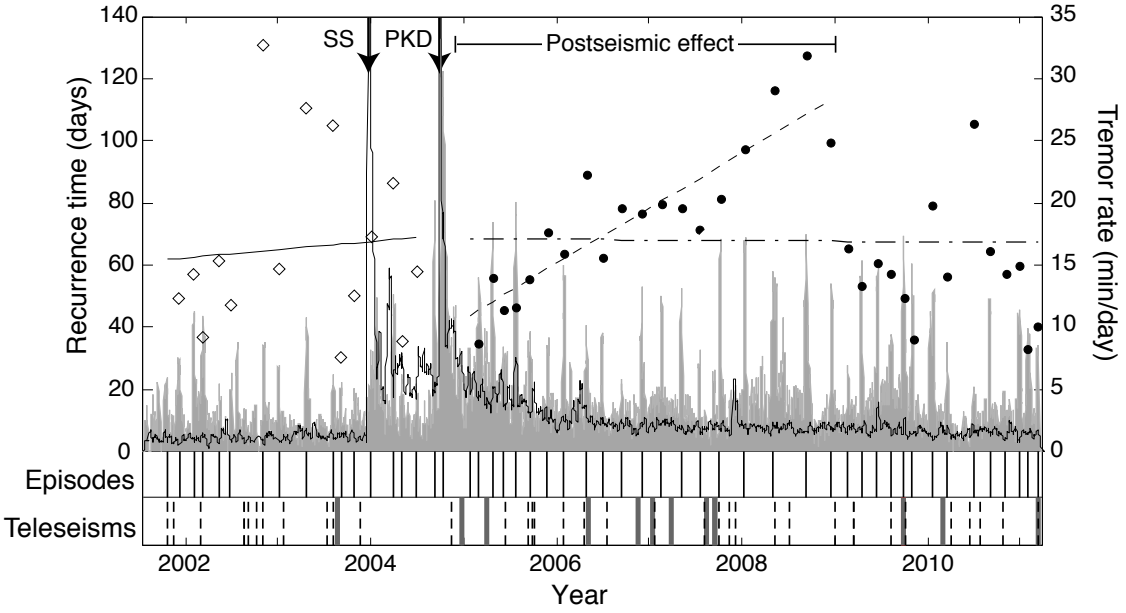


Figure 7.5: Recurrence times of the tremor episodes before (open diamond) and after (black dots) the 2004 Parkfield earthquake. Tremors and earthquake activities are shown (see Figure 1). M7.5 to M8 teleseisms from the ANSS catalog (dashed lines) and the M8+ earthquakes (thick lines) are compared to the episodes times (continuous lines). Linear trends of the recurrence times are added before the 2004 mainshock (solid), after Parkfield until 2009 (dashed), after Parkfield (dashed dotted).

pattern (Figure 7.5).

However, the 2004 Parkfield earthquake strongly modified the recurrence times of the episodes as they first happen more frequently, with recurrence times shorter than 60 days (Figure 7.5). Later, the episodes' repeat times progressively lengthen with a rate of $\sim 17.5$ days/year until 2009 (Figure 7.5). Afterwards, the episode recurrence times significantly decrease, averaging to about 58 days. The average time interval is relatively close to the average recurrence time noticed before the Parkfield earthquake (i.e. 66 days). In addition, tremor bursts during this later period show an increased variability in their repeat times, ranging between 35 and 105 days (Figure 7.5), similar to what was observed prior to the 2004 mainshock.

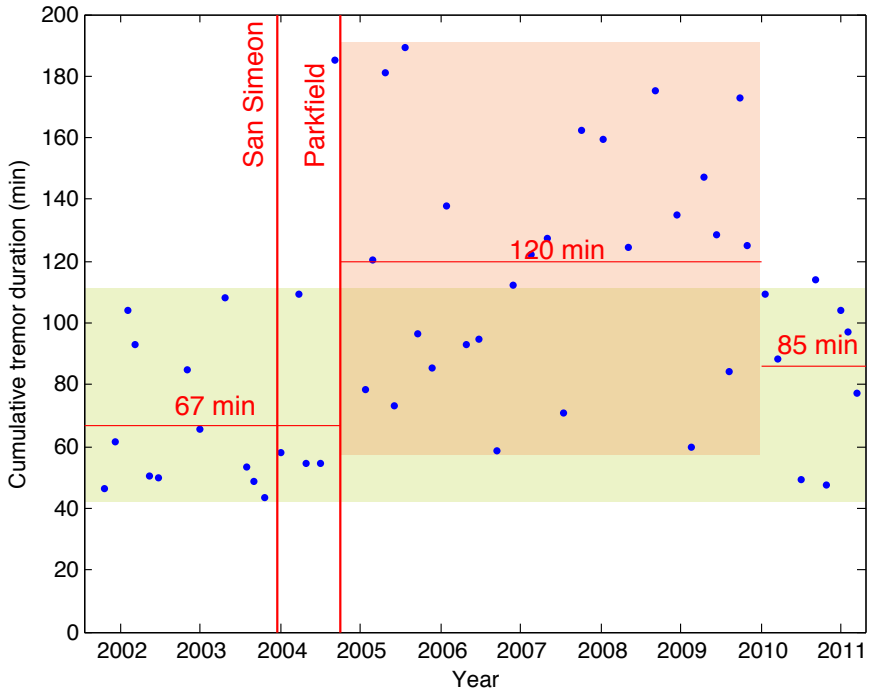


Figure 7.6: Cumulative duration of tremor activity in minutes during episodes (10 day periods). The shaded green area shows the amplitude range before the 2004 Parkfield earthquake. The red area indicates amplitude range of tremor episodes in the post-Parkfield earthquake period.

### 7.4.3 Episode durations

Though not true for all the individual episodes, there is a general tendency for the episodic activity to reach a maximum within about 3 to 4 days of episode initiation and to decay to background over $\sim$ 5 to 6 days from maximum (Figure 7.4a). Because of this observation we focus on the cumulative duration of tremors in minutes recorded during 10 days of NVT activity centered on the peaks.

Figure 7.6 shows that a significant increase in the episode durations occurred in late 2004, after the Parkfield earthquake. The average cumulative duration of the episodes increased by a factor of 1.79 after September 2004, from about 67 minutes to 120 minutes, before the 2004 mainshock and between 2005 and 2010, respectively. Without considering the fore-tremor episode, which corresponds to the only pre-Parkfield episode that exceeds the trend, the recorded maximum amplitude is 109 minutes between 2001 and the 2004 mainshock, and it increases to 189 minutes following the Parkfield earthquake in 2005. This shows that similar

to the recurrence times, the amplitudes of the peaks change over time.

In addition, durations of the bursts become noticeably smaller after 2010. In the late NVT catalog, an average of only 85 minutes of tremors per episode is reported. These late catalog's episode durations are similar to those observed in the pre-2004 Parkfield earthquake period (green shade in Figure 7.6).

The change in the cumulative duration of the bursts also coincides approximately in time with the variations in their recurrence times (i.e. irregular, quasi-periodic, and irregular again). It is important to point out that these episode duration estimates are conservative estimates in that they represent only the portion of activity that exceed the threshold criteria outlined earlier. Nonetheless, it indicates that the tremors near Parkfield that compose the episodes behave in at least two different ways during the nearly 10-year history of recorded tremor activity in central California: one that is directly related to the Parkfield earthquake and another one that is more representative of the long-term activity of the SAF.

## 7.5 Spatial distribution of NVT episodes

Understanding where the episodic NVTs originate helps identify different tremor source regions, and as a consequence, different properties along and across the deep SAF in central California. We analyze the episodic behavior in multiple sub-regions and then compare the spatial and temporal activity of the NVT and LFE catalogs to identify LFE families that follow episodic patterns that are similar to the NVTs. The superior LFE locations helps to better resolve the distribution of the episodic component of NVTs and their possible association with a deep slow-slip zone.

### 7.5.1 Location of episodic component of NVTs

We used the well located tremors (see Chapter 5) to resolve the general distribution of episodic and non-episodic tremors in the Parkfield-Cholame region. The 95% uncertainty bounds for these tremors in the horizontal direction are $\pm$ 4.7 km and $\pm$ 4.5 km in the depth direction. Approximately 94% of the well located tremors occurring in the region occurred near Cholame while the remainder occurred primarily to the north, on the SAF near Monarch Peak (Figure 7.2). Nadeau and Guilhem [2009] found increased rates of tremor activity following the Parkfield mainshock in both areas. However, unlike NVT in the Cholame area, the Monarch Peak tremors do not exhibit strong episodic behavior (Figure 7.7a). In the Cholame area, on the other hand, episodic NVT bursts are clearly apparent (Figure 7.7b). In addition, the episodic NVT behavior is significantly stronger among NVTs occurring on the western side of the SAF, even when taking into account the $\sim$ 4.7 km location uncertainties (Figure 7.7b). Zhang et al. [2010] also observed this difference after locating

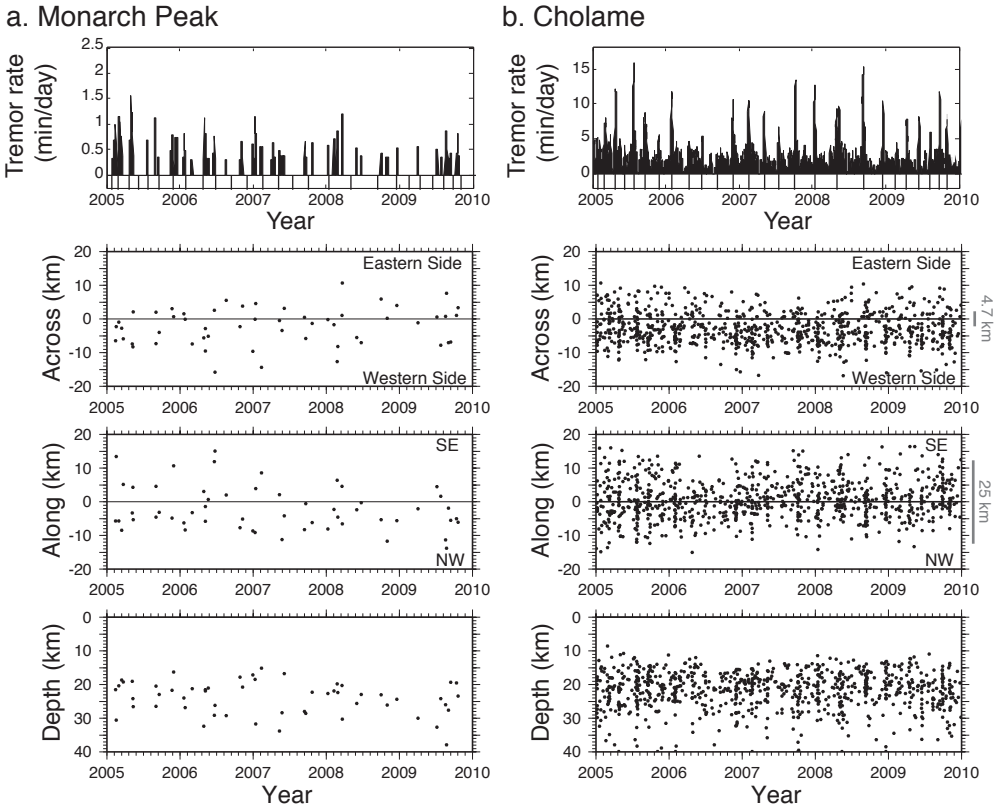


Figure 7.7: Temporal and spatial distribution of the tremor activity and episodes between 2005 and 2009 (across the SAF, along the SAF, and at depth). a) in the Monarch Peak region. b) in the Cholame region. The episodes are mainly on the western side of the SAF in the Cholame region and distributed at depths between 15 and 30 km. 4.7 km corresponds to the average uncertainty in the locations of NVTs.

the NVTs using an advanced station-pair double-difference relocation method which reduced horizontal uncertainties to between 1.7 and 3.7 km.

### 7.5.2 Comparison with episodic LFEs

As mentioned above, LFEs are strongly associated with the intense 3 to 21 minute bursts of NVT activity. The distribution of NVT and LFE are also similarly located in the Monarch Peak and Cholame areas (Figure 7.2). Many LFE families behave periodically and with periodicities similar to those of the NVT episodes, though this may in part be due to the fact that the LFE templates were derived from a catalog of NVT bursts.. Location uncertainties

of the LFE families are significantly lower than those of the NVTs. In order to better constrain the source region of the episodic component of the NVTs, we compared the timing of the NVT episodes with the timing of episodes of 88 LFE families between 2005 and 2010 [Shelly and Hardebeck, 2010]. To obtain a measure of the degree of LFE episodic behavior correlated with tremor episodes, $\beta$, of each LFE family similar to the one observed in the NVT catalog, we use the following equation where $n$ represents the number of episodes considered, $\lambda_{bef}$ the cumulative rate of LFEs occurring over 15-day periods prior to the NVT episode times, and $\lambda_{ep}$ the cumulative rate occurring during the 15 days centered on the episode times:

$$\beta = \frac{\sum_{i=1}^{n} (\lambda_{ep} - \lambda_{bef})}{\sum_{i=1}^{n} (\lambda_{ep} + \lambda_{bef})} \times n^{-1} \tag{7.1}$$

There is no overlap of the two periods of time. We conservatively choose periods of 15 days instead of 10 days to evaluate the temporal behavior of LFEs. A value close to 1 is obtained when the LFE families have a larger number of events during the NVT episodes than before, which indicates that LFEs follow a similar trend that is observed for tremors episodes. Inversely, a value of 0 and lower indicates that LFEs of a given family do not demonstrate the same episodic evolution, if any, because of an equal or higher number of LFEs before the reported episodes (Figures 7.2 and 7.8). The $\beta$ coefficient does not, however, reject the possibility that other periodicities exist for other families that have a negative $\beta$ value, which might reflect other processes taking place.

We find that the $\beta$ coefficient of the LFE families is low in the Monarch Peak area, but is strikingly high for many of the families in the Cholame area (Figures 7.2 and 7.8). In addition, a distinct contrast exists between those families that are on the southwestern side of the SAF, where $\beta$ is high, and those on the northeastern side of the fault, where $\beta$ is low (Figures 7.2 and 7.8), indicating that different processes are occurring across the SAF in this area. This comparison lends additional support to the findings of Nadeau and Guilhem [2009] and Zhang et al. [2010] that the episodic NVTs have a preferred location within a 20-25 km long zone parallel to and on the southwest side of the SAF. These results suggest further that this southwest zone may reflect a fairly narrow throughgoing fault plane that experiences coherent episodic deformation (i.e., slow-slip) over a 20-25 km long fault segment over the time scale of a typical NVT episode (i.e., $\sim$ 10 days). Shelly and Johnson [2011] claim that LFE activity patterns vary markedly depending on depth. From our results with the $\beta$ values, this is arguable because we observe that LFE families located at comparable depths within this area exhibit different $\beta$ degrees (Figure 7.2). The episodic behavior of the NVTs, however, does not vary significantly with depth (between 15 and 30 km) (Figures 7.7 and 7.2). From this, we propose that the zone of episodic NVT represents a fault patch of recurring slow-slip events (SSEs) that is 25 km in along strike dimension and with a depth dimension comparable to the depth range of observable tremor ($\sim$ 15 km).

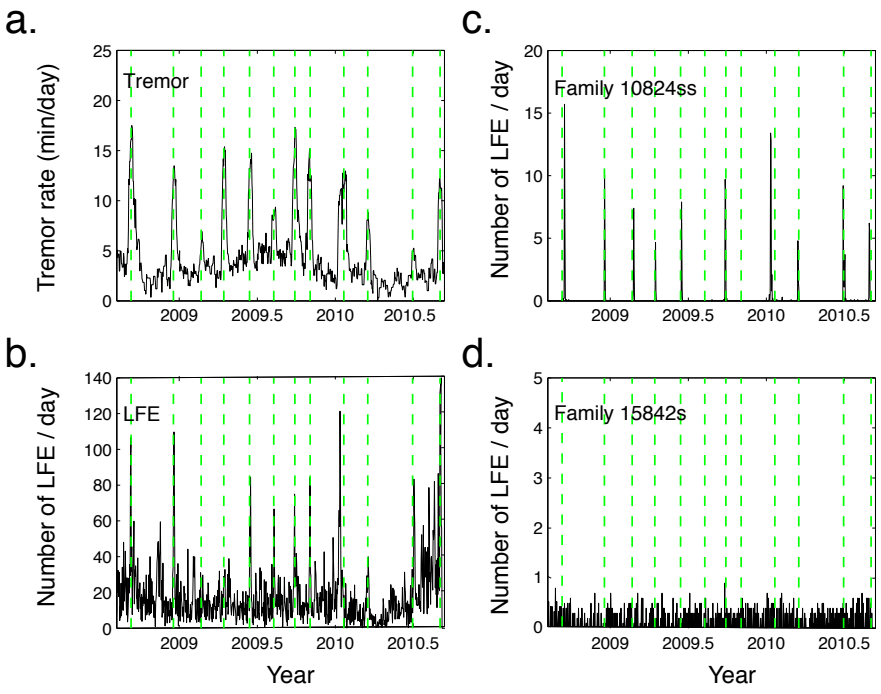


Figure 7.8: Comparison of the tremor catalog with the catalog of 88 LFEs families [Shelly and Hardebeck, 2010 between 2008.6 and 2010.6. a) Tremor catalog (black) smoothed using a 10-day window. Episode times shown by dashed lines and are the same for panels a)-d). b) LFE catalog regrouping 88 LFE families smoothed using a 10-day window. c) LFEs of Family 10824ss located on the western Cholame side smoothed using a 10 day window ($\beta = 0.9$). d) LFEs of Family 15842s located on the eastern Cholame side smoothed using a 10 day window ($\beta = 0$).

## 7.6 Source study of the SSEs illuminated by episodic tremors

### 7.6.1 NVTs: unique in-situ indicator of slow slip events

Even if the surface waves of large regional and teleseismic earthquakes have triggered NVTs in California [Gomberg et al., 2008; Guilhem et al., 2010; Peng et al., 2009] and local moderate earthquakes have been found to strongly modulate the NVT activity [Nadeau and Guilhem, 2009], no consistent direct correlations are observed between the NVT episodes and the occurrence of large teleseismic earthquakes (Figure 7.5), indicating that NVT episodes are indicators of a relatively local process occurring at depth along the SAF. Also, contrary to subduction zones, no deep SSE in the tremor zone has yet been observed using geodetic data in the vicinity of Parkfield, though possible triggering of prolonged fault creep from distant earthquakes has been suggested as a possible explanation for the triggering of delayed tremors [Shelly et al., 2011]. Analysis of the time series of two borehole strainmeters in the area of the Cholame tremors revealed no particular strain change indicating slow slip events [Johnston et al., 2006]. The minimum magnitude of the slow slip events at the depth of the tremors in order to be observable on strain records was estimated to be above 3, and later above 5 [Johnston et al., 2006; Smith and Gomberg, 2009].

The lack of observation however does not rule-out possible SSE events along the SAF. NVTs and LFEs have been shown and/or proposed to correspond to deep slips that migrate along both subduction zones and the SAF [Obara, 2002; Shelly et al., 2009; Shelly and Johnson, 2011]. On contrary, the episodic behavior reported in the previous sections suggests that slips happen at depth, near Cholame, similar to observed in other regions, and indicates that NVT and LFE detections represent so far the unique means toward detecting such events in the vicinity of Parkfield. Also, in the previous section, we have determined that the location of the episodic tremors as well as of episodic families of LFEs gives some indication regarding the dimensions of the source zone of deep SSEs (i.e. about 25 km by 15 km).

In the section below we discuss on the consistency of the characteristics of the SSEs in terms of seismic moment ($Mo$), area ($A$), and displacement ($d$) parameters. We also explore the validity of our $A$ estimate using independently derived values for SSE $Mo$ and slip ($d$).

### 7.6.2 Seismic moment estimates for episodic SSEs

Aguiar et al. [2009] proposed a linear scaling relationship between the moment release of slow-slip events and the total duration of tremor throughout Cascadia. They also suggested that due to the similarity of NVT characteristics in all tectonic settings (including the SAF) that their scaling relationship may be more generally applicable. Obara et al. [2010] used the relationship to qualitatively discriminate the size of tremor bursts in Japan, and we apply it

here to the SAF tremor episodes to evaluate its viability for estimating the seismic moment *Mo* of our episodic SSE zone. Fundamentally, the Aguiar et al. [2009] relationship is based on the calibration of geodetic moment release (*Mo* in Nm) with the cumulative duration of observed tremor activity (*TD* in hour) during distinct episodic tremor and slip (ETS) events in Cascadia:

$$Mo = TD * 5.2(\pm 0.4) \times 10^{16} \tag{7.2}$$

We adhere to their usage by considering cumulative tremor durations for distinct NVT episodes only (i.e., ignoring ambient NVT). Using Equation 7.2 and Equation 7.3, which is:

$$M_w = \frac{2}{3} log_{10}\left(M_0 \times 10^7\right) - 10.7 \tag{7.3}$$

the variation among the cumulative durations of 51 of the 52 NVT episodes (Figure 7.6) leads to variations in their moment magnitudes ($M_w$) that range from 5.0 to 5.4. For the remaining episode, associated most closely with the Parkfield mainshock $M_w$ is 5.6. The cumulative $M_w$ for *Mo* computed for all 52 episodes is 6.4. In the section below that focuses on the consistency of SSE *Mo*, *A* and *d* estimates, we explore in more detail the legitimacy of using the Aguiar et al. [2009] relationship (Equation 7.2) for the SAF NVT.

### 7.6.3 Estimate of cumulative slip on the SSE zone

To date, no estimates of transient sub-seismogenic zone slip associated with any of our SSE episodes exists in the Parkfield region. Resolving the relatively small slips expected for these events on a near-vertical SAF at more than 15 km depth has proven difficult and requires numerous modeling assumptions and data corrections. Longer-term average rates, however, have been estimated for the NVT zone using both geologic and geodetic measurements, and such information can be used to help constrain estimates of cumulative slip occurring on the SSE zone through time. Geodetic studies in this area estimate long-term sub-seismogenic zone (i.e., below $\sim$ 14 km) slip rates to be $\sim$ 33 mm/yr. Also, when modeling slip in the overlying seismogenic zone slip rates at these depths are typically assumed to be constant [Murray and Langbein, 2006; Murray et al., 2001]. This is true independently of the existence of locked zones or the occurrence of larger earthquakes (e.g., M6) in the overlying seismogenic zone. This assumption implies a complete decoupling of slip between the seismogenic and sub-seismogenic zones and that slip transients in either zone have essentially no impact on the slip behavior of the other. However, a transient increase of extended duration in tremor activity and a reduction in seismic velocities from ambient noise measurements that initiated at the time of the 2004 Parkfield earthquake are clearly apparent, and are indicative of post-seismic stress relaxation by creep in the sub-seismognic NVT zone (Figure 7.1; Brenguier et al. [2008]; Nadeau and Guilhem [2009]; Shelly and Hardebeck [2010]; Shelly and Johnson [2011]).

During our study period, a transient like the Parkfield earthquake is likely to increase the rate of sub-seismogenic zone creep in a manner commonly observed for creeping fault adjacent to larger earthquakes. Consider, for example, the behavior of fault creep inferred from REQs along the central SAF [Nadeau and McEvilly, 2004]. In the creeping section at roughly 50 km northwest of the Parkfield rupture (yellow in Figure 7.2), REQ creep rates averaged over a 27.333 year period (1984-April 2011) are $\sim$ 32.8 mm/yr (comparable to the long-term geodetic rate for the SAF of 33 mm/yr), and REQ rates averaged over our NVT study period are only slightly higher, $\sim$ 36.2 mm/yr. The pattern of accumulated slip through time also fails to show a significant increase associated the Parkfield mainshock at this distance (yellow in Figure 7.9). However, further to the southeast at an intermediate distance from the mainshock, $\sim$ 27 km (green in Figure 7.2) the Parkfield transient effect becomes more apparent (Figure 7.9). Here the averaged REQ rate is 33.5 mm/yr over the 27.333 year period, again comparable to the long-term geodetic rate. However, average rates over the study period are larger, $\sim$ 42.1 mm/yr. Furthermore, the pattern of accumulated slip through time shows a notable transient increase associated with the Parkfield event, similar to that seen in the NVT episode response from tremor duration (green and black, respectively in Figure 7.9). Further southeast in the coseismic segment surrounding the northern extent of the Parkfield mainshock rupture (purple in Figure 7.2), 27.333 year averaged rates are again comparable to the long-term rates (i.e., $\sim$ 31.2 mm/yr), but average rates over the study period increase even further to $\sim$ 60.7 mm/yr. Furthermore, the pattern of accumulated slip through time shows a significantly more pronounced transient increase at the time of the Parkfield mainshock (purple in Figure 7.9).

In addition to increases in the study period rates with proximity to the Parkfield rupture, decreases in rates during the pre-mainshock study period with proximity to the mainshock are observed (i.e., 35.6 mm/yr, 26.5 mm/yr, and 15.1 mm/yr for the creeping, intermediate and co-seismic segments, respectively). These diminished pre-event rates coupled with the increased post-event rates are indicative of a deficit accumulation and release process for creeping faults associated with the Parkfield mainshock.

The along strike REQ observations serve to illustrate the evolution of this process as a function of distance from the mainshock within the seismogenic zone and are most likely a function of both the geometry and rheology of the creeping, seismogenic SAF in response the Parkfield event.

This distance dependent response is likely to differ from that of the episodic NVT zone, due to its contrasting geometry and rheologic properties. Instead we propose that for the study period, the portion of the creeping SAF whose slip response to Parkfield (i.e., NW zone in Figures 7.2 and 7.9) mimics the response observed in the episodic NVT zone can serve as a first order estimate of the slip response (in a relative sense) of the episodic NVT zone through time. Furthermore, because both the creeping SAF seismogenic and sub-seismogenic (i.e.

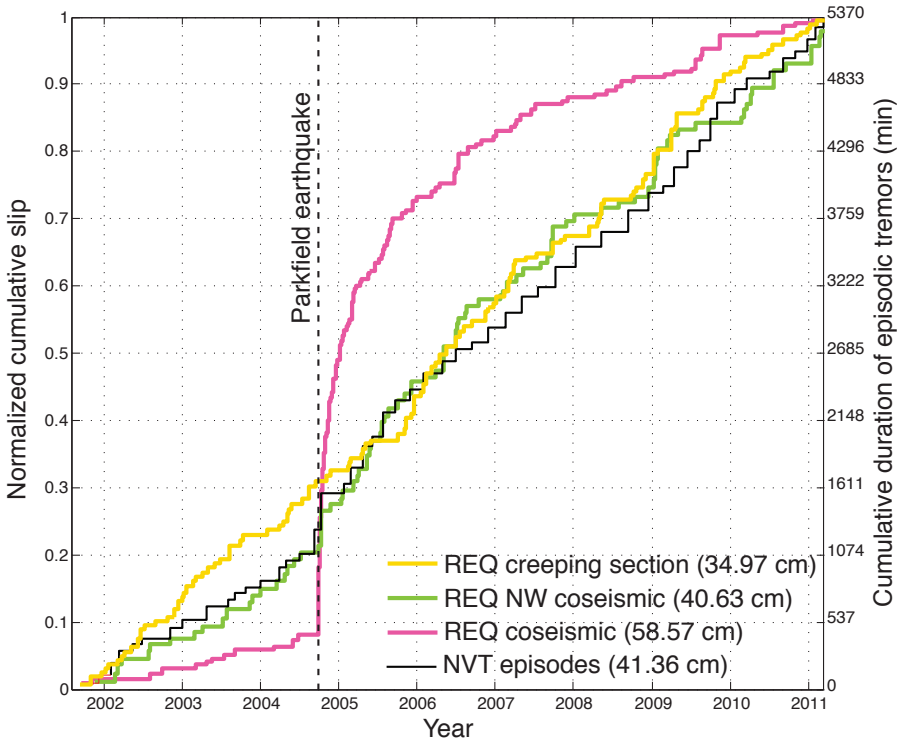


Figure 7.9: Normalized cumulative displacement of the repeating earthquakes (REQ) detected in the Parkfield region and of the episodic tremors since 2001.6. The colors of the REQs correspond to the colors of their symbols in Figure 7.2. The numbers in parentheses correspond to the maximum cumulative slips inferred for each group.

NVT zone) zones slip at comparable long-terms rates, we additionally propose that over the 9.65 year study period the cumulative slip in both regions will be comparable in an absolute sense. Because a clear Parkfield related transient is apparent in the NVT signature, we consider this to provide a more accurate estimate of slip in the SSE zone during our study period than using the average long-term rated estimate of 33 mm/yr. This assumes that the throughgoing structure of correlated NVT and LFE episodicity represents the primary slip surface of the SAF in the episodic NVT zone.

Based on this supposition, $\sim$ 40.63 cm of cumulative slip occurred in the episodic NVT zone during the study period. Over the same period, 5369 minutes of cumulative NVT activity was detected during the 52 episodes. Based on these values, and irrespective of the size of the episode generating zone, the average number of minutes of episodic activity per cm of slip ($R_{epi}$) is $\sim$ 132 min/cm. For comparison, if the estimated long-term rate of 33 mm/yr were used, $R_{epi}$ would be $\sim$ 163 min/cm.

Departures from $R_{epi} = 132$ min/cm occur through time. For example $R_{epi}$ calculated for the pre-mainshock period ($\sim$ 3.17 years) is $\sim$ 151 min/cm while that for the post-mainshock period ($\sim$ 6.48 years) is only $\sim$ 127 min/cm. These departures arise primarily from differences in the secondary features of the REQ slip and episode accumulation histories. Such differences are not unexpected given the large difference in location of the REQ and NVT zones and the likely involvment of secondary, more localized processes. Inherent differences in the sampling times and temporal resolution of the REQ and NVT datasets also contribute to the second order departures, particularly on short time scales. For these reasons and because variations in area $A$ among the individual SSEs are not accounted for, we limit our use of $R_{epi}$ to calculations involving cumulative slip over the entire study period only, and infer slips for the individual SSEs from their $Mo$ and $A$ estimates.

### 7.6.4 Self-consistency of $Mo$, $A$ and cumulative $d$ estimates

Following Smith and Gomberg [2009], we consider a SSE to be a shear dislocation on a plane and that the moment release of the SSE ($Mo$) can be related to its source process by the equation:

$$Mo = \mu A d \tag{7.4}$$

where $\mu$ is the shear modulus of the surrounding fault material (30 GPa), $A$ is the area of the slow-slip plane, and $d$ is the average slip on area $A$ during the SSE.

Given our independent estimates of $Mo$ from Equation 7.2 (Table 7.1), slip area ($A$ = 25 km x 15 km) from our episodicity analysis and a cumulative slip of $\sum$d = 40.63 cm on $A$ over the study period (from REQs in the NW zone) we can evaluate the consistency of these parameter estimates. Taking our estimates of $A$ and the average $Mo$ and slip (d = $\sum$d

/52) of the episodes, Equation 7.4 can be used to derive any one of these three parameters from estimates of the other two. Comparison of these derived parameters with the original parameter estimates shows agreement to within $\sim$ 2 % (Table 7.2). This rather surprising result indicates that on average our estimates of $Mo$, $A$, and cumulative $d$ are internally consistent in the context of the SSE model in Equation 7.4. It also lends support to the suggestion of Aguiar et al. [2009], that their moment duration scaling (Equation 7.2) may be applicable in a variety of tectonic settings, including the SAF.

Table 7.2: Comparison of derived SSE parameters with their original estimates. In orange are the parameters calculated from observations. We use an average tremor duration of 103.2 min, Equation 7.2 to derive the seismic moment ($Mo$), an area of 25 km by 15 km (375 km$^2$), and the total displacement from REQs in the NW zone of 40.63 cm (or 0.781 mm per episode). This gives only a difference on the order of 2% between the measurements.

| | Mo - A | Mo - d | A - d |
|---|---|---|---|
| Mo (Nm) | 8.944e+16 | 8.944e+16 | 8.790e+16 |
| A (km$^2$) | 375 | 382 | 375 |
| d (cm) | 0.795 | 0.781 | 0.781 |
| Mw | 5.23 | 5.23 | 5.23 |

With the exception of the derived $A$ value, these calculations assume a constant slip area among the SSEs. However, the along-strike and depth distributions of the individual NVT episodes (Figure 7.7b) suggest that this is not the case. It is difficult to gauge the variability in $A$ from the locations of the individual sequences alone, due to the combined effect of location uncertainty and the relatively few well resolved locations for individual episodes (generally less than 20). Instead to gage $A$'s variability, we make an assumption similar to that of Smith and Gomberg [2009], that the stress drop ($\Delta\sigma$) among the SSEs is essentially constant. We depart, however, from Smith and Gomberg [2009] in that we make no a priori assumption as to an earthquake-like value for $\Delta\sigma$, nor to the constant value of the slip to rupture dimension ratio ($C$) that it implies. Instead, we derive $C$ empirically using Equation 7.4, our observations of cumulative $Mo$ and $d$, and a generalized model of Kanamori and Anderson (1975) relating $\Delta\sigma$ to $d$ and $A$:

$$\Delta\sigma = \frac{qd}{\sqrt{A}} \tag{7.5}$$

where $q$ depends on the geometry of the rupture and the value of $\mu$.

The assumption of a constant $\Delta\sigma$ for the repeating NVT episodes seems reasonable. Their similar location and distribution among repeated ruptures of the same fault (Figure 7.7) suggest that differences in $\mu$ and in rupture geometries among the episodes are relatively small, and their limited range in size ($\leq$ 0.6 Mw) implies that differences associated with $\Delta\sigma$ scaling (if it exists) is likely to be relatively minor. Based on this hypothesis, Equation 7.5 can be rewritten in the form:

$$C = \frac{d}{\sqrt{A}} \tag{7.6}$$

where $C$ is a constant of proportionality relating slip in a SSE to its area of rupture. Combining this equation with Equation 7.4, one can express the $Mo$ of a SSE in terms of its average slip, $d$ as:

$$Mo = \frac{\mu d^3}{C^2} \tag{7.7}$$

A robust solution for $C$ can be obtained by solving for $C$ in Equation 7.7 using cumulative estimates of $Mo$ ($\sum Mo$) and $d$ ($\sum d$):

$$C = \sqrt{\mu}\left(\frac{\sum d}{\sum (Mo)^{1/3}}\right)^{3/2} \tag{7.8}$$

For the 52 episodes in our study period we find that $\sum Mo^{1/3} = 2.274\times10^7$ and $\sum d = 0.4063$, where units of $Mo$ and $d$ are in units of Nm and m, respectively. This leads to a value of $C = 4.1366 \times 10^{-7}$, which is over 24 times lower than the value of $10^{-5}$ assumed by Smith and Gomberg [2009] that was based on earthquake-like slip to rupture dimension ratios. Our estimate of $C$ also implies a value for $\Delta\sigma \sim 10$ kPa, which is about two orders of magnitude lower than that of regular earthquakes. This is entirely consistent with the constant low-stress drop model for slow earthquakes (including SSEs) proposed by Ide et al. [2007].

With the value $C$, the rupture areas for each episode ($i$) can be estimated from their $Mo_i$ values using a relation derived from Equations 7.4 and 7.6 assuming constant stress drop:

$$A_i = \left(\frac{Mo_i}{\mu C}\right)^{2/3} \tag{7.9}$$

The $A_i$ values derived from Equation 7.9 range from 210 to 751 km$^2$, with the overall distribution centered on 355 km$^2$ (Figure 7.10 and Table 7.1). This corresponds to a value within 5% of our original estimate for the SSE zone area of 375 km$^2$ (i.e. 25 km by 15 km).

Equations 7.4 and 7.6 can also be used to derive an expression relating the average slip of each episode ($i$) $d_i$ from $C$ and $Mo_i$ assuming constant stress drop:

$$d_i = \left(\frac{C^2 Mo_i}{\mu}\right)^{1/3} \tag{7.10}$$

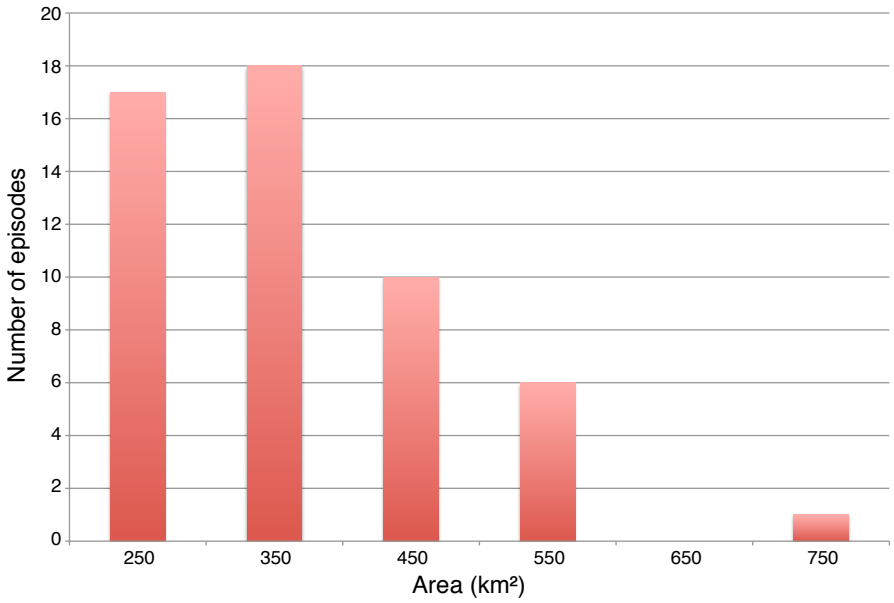


Figure 7.10: Histogram of the distribution of area per episode considering Equation 7.9, Mo from Aguiar et al. [2009], $C$ of 4.1366e-7, $\mu$=30GPa. The distribution is centered in the 300-400 km$^2$ bin, with a median value of 355 km$^2$.

The $d_i$ values derived from Equation 7.10 range from 0.60 to 1.13 cm (Table 7.1) assuming a constant stress drop for the SSEs. Instead, a model that assumes a constant area $A$ of 375 km$^2$:

$$d_i = \left( \frac{Mo_i}{\mu A} \right) \tag{7.11}$$

yields a range in $d_i$ of 0.33 to 2.27 cm. These differences reflect the sensitivity of $d_i$ to the model assumptions. While the cumulative value of $d_i$ over the study period using Equation 7.10 is constrained to be equivalent to our cumulative slip estimate of 40.63 cm cumulative slip, this is not the case for the cumulative $d_i$ value from Equation 7.11. Nonetheless its value is comparable to that using Equation 7.10 (i.e., 41.36 cm). In general, however, we consider the constant stress-drop based models for $A_i$ and $d_i$ (Equations 7.9 and 7.10) to be more appropriate due to the evidence indicating that $A_i$ varies among episodes (Figure 7.7).

### 7.6.5 Consistency with external observations

The source parameters of the SSEs obtained from tremor observations are consistent with external observations in the vicinity of Parkfield as well as with observations in other regions where tremors occur. The empirical relationship derived from ETS in Cascadia by Aguiar et al. [2009] allows us to compare slips inferred from tremor duration to slips from REQ sequences that have been extensively studied [Nadeau and McEvilly, 2004]. We found that they show similar absolute values and temporal patterns prior to and after the 2004 Parkfield earthquake.

Also, our derived values of $C$ and $\Delta\sigma$ may correspond to a more appropriate value for SSE sources than that of Smith and Gomberg [2009], in light of the contrasting rheology of the sub-seismogenic zone. It is also more directly applicable to this region of the SAF, having been derived empirically from locally derived data. The $M_w$ values that we obtained for the SSEs from tremor analysis lie at, or just above the estimated threshold of detectable deep SSE activity in the Parkfield area [Smith and Gomberg, 2009]. Previous efforts to detect slow-slip in the Parkfield area using sensitive borehole strainmeter data were unsuccessful. These efforts focused either on changes occurring over a 2-day period for $\sim 6\%$ of all known tremor bursts (regardless of whether or not they occurred during NVT episodes) [Johnston et al., 2006] or during periods associated with 11 tremor-triggering teleseismic events [Smith and Gomberg, 2009]. These teleseismic events also do not correlate in time with our NVT episodes. It might be possible, therefore, to detect Parkfield NVT episodes geodetically provided the particular timing and source characteristics of these SSE (e.g., dimensions and multi-day durations) are taken into account.

Finally, the stress drops associated with these events either by assuming a constant stress drop of $\sim 10$ kPa (Equation 7.8) or obtained considering subsets of the tremor catalog (Table 7.3 and using Table 9.1 in Lay and Wallace [1995] are low. This is also in agreement with

previous suggestions that stress-drops for SSEs are indeed low, lower than what is observed for regular seismic events [Ide et al., 2007]. Furthermore, a low stress-drop of $\sim$ 1-10 kPa suggests that SSE could often be triggered and possibly generated by stress perturbations of this order. This is consistent with previous results showing that tremors are very sensitive to small stress changes. This has been observed with regional and teleseismic earthquakes transmitting static and/or dynamic stress changes in tremor regions and triggering tremors in central California as well as in other regions where tremors have been found, and also from earth tides [Guilhem et al., 2010; Nadeau and Guilhem, 2009; Peng et al., 2009; Rubinstein et al., 2009; Thomas et al., 2009]

Table 7.3: Average source characteristics of the slow slip events corresponding to NVT episodes.

| | Entire NVT catalog | Before Parkfield | 2005-2009 | After 2009 |
|---|---|---|---|---|
| Average recurrence time (days) | 61 | 61.5 | 71.2 | 66 |
| Average tremor duration (minutes) | 103 | 67.9 | 119.9 | 100.4 |
| Mw | 5.27 | 5.15 | 5.31 | 5.26 |
| Slip (mm) | 5.85 | 5.95 | 6.65 | 6.30 |
| Area ($km^2$) | 510 | 329 | 583 | 459 |
| Length $\times$ width (km) | 25 $\times$ 20.4 | 25 $\times$ 13.2 | 25 $\times$ 23.3 | 25 $\times$ 18.4 |
| Stress drop (kPa) | 5.47 | 8.59 | 4.88 | 6.53 |

## 7.7 Deep SAF slip history

### 7.7.1 Deep slip history

Previously, we found that it was possible to calculate consistent source parameters of the deep SSEs that are revealed by tremor episodes in the Parkfield region by assuming either a constant slip area or a constant stress drop. We found that these estimates are also in agreement with our observation of the location of these episodic tremors and LFEs. These results allow us to further study NVTs in central California for the monitoring of the deep SAF slip in the Cholame region. Figure 7.11 shows the slip rates inferred from the displacements per episode assuming constant stress drop (Equation 7.10) and the recurrence time of the NVT episodes shown in Figure 7.5. 51 of the 52 episodes indicate a slip rate between $\sim$ 20 and $\sim$ 90 mm/yr, with a median slip rate of 43.7 mm/yr. This median value is slightly larger than

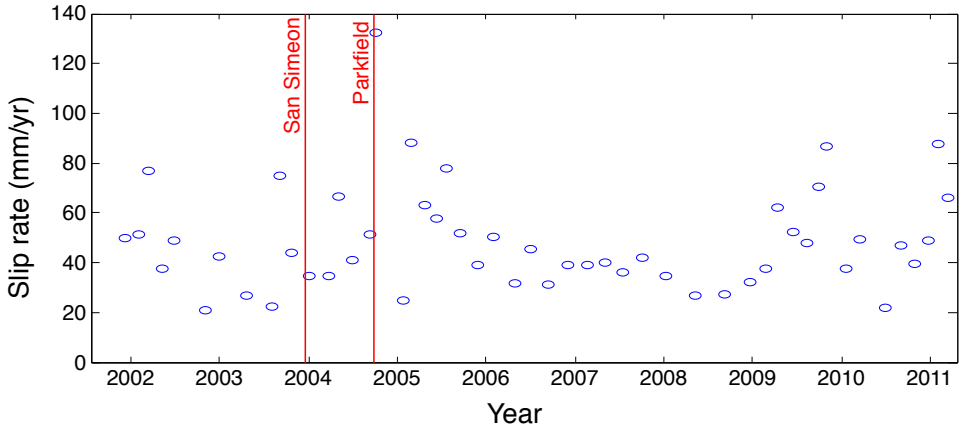


Figure 7.11: Slip rate history per tremor episodes in mm/yr. Obtained assuming a constant stress drop and the resulting slip from 10-day tremor durations over the given preceding recurrence interval.

the geodetic slip rate of the SAF and with slip inferred from REQs during this time period. The largest value is obtained at the time of the 2004 Parkfield earthquake with a slip rate of 132.6 mm/yr.

Interestingly, Figure 7.11 shows that while the slip rate varies significantly between July 2001 and September 2004 when the Parkfield earthquake occurred, it stays remarkably constant between 2006 and 2009 with an average slip rate of 36.7 mm/yr for the two year period. Then after the beginning of 2009, the slip rates return to a variable pattern similar in amplitude to the variations found before the Parkfield earthquake. Also, the slip rates between the 2004 Parkfield earthquake and the beginning of 2009 progressively decrease in a similar way that an aftershock decay (i.e. Omori law). This correlates with our previous observation of the recurrence time between episodes and of the cumulative duration of tremors during episodes (Figures 7.5 and 7.6).

These deep slip events demonstrate that the fault zone below the seismogenic zone does not creep at a constant rate but on contrary slips with a relative stick-slip mechanism similar to the behavior of the upper crust. This emphasizes that tremors occur in a transitional section of the fault, which is not fully creeping, neither fully locked.

### 7.7.2 NVT episodes illuminate postseismic deformation at depth

GPS and InSAR data initially showed that the 2004 M6.0 Parkfield earthquake was followed by a significant dominant afterslip deformation, whose magnitude reached the co-seismic moment magnitude [Johnson et al., 2006; Freed, 2007]. Johnson et al. [2006] found however that the data showed either a deficiency in the afterslip model or a second deformation process contributing to the deformation at later times. Brenguier et al. [2008] compared their observations of seismic velocity changes measured from ambient noise correlations with the NVT activity and concluded that they revealed both co-seismic damage in the shallow fault zone and a deep postseismic relaxation within the SAF zone. Recently, Bruhat et al. [2011] showed that the afterslip interpreted after the 2004 Parkfield earthquake was indeed accompanied by a viscous postseismic deformation in the lower crust. Their models require that the postseismic relaxation over 5 years after the mainshock resulted in a moment release of as much as 200%. In addition, they showed that significant deformation at depth between 20 and 26 km is required for the geodetic data. This is consistent with the tremor depth range even though their analysis does not extend to the Cholame tremor zone and instead it is limited to less than 10 km south of the 2004 Parkfield epicenter along the SAF [Bruhat et al., 2011].

In addition, Lengliné and Marsan [2009] showed that the REQs corresponding to identified asperities within the seismogenic section of the fault are related to different dynamics in response to the M6 earthquake that can be interpreted as differences in stress changes undergone by each asperities. Figure 7.9 shows that this strong change in behavior is not unique to REQ sequences. NVTs illuminate the same deformation at greater depth (i.e. below the seismogenic zone) during the same time period with slight differences however. The contrast in the rates of slip increase of NVTs and REQs in the Cholame area after the earthquake is interpreted as differences in the fault coupling between the seismogenic (brittle) and subseismogenic (transition to ductile) zones. NVTs here directly witness the large-scale postseismic deformation associated with the 2004 Parkfield earthquake that reaches the lower crust / upper mantle area. But since 2009 the return to the NVT activity pre-2004 mainshock suggests that the postseismic deformation associated with the Parkfield earthquake has no longer a significant effect in the tremor region, and that the SAF has entered an interseismic period, in which the stressing rate at depth is linked to the plate tectonic motion. This shows that similar to REQs, NVT episodes mark the beginning and the end of the triggering postseismic deformation associated with the 2004 Parkfield earthquake and they help better monitor variations of stress at greater depth than regular earthquakes do.

Finally, we found that the emergence of tremor bursts is linked to episodes of stress re-adjustments, due to both coseismic and postseismic perturbations. One can interpolate that, because of the decreasing stressing rate after the Parkfield earthquake, additional time is needed between successive episodes to accumulate the necessary amount of stress leading

to failure and thus to trigger a deep crust deformation. However, the amplitudes of the tremor episodes do not vary accordingly with the recurrence time, indicating that both time-predictable model and slip-predictable model do not fully explain the data.

## 7.8 Discussion and conclusion

### 7.8.1 Creeping zone versus locked zone

We find that the episodic tremors are located in a specific subregion of the known tremor source area in the vicinity of Parkfield. The spatio-temporal NVT activity indicates variations in the fault rheology and mechanics. Obara et al. [2010] found a clear bimodal distribution for all the NVTs in the western Shikoku, Japan where updip tremor activity is mainly composed of major episodic bursts unlike the downdip tremor zone that exhibits more frequent minor bursts. In central California, we do not observed a strong depth-dependency of the NVTs unlike what Shelly and Johnson [2011] presented for LFEs. On the other hand, we notice an along-strike dependency of the tremors (Figure 7.7). This, however, suggests that tremor activity is controlled by modifications in physical fault zone properties similar to what Obara et al. [2010] proposed. The events are located along a portion of the SAF whose strength gradually transitions from purely locked in the south to fully creeping in the north (Figure 7.2). The coupling strength near Cholame where stick-slip tremors (i.e. episodes or slow slips) are observed is greater than near Monarch Peak, where tremor activity is reduced and preferentially steady. Finally, similarly to Japan and to Cascadia we notice a gap in the tremor locations that is visible in both the tremor and LFE catalogs and that is located below the main Parkfield earthquake rupture [Obara et al., 2010; Wech et al., 2009].

### 7.8.2 Fluid circulation

Though the envelope-based locations have limited resolution, the fact that we see adjacent zones in the Cholame region exhibiting distinct temporal behaviors suggests that there is indeed a broad tremor distribution normal to the SAF rather than a confinement to a single narrow fault zone [Shelly et al., 2009]. Gutjahr and Buske [2011] re-processed a reflection profile acquired in 1981 that passed near Cholame and imaged the crust and the uppermost mantle down to approximately 40 km depth. They found a broad zone of high reflectivity located at depths between 20 km to 35 km on the southwest side of the SAF. Most of the tremors are located at the top of the high reflectivity body and below a strong southwest dipping reflector that may be interpreted as the base of the Salinian Batholith. This high reflectivity body could indicate the presence of high-pressurized fluids, and tremors as shear failures on a critically stressed fault zone in the presence of near-lithostatic pore pressure [Gutjahr and Buske, 2011].

Comparable results are obtained by Becken et al. [2011] who recently presented evidence for a deep zone of anomalously low electrical resistivity imaged by magnetotelluric data in the region. They interpreted it as aqueous fluid networks likely to be involved in the generation of deep NVTs located in the adjacent eastern high resistivity zone. Even though the location of this fluid source zone varies laterally between Gutjahr and Buske [2011] and Becken et al. [2011], these two independent studies agree on its position in the western side of the SAF and on its relation to tremor activity.

In addition, the two main tremor sources (Cholame and Monarch Peak) appear to be spatially correlated with pronounced high magnetic anomalies in central California that could be associated with a partially serpentinized ultramafic body in the midcrust containing a significant amount of fluids [Ellsworth, 2008; Griscom and Jachens, 1990; McPhee et al., 2004].

The cluster of episodic tremors between the San Juan Fault and the SAF near Cholame may also give insights on the rheology and fluid circulation at depth. The faults can be interpreted as fluid boundaries. The tremor pulsing that we observe may correspond to the combination of the stress perturbation in the tremor source region due to the nearby M6 earthquakes as well as to periodic increases in the pore pressure in between the two faults that leads to deep slips. This would explain the lack of direct relationship between episode return times and their amplitudes.

### 7.8.3 Conclusion

We find that one third of the tremor activity near Parkfield occur in episodes. The properties of these episodes changed over time both in the cumulative duration of tremor activity and in their recurrence time. We show that they reveal the occurrence of slow slip events occurring at depth after comparing the LFE and the REQ catalogs. Even though Aguiar et al. [2009] relationship was determined using Cascadia ETS events, it is possible to obtain reasonable characteristics regarding the size of the rupture zone that they illuminate, their magnitude range, their associated stress drops, and finally the long-term slip at depth along the SAF. These results open perspectives for further modeling of the SSEs and for a better calibration of strainmeter data analyses. The changes in the behavior of the episodic tremors or slow slips give information on variations in the state of stress in the deep fault zone, which is important to monitor for earthquake hazard in the region where the last major Fort Tejon earthquake originated in 1857 with an estimated magnitude of 8. This event is now overdue with a recurrence time of 140 years $\pm$ 40 years. Finally, this study emphasizes the importance of studying NVTs in the goal of estimating the fault stress regimes and the eventual modifications in the stress level at depth revealing stress concentration or relaxation. They indeed correspond to in-situ slow slip events that give information on sensitive changes in the properties of the fault and that other geophysical techniques have not yet successfully

illuminated.

# Chapter 8

# Testing the Accelerating Moment Release (AMR) Hypothesis in Areas of High Stress

Advisor: Roland Bürgmann
Collaborators: Andrew M. Freed (Purdue University) and Tabrez Ali (University of Wisconsin-Madison)

## 8.1 Introduction

The search for evidence of spatio-temporal interactions between earthquakes is critical for understanding the interseismic evolution of stress in the lithosphere and the associated distribution of earthquakes in space and time. In 1910, the elastic rebound theory by Reid first introduced the relationship between elastic stress accumulated along a fault zone and earthquake occurrence. The recognition that continuous plate motions are primarily accommodated by earthquakes on major faults, which release the accumulated stress since the last mainshock, constitutes the basic premise of earthquake forecasting, especially if one can quantify the slip-deficit accumulation rate, the time since the last earthquakes (or the times between several events), and the slip of a characteristic event. If it were possible to establish from seismicity patterns that stress has reached near-critical levels, it might be possible to improve upon such standard forecasting approaches.

Over the past decades, several retrospective analyses for precursory seismicity patterns, which consider the evolution of seismicity in relation to rising stress levels, have been undertaken. These studies have focused on both simple changes in the rate of seismicity (i.e. quiescence and activation) as well as on more complex spatial and temporal schemes. It has been suggested that significant increases in moment release occurred prior to many large earthquakes of recent times in California, as well as in other regions of the world [Bowman and King, 2001; Bowman et al., 1998; Bufe and Varnes, 1993; Ellsworth et al., 1981; Kanamori, 1981; Lindh, 1990; Sammis et al., 2004; Sykes and Jaumé, 1990]. The Acceler-

ating Moment Release (AMR) hypothesis promoted by Bowman et al. [1998] is based on a simple physical model linking static stress changes in the lithosphere to increases in the rate of smaller sized earthquakes before a mainshock. It was retrospectively demonstrated for all eight M6.5+ earthquakes between 1950 and 1994 in Southern California. If correct, this hypothesis has significant potential for earthquake forecasting as suggested by Jiang and Wu [2005] who performed a systematic search for AMR in China between 1970 and 2003 and reported accelerating seismicity prior to the majority of the 65 studied earthquakes. Mignan [2011] provides a comprehensive review of publications on accelerating seismicity preceding major earthquakes.

However, evidence for AMR in retrospective studies strongly depends on the choice of several parameters such as the magnitude range of earthquakes included in the analysis, the area surrounding the mainshock being considered and the time period prior to a target event [Hardebeck et al., 2008; Jiang and Wu, 2006]. Some AMR studies found that these three variables have to be appropriately scaled with the magnitude of the mainshock [Bowman et al., 1998; Jiang and Wu, 2005; Wang et al., 2004]. Initial AMR studies used a search over circular regions of various radii [Bowman et al., 1998; Jiang and Wu, 2005], while the latest approach has been to consider the critical region of high stress determined with a back-slip dislocation model of the final rupture [Bowman and King, 2001; King and Bowman, 2003; Mignan et al., 2006]. Because the choice of these three variables in the AMR analysis appear to be case-specific (i.e., they are generally optimized to produce AMR for a given historic event), and because the use of the back-slip dislocation model for earthquake forecasting is complicated, since it requires a-priori knowledge of the fault segment(s) that will rupture, both methods (i.e. circular region and back-slip model) have raised doubts about their utility [Hardebeck et al., 2008; Michael et al., 2006]. The published observations of apparent AMR have been suggested to be the result of a data-fitting exercise, in which the search variables were tuned such as to maximize the apparent AMR behavior prior to historic mainshocks [Hardebeck et al., 2008; Michael et al., 2006]. Hardebeck et al. [2008] conclude that apparent observations of AMR in California and Nevada resulted from a combination of data-fitting and the inherent spatiotemporal clustering of earthquakes.

As opposed to previous studies that searched retrospectively for AMR prior to large earthquakes with optimal parameters, we carry out a systematic grid search for AMR in space and time and we compare its results with calculated models of stress accumulation in southern California. If seismicity rates do indeed rise in areas where peak stress increases, and prior to large events, our approach would be the appropriate method to test and implement the AMR concept in earthquake forecasting efforts. To evaluate more directly the underlying concept of enhanced seismicity in areas of high stress and impending large earthquake ruptures, we consider that lithospheric stress evolves dynamically such that stress accumulates because of the tectonic plate motions, is punctuated by the occurrence of earthquakes, and is governed by the elastic and viscous properties of the lithosphere [Freed et al.,

2007]. Thus, we regard a mechanical model of stress evolution over the last two centuries, rather than assuming a complete stress drop on all fault segments surrounding an eventual rupture implied by the back-slip stress lobe method [Bowman and King, 2001]. As mentioned by Bowman and King [2001], the precise definition of regions with increased stress requires modeling the contributions of events over a long period of time. We rigorously evaluate inferred stress levels determined from physical models of southern California stress evolution that incorporate coseismic stress changes from M $>$ 6.5 events since 1812, their corresponding postseismic relaxation in the viscoelastic lower crust and upper mantle, and the interseismic stress accumulation derived from the current surface strain field [Freed et al., 2007]. Even if a time period of 200 years is short with respect to the repeat time intervals of many faults in southern California we believe that a careful analysis of AMR behavior in regions of high stress determined from our calculation is justified as a means towards testing the underlying concepts of statistical physics and mechanical fault interaction. Finally, we evaluate the performance of the AMR approach by focusing on the region of the quasi-regular Parkfield, central California M$\sim$6 earthquakes. Here we consider seismicity spanning the last two earthquake cycles of this well studied rupture sequence.

## 8.2 Data and Method

### 8.2.1 Study area

California is one of the best-studied seismically active regions in the world with both dense seismic and geodetic networks. We study the regional M $\geq$ 4.5 seismicity compiled from the Advanced National Seismic System (ANSS) catalog between 32°N and 37.5°N latitude, for the time period from 1910 to 2010. Because the earthquake catalog of this region in California is large, both in terms of duration and magnitude range of the events, it allows for relatively complete AMR analyses, especially after 1950, as pre-1950 seismicity can reflect major instrumentation and data processing changes [Hardebeck et al., 2008; Toppozada and Branum, 2002]. Five earthquakes with magnitude larger than 7 have been recorded in this time period, the largest one being the M7.5 Kern County earthquake in 1952. Twelve earthquakes are reported in the catalog with a magnitude between 6.5 and 7 (Figure 8.1).

We later focus on the seismicity in the vicinity of the Parkfield segment along the San Andreas Fault (SAF) in central California, which is the site of moderate-size earthquakes of magnitude 6 that have repeated at fairly regular intervals: 1857, 1881, 1901, 1922, 1934, 1966, and 2004. As suggested by Mignan et al. [2007], if seismicity rates vary according to regional stress levels, AMR should be observed during the entire earthquake cycle and not only in the last several years before a mainshock. The long time between large events, often on the order of a century or more, rarely allows for complete observations of seismicity

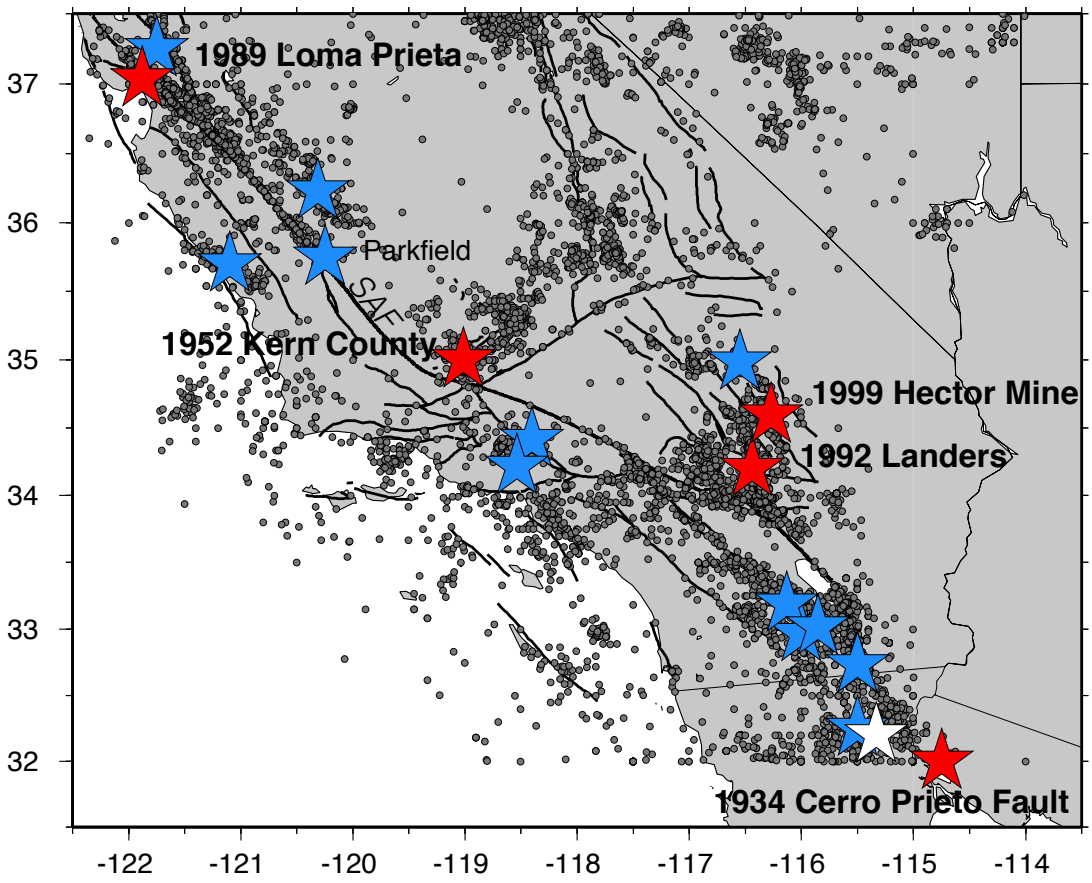


Figure 8.1: Seismicity map of the study area. The earthquakes with M > 3.5 from the ANSS catalog are plotted as small circles. The 6.5≤M≤7 events and M7+ mainshocks between 1910 and 2010 are shown by the blue and red stars respectively. The locations of the Parkfield segment and the M7+ earthquakes are labeled. The white star shows the location of the 2010 M7.2 El Mayor-Cucapah earthquake that is mentioned in the text below.

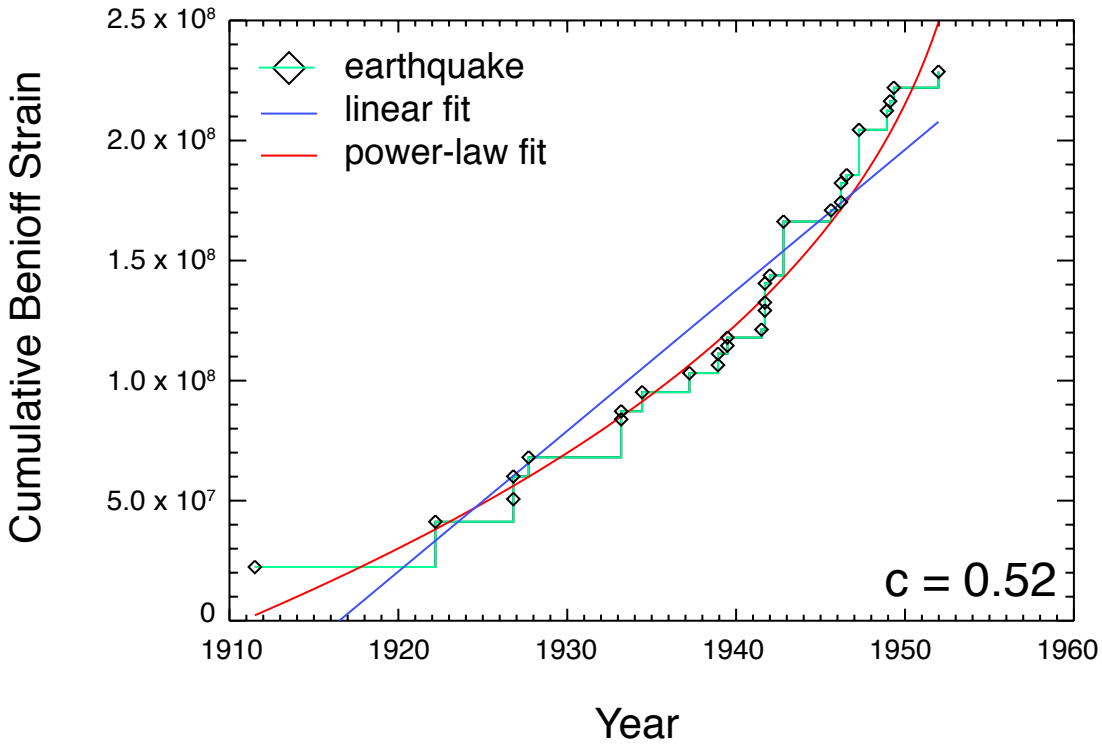


Figure 8.2: AMR search for the 1952 M7.5 Kern County earthquake. The cumulative Benioff strain is the green line, the power law fitting the data is the red curve and the linear fit is the blue line. This AMR calculation uses the identical parameters estimated by Bowman et al. [1998] (i.e. $5.5 \leq M \leq 7.5$ events between 1910 and 1952, within a circular area of 325 km radius about the epicenter).

through an entire earthquake cycle. Thus, the short duration of the earthquake cycle in the Parkfield region provides the opportunity to explore changes in regional seismicity rates over multiple earthquake cycles.

### 8.2.2 Description of the AMR hypothesis

In the AMR hypothesis, changes in seismicity rate are inferred from an increase over time in the slope of the cumulative Benioff strain (cumulative square root of the seismic moment or energy), which represents a measure of the cumulative seismic energy of the earthquakes considered prior to a mainshock [Bowman et al., 1998; King and Bowman, 2003; Mignan et al., 2007]. Figure 8.2 shows an example for the M7.2 Kern County earthquake, where the

observed cumulative Benioff strain:

$$\varepsilon(t) = \sum_{i=1}^{N} \sqrt{E_i(t)} \tag{8.1}$$

is fit by a power law time-to-failure relation [Bowman et al., 1998]:

$$\varepsilon(t) = A + B \cdot (t_c - t)^m \tag{8.2}$$

Here, $N$ is the number of earthquakes considered, $E$ is the energy of individual earthquakes (see below), $t_c$ is the time for which AMR is being evaluated, such as the occurrence time of a large earthquake assuming a retrospective analysis, $A$ is the value of the Benioff strain (including the mainshock) at the time of the earthquake $t_c$, $B$ is a negative fitting constant, and $m$, which determines the curvature of the calculated accelerating moment release curve is often found to be equal to 0.3 [Bufe and Varnes, 1993; Mignan et al., 2006]. The $m$ exponent can also be inverted for to better fit the observed evolution of regional seismicity [Hardebeck et al., 2008]. In our analysis, we use $m = 0.3$ to directly compare our results with previously published work. Based on Kanamori and Anderson [1975] the energy ($E$) of each particular seismic event is defined as a function of their magnitude (M) by:

$$log(E) = 4.8 + 1.5M \tag{8.3}$$

To quantify the AMR, one examines the ratio, called the $c$-value, between the root-mean-square of the best-fit power-law time-to-failure function given above and the root-mean-square of a linear fit to the observed cumulative Benioff strain of the events. If the accelerating power law fits the data better than a linear fit, $c$ will be less than 1. Bowman et al. [1998] defined a successful AMR detection when the $c$-value is less than 0.7, but other studies used threshold values of the $c$ ratio as low as 0.5 [Bowman and King, 2001; Mignan et al., 2006].

In retrospective studies the search for AMR requires several parameters to be specified for each target mainshock. This includes the magnitude range of the earthquakes considered, the size of the search area (e.g., radial distance from a mainshock if we consider a circular search area), and the length of the time period prior to the target earthquake. Different $c$-values are obtained depending on the choice made for the three parameters [Bowman et al., 1998]. In most previous studies the variables were optimized to obtain the lowest $c$-value and as a consequence the most favorable case for AMR at the time of known historic mainshocks (e.g., see example in Figure 8.2). The empirical analyses of AMR found in several regions like in California, in Australia, and in Indonesia preceding the great December 2004 $M_w$9.2 Sumatra earthquake [Bowman et al., 1998; Jiang and Wu, 2005; Wang et al., 2004]

suggest that the optimal region size for best-fitted AMR scales with the magnitude of the target event, but that the scaling may differ from one region to another [Hardebeck et al., 2008; Wang et al., 2004]. However, there is no apparent relation between the duration of the pre-earthquake time period being considered and the magnitude of the mainshock.

As Figure 8.3 shows, using the example of the 1992 Landers earthquake, the choice of the duration of time considered prior to the mainshock (Figure 8.3a) and the magnitude range of the seismicity considered (Figure 8.3b) strongly affect the standard AMR analysis for a given search area. We find that the cumulative Benioff strain can be both better fit by a power-law ($m$=0.3) time-to-failure-function (acceleration of seismicity) when the $c$-values are less than 0.7, and by a linear trend indicating either no clear change in the seismicity rate and/or deceleration of seismicity when $c$-values are larger than 1 (Figure 8.4). We use a minimum number of seven earthquakes to follow Bowman's previously published method in order to calculate the $c$-value. When this number is not reached either because the distance range is not large enough to allow the consideration of more events or because the minimum magnitude is too large for the region, the $c$-value is fixed to 1 as shown in Figure 8.3. Varying the size of the studied region, even by a small percentage, can strongly increase or decrease the number of earthquakes considered as it can include or not major active fault segments and can result in a strong change of the shape of the cumulative Benioff strain curve (Figure 8.4) [Hardebeck et al., 2008]. As demonstrated in Figure 8.3 and by Michael et al. [2006] and Hardebeck et al. [2008], the AMR concept can be interpreted as a data-fitting exercise, since there is no general relationship between the search radius, the magnitude range of the catalog used, and the period of time before the mainshock according to its expected magnitude. Most published retrospective AMR studies determine case-specific optimal parameters that produce an acceleration in the regional seismicity, making it difficult to evaluate any real predictive power of the AMR method [Mignan, 2011].

### 8.2.3 Grid Search application of the AMR method

We perform AMR calculations by extracting events from the ANSS catalog following the systematic approach employed in previous studies [Bowman and King, 2001; Bowman et al., 1998]. We use Nutcracker [http://geology.fullerton.edu/dbowman/Site/Downloads.html], a stress and seismicity analysis software to perform all the AMR calculations [Bowman et al., 1998] and to directly compare our findings with previously published results [Bowman and King, 2001; Bowman et al., 1998; King and Bowman, 2003]. We favor the circular search [Bowman et al., 1998] because it is a general method as opposed to the more specific approach using the back-slip search that requires knowing in advance the location and size of an event [Bowman and King, 2001]. Here, $m$ is fixed to 0.3 and $A$ and $B$ are adjusted to the dataset to better fit it.

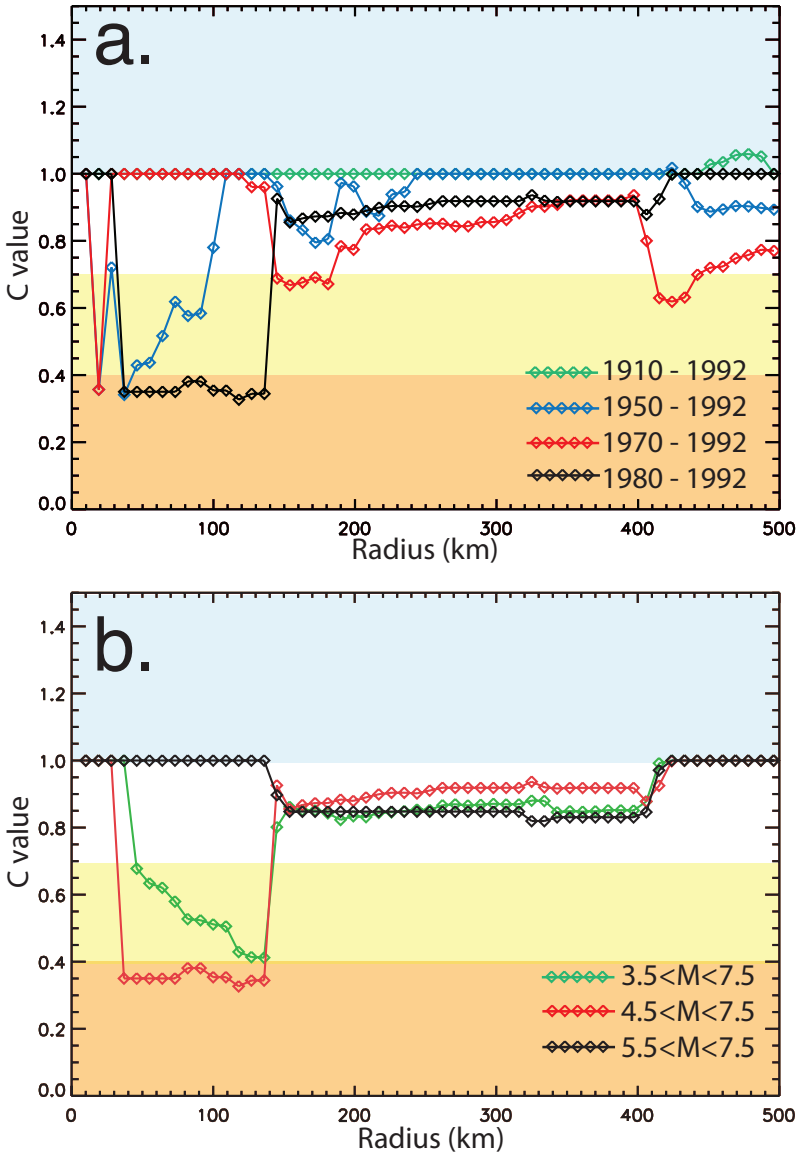


Figure 8.3: Influence of the time period, magnitude range and circular search area on the analysis of AMR prior to the 1992 M 7.4 Landers earthquake. a) Variation of the considered search period while fixing the magnitude range to $4.5 < M < 7.5$. b) Variation of the magnitude range with a fixed pre-mainshock time period of 12 years (1980 to 1992) [Bowman and King, 2003]

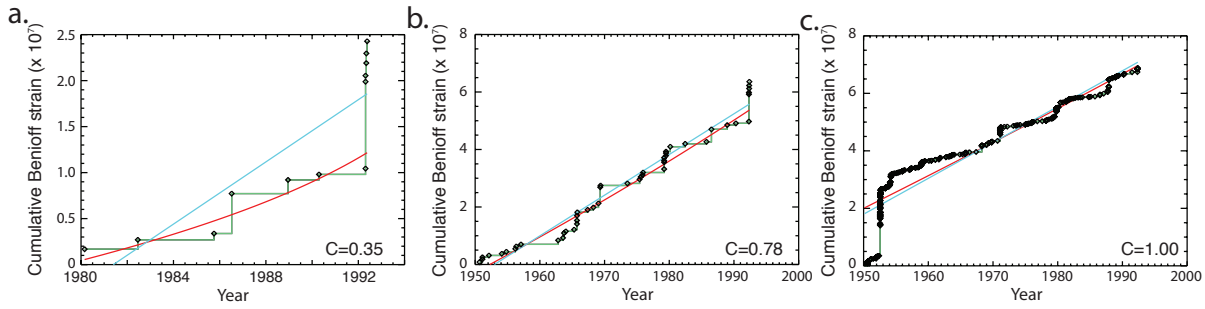


Figure 8.4: Examples of cumulative Benioff strains obtained for the 1992 Landers earthquake (Figure 8.3) exhibiting different behaviors and *c*-values. a) For 1980-1992, M4.5+ earthquakes, and 100 km distance. b) For 1950-1992, M4.5+ earthquakes, and 100 km distance. c) For 1950-1992, M4.5+ earthquakes, and 300 km distance. The Kern County earthquake in 1951 is responsible for the step-like shape of the cumulative Benioff strain in the early time period. In red is the best-fitted power-law trend and in blue the best-fitted linear trend of the cumulative Benioff strain.

Rather than optimizing the size of the region, the temporal search window and other parameters in the power-law relation in a retrospective analysis of AMR around historical earthquake ruptures, we carry out a systematic analysis for AMR throughout southern California at various times. Jiang and Wu [2006] performed a systematic Benioff strain release analysis in China and presented a set of results rather than the best-fitting AMR curves shown by Bowman et al. [1998] using a range of fixed parameters (i.e. 8-yr period, earthquakes with magnitude larger than 3, and three circular areas whose sizes are dependent on the number of pre-shocks for each mainshock) before 65 M6+ earthquakes in China between 1978 and 2003. We follow a similar approach by performing grid search analyses of AMR to evaluate the degree of dependence of the three parameters on the AMR results using a 30-year period of time and three radii for the considered region: 150 km, 200 km and 250 km. We also fix a minimum magnitude for the pre-events of 4.5. A 30-year period does not represent a full earthquake cycle in southern California but it represents an average of the time periods fitted for the series of earthquakes considered by Bowman et al. [1998], the shortest one being only three years for the 1983 Coalinga earthquake and the maximum one being 80 years for the 1989 Loma Prieta mainshock. We later compare the information contained in the AMR maps with maps of modeled coseismic, postseismic and interseismic stress changes over the last century described in the next section [Freed et al., 2007]. Because both AMR and stress-change maps are meant to give us insights on the relative level of stress within the lithosphere, we search for similarities and differences between the two datasets.

### 8.2.4 Stress evolution model

We use the stress evolution model of Freed et al. [2007], which considers historic stress changes over the last 200 years in the San Andreas Fault (SAF) system in southern California, and search for corresponding seismicity rate increases in areas of high crustal stress. The stress evolution is based on contributions of coseismic, postseismic and interseismic processes, governed by the elastic and viscous properties of the lithosphere. The interseismic surface deformation field in southern California is well described by successive geodetic campaigns and increasing number of continuous GPS stations that allow for the modeling and computation of stressing rates in the upper crust across the study area [Freed et al., 2007]. The surface velocities from the Southern California Earthquake Center (SCEC) Crustal Motion Map (http://epicenter.usc.edu/cmm3/) are used for the calculation of the interseismic strain rates and for the interseismic stress rates assuming that accumulated interseismic strains in the upper crust are uniform with depth. In addition, we calculate Coulomb stress changes based on the critical Coulomb failure criterion at 8 km depth on vertical right-lateral strike-slip faults striking parallel to the SAF (N40°W) assuming an effective coefficient of friction of 0.4 [Freed et al., 2007] from all the M6.5+ earthquakes since the 1812 Wrightwood earthquake. Finally, we consider the important contributions of postseismic relaxation processes in time-dependent stress transfer in the last 200 years [Freed et al., 2007]. Deng and Sykes [1997] showed that a significant percentage of 138 magnitude 5+ earthquakes from 1932 and 1995 occurred on faults with Coulomb stress increases from major events and interseismic loading since 1812. Similarly, Freed et al. [2007] found that about 70% of the events since 1812 occurred in regions that experienced Coulomb stress increase. Both interseismic loading and postseismic relaxation generally enhanced the area and magnitude of coseismic stress change contributions [Freed et al., 2007]. Also, they found that the current state of stress is characterized by unrelieved stress increases along the San Bernardino Mountain and Coachella Valley segments of the SAF and the San Jacinto fault zone. Because shallow interseismic fault creep was not incorporated in the models of Freed et al. [2007], the creeping central section of the SAF northwest of Parkfield is modeled as being under apparent high stress. However, creep at rates close to SAF long-term values appears to relax most all strike-slip shear stress in that area [e.g., Ryder and Bürgmann [2008]]. If areas of high stress do indeed experience higher seismicity rates, AMR as an earthquake forecasting method should be evident in these areas.

## 8.3 Results of grid search for AMR

### 8.3.1 Grid search with dependent parameters

Considering that AMR is based on the idea that stress and corresponding seismicity rates evolve with time around the area of a future earthquake, we apply a grid search for $c$-values at the time of three major earthquakes of California: M7.5 Kern County in 1952, M6.9 Loma

Prieta in 1989, and M7.3 Landers in 1992. Because evidence for strong AMR was published for the three earthquakes [Bowman and King, 2001; Bowman et al., 1998; King and Bowman, 2003] we initially make use of their published predefined fitting parameters and calculate the $c$-values for every point of a grid centered over the region with an interval of 0.5° in latitude and longitude (Figure 8.5a, b, c).

By applying the optimal values for the different variables (i.e. time, magnitude and distance ranges) determined by Bowman et al. [1998] for each of the three events we find that the epicenters are located within the main areas of low $c$-values (Figure 8.5a, b, c). The choice made in the AMR parameters in previous studies does not result in any other obvious regions of apparent AMR and is relatively restricted to the epicentral area. This is encouraging for the AMR hypothesis, showing that the AMR result is stable once the parameters are defined. However as stated previously we still have to adjust the three parameters according to the studied mainshock and no direct relationship between the region size, time range, and the magnitude of the earthquake can be inferred (see also Hardebeck et al. [2008]).

### 8.3.2 Grid search with independent parameters

Figure 8.5d, e, f shows results for the spatial distribution of the AMR $c$-value for the times of the same three earthquakes assuming the parameter choices described in Section 8.2.3; i.e., minimum magnitude of M4.5, a distance radius of 200 km, and a pre-mainshock time period of 30 years. Contrary to what was obtained when using adjusted parameters, the Kern County and the Loma Prieta earthquakes do not locate within an area of significant low $c$-values. Landers on the other hand, is located in a region where the $c$-values vary between 0.6 and 0.7 but it does not correspond to the zone where the minimum $c$-values are found.

More generally, Figure 8.6 presents a series of maps showing the result of the grid search analysis for a potential major earthquake in southern California in 30-year intervals using M4.5+ earthquakes between 1965 and 2005. The choice of the search radius (i.e. between 100 and 250 km) does not substantially affect the regional pattern of AMR $c$-values in southern California for a given time period. The areas where the $c$-values are either small (i.e. below 0.6) or large (i.e. above 1.0) are relatively stable. However, within these regions with relatively stable properties, the $c$-values may strongly vary.

On the other hand, Figure 8.6 shows very different patterns of the distribution of areas of high and low $c$-values when considering different time periods. This strong time dependence is the result of the earthquake activity occurring in a given search region during the analysis, in particular the large M6.5 events shown by purple, green, and orange stars in Figure 8.6. The occurrence of large earthquakes during the search period tends to influence the $c$-value depending on if they occur early (i.e. purple and green stars in Figure 8.6) or late (i.e.

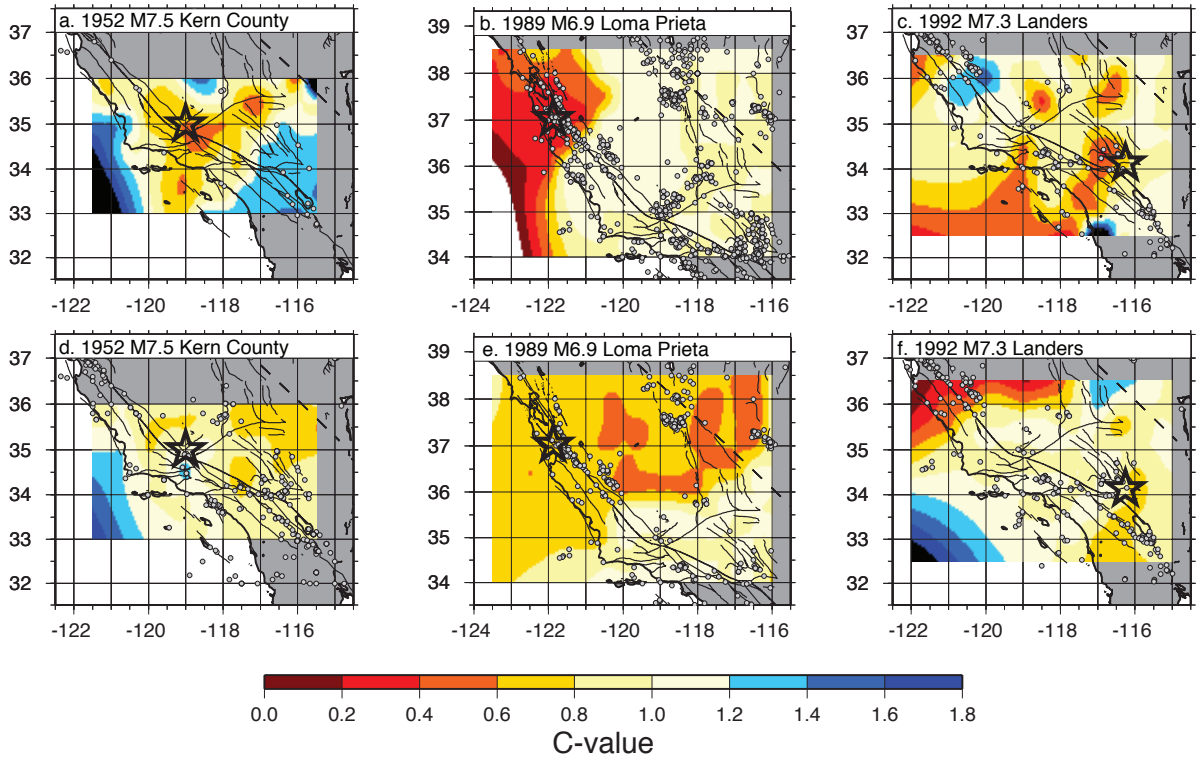


Figure 8.5: Grid search of AMR with dependent and independent parameters for the M7.5 Kern County (a, d), M6.9 Loma Prieta (b, e), and M7.3 Landers (c, f) earthquakes. a) Analysis performed with a region radius of 325 km and $5.5 < M < 7.5$ events (gray circles) between 1910 and 1952, which are the parameters for the Kern County earthquake (star) given by Bowman and King [2001]. b) Analysis performed with a region radius of 270 km and $4.5 < M < 7.5$ events (gray circles) between 1910 and 1989, parameters for the Loma Prieta mainshock (star) given by Bowman and King [2001]. c) Analysis performed with a region radius of 125 km and $4.5 < M < 7.5$ events (gray circles) between 1970 and 1992, parameters for the Landers earthquake (star) given by Bowman and King [2001]. d), e), and f) show the results of the analysis using a fixed minimum magnitude of the events (i.e. 4.5), a fixed time period of 30 years, and a fixed distance radius of 200 km.

orange stars in Figure 8.6) in a given 30-year period. We find that when one or several large earthquakes followed by their aftershock sequences occur early in the time period considered, the resulting cumulative Benioff strain will not be well fit with an accelerating power-law curve and the $c$-value will be high (see Figure 8.4c). On the other hand, we observe the opposite pattern when major earthquakes occur near the end of the studied time range. In this case the $c$-value will be low because of the increase in the slope of the cumulative Benioff strain towards the end of the analysis. For example, low $c$-values are found between 1965 and 1995 (Figure 8.6) in a region south of 35°N latitude where three out of five earthquakes with magnitude larger than 6.5 (i.e. the 1987 M6.7 Superstition Hills, 1992 M7.3 Landers and the 1994 M6.7 Northridge earthquakes) occurred after 1980, which corresponds to the middle of the period. Of course, such large, late events could then be considered as the culmination of a stress accumulation cycle within their epicentral region. This is also observed in Figure 8.5f where the regions with the lowest $c$-values are found in the proximity of the 1989 Loma Prieta earthquake that occurred less than 3 years before the 1992 Landers earthquake.

Finally, the latest period shown in Figure 8.6 between 1975 and 2005 shows no significant areas of low $c$-values. Nonetheless the M7.2 El Mayor-Cucapah earthquake struck northern Mexico (32.26°N -115.29°E) in April 2010, south of the area studied here in the grid search (white star in Figure 8.1). The absence of low $c$-value in this region is partly due to the occurrence of several M6.5+ in 1990s in southern California (green stars in Figure 8.6) that does not highlight the epicentral area of this event.

## 8.4 AMR and regions of stress increases

### 8.4.1 Comparison of AMR grid search with stress maps

Following the elastic rebound theory [Reid, 1910], which states that stress accumulates over time along locked segments of faults and is suddenly released in an earthquake, it is important to understand the state of tectonic stress in seismically active regions as well as its temporal evolution. This motivated King and Bowman [2003] to propose an analysis explicitly focused on stress-accumulation patterns, by assuming complete stress drop on all fault segments surrounding a target rupture for which AMR is being examined. For this purpose, they calculate the stress fields associated with back-slip rupture models to better constrain the area of interest instead of using a simple circular search region. Because explicit connections are drawn between the evolution of stress and the AMR hypothesis one should be able to resolve some degree of correlation between maps of modeled stress increases over the last two centuries and AMR behavior over a region of interest prior to a major seismic event.

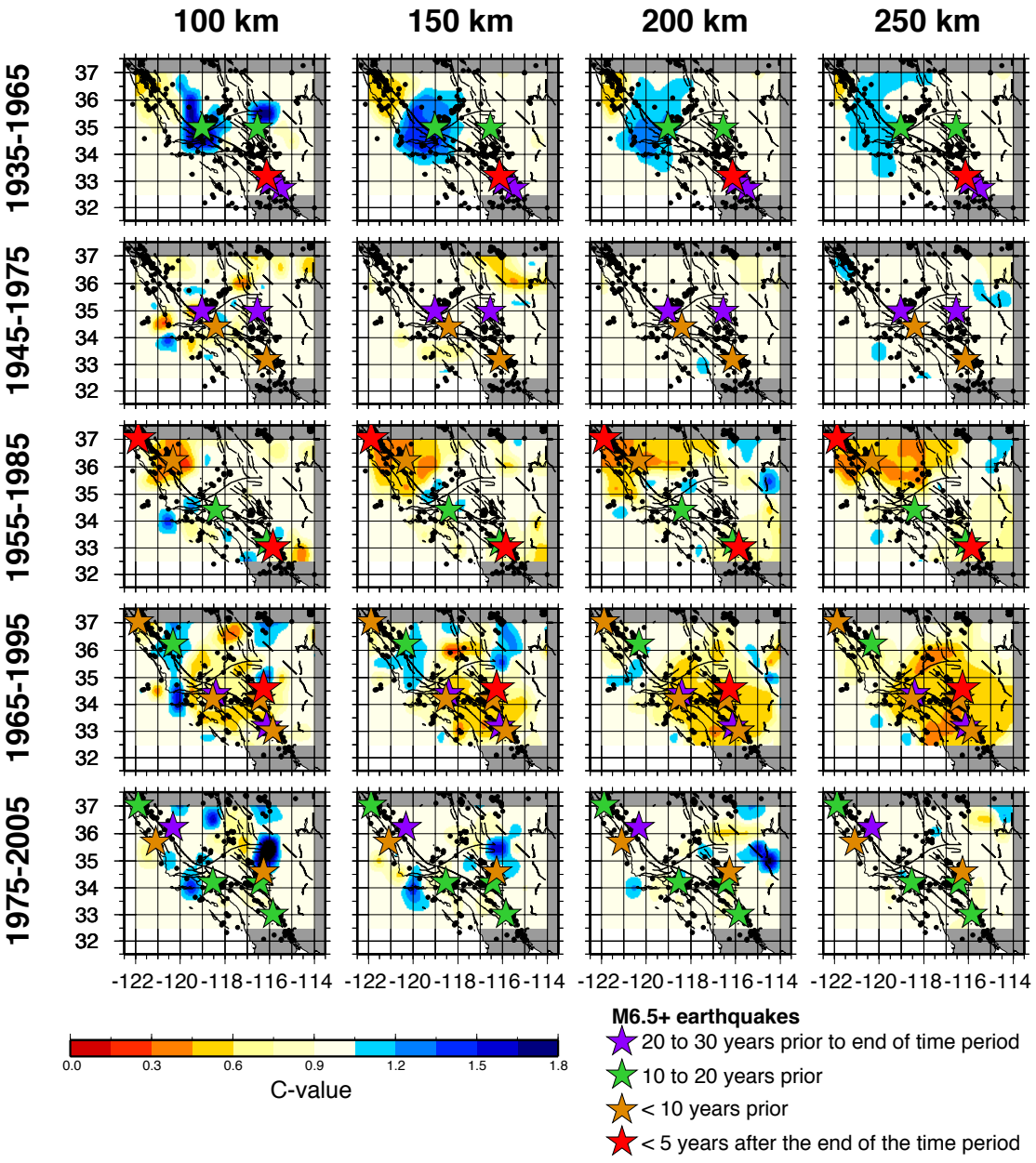


Figure 8.6: AMR grid search with fixed parameters between 1935 and 2005 in 30-year intervals. Columns show search results for AMR based on seismicity within 100 to 250 km radius distances from potential epicenters located every 0.5° in latitude and longitude and at the end of the 30 years considered as labeled on left from top to bottom. Black dots show the M4.5+ earthquakes considered in the calculation, stars represent M6.5+ earthquakes that occurred during the time period considered as well as within the next 5 years, color-coded with respect to the end of the time period scanned.

Figure 8.7 presents maps of $c$-values from 1935 to 2005 directly compared to maps of the modeled stress state for similar time periods. Here we show the AMR grid search results obtained using a 200-km-radius circular area (Figure 8.6) and stress models incorporating contributions of 200 years of major historic earthquakes, postseismic relaxation and interseismic strain [Freed et al., 2007]. Areas inferred to be highly stressed (i.e. positive stress values shown in warm color in Figure 8.7) and thus presumably closer to a potential rupture could be expected to also show evidence of accelerating seismicity. As shown in Figure 8.7b, except for the contributions from the coseismic and postseismic loading associated with the largest earthquakes (i.e. M>7), there is only modest variation in the large-scale stress pattern with time over the relatively short time periods considered (i.e. 30 years). This contrasts with the $c$-value maps (Figure 8.6 and 8.7), which show strong time dependency.

### 8.4.2 AMR in highly stressed areas

To complete the analysis of AMR in Southern California, we examine AMR in apparent high stress regions ($\Delta\sigma$>1 bar) in the models of Freed et al. [2007] between 1950 and 2010 (Figure 8.8). We pose the hypothesis that regions that accumulated the largest Coulomb stress increases since 1812 represent the locations of potential events and where significant AMR should be observed if the AMR method was valid. Nonetheless, it is worth recalling that the state of stress in 1812 is unknown and that recurrence intervals on major faults in California are on the order of a few centuries. The tests are performed on events with magnitude larger than 3.5 for a range of time periods, each ending in December 2009 and starting since 1950 with a 10-year increment. We calculate the $c$-values in each case considering a mainshock in June 2010 (i.e. six months after the end of the analyzed earthquake catalog) (Figures 8.8 and 8.9).

The northern high-stress region, which corresponds to the larger Parkfield area that we study in more detail below, gives similar results as previously observed. Considering all events in areas of $\Delta\sigma$ >1 bar in the area, the $c$-values stay close to 1. We added a distance criteria of 150 km radius for events located in the areas where $\Delta\sigma$ equals 1 bar in order to focus on this region. The $c$-values decrease slightly (i.e. 0.7) for events at $\Delta\sigma > 25$ bars (Figure 8.8b). It is worth recalling that this region of apparent high stress has to be considered carefully because it includes the southern section of the creeping SAF, which is not accounted for in the stress models.

If we search for AMR in the southern highly stressed region (Figure 8.8c) by considering the seismicity located where the change of stress is larger than 1 bar, no clear case of AMR is observed ($c$-values between 0.7 and 1) except when considering only events since 2000 and/or occurring at $\Delta\sigma > 30$ bars where $c$ is found less than 0.6. Same as for the Parkfield segment, we limited the region radius to 300 km for events located in regions where $\Delta\sigma$

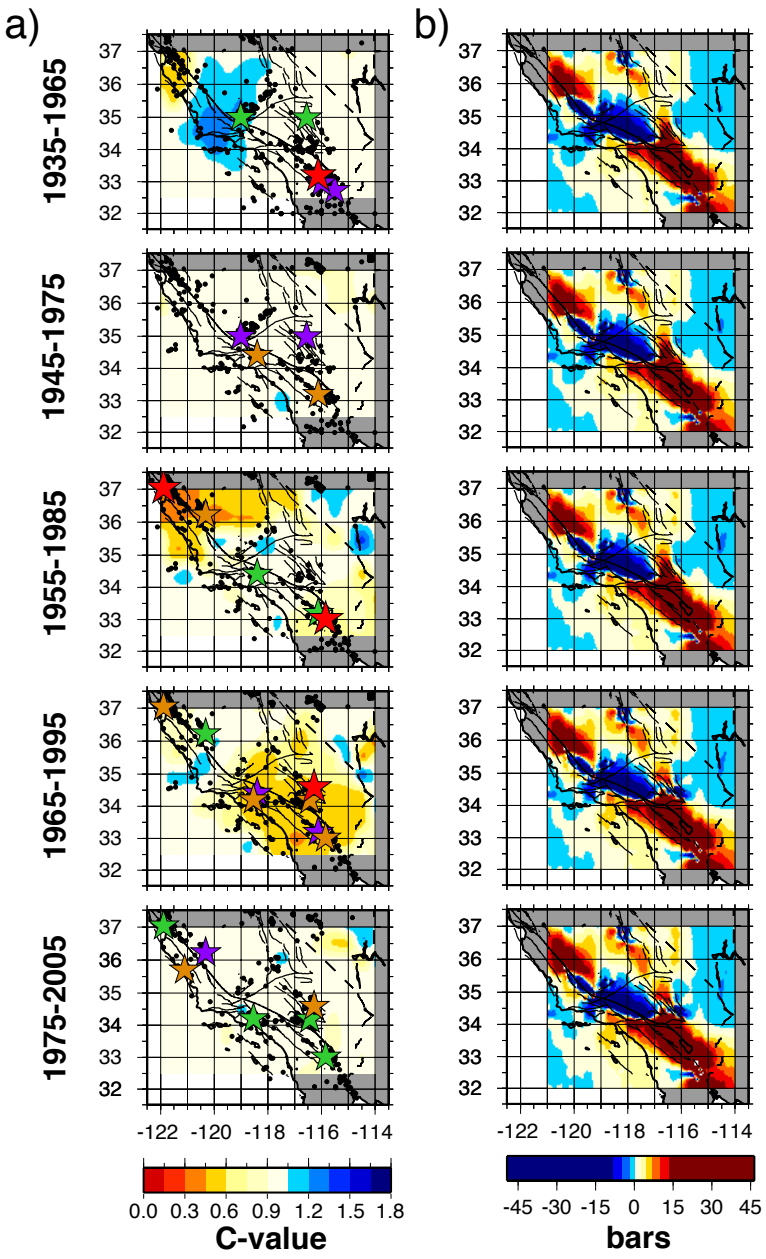


Figure 8.7: Comparison of the maps of the AMR grid search (a.) and modeled stress changes (b.) over time in southern California. a) $c$-values calculated for 200-km-radius regions over period of 30 years (see description Figure 8.6). b) State of Coulomb stress in bars in 1965, 1975, 1985, 1995 and 2005 (from top to bottom, respectively) computed over the region, considering coseismic stress transfers, postseismic relaxation, and interseismic loading in the crust and upper mantle, since 1812 [Freed et al., 2007].

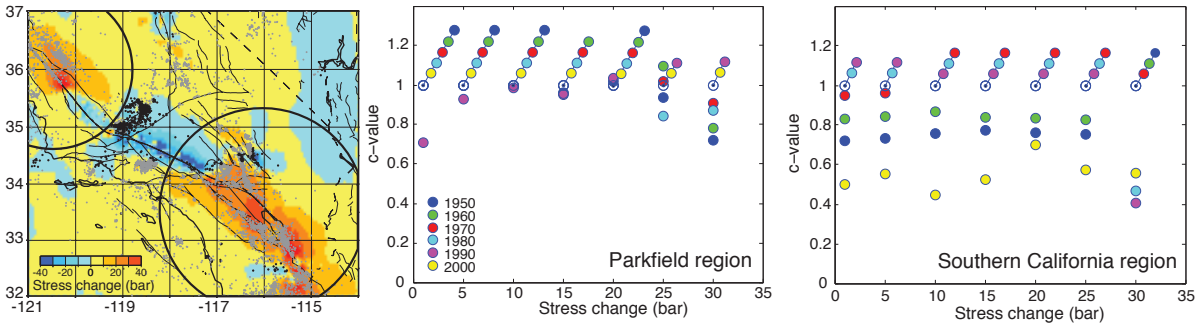


Figure 8.8: AMR in high stressed regions. Left) Map of Coulomb stress changes on SAF-parallel strike-slip faults in Southern California [Freed et al., 2007] computed for 2005. The M>3.5 earthquakes from 1950 through 2009 located within regions with positive $\Delta\sigma$ are shown in gray, else in black. Center) *C*-values obtained for events in zones of stress greater or equal to a range of values in the northern high-stress region with varying starting period times (end time: December 2009). Right) *C*-values obtained for the southern high stress region. AMR in high stressed regions. Left) Map of Coulomb stress changes on SAF-parallel strike-slip faults in Southern California [Freed et al., 2007] computed for 2005. The M¿3.5 earthquakes from 1950 through 2009 located within regions with positive ? are shown in gray, else in black. Center) C-values obtained for events in zones of stress greater or equal to a range of values in the northern high-stress region with varying starting period times (end time: December 2009). Right) C-values obtained for the southern high stress region.

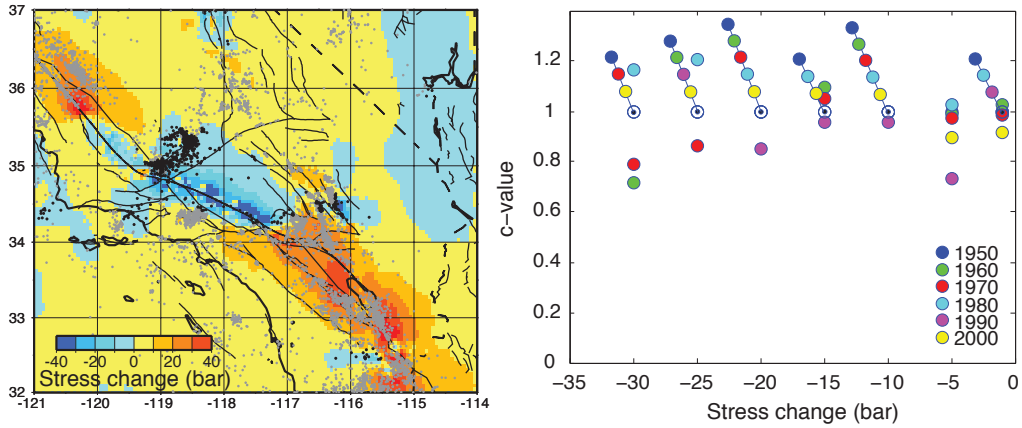


Figure 8.9: Left) Map of low-stress region in the enduring stress shadow of the M7.9 1857 Fort Tejon earthquake [Freed et al., 2007] computed for 2005. The earthquakes located within regions with $\Delta\sigma \leq$ -1 bar are shown in black, else in grey between 1950 and 2009 (M>3.5). Right) $C$-values obtained for various time and stress conditions (start year for each variable-length search period is indicated by color and $c$-values are computed for all events at stress less or equal to the value given).

equals 1 bar to focus on this area. In general, in the two positively stressed regions the $c$-values are close to 1 independent of the time range and stress level. The only exception is found when we consider earthquakes located in regions demonstrating 30+ bars stress changes. In these cases, the $c$-values decrease slightly especially for the southernmost region of interest, along the SAF system, and for the more recent time ranges. The 2010 M 7.2 El Mayor-Cucapah earthquake occurred within this high-stress region where the $c$-values are below 0.6 since 1980. Its occurrence would be consistent with the low $c$-values found in this high stress region in the last 30 years. However, we note that the $c$-value maps shown in Figures 8.6 and 8.7 do not indicate evidence for AMR in this southernmost region.

We also perform an AMR search in the areas of reduced stress ($\Delta\sigma <$ -1 bar), due in large part to the enduring stress shadow of the great 1857 Fort Tejon earthquake (Figure 8.9). Once again, the detection of accelerating seismicity is variable depending on the time range considered. We find similar $c$-values as previously obtained in the two high-stress regions (i.e. between 0.7 and 1). Because no difference is seen in evidence of AMR between the low and high stress areas, these results suggest that current stress levels do not correlate with seismicity rate changes. The low-stress regions appear to show comparable evidence for AMR as the highly stressed regions. The lack of strong recent earthquakes in either the especially highly stressed/unstressed areas so far in our study region, with the exception of the M7.2 El Mayor Cucapah earthquake mentioned earlier, indicates that the obtained

distribution of AMR does not appear to reflect regionally varying stress levels.

## 8.5 AMR analysis spanning two earthquake cycles at Parkfield

Mignan et al. [2007] propose a mathematical formulation of AMR obtained from a simple stress transfer consideration. In this stress accumulation model, which is based on the concept of the elastic rebound theory, AMR would result as the consequence of the decreasing size of the stress shadow generated by a previous earthquake. Such stress shadows following large seismic events have been revealed in several cases in California [Harris and Simpson, 1996, 1998; Kenner and Segall, 1999; Parsons, 2002]. Mignan et al. [2007] propose that acceleration should be found for the cumulative number of events, as well as for the cumulative Benioff strain. Furthermore, they suggest that a steady acceleration of seismicity should be evident throughout the entire seismic cycle, but would become more pronounced later during the earthquake cycle. To demonstrate this is a difficult task, because of the long recurrence intervals for most fault segments in California and elsewhere – often on the order of several centuries for major earthquakes – and the lack of complete earthquake catalogs available for such studies.

The Parkfield region in central California, which has been the site of several characteristic M6.0 earthquakes that have repeated over a relatively short earthquake cycle ($\sim$24 years in average) since 1857, represents a unique opportunity to evaluate seismicity rate changes spanning full recurrence intervals [Bakun et al., 2005; Murray and Langbein, 2006; Wallace, 1990]. In this case, the mainshock is smaller in magnitude than the usual target events of prior AMR studies (i.e. M>6.5) and requires lowering the minimum magnitude of the pre-events. Hardebeck et al. [2008] found that there is no significant systematic correlation between the mainshock magnitude and the corresponding $c$-value. Moreover, dropping the target event magnitude to M 6 should not affect the AMR behavior because based on the simple stress accumulation view of AMR, it should be magnitude invariant such that events of any size should have local AMR behavior as long as the catalog of surrounding seismicity is large enough.

We search for AMR during the last two earthquake cycles, from 1935 to 1966 and 1967 to 2004, using the ANSS seismicity catalog with M$\geq$2.0 in a 5°-by-5° region centered on the nucleation zone. Computation of AMR in the area is performed using various magnitude and distance ranges (Figure 8.10). The completeness of the catalog evolved with time over the region (Figure 8.10b), especially in the early 1970's, and we carry out the analysis with a range of lower-magnitude cutoffs for the earlier period. The 1966 Parkfield earthquake is also remarkably absent in the ANSS catalog at the time of the analysis. The lowest $c$-value

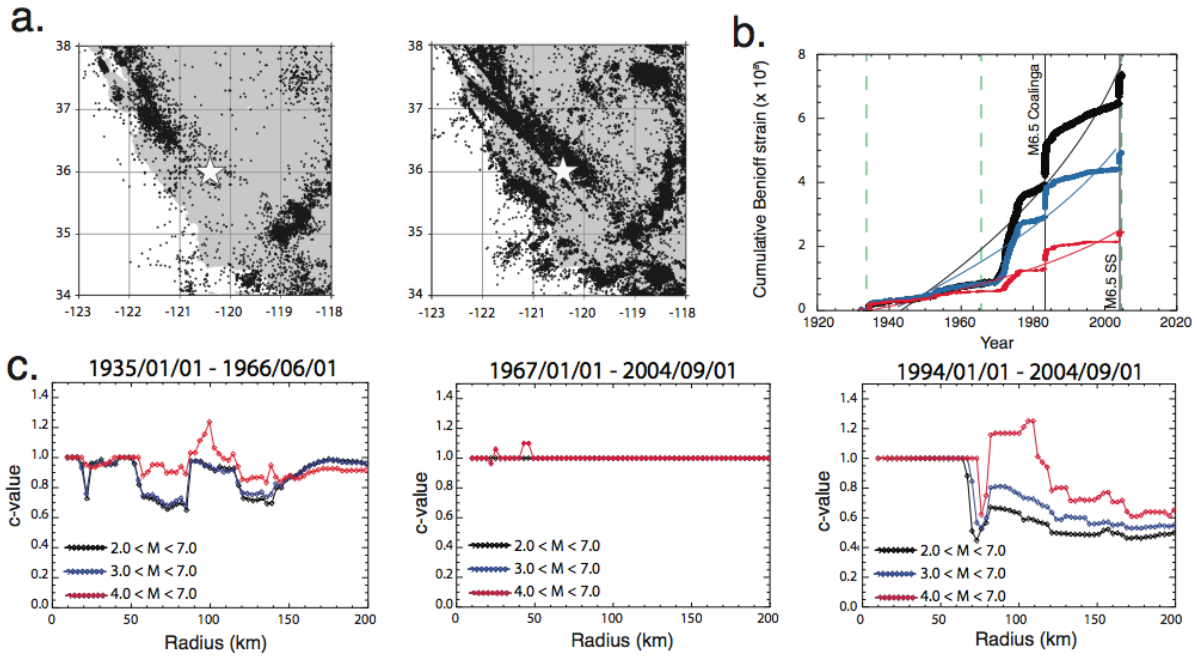


Figure 8.10: AMR analysis in the Parkfield region over the past two earthquake cycles of M6 earthquakes on the SAF (1935-1966 and 1967-2004). a) Maps of the M2+ earthquakes (dots) recorded between 1932 and 1966 (left) and between 1967 and 2004 (right). The star shows the Parkfield earthquake location (35.9°N -120.45°E) b) Cumulative Benioff strain between 1911 and 2004 using M2+ (black), M3+ (blue), and M4+ (red) earthquakes within 100 km distance from Parkfield. Network sensitivity changes in early 1970's and the occurrence of the 1983 Coalinga and 2003 San Simeon (SS) earthquakes explain the large step increases in the cumulative Benioff strain. The M6 Parkfield earthquakes of 1933, 1966, and 2004 are shown by the green dashed lines. c) Calculated $c$-values over the region between January 1935 and June 1966 (left), between 1967 and September 2004 (center), and between 1994 and September 2004 (right) using variable magnitude and distance ranges.

observed during the first earthquake cycle (about 32 year long, from 1934 to 1966) is 0.65 (i.e. <0.7) for a region of 85 km radius, indicating that AMR is observed during the time period (Figure 8.10a,c). When searching for AMR with magnitudes larger than 4.0 the lowest $c$-value is larger, i.e. about 0.85. The second earthquake cycle (i.e. from 1967 to 2004) does not show any acceleration of seismicity and the $c$-value is equal to 1 over most of the search radii considered (0 to 200 km) (Figure 8.10c) with no difference between the various ranges of magnitude of the seismicity. In this latest period, the AMR results are very sensitive to the occurrences of the nearby 1983 M6.5 Coalinga-Nunez earthquake sequence and 2003 M6.5 San Simeon thrust earthquake and to their aftershock sequences.

According to Mignan et al. [2007], AMR might not be observable during an entire earthquake cycle because of temporal variation in the background seismicity and/or because of its sensitivity to a few large earthquakes during a given time interval. Thus, we also search for AMR over a shorter period of time than the full length of the last Parkfield earthquake cycle, starting in 1994 (Figure 8.10c). We find lower $c$-values for a distance range of 80+ km after 1994, as this time interval excludes the aftershock sequence of the 1983 Coalinga earthquake. However, because the 2003 San Simeon aftershock sequence occurred less than a year prior to the 2004 earthquake, its effects are dominant in the AMR calculation. But even if the two mainshocks (i.e. 1983 Coalinga and 2003 San Simeon) triggered earthquakes along the Parkfield segment, they showed reverse mechanisms instead of a purely strike-slip motion and represent different stress loading conditions.

In order to properly test AMR in the Parkfield region it may be important to more closely focus on the vicinity of the 1966 and 2004 ruptures, and on the area of expected stress accumulation about the rupture zone. Parkfield is located in a relative straight transitional section of the SAF with the main creeping segment of the fault from Parkfield to San Juan Bautista to the north and the fully locked portion of the fault that last ruptured in the 1857 Fort Tejon earthquake to the south [Wallace, 1990]. The successive 1934, 1966 and 2004 Parkfield ruptures were collocated with similar dimensions as modeled by Murray and Langbein [2006] (see their Figure 5), although the 2004 event nucleated at the opposite end of the Parkfield segment compared to the previous two events. We define an initial rectangular 40 km-by-10 km search area (Figure 11) to encompass the historic Parkfield rupture areas [Kim and Dreger, 2008; Murray and Langbein, 2006] along the fault. This area roughly delimits the region of stress accumulation in a simple model of free creep to the north and the locked Cholame fault segment to the south. We evaluate for acceleration of the seismicity within successive boxes incremented by 10 km on all sides centered on the segment, while fixing the boundary to the NW where the SAF is fully creeping.

Figure 8.11 shows that the $c$-values calculated for the rectangular search areas vary between 0.7 and about 1 over different time and distance ranges using M3+ earthquakes. Both small decelerations and accelerations of seismicity are obtained. Considering the entire 1935-

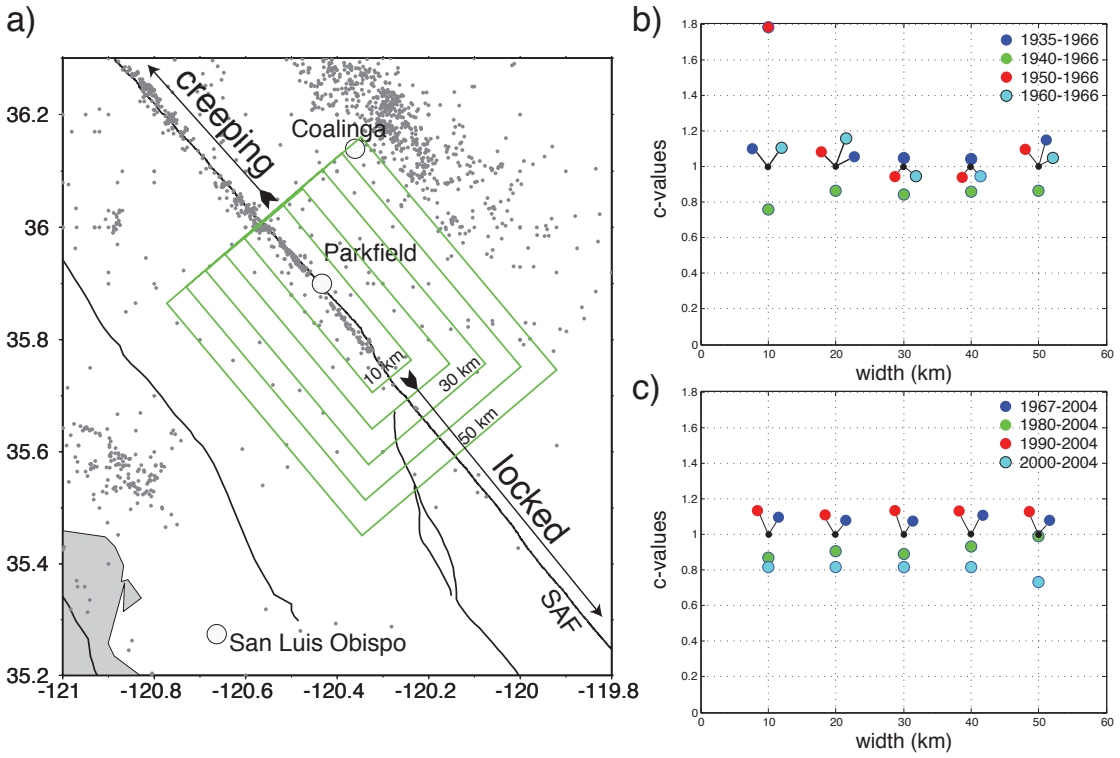


Figure 8.11: Variation of c-values in the restricted Parkfield rupture region. (a) Map of the M3.0+ earthquake between 1950 and 2010. The smaller box has dimensions of 40 km by 10 km. Others are 10 km larger in both sides. (b) Variation of $c$-value for the two earthquake cycles considered depending on the size of the box and on the time range. c) Same as b) for 1967 to 2004.

1966 and 1967-2004 earthquake cycles no AMR is observed (i.e. the $c$-values are about 1.0). When using earthquakes since 2000, lower $c$-values are observed without passing beneath the 0.7 threshold value for AMR detection. Based on the results of the analysis no conclusive acceleration of seismicity can be noticed using both small and larger areas in this short and regular earthquake cycle region.

## 8.6 Discussion and Conclusion

The findings of AMR are strongly dependent on the choices of the three parameters used (i.e., magnitude, time interval, and area size ranges) to calculate the cumulative Benioff strain relative to target events of interest. We find that once the parameters have been found to best support an acceleration of seismicity before three historic earthquakes, they are specific to these events and they would not strongly indicate any other AMR elsewhere in the region except in the target event locations (Figure 8.5). This is somehow encouraging because it suggests the specificity of the solution to the location of the target mainshock instead of diverging to other regions that would result in false alarms. However because the parameters are specific to a chosen mainshock it becomes difficult to use this AMR approach in a more general perspective. By fixing the three parameters for the three earthquakes in question to common values, the results differ significantly and would not have indicated AMR that could have informed earthquake forecasting prior to these events. Understanding the relationships between the three variables and the target events is the key for the eventual success of AMR. More strictly, in order to use AMR in a direct manner for earthquake forecasting, independent parameters are required without a-priori knowledge of the expected earthquake magnitude and location.

As previously noted by Hardebeck et al. [2008], we demonstrate that AMR can be biased by the occurrence of a few large earthquakes during the studied period (Figure 8.8). Indeed, a large event at the beginning of a chosen observation cycle tends to dominate the cumulative Benioff strain and will result in an increase of the $c$-value (Figure 8.4c). On the other hand a mainshock and its following aftershock sequence occurring near the end of the time period tend to significantly decrease the $c$-value and support the case for AMR.

This leads to the question of whether or not to decluster the earthquake catalog. This remains a controversial option as AMR has been observed in previous studies on both complete and declustered catalogs. Declustering might appear as a solution to obtain a proper image of the evolution of seismicity, nonetheless mainshocks and aftershock sequences are important components of the seismic activity of a region such as southern California. They can generate stress changes that can act as triggers for potentially large earthquakes like the 1992 M7.3 Landers earthquake that was preceded by the M6.1 Joshua Tree earthquake,

which struck the region two months earlier and was followed three hours later by the M6.3 Big Bear earthquake. In this current study we did not decluster the earthquake catalog. Indeed, even if the catalog can be more or less modified to account for seismic clusters it appears that it would correspond to another parameter (i.e. with or without declustering) that would need to be considered in the analysis. Also, because opposite results can be possibly observed before and after declustering this would be accounted as another free parameter in a data-fitting analysis. In addition one could question the need for declustering the earthquake catalog if AMR was confirmed and how to proceed when considering detecting AMR in a routine procedure.

Finally, the original description of the AMR idea [Bowman and King, 2001; Bowman et al., 1998; King and Bowman, 2003] first appeared as an appropriate hypothesis proposed for earthquake forecasting because it was based on the stress evolution on a fault. Each earthquake releases stress over some volume in its surrounding neighborhood and AMR has been explicitly linked to static stress build-up and release such that they are important factors to take into account (e.g., King and Bowman [2003]; Mignan et al. [2006]). For the very simple system of an isolated rupture asperity under increasing load, it makes sense to expect AMR, or accelerating seismic release in general, in areas of rising stress through the earthquake cycle [Mignan, 2011]. The cumulative Benioff strain itself is derived from the cumulative seismic moment, which is dependent on the variation of stress by stress loading and transfer in the uppermost part of the Earth and therefore differs from other methods that make use of sudden changes in the rate of earthquakes without taking into consideration their seismic moment [Reasenberg and Matthews, 1988]. However, when we explicitly evaluate AMR in areas of high stress indicated by a stress evolution model that takes into consideration 200 years of stress change from coseismic, postseismic and interseismic loading, no conclusive accelerations are observed. Indeed no correlations are found between the AMR results and the stress level in the region (i.e. high or low). Even if the stress changes shown on the maps can be questionable, the areas that sustained stress increases that approach plausible stress drop values should be closer to failure and should differ from c-values obtained from a random earthquake catalog analysis (i.e. close to 1).

The absence of relationships between the various parameters, the observation of both accelerating and decelerating seismicity for the same event, and the absence of clear distinction of the AMR pattern in areas of opposite stress loading lead us to consider it very carefully for earthquake forecasting purposes. We find it unsuitable to provide any improvement towards future earthquake assessments when using fixed parameters in an approach that would better accommodate realtime seismicity variation and earthquake forecasting (i.e. without prior modification of the earthquake catalog using a declustering technique). The spatio-temporal juxtaposition of different earthquake recurrence times and fault zones is opposed to the model proposed by Bowman et al. [1998] and Bowman and King [2001], which takes into account a single fault plane. This appeared to be limited for real earthquake analysis

in southern California where different scale fault systems are located. Finally, this method considers that all the earthquakes can potentially lead to the failure of a fault segment without taking into account the focal mechanisms of the pre-seismicity which can either bring the fault system closer to failure or on contrary inhibit it when decreasing the stress changes associated with earthquakes. Future approaches should strive to open the discussion to the discrimination of the earthquake source mechanisms and associated stress transfers in the study of possible accelerating seismicity.

# Chapter 9

# Conclusions

It is clear that the analysis of unusual seismicity in northern and central California helps obtain a better understanding of the fault rheology and kinematics. If carefully detected and monitored, unusual seismic events provide unique information that has not previously been obtained from regular earthquake catalogs. They give the promise for higher-resolution monitoring of stress changes in the nucleation region of the fault zones. This offers the possibility to look for improved earthquake forecasting methodology as they give insights on the various conditions at which slip rates change at depth.

In Chapter 2, I described slow earthquakes occurring in the Mendocino Triple Junction (MTJ) region. I showed that even if their number is limited and cannot permit high-resolution description of the fault zones where they are located, they correspond to a particular class of seismic events that is worth studying. By using different techniques similar to the one used for the detection of repeating earthquakes in northern California [Nadeau and McEvilly, 2004], or by focusing the earthquake detection on long period waves and on moment tensor analyses [Ekström, 2006; Kawakatsu, 1998], I demonstrated that additional missing slow earthquakes could potentially be detected. This would enhance our understanding of these events that illuminate contrasting slips and/or rupture dimensions on adjacent fault segments where both slow and regular earthquakes occur.

In Chapter 3, I showed that the method proposed by Kawakatsu [1998] that makes use of continuous inversions of moment tensors on streaming long-period data for the detection and characterization of seismic events is implementable in the seismically active region of the MTJ. I found that this approach does not only allow the rapid detection of M3.5 to 7 earthquakes (regular and possibly slow) occurring in the region, but that if scaled appropriately (i.e. using longer period waves) it can also allow the rapid detection of megathurst earthquakes. I further showed that this method is improved if instead of considering point-source Green's functions the system considers quasi-finite-source Green's functions. These are needed for the consideration of the rupture finiteness and directivity in the near-field. Solutions can be obtained within several minutes after the origin time of the earthquake using a limited number of stations, and could therefore be used as part of a near-source tsunami

early warning system, capable of providing tens of minutes of possible warning depending on the distance of the earthquake rupture from the coast.

In Chapter 4, I directly demonstrated that the method presented in Chapter 3 is applicable to other regions and allows the rapid detection (i.e. within 8 minutes) of the M9 Tohoku-oki earthquake that occurred on 11 March 2011 offshore Japan. Using strong-motion data the earthquake was correctly detected, located, and characterized, and without magnitude saturation. I conclude that this powerful analysis can be adapted to the type of available data, either displacement, velocity, and/or acceleration from seismic stations, or from GPS records. Nonetheless, this requires the continuous recording of the seismic field from accelerometers and/or GPS.

Nonvolcanic tremors in a different tectonic setting along the San Andreas Fault (SAF) in central California show much promise for a high-resolution monitoring of stress changes and slip rate of the SAF at depth unlike other seismic events. In Chapter 5, I showed that tremors are more sensitive to static stress changes in their source region associated with local and regional earthquakes than regular seismic events are. This high sensitivity of tremors to stress changes on the order of kPa could make them a useful dataset for monitoring deep fault-zone processes.

In addition, in Chapter 6, I showed first-time evidences that tremors can be dynamically triggered by the passage of the surface waves of large regional earthquakes. The absence of their detections in previous studies resulted in the limited frequency bands at which they were looked for. However, I demonstrated that tremors (triggered and ambient) have a larger frequency spectrum than what was initially believed and that they have energy at up to $\sim 50$ Hz. This is an important result as it opens a broader frequency range at which to search for tremors in regions where they have not yet been observed. Also, in agreement with the results found in Chapter 5, tremors are found to be dynamically triggered by large-amplitude, long-period waves when the minimum triggering dynamic stress is larger than $\sim$1 kPa.

The nearly 10 year tremor activity in the Parkfield region shows various types of tremor behavior: ambient, triggered, and episodic. In Chapter 7, I carefully analyzed the spatio-temporal activity of the last class of tremors. I argued that the episodes of tremors reveal slow-slip events (SSEs) occurring at depth, and as a consequence that they correspond to the only means so far for the identification of SSEs along the SAF. Using additional datasets from repeating earthquake sequences and low-frequency earthquakes I constrained their source region and characterized the source parameters of these deep slips. This constitutes an important result that allows a high-resolution analysis of the slip rate of the SAF at depth over time, in a transitional section of the fault. Also, the greater sensitivity of tremors to stress changes associated with transients or with the long-term slip of the SAF makes the analysis of tremors essential for the monitoring of this segment of the SAF that corresponds

to the initiation zone of the 1857 M7.9 Fort Tejon earthquake.

Finally in Chapter 8, I searched for evidence of interactions between earthquakes in space and time following the hypothesis promoted by Bowman et al. [1998]: the Accelerating Moment Release (AMR). Carrying a systematic grid search analysis for AMR instead of a case-specific approach and comparing AMR maps with stress maps in southern California, I found no strong evidence supporting AMR. Also, when focusing on apparent high and low stress regions no distinction in the seismicity change of these contrasting regions can be made. This does not satisfy the hypothesis of AMR that there is increased regional seismic activity prior to a mainshock where the stress increases. Thus, I find that the concept of AMR is inadequate and cannot be considered for improved earthquake forecasts.

These results demonstrate that the analysis of unusual seismicity is essential for a better understanding of the earthquake physics. They indeed behave differently and give insights on different types of slip (i.e. slow, fast, energetic, not energetic, etc) that is important to consider for a correct and complete comprehension of the process of deformation and stress accumulation beneath locked segments of fault. Nonetheless, because they are not detected using routine procedures, they would not have been examined without the continuous recording of the seismic activity. This emphasizes the need to pursue the development and implementation of continuously recording seismic networks including various types of instrument (broadband, strong-motion, GPS, strainmeter, etc). This would not only encourage their analysis but also favor the enhanced detection and characterization of damaging seismic events like tsunamigenic megathrust earthquakes. Finally, this would help the seismological community to develop better earthquake and fault models in the future.

# Bibliography

Abercrombie, R. E. and Ekström, G. (2003). A reassessment of the rupture characteristics of oceanic transform earthquakes. *J. Geophys. Res.*, 108(B5):2225.

Aguiar, A., Melbourne, T. I., and Scrivner, C. W. (2009). Moment release rate of Cascadia tremor constrained by GPS. *J. Geophys. Res.*, 114:B00A05.

Ammon, C. J., Lay, T., Kanamori, H., and Cleveland, M. (2011). A rupture model of the 2011 off the Pacific coast of Tohoku earthquake. *Earth Planets Space*, 63:693–696.

Amoruso, A., Crescentini, L., Dragoni, M., and Piombo, A. (2004). Fault slip controlled by gouge rheology: a model for slow earthquakes. *Geophys. J. Int.*, 159:347–352.

Atwater, B. F. (1987). Evidence for Great Holocene earthquakes along the outer coast of Washington State. *Science*, 236:942–944.

Avallone, A. et al. (2011). Very high rate (10 hz) GPS seismology for moderate-magnitude earthquakes: The case of the Mw6.3 L'Aquilla (central Italy) event. *Geophys. Res. Lett.*, 116:B02305.

Baise, L. G., Dreger, D. S., and Glaser, S. D. (2003). The effect of shallow San Francisco Bay sediments on waveforms recorded during the Mw 4.6 Bolinas, California, earthquake. *Bull. Seism. Soc. Am.*, 93(1):465–479.

Bakun, W. H. et al. (2005). Implications for prediction and hazard assessment from the 2004 Parkfield earthquake. *Nature*, 437:969–974.

Becken, M., Ritter, O., Bedrosian, P. A., and Weckmann, U. (2011). Correlation between deep fluids, tremors and creep along the central san andreas fault. *Nature*, 480:87–90.

Blewitt, G., Hammond, W. C., Kreemer, C., H.-P., Stein, S., and Okal, E. (2009). Gps for real-time source determination and tsunami warning systems. *Journal of Geodesy*, 83(3):335–343.

Bowman, D. D. and King, G. C. P. (2001). Accelerating seismicity and stress accumulation before large earthquake. *Geophys. Res. Lett.*, 28:4039–4042.

Bowman, D. D., Ouillon, G., Sammis, C., Sornette, A., and Sornette, D. (1998). An observational test of the critical earthquake concept. *J. Geophys. Res.*, 103(B10):24349–24372.

Boyd, O. S. et al. (2011). Deviatoric moment tensor analysis at the Geysers Geothermal Field. In *SSA 2011 Annual Meeting*.

Brantut, N., Schubnel, A., and Gueguen, Y. (2010). Damage and rupture dynamics at the brittle/ductile transition: the case of gypsum. *J. Geophys. Res.*, 116(B01404).

Braunmiller, J. and Nabelek, J. (2008). Segmentation of the Blanco Transform Fault Zone from earthquake analysis: Complex tectonics of an oceanic transform fault. *J. Geophys. Res.*, 113:B07108.

Brenguier, F. et al. (2008). Postseismic relaxation along the San Andreas Fault at Parkfield from continuous seismological observations. *Science*, 321:1478.

Brodsky, E. E. and Prejean, S. G. (2005). New constraints on mechanisms of remotely triggered seismicity at Long Valley Caldera. *J. Geophys. Res.*, 110:B04302.

Brudzinski, M. R. and Allen, R. (2007). Segmentation in episodic tremor and slip all along Cascadia. *Geology*, 35(10):907–910.

Brudzinski, M. R., Hinojosa-Prieto, H. R., Schlanser, K. M., Cabral-Cano, E., Arciniega-Ceballos, A., Diaz-Molina, O., and DeMets, C. (2010). Non-volcanic tremor along the Oaxaca segment of the Middle America Subduction Zone. *J. Geophys. Res.*, 115:B00A23.

Bruhat, L., Barbot, S., and Avouac, J.-P. (2011). Evidence for postseismic deformation of the lower crust following the 2004 Mw6.0 Parkfield earthquake. *J. Geophys. Res.*, 116:B08401.

Bryant, E. (2001). *Tsunami : The underrated hazard*. Cambridge University Press, Melbourne.

Bufe and Varnes (1993). Predictive modeling of the seismic cycle of the greater San Francisco Bay region. *J. Geophys. Res.*, 98:9871–9883.

Clarke, S. H. and Carver, G. A. (1992). Late Holocene tectonics and paleoseismicity, southern Cascadia Subduction Zone. *Science*, 255(5041):188–192.

Clinton, J. F. and Heaton, T. H. (2002). The potential advantages of a strong-motion velocity meter over a strong-motion accelerometer. *Seismol. Res. Lett.*, 73(3).

Deng, J. and Sykes, L. R. (1997). Evolution of the stress field in southern California and triggering of moderate-size earthquakes: A 200-year perspective. *J. Geophys. Res.*, 102:9857–9886.

Dicke, M. (1998). Seismicity and crustal structure at the Mendocino Triple Junction, northern California. Master's thesis, University of California, Berkeley.

Dreger, D. S. (2010). January 10, 2010 Mw6.5 Gorda Plate Earthquake: Automated finite-source modeling.

Dreger, D. S., Gee, L., Lombard, P., Murray, M. H., and Romanowicz, B. (2005). Rapid finite-source analysis and near-fault strong ground motions: Application to the 2003 Mw 6.5 San Simeon and 2004 Mw 6.0 Parkfield earthquakes. *Seismological Research Letters*, 76(1):40–48.

Dreger, D. S. and Helmberger, D. V. (1993). Determination of source parameters at regional distances with single station or sparce network data. *J. Geophys. Res.*, 98:8107–8125.

Dreger, D. S. and Kaverina, A. (2000). Seismic remote sensing for the earthquake source process and near-source strong shaking: A case study of the October 16, 1999 Hector Mine earthquake. *Geophys. Res. Lett.*, 27:1941–1944.

Dreger, D. S., Uhrhammer, R., Pasyanos, M., Franck, J., and Romanowicz, B. (1998). Regional and far-regional earthquake locations and source parameters using sparse broadband networks: A test on the Ridgecrest Sequence. *Bull. Seism. Soc. Am.*, 88:1353–1362.

Duputel, Z., Rivera, L., Kanamori, H., Hayes, G. P., Hirshorn, B., and Weinstein, S. (2011). Real-time W phase inversion during the 2011 off the Pacific coast of Tohoku Earthquake. *Earth Planets Space*, 63(6):535–539.

Dziewonski, A. M. and Woodhouse, J. H. (1983). An experiment in systematic study of global seismicity: Centroid-moment tensor solutions for 201 moderate and large earthquakes of 1981. *J. Geophys. Res.*, 88(B4):3247–3271.

Ekström, G. (2006). Global detection and location of seismic sources by using surface waves. *Bull. Seism. Soc. America*, 96(4A):1201–1212.

Ellsworth, W. L. (2008). Origin of nonvolcanic tremor beneath the San Andreas Fault in central California. In *Report on the Aseismic Slip, Tremor, and Earthquakes Workshop*. U.S. Geol. Surv. Open File Report 2008-1343.

Ellsworth, W. L., Lindh, A. G., Prescott, W. H., and Herd, D. G. (1981). *The 1906 San Francisco earthquake and the earthquake cycle*. American Geophysical Union.

Freed, A. M. (2005). Earthquake triggering by static, dynamic, and postseismic stress transfer. *An. Rev. Earth Planet. Sci.*, 33:335–367.

Freed, A. M., Ali, S., and Bürgmann, R. (2007). Evolution of stress in Southern California for the past 200 years from coseismic, postseismic and interseismic stress changes. *Geophys. J. Int.*, 169.

Frohlich, C. (1994). Earthquakes with non-double-couple mechanisms. *Science*, 264(5160):804–809.

Fukuyama, E., Ishida, M., Dreger, D., and Kawai, H. (1998). Automated seismic moment tensor determination by using on-line broadband seismic waveforms. *Zishin*, 51:149–156.

Gayes, G. P. and Wald, D. J. (2009). Developing framework to constrain the geometry of the seismic rupture plane of subduction interface a priori - a probabilistic approach. *Geophys. Journal International*, 176:951–964.

Gee, L., Neuhauser, D., Dreger, D., Pasyanos, M., Uhrhammer, R., and Romanowicz, B. (2003). The rapid earthquake data integration system. In *International Handbook of Earthquake and Engineering Seismology*, pages 1261–1273. IASPEI.

Gee, L. S., Neuhauser, D. S., Dreger, D. S., Pasyanos, M., Uhrhammer, R. A., and Romanowicz, B. (1996). Real-time seismology at UC Berkeley: The rapid earthquake data integration project. *Bull. Seism. Soc. America*, 86:936–945.

Goldfinger, C. et al. (2008). Late holocene rupture of the northern San Andreas Fault and possible stress linkage to the Cascadia Subduction Zone. *Bulletin of the Seismological Society of America*, 98:861–889.

Goldstein, P., Dodge, D., Firpo, M., , and Minner, L. (2003). *SAC2000: Signal processing and analysis tools for seismologists and engineers*, volume The IASPEI International Handbook of Earthquake and Engineering Seismology, Part B. Academic Press London.

Gomberg, J., Rubinstein, J. L., Peng, Z., Creager, K. C., Vidale, J. E., and Bodin, P. (2008). Widespread triggering of nonvolcanic tremor in California. *Science*, 319:173.

Gonzales, F. I., Satake, K., Boss, E. F., and Mofield, H. O. (1995). Edge wave and non-trapped models of the 24 April 1992 Cape Mendocino tsunami. *PAGEOPH*, 144:409–426.

Griscom, A. and Jachens, R. C. (1990). Crustal and lithospheric structure from gravity and magnetic studies. In Wallace, R. E., editor, *The San Andreas Fault System, California*. U.S. Geol. Surv. Prof. Pap. 1515.

Guilhem, A. and Dreger, D. (2011). Rapid detection and characterization of large earthquakes using quasi-finite-source Green's functions in continuous moment tensor inversion. *Geophys. Res. Lett.*, 38:L13318.

Guilhem, A. and Nadeau, R. M. (2008). Nonvolcanic tremor activity in the parkfield-cholame region of California and the 2003 M6.5 San Simeon and 2004 M6.5 Parkfield Earthquakes. In *Eos Trans. AGU, Fall Meet. Suppl.*, volume 89, page 53.

Guilhem, A., Peng, Z., and Nadeau, R. M. (2010). High-frequency identification of non-volcanic tremor triggered by regional earthquakes. *Geophys. Res. Lett.*, 37:L16309.

Gutjahr, S. and Buske, S. (2011). Seismic images of the tremor region at the san-andreas-fault system around cholame. In *2011 EGU meeting*.

Hardebeck, J. L. et al. (2004). Preliminary report on the 22 December 2003 M6.5 San Simeon, California, earthquake. *Seismol. Res. Lett.*, 75:155–172.

Hardebeck, J. L., Felzer, K. R., and Michael, A. J. (2008). Improved tests reveal that the accelerating moment release hypothesis is statistically insignificant. *J. Geophys. Res.*, 113:B08310.

Harris, R. A. and Simpson, R. W. (1996). In the shadow of 1857: the effect of the great Fort Tejon earthquake on subsequent earthquakes in southern California. *Geophys. Res. Lett.*, 23:229–232.

Harris, R. A. and Simpson, R. W. (1998). Suppression of large earthquakes by stress shadows; a comparison of Coulomb and rate-and-state failure. *J. Geophys. Res.*, 103:24439–24451.

Hayashi, Y., Tsushima, H., Hirata, K., Kimura, K., and Maeda, K. (2011). Tsunami source area of the 2011 off the Pacific coast of Tohoku earthquake determined from tsunami arrival times at offshore observation stations. *Earth Planets Space*, 63:809–813.

Hayes, G. P., Earle, P., Benz, H., Wald, D., Briggs, R., and the USGS/NEIC Earthquake Response Team (2011). 88 hours: The US Geological Survey National Earthquake Information Center response to the March 11, 2011 Mw 9.0 Tohoku earthquake. *Seismol. Res. Lett.*, 82(4):481–493.

Heaton, T. H. and Hartzell, S. H. (1987). Earthquake hazards on the Cascadia Subduction Zone. *Science*, 236:162–168.

Hellweg, M. (2000). *Volcanic tremor and physical source model: Lascar volcano, Chile*. PhD thesis, University of Stuttgart - Institute of Geophysics.

Henstock, T. J. and Levander, A. (2003). Structure and seismotectonics of the Mendocino Triple Junction, California. *J. Geophys. Res.*, 108(B5):2260.

Hickman, S., Zoback, M. D., and Ellsworth, W. (2004). Introduction to special section: Preparing for the San Andreas Fault Observatory at Depth. *Geophys. Res. Lett.*, 31:L12S01.

Hill, D. P. (2008). Dynamic stresses, coulomb failure, and remote triggering. *Bull. Seismol. Soc. Am.*, 98(1):66–92.

Hill, D. P. (2010). Surface wave potential for triggering tectonic (non-volcanic) tremor. *Bull. Seismol. Soc. Am.*

Hill, D. P. et al. (1993). Seismicity remotely triggered by the magnitude 7.3 Landers, California, earthquake. *Science*, 260:1617–1623.

Hill, D. P. and Prejean, S. G. (2007). Dynamic triggering. In Schubert, G., editor, *Treatise on Geophysics*, volume 4, chapter Earthquake Seismology, pages 257–292. Elsevier Amsterdam.

Hiramatsu, Y., Watanabe, T., and Obara, K. (2008). Deep low-frequency tremors as a proxy for slip monitoring at plate interface. *Geophys. Res. Lett.*, 35:L13304.

Hirose, H. and Obara, K. (2006). Short-term slow slip and correlated tremor episodes in the Tokai region, central Japan. *Geophys. Res. Lett.*, 35:L17311.

Hirshorn, B. and Weinstein, S. (2009). Rapid estimates of earthquake source parameters for tsunami warning. In Meyers, A., editor, *Encyclopedia of Complexity and Systems Science*. Springer.

Ide, S., Beroza, G. C., Prejean, S. G., and Ellsworth, W. L. (2003). Apparent break in earthquake scaling due to path and site effects on deep borehole recordings. *J. Geophys. Res.*, 108(B5):2271.

Ide, S., Beroza, G. C., Shelly, D. R., and Uchide, T. (2007). A scaling low for slow earthquakes. *Nature*, 447:76–79.

Jiang, C. and Wu, Z. (2005). Test of the preshock accelerating moment release (amr) in the case of the 26 December 2004 Mw9.0 Indonesia Earthquake. *Bull. Seismol. Soc. Am.*, 95(5):2016–2025.

Jiang, C. and Wu, Z. (2006). Benioff strain release before earthquakes in China: Accelerating of not? *Pure appl. Geophys.*, 163:1965–1976.

Johanson, I., Fielding, E. J., Rolandone, F., and Bürgmann, R. (2006). Coseismic and postseismic slip of the 2004 Parkfield earthquake from space-geodetic data. *Bull. Seism. Soc. Am.*, 96(48):5269–5282.

Johnston, M. J. S., Borcherdt, R. D., Linde, A. T., and Gladwin, M. T. (2006). Continuous borehole strain and pore pressure in the near-field of the September 28, 2004 Parkfield Earthquake: Implications for nucleation, fault response, earthquake prediction and tremor. *Bull. Seismol. Soc. Am.*, 96:56–72.

Jost, M. L. and Hermann, R. B. (1989). A student's guide to and review of moment tensors. *Seismological Research Letters*, 60:37–57.

Julian, B. (2002). Seismological detection of slab metamorphism. *Science*, 296:1625–1626.

Julian, B. R., Miller, A. D., and Foulger, G. R. (1998). Non-double-couple earthquakes, 1 Theory. *Reviews of Geophysics*, 36(4):525–549.

Kanamori, H. (1981). The nature of seismicity patterns before large earthquakes. In Simpson, D. W. and Richards, P. G., editors, *Earthquake Prediction: An International Review*, pages 1–19. American Geophysical Union.

Kanamori, H. and Anderson, D. L. (1975). Theoretical basis of some empirical relations in seismology. *Bull. Seism. Soc. Am.*, 65(5):1073–1095.

Kanamori, H. and Rivera, L. (2008). Source inversion of W phase: speeding up seismic tsunami warning. *Geophys. Journal International*, 175:222–238.

Katsumata, A. and Kamaya, N. (2003). Low-frequency continuous tremor around the Moho discontinuity away from volcanoes in the southwest Japan. *Geophys. Res. Lett.*, 30:1020.

Kawakatsu, H. (1995). Automated near-realtime cmt inversion. *Geophys. Res. Lett.*, 22:2569–2572.

Kawakatsu, H. (1998). On the realtime monitoring of the long-period seismic wavefield. *Bull. Earth. Res. Inst.*, 73:267–274.

Kedar, S., Sturtevant, B., and Kanamori, H. (1996). The origin of harmonic tremor at Old Faithful Geyser. *Nature*, 379:708–711.

Kennedy, B. M. and van Soest, M. C. (2007). Flow of mantle fluids through the ductile lower crust: helium isotope trends. *Science*, 318:1433–1436.

Kenner, S. and Segall, P. (1999). Time-dependence of the stress shadowing effect and its relation to the structure of the lower crust. *Geology*, 27(2):119–122.

Kim, A. and Dreger, D. S. (2008). Rupture process of the 2004 Parkfield earthquake from near-fault seismic waveform and geodetic records. *J. Geophys. Res.*, 113:B07308.

King, G. C. P. and Bowman, D. D. (2003). The evolution of regional seismicity between large earthquakes. *J. Geophys. Res.*, 108.

King, G. C. P., Stein, R. S., and Lin, J. (1994). Static stress changes and the triggering of earthquakes. *Bull. Seismol. Soc. Am.*, 84:935.

Konstantinou, K. I. and Schlindwein, V. (2002). Wavefield properties and source mechanism of volcanic tremor : a review. *Journal of Volcanology and Geothermal Research*, 119(161-187).

Langbein, J. et al. (2005). Preliminary report on the 28 September 2004, M 6.0 Parkfield, California earthquake. *Seismol. Res. Lett.*, 76:10–26.

Larson, K. M., Bodin, P., and Gomberg, J. (2003). Using 1 hz GPS data to measure deformations caused by the Denali Fault earthquake. *Science*, 300:1421–1424.

Lay, T. et al. (2005). The great Sumatra-Andaman earthquake of 26 December 2004. *Science*, 308.

Lay, T., Yamazaki, Y., Ammon, C. J., Cheung, K. F., and Kanamori, H. (2011). The 2011 Mw9.0 off the Pacific coast of Tohoku earthquake: Comparison of deep-water tsunami signals with finite-fault rupture model predictions. *Earth Planets Space*, 63:797–801.

Lengliné, O. and Marsan, D. (2009). Inferring the coseismic and postseismic stress changes caused by the 2004 Mw=6 Parkfield earthquake from variations of recurrence times of microearthquakes. *J. Geophys. Res.*, 114(B10303).

Lindh, A. G. (1990). The seismic cycle pursued. *Nature*, 348:580–581.

Liu, Y. and Rice, J. R. (2007). Aseismic slip transients emerge spontaneously in three-dimensional rate and state modeling of subduction earthquake sequences. *J. Geophys. Res.*, 112:B09404.

Lomax, A. and Michelini, A. (2009). Tsunami early warning using earthquake rupture duration. *Geophys. Res. Lett.*, 36:L09306.

McCrory, P. A. (2000). Upper plate contraction north of the migrating Mendocino Triple Junction, northern California: implications for partitioning of strain. *Tectonics*, 19(6):1140–1160.

McPhee, D. K., Jachens, R. C., and Wentworth, C. M. (2004). Crustal structure across the San Andreas Fault at the SAFOD site from potential field and geologic studies. *Geophys. Res. Lett.*, 31:L12S03.

Melbourne, T. I. and Webb, F. H. (2003). Slow but not quite silent. *Science*, 300:1886–1887.

Meltzner, A. J. and Wald, D. J. (1999). Foreshocks and aftershocks of the great 1857 California earthquake. *Bull. Seismol. Soc. Am.*, 89:1109.

Merritts, D. J. (1996). The Mendocino triple junction: Active faults, episodic coastal emergence, and rapid uplift. *J. Geophys. Res.*, 101(B3):6051–6070.

Michael, A. J., Felzer, K., and Hardebeck, J. (2006). Precursory accelerating moment release: fact or data-fitting fiction. *Seismol. Res. Lett.*, 77.

Mignan, A. (2011). Retrospective on the Acceleration Seismic Release (ASR) hypothesis: Controversy and new horizons. *Tectonophysics*, 505:1–16.

Mignan, A., Bowman, D. D., and King, G. C. P. (2006). An observational test of the origin of accelerating moment release before large earthquakes. *J. Geophys. Res.*, 111:B11304.

Mignan, A., King, G. C. P., and Bowman, D. (2007). A mathematical formulation of accelerating moment release based on the stress accumulation model. *J. Geophys. Res.*, 112:B07308.

Minson, S., Dreger, D., Bürgmann, R., Kanamori, H., and Larsen, K. (2007). Seismically and geodetically determined non-double-couple source mechanisms from the 2000 Miyakejima volcanic earthquake swarm. *J. Geophys. Res.*, 112:B10308.

Miyazawa, M. and Brodsky, E. E. (2008). Deep low-frequency tremor that correlates with passing surface waves. *J. Geophys. Res.*, 113:B01307.

Miyazawa, M., Brodsky, E. E., and Mori, J. (2008). Learning from dynamic triggering of low-frequency tremor in subduction zones. *Earth Planets Space*, 60:17–20.

Miyazawa, M. and Mori, J. (2005). Detection of triggered deep low-frequency events from the 2003 Tokachi-oki earthquake. *Geophys. Res. Lett.*, 32:L10307.

Miyazawa, M. and Mori, J. (2006). Evidence suggesting fluid flow beneath japan due to periodic seismic triggering from the 2004 Sumatra-Andaman earthquake. *Geophys. Res. Lett.*, 33:L05303.

Mori, N., Takahashi, T., Yasuda, T., and Yanagisawa, H. (2011). Survey of the 2011 Tohoku earthquake tsunami inundation and run-up. *Geophys. Res. Lett.*, 38:L00G14.

Murray, J. and Langbein, J. (2006). Slip on the San Andreas Fault at Parkfield, California, over two earthquake cycles, and the implications for seismic hazards. *Bull. Seism. Soc. America*, 96(4B):S283–S303.

Murray, M., Segall, P., Cervelli, P., Prescott, W., and Svarc, J. (2001). Inversion of GPS data for spacially variable slip-rate on the San Andreas Fault near Parkfield, CA. *Geophys. Res. Lett.*, 28:359–362.

Nadeau, R. M. and Dolenc, D. (2005). Nonvolcanic tremors deep beneath the San Andreas Fault. *Science*, 307:389.

Nadeau, R. M. and Guilhem, A. (2009). Nonvolcanic tremor and the 2003 San Simeon and 2004 Parkfield, California earthquakes. *Science*, 325:191–193.

Nadeau, R. M. and McEvilly, T. V. (2004). Periodic pulsing of characteristic microearthquakes on the San Andreas Fault. *Science*, 303:220–222.

Nishide, N. et al. (2000). Nationwide activity of low-frequency earthquakes in the lower crust in Japan. In *Japan. Earth Planet. Sci. Joint Meeting*.

Obara, K. (2002). Nonvolcanic deep tremor associated with subduction in southwest Japan. *Science*, 296:1679.

Obara, K. and Hirose, H. (2006). Non-volcanic deep low-frequency tremors accompanying slow slips in the southwest Japan subduction zone. *Tectonophysics*, 417(33-51).

Obara, K., Hirose, H., Yamamizu, F., and Kasahara, K. (2004). Episodic slow slip events accompanied by non-volcanic tremors in southwest Japan subduction zone. *Geophys. Res. Lett.*, 31:L26302.

Obara, K., Tanaka, S., Maeda, T., and Matsuzawa, T. (2010). Depth-dependent activity of non-volcanic tremor in southwest japan. *Geophys. Res. Lett.*, 37:L13306.

Ohmi, S. and Obara, K. (2002). Deep low-frequency earthquakes beneath the focal region of the Mw 6.7 2000 Western Tottori earthquake. *Geophys. Res. Lett.*, 29:1807.

Okada, Y. (2011). Preliminary report of the 2011 off the Pacific coast of Tohoku Earthquake.

Oppenheimer, D. (1993). The Cape Mendocino, California, earthquakes of April 1992: Subduction at the Triple Junction. *Science*, 261:433–438.

Oppenheimer, D. (2007). Mendocino Triple Junction offshore northern California, USGS. *USGS website*.

Oppenheimer, D., Klein, F., Eaton, J., and Lester, F. (1993). USGS open file report 93-578.

Parsons, T. (2002). Post-1906 stress recovery of the San Andreas fault system calculated from three-dimensional finite element analysis. *J. Geophys. Res.*, 107:2162.

Pasyanos, M. E., Dreger, D. S., and Romanowicz, B. (1996). Towards real-time determination of regional moment tensors. *Bull. Seism. Soc. Am.*, 86:1255–1269.

Payero, J. S., Kostoglodov, V., Shapiro, N., Mikumo, T., Iglesias, A., Pérez-Campos, X., and Clayton, R. W. (2008). Nonvolcanic tremor observed in the Mexican Subduction Zone. *Geophys. Res. Lett.*, 35:L07305.

Peng, Z. and Chao, K. (2008). Non-volcanic tremors underneath the Central Range in Taiwan triggered by the 2001 Mw7.8 Kunlun earthquake. *Geophys. J. Int.*, 175:825–829.

Peng, Z., Long, L. T., and Zhao, P. (2010). High-frequency artifact caused by the analysis procedure during large-amplitude surface waves. *Seismol. Res. Lett.*

Peng, Z., Vidale, J. E., Ishii, M., and Helmstetter, A. (2007). Seismicity rate immediately before and after main shock rupture from high-frequency waveforms in Japan. *J. Geophys. Res.*, 112:B03306.

Peng, Z., Vidale, J. E., Wech, A. G., Nadeau, R. M., and Creager, K. C. (2009). Remote triggering of tremor along the San Andreas Fault in central California. *J. Geophys. Res.*, 114:B00A06.

Pérez-Campos, X., McGuire, J. J., and Beroza, G. C. (2003). Resolution of the slow earthquake/high apparent stress paradox for oceanic transform fault earthquakes. *J. Geophys. Res.*, 108(B9):2444.

Prentice, C. S., Keefer, D. K., and Sims, J. (1992). Geomorphic response to the Cape Mendocino earthquake. *Earthquakes Volcanoes*, 23:123–134.

Raleigh, C. B. and Paterson, M. S. (1965). Experimental deformation of serpentinite and its tectonic implications. *J. Geophys. Res.*, 70:3965.

Reasenberg, P. and Matthews, M. V. (1988). Precursory seismic quiescence: a preliminary assessment of the hypothesis. *Pure appl. Geophys.*, 126:373–406.

Reid, H. F. (1910). The mechanics of the earthquake: the California Earthquake of April 18, 1906. *Report of the State Investigation Commission*, 2.

Richardson, E. and Marone, C. (2008). What triggers tremor? *Science*, 319:166–167.

Rogers, G. and Dragert, H. (2003). Episodic tremor and slip on the Cascadia subduction zone: the chatter of silent slip. *Science*, 300:1942.

Rolandone, F., Dreger, D., Murray, M., and Burgmann, R. (2006). Coseismic slip distribution of the 2003 Mw 6.6 San Simeon earthquake, California, determined from GPS measurements and seismic waveform data. *Geophys. Res. Lett.*, 33:L16315.

Rubinstein, J. L., Gomberg, J., Vidale, J., Wech, A., Kao, H., Creager, K., and Rogers, G. (2009). Seismic wave triggering of nonvolcanic tremor, episodic tremor and slip, and earthquakes on Vancouver Island. *J. Geophys. Res.*, 114:B00A01.

Rubinstein, J. L., Rocca, M. L., Vidale, J., Creager, K., and Wech, A. (2008). Tidal modulation of non-volcanic tremor. *Science*, 319:186–189.

Rubinstein, J. L., Shelly, D. R., and Ellsworth, W. L. (2006). Non-volcanic tremor: A window into the roots of fault zones. In Cloetingh, S. and Negendank, J., editors, *New Frontiers in Integrated Solid Earth Sciences*, pages 287–314. Springer Netherlands.

Rubinstein, J. L., Vidale, J. E., Gomberg, J., Bodin, P., Creager, K. C., and Malone, S. D. (2007). Non-volcanic tremor driven by large transient shear stresses. *Nature*, 448:579–582.

Ryder, I. and Bürgmann, R. (2008). Spatial variations in slip deficit on the central San Andreas Fault from InSAR. *Geophys. J. Int.*, 175:837–852.

Rymer, J., Lisowski, M., and Burford, R. O. (1984). Structural explanation for low creep rates on the San Andreas fault near Monarch Peak, central California. *Bull. Seismol. Soc. Am.*, 74:925.

Sammis, C. G., Bowman, D., and King, G. C. P. (2004). Anomalous seismicity and accelerating moment release preceding the 2001 and 2002 earthquakes in Northern Baja California, Mexico. *Pure appl. Geophys.*, 161:2369–2378.

Satake, K., Shimizaki, K., Tsuji, Y., and Ueda, K. (1996). Time and size of a giant earthquake in Cascadia inferred from Japanese tsunami records of January 1700. *Nature*, 379:246–249.

Savage, J. and Langbein, J. (2008). Post-earthquake relaxation after the 2004 M6 Parkfield, California, earthquake and rate-and-state friction. *J. Geophys. Res.*, 113:B10407.

Schramm, K. and Stein, S. (2009). Apparent slow oceanic transform earthquakes due to source mechanism bias. *Seismol. Res. Lett.*, 80(1):102–107.

Schwartz, S. and Hubert, A. (1997). The state of stress near the Mendocino Triple Junction from inversion of earthquake focal mechanisms. *Geophys. Res. Lett.*, 24(10):1263–1266.

Schwartz, S. Y. and Rokosky, J. M. (2007). Slow slip events and seismic tremor at circum-Pacific subduction zones. *Rev. Geophys.*, 45:RG3004.

Scott, R. D. and Kanamori, H. (1985). On the consistency of moment tensor source mechanisms with first-motion data. *Physics of the Earth and Planetary Interiors*, 37:97–107.

Shao, G., Li, X., Ji, C., and Maeda, T. (2011). Preliminary result of the March 11th, 2011 Mw9.1 Honshu earthquake.

Shelly, D. R., Beroza, G. C., Ide, S., and Nakamula, S. (2006). Low-frequency earthquakes in Shikoku, Japan, and their relationship to episodic tremor and slip. *Nature*, 442:188–191.

Shelly, D. R., Ellsworth, W. L., Ryberg, T., Haberland, C., Fuis, G. S., Murphy, J., Nadeau, R. M., and Bürgmann, R. (2009). Precise location of San Andreas Fault tremors near Cholame, California using seismometer clusters: Slip on the deep extension of the fault? *Geophys. Res. Lett.*, 36:L01303.

Shelly, D. R. and Hardebeck, J. L. (2010). Precise tremor source locations and amplitude variations along the lower-crustal central San Andreas Fault. *Geophys. Res. Lett.*, 37:L14301.

Shelly, D. R. and Johnson, K. M. (2011). Tremor reveals stress shadowing, deep postseismic creep, and depth-dependent slip recurrence on the lower-crustal San Andreas fault near Parkfield,. *Geophys. Res. Lett.*, 38:L13312.

Shelly, D. R., Peng, Z., Hill, D. P., and Aiken, C. (2011). Triggered creep as a possible mechanism for delayed dynamic triggering of tremor and earthquakes. *Nature Geoscience*, 4:384–388.

Sieh, K. (1978). Slip along the San Andreas Fault associated with the great 1857 earthquake. *Seismol. Soc. America Bull.*, 68:1421–1428.

Smith, E. F. and Gomberg, J. (2009). A search in strainmeter data for slow slip associated with triggered and ambient tremor near Parkfield, California. *J. Geophys. Res.*, 114:B00A14.

Sykes, L. R. and Jaumé, S. (1990). Seismic activity on neighboring faults as a long- term precursor to large earthquakes in the San Francisco Bay Area. *Nature*, 348:595–599.

Szeliga, W., Melbourne, T. I., Miller, M. M., and Santillan, V. M. (2004). Southern Cascadia episodic slow earthquakes. *Geophys. Res. Lett.*, 31:L16602.

Taira, T. and Nadeau, R. M. (2011). Source characterization of Mendocino offshore earthquakes for improvements in monitoring active deformation and estimates of earthquake potential in the Mendocino Triple Junction Region. *BSL annual report*.

Templeton, D. C., Nadeau, R. M., and Bürgmann, R. (2008). Behavior of repeating earthquake sequences in central california and the implications for subsurface fault creep. *Bull. Seism. Soc. Am.*, 98:52–65.

Thomas, A., Nadeau, R. M., and Burgmann, R. (2009). Tremor-tide correlations and near-lithostatic pore pressure on the deep San Andreas fault. *Nature*, 462:24–31.

Tkalcic, H., Dreger, D. S., Foulger, G. R., and Julian, B. R. (2009). The puzzle of the 1996 Bardarbunga, Iceland, Earthquake: No volumetric component in the source mechanism. *Seismol. Res. Lett.*, 99:3077–3085.

Toda, S., Stein, R. S., Richards-Dinger, K., and Bozkurt, S. (2005). Forecasting the evolution of seismicity in southern California: Animations built on earthquake stress transfer. *J. Geophys. Res.*, 110:B05S16.

Toppozada, T. R. and Branum, D. M. (2002). California earthquakes of M>5: their history and areas damages. In Lee, W. H. K., editor, *International Handbook of Earthquake and Engineering Seismology*, volume A, pages 793–796. Academic Press.

Tsuruoka, H., Kawakatsu, H., and Urabe, T. (2009a). Grid MT (grid-based real-time determination of moment tensors) monitoring the long-period seismic wavefield. *Physics of the Earth and Planetary Interiors*, 175:8–16.

Tsuruoka, H., Rivera, L., Kawakatsu, H., and Kanamori, H. (2009b). Realtime source inversion using W-phase and GRiD MT for regional tsunami early warning. In *AGU meeting*.

Uhrhammer, R. A., Dreger, D., and Romanowicz, B. (2001). Best practice in earthquake location using broadband three-component seismic waveform data. *Pure appl. Geophys.*, 158:259.

USGS (2008). Working Group on California Earthquake Probabilities. 2007-1437.

Velasco, A. A., Ammon, C. J., and Lay, T. (1994). Recent large earthquakes near Cape Mendocino and in the Gorda plate: broadband source time functions, fault orientations, and rupture complexities. *J. Geophys. Res.*, 99(B1):711–728.

Vigny, C. et al. (2011). The 2010 Mw8.8 Maule megathrust earthquake of central Chile monitored by GPS. *Science*, 332(6036):1417–1421.

Wallace, R. E., editor (1990). *U.S. Geological Survey Professional Paper, 1515*, volume 238. Washington, CC.

Wang, Y., Yin, C., Mora, P., Yin, X.-C., and Peng, K. (2004). ), spatio-temporal scanning and statistical test of the accelerating moment release (AMR) model using Australian Earthquake Data. *Pure appl. Geophys.*, 161:2281–2293.

Wech, A. G., Creager, K. C., and Melbourne, T. I. (2009). Seismic and geodetic constraints on Cascadia slow slip. *J. Geophys. Res.*, 114(B10316).

Wells, D. L. and Coppersmith, K. J. (1994). New empirical relationship among magnitude, rupture length, rupture width, rupture area, and surface displacement. *Bull. Seism. Soc. Am.*, 84(4):974–1002.

Yamazaki, Y. and Cheung, K. F. (2011). Shelf resonance and impact of near-field tsunami generated by the 2010 Chile earthquake. *Geophys. Res. Lett.*, 38:L12605.

Yue, H. and Lay, T. (2011). Inversion of high-rate (1sps) GPS data for rupture process of the 11 March 2011 Tohoku earthquake (Mw9.1). *Geophys. Res. Lett.*, 38:L00G09.

Zhang, H., Nadeau, R. M., and Toksoz, M. N. (2010). Locating nonvolcanic tremors beneath the San Andreas Fault using a station-pair double-difference location method. *Geophys. Res. Lett.*, 37:L13304.